POLITECNICO DI MILANO
DIPARTIMENTO DI ELETTRONICA, INFORMATICA E BIOINGEGNERIA
DOCTORAL PROGRAMME IN TELECOMMUNICATION ENGINEERING

SYNCHRONIZATION AND PERFORMANCE EVALUATION OF FUTURE WIRELESS CELLULAR SYSTEM BASED ON THE USE OF NEW MULTI-CARRIER TRANSMISSION TECHNIQUES

Doctoral Dissertation of:
Atul Kumar

Supervisor:
Prof. Maurizio Magarini

Tutor:
Prof. Andrea Monti Guarnieri

The Chair of the Doctoral Program:
Prof. Andrea Bonarini

CERTIFICATE

This is to certify that the thesis entitled as "**Synchronization and Performance Evaluation of Future Wireless Cellular System Based on the Use of New Multi-Carrier Transmission Techniques**", submitted by "**Atul Kumar (10450012)**" in Telecommunication Engineering of the Dipartimento di Elettronica, Informatica e Bioingegneria, POLITECNICO DI MILANO, Milano, ITALY, for the award of Degree of Doctor of Philosophy, is a bonafide record of the research work carried out by him under supervision of "**Prof. Maurizio Magarini**" and his guidance. The contents of this Thesis, in full or parts, have not been submitted to any other Institute or University for the award of any other degree or diploma.

Prof. Maurizio Magarini
Department di Elettronica, Informazione e Bioingegneria.
Politecnico di Milano, Italy.

I

ACKNOWLEDGEMENT

I would like to thank all those who offered me the opportunity to complete my PhD. I want to thank the Department di Elettronica, Informazione e Bioingegneria of **POLITECNICO DI MILANO** for giving me such a golden opportunity to complete my PhD.

I express our deepest gratitude to **Prof. Maurizio Magarini** who encouraged me to go ahead with PhD. It is a matter of pride and privilege for me to complete my PhD under his close supervision. Whatever is said in the praise of **Prof. Maurizio Magarini** is not enough, his soul touching humility, his straight forward attitude, his methodological approach, his eagerness to share his wisdom, his aim for perfection and his never ending encouragement and patience are but a few of his noble qualities.

It is certainly good karma to have **Prof. Maurizio Magarini** for supervising me as his advice, his words of wisdom and valuable guidance have allowed the completion of our work without any hassle.

My special appreciation goes to professors, who has inspired and guided me during my PhD in this institution by their brilliant and expert teaching. I gratefully acknowledge the help and cooperation extended by the library staff of the faculty as well as university.

My heart gratitude goes to my parents and all friends for their invaluable inspiration extended in the pursuit of this work.

ABSTRACT

IN recent years, the evolution of cellular technology and connectivity has led to a major revolution in the wireless communication industry, with differnt major application scenarios *i.e.* enhanced mobile broadband (eMBB), massive machine type communication (mMTC), ultra-reliable and low latency communications (URLLC), and vehicle-to-everything (eV2X).

In order to, target mMTC applications, the important scenario considered here is Internet of Things (IoT). Physical layer (PHY) requirements for mMTC application are: low latency; large number of connected devices; high reliability; asynchronous transmission; and dynamic fragmented spectrum access.

Current (4th generation) cellular transmission schemes, which are based on Long-Term Evolution (LTE) and LTE-Advanced (LTE-A), employ orthogonal frequency division multiplexing (OFDM) waveform in PHY design. As is well known, synchronization represents one of the most challenging issues and plays a major role in PHY design and its impact can also be higher in future wireless cellular system, where the use of non-proportional sub-carrier spacing will be required to accommodate the necessary bandwidth. Motivated by this, I studied and realized this Thesis work that concerns with "Synchronization and Performance Evaluation of Future Wireless Cellular System Based on the Use of New Multi-Carrier Transmission Techniques".

With this aim, I started studying about the two categories of multi-carrier waveforms: legacy OFDM waveforms and new waveforms for future wireless cellular systems. For the legacy OFDM waveforms, I studied mainly about the cyclic prefix (CP)-based OFDM system and also an OFDM system with an advanced transformation tool, known as discrete fractional Fourier transform (DFrFT). DFrFT-based OFDM system is analogous to the conventional OFDM one with the difference that DFT and inverse DFT (IDFT) are replaced by DFrFT and inverse DFrFT (IDFrFT), respectively. DFrFT is a generalization of the ordinary DFT with an DFrFT angle parameter (α). Moreover, I started analyzing the effect of synchronization issues, in particular, the problem of evaluating performance in the presence of symbol timing offset (STO) and carrier fre-

quency offset (CFO). Here, we consider the chirp-based DFrFT method for both CFO and STO estimation. From the demonstrated results of mean square error (MSE) performance of CFO and STO estimations, it is realized that CFO and STO estimators with chirp-based DFrFT method performs better than other methods available in literature in case of the transmission over multipath fading channel.

However, in the presence of oscillator drifts and time-varying Doppler shifts, residual CFO and STO are still present in the received signal after the application of synchronization algorithms. In order to improve the robustness to residual CFO and STO, an OFDM system based on DFrFT is considered. Therefore, it would be better to analyse the analytical symbol error probability (SEP) performance of the DFrFT-based OFDM by considering residual CFO and STO together. This is demonstrated by quantifying its effect in an analytical expression of the term responsible for introducing inter carrier interference (ICI) and inter symbol interference (ISI), which is one of the novel contributions of this Thesis. The results of the SEP performance of the DFrFT-based OFDM system in the presence of residual synchronization errors, *i.e.*, CFO and STO, demonstrate that the performance of DFrFT-based OFDM system depends on the DFrFT angle parameter (α) and, by properly selecting its optimal value α_{opt}, DFrFT-based OFDM system performs better than the one based on the DFT. Therefore, the calculation of optimal DFrFT angle parameter is important for better performance of DFrFT-based OFDM system. In this Thesis, we also derived an analytical expression to calculate the optimal value of α_{opt} based on CFO and STO values. This is another novel contribution of this Thesis. Finally, we also considered more practical aspects related to the realization of a Software Defined Radio (SDR) system which is used to implement hardware co-simulation of multi-carrier transmission techniques. We have considered field-programmable gate array (FPGA)-in-the-Loop (FIL) co-simulation of receiver with equalization of DFrFT-based OFDM system transmission over a frequency selective Rayleigh fading channel in presence of CFO. My simulation results clearly demonstrate that the FPGA implementation of a DFrFT-based OFDM system in presence of CFO has the same performance as that obtained from Monte Carlo simulation. Also, the performance is validated with the fixed-point model of DFrFT-based OFDM. The approach described in the thesis constitutes an efficient way to convert the floating-point model into a fixed-point one to be run in an FPGA and then verifies its correctness through FIL co-simulation.

However, as it is well known, CP-based OFDM uses fixed set of waveform parameters, including sub-carrier spacing and length of CP that, are uniformly applied across the entire system bandwidth. Due to the lack of flexibility in supporting mixed services with different waveform parameters within one carrier, which is a key requirement in the PHY design of future cellular network. Additionally, high out-of-band (OOB) emission in frequency-domain is introduced by the time-domain rectangular pulse shaping filter. Also, OFDM signal with one CP per symbol may have a prohibitive low spectral efficiency and also increase the OFDM symbol duration. For this reason, new waveforms that are able to support variable and customizable pulse shaping filters in order to achieve a better trade-off between time-domain and frequency-domain localization is one of the research priorities. With this aim, generalized frequency division multiplex-

ing (GFDM) is one of the proposed multi-carrier waveforms for future wireless cellular systems, which is based on the use of circular filtering at sub-carrier level. Compared to CP-based OFDM, the important advantages of GFDM consist in a reduction of OOB emission, achieved by means of filtering at sub-carrier level, in an increase of spectral efficiency, obtained through the introduction of tail biting, which makes the length of the CP independent from that of pulse shaping filter. Moreover, the flexible frame structure of GFDM is achieved, by changing the number of time slots and sub-carriers in a frame, covering both conventional OFDM and DFT-spread OFDM. (DFT-s-OFDM), which results in complete backward compatibility with LTE.

Motivated with the GFDM, we focus on the integration of GFDM in the time-frequency grid of LTE system and then analyse the impact of "Better than Nyquist" pulse shaping filters on OOB emission and symbol error rate (SER). Moreover, we also consider the concept of wavelet for better time-frequency localization of pulse shaping filters by using the Meyer auxiliary function. After the impact of pulse shaping filter, for an efficient implementation of receiver in time-domain, a relationship between GFDM signal and discrete Gabor transform (DGT) is investigated for reducing the complexity. After that, we implement DGT-based GFDM when the synthesis function, *i.e.* pulse shaping filter, and the analysis function, *i.e.* receiving filter, satisfy the *Wexler-Raz* identity. Choosing functions that satisfy the Wexler-Raz condition allows for optimal symbol-by-symbol detection after DGT-based receiver in case of ideal channel. However, when transmission takes place over a frequency selective channel, symbol-by-symbol detection of sub-symbols is no longer optimal due to inter-sub-symbol interference (ISSI) generated by sub-symbols transmitted over the same sub-carrier, to improve the performance maximum likelihood detection (MLD) is implemented as a optimal detector for all the sub-symbols on the same sub-carrier, which is another novel contribution of this thesis. Finally, we derive exact SEP expressions for GFDM waveform in the presence of CFO in AWGN channel and frequency selective Rayleigh fading channel. The analytical expressions of SEP are derived when matched filtering is implemented at the receiver for BPSK, QPSK, and 16-QAM in case of AWGN channel and for BPSK only in case of frequency selective Rayleigh fading channel which is another contribution. Monte Carlo simulations are presented to demonstrate the exactness of the derived SEP expressions.

SOMMARIO

Negli ultimi anni l'evoluzione tecnologica nell'ambito delle comunicazioni radiomobili cellulari ha portato a una grande rivoluzione nel settore delle comunicazioni wireless, con nuovi scenari applicativi quali l'aumento della velocità di trasmissione a banda larga (eMBB, enhanced mobile broadband), le comunicazioni tra un numero elevatissimo di macchine (mMTC, massive machine type communication), le comunicazioni ad altissima affidabilità e a bassa latenza (URLLC, ultra-reliable and low latency communications) ed, infine, quelle veicolari ed infrastutture fisse e mobili (eV2X, vehicle-to-everything).

Per quanto riguarda le applicazioni mMTC lo scenario più importante qui considerato è l'internet delle cose (IoT, Internet of Things). I requisiti del livello fisico (PHY) per applicazioni mMTC sono la bassa latenza, il gran numero di dispositivi connessi, l'alta affidabilità, la trasmissione asincrona e un accesso dinamico allo spettro frammentato.

Gli attuali schemi di trasmissione cellulare di quarta generazione, basati su LTE (Long-Term Evolution) e LTE-Advanced (LTE-A), impiegano forme d'onda con multiplazione a divisione di frequenza ortogonale (OFDM) a livello fisico. Come è noto, la sincronizzazione rappresenta uno dei problemi più impegnativi e svolge un ruolo importante nella progettazione del livello fisico. Il suo impatto può anche essere maggiore nei futuri sistemi cellulari in cui verrà richiesto l'uso di una spaziatura tra sottoportanti variabile per allocare la banda necessaria. Con tale motivazione, in questo lavoro di tesi ho studiato ed analizzato il problema della sincronizzazione e la relativa valutazione delle prestazioni nei sistemi cellulari di prossima generazione che sono basati sull'impiego nuove modulazioni multi-portante.

A tal fine mi sono concentrato su due categorie di forme d'onda multi-portanti: i) "OFDM compatibili"; ii) "nuove forme d'onda". Per quanto riguarda le forme d'onda "OFDM compatibili" ho studiato principalmente il sistema OFDM basato sul prefisso ciclico (CP) e quello basato su una tecnica avanzata di trasformazione nota come "trasformata frazionaria di Fourier discreta (DFrFT)". Il sistema OFDM basato su DFrFT è analogo a quello OFDM convenzionale con la differenza che trasformata

discreta di Fourier (DFT) e la sua anti trasformata (IDFT) sono sostituiti, rispettivamente, dalla DFrFT e dalla anti trasformata DFrFT (IDFrFT). La DFrFT è una generalizzazione della DFT ordinaria che è definita da un parametro $alpha$, che definisce l'angolo tra la dimensione temporale e quella frequenziale. Durante l'attivitÃ mi sono occupato anche dei problemi relativi ai problemi di sincronizzazione, con particolare riferimento alla valutazione delle prestazioni in presenza di offset nella sincronizzazione di simbolo (STO, symbol-timing offset) e di frequenza portante (CFO, carrier frequency offset). Nella tesi ho considerato la DFrFT basata su chirp per effettuare sia la stima di CFO che di STO. Dai risultati ottenuti, misurati in termini di errore quadratico medio nell'errore nella stima di CFO e STO, si evince che gli stimatori di CFO e STO con DFrFT basata su chirp offrono migliori prestazioni rispetto ad altri metodi disponibili in letteratura nel caso di trasmissione su canale selettivo in frequenza.

In presenza di derive temporali dell'oscillatore e spostamenti Doppler, si verifica che CFO e STO residui sono ancora presenti nel segnale ricevuto dopo le correzioni apportate dagli algoritmi di sincronizzazione. Al fine di migliorare la robustezza nei confronti di CFO e STO residui si è considerato un sistema OFDM basato su DFrFT. Per tale sistema si Ã¨ effettuata l'analisi delle prestazioni considerando il calcolo analitico della probabilitÃ di errore sul simbolo (SEP) di un sistema OFDM basato su DFrFT in cui si considera la presenza simultanea di CFO e STO residui. Il loro effetto congiunto Ã¨ stato quantificato in un'espressione analitica che tiene conto del termine responsabile dell'introduzione dell'interferenza tra sotto-portanti (ICI) e interferenza intersimbolica (ISI), che è uno dei nuovi contributi di questa tesi. I risultati delle prestazioni SEP del sistema OFDM basato su DFrFT in presenza di errori di sincronizzazione residui dimostrano che le prestazioni del sistema OFDM basato su DFrFT dipendono dal parametro α. Selezionando opportunamente il valore ottimo α_{opt}, il sistema OFDM basato su DFrFT permette di ottenere prestazioni migliori di quello basato su DFT. Pertanto, il calcolo del parametro α ottimo Ã¨ importante per migliorare le prestazioni del sistema OFDM basato su DFrFT. In questa tesi, ho anche derivato un'espressione analitica per calcolare il valore ottimale di α_{opt} in funzione dei valori dati di CFO e STO. Questo rappresenta un altro contributo importante del lavoro di tesi. Infine, ho preso in considerazione anche aspetti più pratici legati alla realizzazione di un sistema "Software Defined Radio (SDR)", che viene utilizzato per implementare la co-simulazione hardware delle tecniche di trasmissione multi-portante. Ho preso in considerazione la co-simulazione di FPGA che implementa l'equalizzazione della trasmissione del sistema OFDM basata su DFrFT su un canale soggetto a fading di Rayleigh selettivo in frequenza in presenza di CFO. I risultati della mia simulazione dimostrano chiaramente che l'implementazione FPGA di un sistema OFDM basato su DFrFT in presenza di CFO ha le stesse prestazioni ottenute con la simulazione Monte Carlo. Inoltre, le prestazioni sono validate con il modello a virgola fissa di un sistema OFDM basato su DFrFT. L'approccio descritto nella tesi costituisce un modo efficace per convertire il modello in virgola mobile in uno a virgola fissa da eseguire in un'FPGA e, quindi, consente di verificarne la correttezza attraverso la co-simulazione FPGA-in-the loop.

Come è ben noto, l'OFDM basato su CP utilizza un insieme predefinito di parametri,

tra cui la spaziatura tra le sotto-portanti e la lunghezza di CP, che vengono applicati sull'intera larghezza di banda del sistema. Tutto ciò provoca una mancanza di flessibilità nell'offerta di servizi con diversi requisiti. Inoltre, un altro problema è legato all'elevata emissione fuori banda (OOB) nel dominio della frequenza che viene introdotta dal filtro di trasmissione ti tipo rettangolare nel dominio del tempo. Inoltre, il segnale OFDM con un CP per simbolo può avere una bassa efficienza spettrale. Per tale motivo, una delle priorità di ricerca riguarda a definizione di nuove forme d'onda in grado di supportare filtri a spaziatura variabile e modificabili al fine di ottenere un migliore compromesso tra la localizzazione del dominio del tempo e della frequenza. Con tale finalità, la multiplazione a divisione di frequenza generalizzata (GFDM) rappresenta una delle tecniche multi-portante proposte per i futuri sistemi cellulari wireless, che si basa sull'uso di filtri circolari a livello di sotto-portante. Rispetto all'OFDM basato su CP, i vantaggi importanti del GFDM consistono in una riduzione dell'emissione di OOB, ottenuta mediante filtraggio a livello di sotto-portante e in un aumento dell'efficienza spettrale, ottenuta attraverso l'introduzione del "tail-biting", che rende la lunghezza del CP indipendente da quella del filtro di trasmissione. La struttura flessibile della trama GFDM è ottenuta modificando il numero di slot-temporali e sotto-portanti in una trama, permettendo di ottenere sia l'OFDM convenzionale che il DFT-spread OFDM. (DFT-s-OFDM), che permettono quindi di ottenere una retro-compatibilità completa con l'LTE.

Con tale motivazione, mi sono concentrato sull'integrazione del GFDM nella griglia tempo-frequenza del sistema LTE e ho quindi analizzato l'impatto di filtri di forma che realizzano impulsi di Nyquist ottimizzati che permettono di ridurre l'emissione OOB e migliorare il tasso di errore sul simbolo (SER). Inoltre, ho considerato anche il concetto di ondina (wavelet) per migliorare la localizzazione in frequenza e nel tempo dei filtri di forma usati in trasmissione attraverso la funzione ausiliaria di Meyer. Successivamente, per studiare l'impatto dei filtri di trasmissione e ricezione, ho studiato la relazione esistente tra il segnale GFDM e la trasformata di Gabor discreta (DGT) al fine di ridurre la complessità. In particolare, mi sono focalizzato sull'implementazione della GFDM basata su DGT, in cui il filtro di trasmissione e quello di ricezione soddisfano l'identità di Wexler-Raz. La scelta delle funzioni che soddisfano la condizione Wexler-Raz consente la rivelazione ottimale simbolo per simbolo nel caso di trasmissione su canale ideale. Tuttavia, quando la trasmissione avviene su un canale selettivo di frequenza, la rilevazione simbolo per simbolo non è più ottimale a causa dell'interferenza inter-simbolica tra simboli inviati con la stessa sotto-portante. Per migliorare la prestazione si considera l'implementazione a massima verosimiglianza (MLD) in cui tutti i sotto-simboli trasmessi sulla stessa sotto-portante sono rivelai in modo ottimo. Tale aspetto rappresenta un altro contributo innovativo di questo lavoro di tesi. Per concludere, ho derivato le espressioni esatte di SEP per la forma d'onda GFDM in presenza di CFO per trasmissione su canale AWGN e su canale con fading di Rayleigh selettivo in frequenza. Le espressioni analitiche del SEP sono state derivate per le modulazioni BPSK, QPSK e 16-QAM nel caso di canale AWGN e per la sola BPSK nel caso di canale con fading di Rayleigh selettivo in frequenza. L'esattezza delle espressioni di SEP ottenute è stata dimostrata mediante

LIST OF ABBREVIATIONS

S.No.	Abbreviation	Description
1	1G	First Generation
2	2 G	Second Generation
3	2.5 G	Third Generation
4	3GPP	3G Partnership Project
5	4G	Fourth Generation
6	5GNOW	5th Generation Non-Orthogonal Waveforms for Asynchronous Signalling
7	ADC	Analog-to-digital converter
8	ADSL	Asymmetric Digital subscriber lines
9	AMPS	Advanced Mobile Phone System
10	AMTS	Advanced Mobile Telephone System
11	AWGN	Additive White Gaussian Noise
12	BER	Bit Error Rate
13	BW	Band Width

14	CCDF	Complementary Cumulative Distributive Function
15	CDMA	Code Division Multiple Access
16	CFO	Carrier Frequency Offset
17	CP	Cyclic Prefix
18	DAB	Digital Audio Broadcasting
19	DAC	Digital-to-Analog converter
20	DFrFT	Discrete Fractional Fourier Transform
21	DFT	Discrete Fourier Transform
22	FFT	Fast Fourier Transform
23	DSP	Digital Signal Processing
24	DVB-T	Terrestrial Digital Video Broadcasting
25	FDD	Frequency Division Duplex
26	FDM	Frequency Division multiplexing
27	FDMA	Frequency Division multiplexing Access
28	FEQ	Frequency Domain Equalizer
29	FFO	Fractional Frequency Offset
30	FM	Frequency Modulation
31	SEP	Symbol error probability
32	FT	Fourier Transform

33	Gbps	Giga bit per second
34	HDSL	High Bit Rate Digital Subscriber line
35	HPA	High Power Amplifier
36	ICI	Inter Carrier Interference
37	IDFT	Inverse Discrete Fourier Transform
38	IFFT	Inverse Fast Fourier Transform
39	IFO	Integer Frequency Offset
40	Kbps	Kilobit Per Sec
41	MB-OFDM	Multiband OFDM
42	MC	Multi Carrier
43	MCM	Multi Carrier Modulation
44	MC-CDMA	Multi Carrier CDMA
45	MMSE	Minimum Mean-Square Error
46	M-PSK	M-ary Phase shift keying
47	M-QMA	M-ary Quadrature Amplitude Modulation
48	OFDM	Orthogonal Frequency Division Multiplexing
49	OFDMA	Orthogonal Frequency Division Multiplexing Access
50	PAPR	Peak to Average Power Ratio
51	SC	Single Carrier
52	SIR	Signal to interference Ratio

53	SNR	Signal to Noise Ratio
54	TDD	Time Division Duplex
55	TDM	Time Division Multiplexing
56	TDMA	Time Division Multiplexing Access
57	W-CDMA	Wideband CDMA
58	DSP	Digital Signal Processing
59	FPGA	Field Programmable Gate Array
60	SDR	Software Defined Radio
61	ZED	Zynq^{TM} Evaluation and Development
62	EPP	Extensible Processing Platform
63	PS	Processing System
64	PL	Programmable Logic
65	ISI	Inter-Symbol Interference
66	FBMC	Filter Bank Multi-Carrier
67	GFDM	Generalized Frequency Division Multiplexing
68	UFMC	Unified Frequency Multi-Carrier
69	HST	High-speed trains
70	RTL	Register-Transfer Level
71	STO	Symbol Timing Offset
72	VHDL	VHSIC Hardware Description Language

73	BFDM	Bi-orthogonal Frequency Division Multiplexing
74	MIMO	multiple-input multiple-output
75	Fi	Fixed point representation
76	HDL	Hardware Description Language
77	LTE-A	Long Term Evolution - Advanced
78	MTC	Machine-Type-Communication
79	M2M	Machine-To-Machine
80	RF	Radio Frequency
81	ESM	Emission Spectrum Mask
82	PHY	Physical Layer
83	CoMP	Coordinated Multipoint
84	UMTS	Universal Mobile Telecommunications System
85	MAC	Medium Access Layers
86	W-OFDM	Weighted Overlap and Add (WOLA) based OFDM
87	F-OFDM	Filter-OFDM
88	SDR	Software Defined Radio
89	ISI	Inter-symbol interference
90	DGT	Discrete Gabour transform

91	eMBB	Enhanced mobile broadband
92	mMTC	Massive machine type communication
93	URLLC	Ultra-reliable and low latency communications
94	ITU	International Telecommunication Union
95	IMT	International Mobile Telecommunications

LIST OF SYMBOLS

S. No	Symbols	Description
1	$\Delta\epsilon$	Carrier-frequency offset normalized by sub-carrier spacing
2	$\Re[x]$	Real part of x
3	$\Im[x]$	Imaginary part of x
4	γ or ϱ	Average signal-to noise ratio (SNR)
5	α	DFrFT angle parameter
6	P_ξ	Conditional BER
7	τ_l	Propagation Delay of the lth path
8	σ_l^2	Variance of each lth path
9	σ_w^2	Variance of AWGN
10	σ_{ICI}^2	ICI Power of the q^{th}Sub-Carrier
11	τ_{max}	Maximum channel delay spread
12	Δf	Carrier-frequency offset (CFO)
13	$E[\cdot]$	Expectation average

14	$f_k = k/T_u$	Sub-carrier Frequency of the kth sub-carrier
15	G or CP	Total Number of sub-carrier in Guard Band (CP)
16	$h(\tau, t)$	Multipath fading channel impulse response
17	$h_l(t)$	complex amplitude or tap coefficient of the lth path
18	$H(k)$ or $\beta(k)$	Channel Response in frequency domain
19	L	Total number of path
20	N_0	Noise power spectral density
21	N	Total Number of sub-carrier
22	$r(i, t)$	Received signal in time domain
23	$r(i, n)$	Received signal in frequency domain
24	$S(k - p + \varepsilon)$	ICI Coefficient
25	SIR_q	Signal to interference ratio on q^{th} sub-carrier
26	T_s	Sampling time
27	T_u	Useful symbol duration
28	T_g	Guard band time
29	T_{sym}	Symbol time
30	T_{th}	Threshold time
31	$w(i, t)$	AWGN noise
32	$\varphi(\omega)$	Output of characteristic function

33	$P_b(\xi)$	Conditional BER
34	P_b	Unconditional BER
35	β_k	Real part of ICI term
36	δ_k	Imaginary part of ICI term
37	$\triangle\,\theta$	Symbol timing offset
38	$g(\cdot)$	Raised cosine impulse response
39	$sgn(\cdot)$	Signum function
40	$H(\cdot)$	Hermitian transpose
41	$\overline{(\cdot)}$ or $(\cdot)^{*}$	Complex conjugate
42	$\otimes$	Convolution

List of Figures

List of Figures

List of Tables

Contents

Contents

CHAPTER *1*

Introduction

T HIS chapter consists of motivation and background for future generation cellular systems. Then limitations of the current (4th generation) cellular system at physical layer (PHY). It also consists of comparative studies of different waveforms and then by using the different advanced transformation tools to improve the limitation of the waveforms. Finally, problem formulation and main contributions of the Thesis are given.

1.1 Motivation and background

Historically, the evolution of wireless cellular systems has been fueled by the need for increased throughput. Indeed, the need for larger data-rates has been the main driver of the path that has led us from second generation (2G) cellular systems [1] to fourth generation (4G) cellular systems, with data-rates evolving from tens of kbit/s up to the current state-of-the-art order of Gbit/s. Focusing on the physical layer (PHY), and in particular on the adopted modulation schemes, the transition has been from binary modulations such as the Gaussian minimum shift keying (GMSK), used in 2G GSM system to quadrature-amplitude-modulation (QAM) schemes being used in 4G systems [2].

Unlike previous generations of cellular systems, for future cellular system, International Telecommunication Union (ITU) has categorized the usage scenarios for In-

---

[1]Indeed analog first generation (1G) cellular systems had no data transmission capability; they just offered voice services.
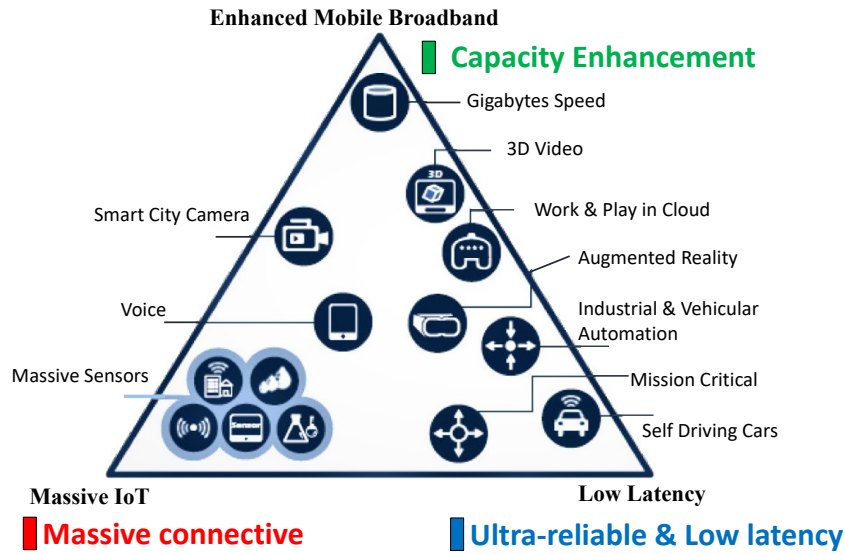
Figure 1.1: *Future use cases and their requirements by IMT in 2020 time frame.*

ternational Mobile Telecommunications (IMT) in 2020 time frame and beyond into three main groups [3–5]: enhanced mobile broadband (eMBB) [6], massive machine type communication (mMTC) [7], and ultra-reliable and low latency communications (URLLC) [8]. The different varieties of services and emerging new applications associated with each group are shown in Fig 1.1. Apart from this, enhanced vehicle-to-everything (eV2X) communication are also considered as an important service for the future cellular system [3].

These scenarios require not only high data throughput but also massive connectivity with low round-trip latency and high reliability with high system throughput and improved spectral efficiency [3]- [9]. From Fig. 1.1, it is clearly visible that all these mentioned use cases can be broadly divided into three main groups and each group has its own requirements depending on the applications given in Table 1.1 [10]- [11]. Strict requirements of each group are described as [12]:

- **Massive connectivity**: mMTC supports a massive number of Internet of Things (IoT) devices, which are only sporadically active and send small data payloads. The objective in the design of mMTC is to maximize the arrival rate that can be supported in a given radio resource. The targeted packet error rate (PER) of an individual mMTC transmission is typically low [13].

- **Ultra-reliable and low latency**: URLLC supports low-latency transmissions of small payloads with very high reliability from a limited set of terminals, which are active according to patterns typically specified by outside events, such as alarms. To guarantee the low latency requirements, URLLC transmissions should be localized in time. The rate of URLLC transmissions is relatively low, and the main

Table 1.1: *Key capabilities of IMT 2020 and their enhancements with respect to IMT-Advanced*

Key Capability	IMT-Advanced	IMT-2020
Peak data rate	1 Gbit/s	20 Gbit/s
User experienced data rate	10 Mbit/s	100 Mbit/s
Latency	10 ms	1 ms
Mobility	350 km/h	500 km/h
Connection density	10^5 devices/km^2	10^6 devices/km^2
Network energy efficiency	1X	100X
Spectrum efficiency	1X	3X
Area traffic capacity	0.1 Mbit/s/m^2	0.1 Mbit/s/m^2

requirement is to ensure a high reliability level, with a PER typically lower than 10^{-5}, despite the small block lengths [14].

- **Capacity enhancement**: eMBB supports stable connections with very high peak data rates, as well as moderate rates for cell-edge users. The objective of eMBB service is to maximize the data rate, while guaranteeing a moderate reliability, with PER on the order of 10^{-3} [15].

It is expected that each group and its deployment scenario will prefer different physical signaling formats for achieving the best possible performance [10, 11]. For instance, a smaller sub-carrier spacing would help to support the massive connections required for mMTC and also due to the use of many cheap devices for mMTC, while a larger one with shorter symbol duration may help to reduce latency for URLLC services [14]. The use of short frames has a positive impact on mobility support and operational frequencies. By reducing the frame duration, it is possible either to support higher mobility or to operate in a higher frequency range [16]. Finally, a short frame brings benefits to upper protocol layers, although the latency requirements of real-time applications demand a robust PHY to avoid retransmissions of the frame [14]. In order to target all three groups, a flexible air interface framework would be required [17]. Therefore, the waveform, as the shaping component of any air interface, has to be designed carefully to enable such flexibility.

The impact of synchronization issues can also be higher in future wireless cellular system, where the use of non-proportional sub-carrier spacing will be required to accommodate the necessary bandwidth [16]. As its consequence, orthogonality is destroyed and inter-carrier interference (ICI) among the sub-carriers and inter-symbol

interference (ISI) will arise [18]. A possible solution to this problem, that has been recently investigated, consists in abandoning strict orthogonality among sub-carriers partially or altogether and controlling the impairments instead.

To this aim, a flexible multi-carrier waveform concept has come into existence [17]. Concerning with 5th generation (5G) New Radio (NR), different variants of OFDM, i.e., DFT-spread OFDM, filtered OFDM, and windowed-OFDM, will play a key role in the scenarios categorized in the 2020 time frame by ITU. The waveforms discussed in this Thesis are broadly classified into two categories [4]: legacy OFDM waveforms [19] and new waveforms [9, 20, 21]. The waveforms based on the legacy orthogonal frequency-division multiplexing (OFDM) can be considered as straightforward but non-trivial enhancements of CP-based OFDM, including windowed OFDM (W-OFDM) [22], universal filtered multi-carrier (UFMC) [20], and filtered OFDM (F-OFDM) [23]. The second category utilizes new waveform structures that are different from CP-OFDM. The waveforms in this category include filter-band multi-carrier (FBMC) [24] and generalized frequency-division multiplexing (GFDM) [8].

In recent years, the use of different signal transformation tools in the implementation of above mentioned waveforms have increased significantly [25–27]. Due to this, we have benefits into many folds, starting from better time-frequency localization depending on the form and length of analysis window. It allows better and efficient transient phenomena [26], that yields into better performance in terms of symbol error rate (SER), throughput, spectral efficiency, and OOB. Furthermore, it also allows low computational complexity implementation [27]. Therefore, the advance tool of signal transformations gives additional degree of freedom in the implementation of these waveforms. Due to all these benefits, researchers are more attracted towards the uses of these tools in the implementation of both categories of waveforms [1, 28–32]. There are many tools for digital signal processing as a practical means of performing time-frequency analysis. In the context of wireless communication, the use of transform is a method to convert a signal from one domain to another domain for extracting some other information contained in the signal, which cannot be extracted from the signal in the first domain [33]. The family of transformation constitutes of many important transforms like: Fourier transform (FT) [33], fractional Fourier transform (FrFT) [34, 35], Gabor transform (GT) [1], Zak transform (ZT) [36], Hartley transform [37], Mellin transform, Hilbert transform, etc [33]. In this Thesis, we use some of above mentioned transformation tools (*i.e.*, FFT, FrFT, GT, etc.) in both CP-based OFDM system and also in GFDM system for better performance and less complexity of the waveforms in the presence of different impairments, *i.e*, synchronization errors (CFO and STO).

The main contribution of this Thesis concentrated two main parts depending on the applications and scenarios of different multi-carrier waveforms of both categories: legacy OFDM waveforms and new waveforms; and by exploiting the use of different transformation tools in the above mentioned waveforms, we evaluated the performance in presence of synchronization errors. We divide our Thesis in two parts: in part I, we studied about the legacy OFDM waveforms, in particular, CP-based OFDM and also the use of DFrFT transformation tool in the OFDM system and in part II, we studied about the new waveforms, in particular, GFDM system which may be used in future

cellular system, and also the use of DGT transformation tool in the GFDM.

1.2 Physical layer requirements

Current cellular transmission scheme (4G) based on Long-Term Evolution (LTE) and LTE-Advanced (LTE-A) systems employ OFDM in PHY [6]. The important advantages of OFDM are channel estimation, low-complexity equalization in frequency domain, efficient hardware implementation, and easy realization of multiple-input multiple-output (MIMO) transmission [9]. Due to all these supportive properties, OFDM system has been adopted by many standards, such as wireless IEEE 802.11a/g/n, local area networks, *i.e.*, wireless metropolitan area networks, *i.e.*, IEEE802.16a, terrestrial digital video broadcasting systems, and wireless cellular networks, *i.e.*, 4th generation Long Term Evolution and 5th generation New Radio (NR) [9, 38, 39].

On the other hand, in pursuit of orthogonality, a single and uniform parameter configuration was required in the PHY of LTE-A system based on OFDM waveform. For this reason, a one-size-fits-all approach was adopted in LTE [9, 40]. To be specific, a fixed set of waveform parameters, including sub-carrier spacing and length of cyclic prefix (CP), has been uniformly applied across the entire system bandwidth. While it is easy to implement, the main issue of such a fixed design is lack of flexibility to support mixed services with different waveform parameters within one carrier, which, as mentioned earlier, is a key requirement in PHY design of future wireless cellular system [16, 40]. Additionally, high OOB emission (OOBE) of OFDM is introduced by the time-domain rectangular pulse shaping filter that affects all the sub-carriers in frequency domain, by extending large tails because of the sinc behavior which poses a challenge for opportunistic and dynamic spectrum access [40]. OFDM signals with one CP per symbol may present a prohibitive low spectral efficiency and also increased the OFDM symbol duration [41]. Furthermore, due to the use of many cheap devices for mMTC, relaxed synchronization conditions are required in terms of time and frequency misalignments, if one wants to reduce network overhead and latency [41].

1.2.1 Limitations of current cellular system

Due to these limitations 4G system based on LTE is leading to the following issues:

Poor spectrum utilization: Large frequency guard bands are needed at both edges of the system bandwidth for the signal to reach enough attenuation to meet the requirements of spectrum mask and adjacent channel leakage ratio (ACLR). This implies a significant loss in spectrum efficiency. For instance, 10% of the system bandwidth was reserved as guard bands in LTE.

Stringent synchronization requirement: To achieve interference-free reception, the uplink signals from different users should arrive at base station at same time. Any timing misalignment larger than the CP duration, especially between the signals closely located in the frequency domain, would lead to severe inter-user interference and ICI, and hence large performance degradations. It also leads to in-band interference whenever there is frequency offset between users. Therefore, in LTE, frequent timing ad-

vance (TA) signals are transmitted from the base station to mobile users to maintain the orthogonality in reception.

Above mentioned limitation of current LTE waveform is summarized as:

- Cyclic prefix overhead

- Less tolerance to inter sub-carrier interference

- Large Peak to average power ratio (PAPR)

- High out of band side lobe

1.2.2 Requirements

To overcome the above mentioned problem associated with LTE system based on OFDM, it is worth investigating about new waveforms that should be considered for PHY of future wireless cellular system. On the one hand, the waveform candidate should inherit all the advantages of CP-based OFDM. On the other hand, new waveforms should be able to provide the flexibility required for efficient support of diverse services and deployment scenarios in one carrier [10, 11]. Furthermore, the new waveform needs to have sufficiently good spectrum confinement, yielding higher spectrum efficiency. The following design criteria are essential in selecting and designing the waveforms for future cellular system.

High flexibility:

- **Flexibility of multi-numerology existence**: The future waveforms should be able to support flexibly configured numerology and multi-numerology coexistence, to enable tailored services for different applications in associated deployment scenarios [11]. To reduce scheduling constraints, frequency domain multiplexing of different numerologies is of interest. In addition, for smooth evolution and efficient resource utilization, dynamic allocation of bandwidth for different services should also be supported.

- **Band-width extension**: The future waveform should enable straightforward and scalable extension to support ultra-wideband operations (*e.g.*, ≥ 100 MHz), with affordable complexity.

High spectrum efficiency:

- **Frequency-domain localization**: Sufficient spectral confinement is essential for achieving high spectrum efficiency. It is also highly related to the guard band overhead for supporting neighboring but non-orthogonal transmissions.

- **Time-domain localization**: To reduce the time-domain overhead due to tails of filtering or pulse shaping, and to achieve a high spectrum efficiency, a time-domain localized waveform is preferred.

- **MIMO support**: MIMO, especially massive MIMO, has to be supported by the new waveform, without requiring much additional effort, in either open or closed-loop operations.

- **High-order modulation support**: To boost the peak spectrum efficiency, high-order modulations, such as 256-QAM, are likely to be used in a wider range of scenarios in the future cellular system. The new waveform should be able to support such high-order modulations.

- **High symmetry support**: Having a symmetric waveform would be beneficial for the unification of access, sidelink, and backhauling functions. Although the design principles for the downlink (DL) and uplink (UL) might be different (e.g., UL transmission would be subject to strict PAPR restrictions due to the nonlinearity of the power amplifiers), the waveforms for DL and UL are still preferred to be as similar as possible to facilitate interference cancellation. To form the desired symmetry while alleviating PAPR restrictions, PAPR reduction schemes that are transparent to standards (e.g., clipping, companding) can be applied if coverage or power efficiency becomes of greater relevance.

1.3 Waveforms comparison

As mentioned before about the limitation of 4G system based on OFDM, our focus is on the most discussed and promising candidates of both categories: legacy OFDM waveforms and new waveforms. However, there are several waveforms in the group of legacy OFDM waveforms: starting from different variants of CP-based OFDM, including W-OFDM, UFMC, and F-OFDM [16]- [42]. Moreover, in the new waveforms group FBMC and GFDM exist [24]. A common motivation for these waveforms is to reduce the OOBE, reduce guard band overhead and improve spectrum utilization. Along with this categorization, the most important and fundamental aspects of the shortlisted candidates and their implications for the future waveform are discussed.

1.3.1 Legacy OFDM based waveforms

In this sub-section, a comparative studies of different waveforms belonging to the categories of Legacy OFDM based waveforms is given. Moreover, a summary of these waveforms is given in Table 1.2. To maintain the benefits of CP-based OFDM while reducing the OOBE, straightforward enhancements can be made by using windowing approach to smooth the time-domain symbol transitions and filtering to suppress spectrum leakage, both of which are simple but an effective tool should be used in the following waveforms such as W-OFDM, UFMC, and F-OFDM [43]- [42]. In this categories of waveforms, the modulation process may largely reuse that of CP-OFDM. The most obvious advantage of W-OFDM is its simplicity, as only low-complexity time-domain multiplications and additions are involved. However, its disadvatages are limited OOBE improvement and non-negligible guard bands needed at both edges of the system bandwidth. However, additional OOBE improvement of W-OFDM often comes

Table 1.2: *Comparison of different waveforms belonging to legacy OFDM group*

Waveforms		Discussion
CP-OFDM	Basics	Multi-carrier waveform currently used in LTE for down link transmissions
	Pros	Easy integration with MIMO, simple transceiver design, robustness against frequency selective channels, well-localization in time-domain, dynamically allocate band-width to users
	Cons	High PAPR, sensitivity to phase noise, high OOBE, transmission overhead due to CP addition, CFO and STO
	Parameters	Sub-carrier spacing, FFT Size, CP length
	Operations	QAM + S/P + IFFT per group + CP Insertion
W-OFDM	Basics	Non-rectangular window with smooth transition at symbol edges is used with CP-OFDM to enable smoother temporal transitions between the successive OFDM symbols,
	Pros	Low OOBE with respect to CP-based OFDM, simple implementation using time domain windowing, easy integration with MIMO
	Cons	Only limited OOBE improvement can be achieved, and non-negligible guard bands are still needed at both edges of the system bandwidth, losing the efficiency in multi-path channels due to reduced effective CP length
	Parameters	Sub-carrier spacing, FFT Size, CP length, window
	Operations	QAM + S/P + IFFT per group + CP Insertion + windowing
F-OFDM	Basics	The assigned bandwidth is split up into several sub-bands, in this sub-bands group of adjacent sub-carrier are digitally passband filtered and a CP is appended, different types of services are accommodated in different sub-bands with the most suitable waveform and numerology, ISI caused by the end-to-end filtering is negligible, even considering the channel multi-path spread, the bandwidth of each sub-band is not fixed, the filtering granularity can be configured to any value larger than the bandwidth of a physical RB in 4G LTE, the filter length is not limited to the length of CP.

	Pros	Increased robustness against non-perfect time and frequency alignment for multi-user uplink, possibility to operate each sub-band with a different numerology or signal format, improved spectrum efficiency due to reduced guard band reasonably low complexity for wide-band operations due to customizable filtering granularity, OOBE can be suppressed to a desirable level with a relatively long filter length, only a few edge sub-carriers in sub-band are affected by filtering
	Cons	More complexity at transmitter and receiver, subject to ISI, processing delay
	Parameters	Sub-carrier spacing, FFT Size, Sub-band Filters, CP
	Operations	QAM + grouping of symbols + S/P + IFFT per group + CP insertion + group wise filtering

with reduced effective CP length and efficiency in multi-path channels. Furthermore, to suppress the interference from adjacent non-orthogonal signals (e.g., asynchronous transmission), advanced receiver windowing can also be applied, which will further reduce the length of effective CP [44].

An alternative solution to reduce the OOBE of CP-based OFDM is to introduce sub-band filtering. Moreover, for the sub-bands filtering approach the system bandwidth is divided into several sub-bands, and a conventional OFDM signal is contained in each sub-band. Filtering operation is performed on each sub-band to reduce its OOBE and facilitate its coexistence with the adjacent sub-bands. However, with reduced guard band, this mixed numerology feature can enable multi-service coexistence with improved spectrum efficiency, as compared with the traditional guard band based fragmented carrier operation.

In addition, with reduced OOBE, improved tolerance to interference from asynchronous transmissions can be provided, with which the requirement on synchronization can be relaxed. UFMC and F-OFDM are the two most discussed waveforms along this line. For UFMC, the bandwidth of each sub-band is kept fixed and performs filtering with fixed frequency-domain granularity. However, to prevent ISI due to the filtering operation, zero prefix (ZP) is typically used in UFMC, instead of CP. Filter length of UFMC is typically less than or equal to the length of ZP. Due to this, filter tails extend in to ZPs without overlapping with each other. Due to sub-band filtering with short filter length in UFMC leads to a reduced OOBE as compared to CP-based OFDM, but the implementation complexity increases quickly at both the transmitter and the receiver, with increasing the operating bandwidth. Furthermore, without CP and circular convolution, the linear convolution of the signal with the channel impulse response, zero-padding and a double-sized FFT is typically used at the receiver, which further increases the complexity [20].

In contrast to UFMC, F-OFDM maintains the CP used OFDM. Moreover, the filtering granularity in F-OFDM can be configured to any value larger than the bandwidth of a physical RB in 4G LTE (i.e., 180 kHz). Furthermore, the filter length is not limited to the length of CP. The main benefit of a customizable filtering granularity is reasonably

low complexity for wide-band operations. The main draw-back of F-OFDM, compared with W-OFDM, is its relatively high complexity due to the filtering operation [23].

1.3.2 New Waveforms

As it is well known, high OOBE of OFDM is introduced by the time-domain rectangular pulse shaping filter that affects all the sub-carriers in frequency domain, leading to large tails because of the sinc behavior, which poses a challenge for opportunistic and dynamic spectrum access. Due to this reason, researchers are more motivated towards the waveforms that support variable and customizable pulse shaping (instead of a simple rectangular window) to achieve a better trade-off between time-domain and frequency-domain localization. The summary of these waveforms are given in the Table 1.3.

In this category of waveforms, FBMC and GFDM are the most mentioned waveforms. The main motivation is: pulse shaping and filtering performed at the sub-carrier level. The modulator is generally more complicated than a single inverse FFT used in OFDM [5]- [24]- [45].

In FBMC the sub-carriers are pulse shaped individually to reduce the OOBE, because the sub-carriers have narrow bandwidth. FBMC can achieve good spectral efficiency only if the number of transmit symbols is large. In the meantime, to maintain Nyquist-rate transmission, adjacent FBMC symbols are overlapped with each other in time domain. To minimize the interference among them, staggering of in-phase and quadrature-phase symbols in both time and frequency domain is applied, which is widely referred to as offset-QAM (OQAM). Moreover, unlike CP-based OFDM, OQAM-based FBMC is orthogonal in the real field only, not in the complex field. With its excellent frequency localization, FBMC-OQAM requires no more than one sub-carrier as guard band for neighboring but non-orthogonal transmissions.

Apart from these some advantage, still there are some disadvantages exist in FBMC-OQAM. Due to complex communication channels real-field orthogonality of FBMC-OQAM in practical systems is quite limited. The very first challenge for OQAM based FBMC is pilot design. More complicated pilot schemes such as data-dependent auxiliary pilots are often needed to take care of the interference from complex field. Furthermore, with extended pulse shaping, long filter tails appear at both ends of the signal burst, which causes extra overhead and must be taken care of properly. To avoid the above-mentioned limitations of FBMC-OQAM, efforts have been made to reduce the intrinsic interference in complex field and thus enable QAM transmission. The basic idea in QAM based FBMC is to apply different filter banks for different sub-carriers, offering additional freedom to suppress the interference between adjacent symbols in both the frequency and time domains. In this case, if the signal-to-interference ratio (SIR) can be made sufficiently high, pilot design and MIMO transmission can be as simple as that in CP-OFDM systems. However, as shown in the next section, the SIRs provided by the pulse shaping filters proposed for QAM based FBMC are still not high enough to support 64-QAM transmission without a large gap from CP-OFDM. In addition, the filter tail issue still exists with QAM based FBMC. Apart from these challenges, one of the main drawback of FBMC is that it does not provide backward

Table 1.3: *Comparison of the different waveforms belonging to new waveforms group*

Waveforms		Discussion
FBMC-QAM	Basics	Pulse shaping/filtering is performed at sub-carrier level, the pulse duration is extended in time-domain to multiple times of a symbol duration, adjacent FBMC symbols are overlapped with each other in time domain, to minimize the interference among the symbols, apply different filter banks for different sub-carriers.
	Pros	Lower OOBE compared to CP-based OFDM, requires not more than one sub-carrier as guard band for neighboring, the edge-smoothed pulse shape in time-domain makes it less sensitive to multi-path spreading, which reduces the necessity for cyclic pre-fixing, enables to achieve high spectrum efficiency
	Cons	No longer preserves complex-domain orthogonality, intrinsic ICI is non-negligible and will cause obvious performance loss, complicates the application of MIMO, long filter tails appear at both ends of the signal burst, which causes extra overhead and must be taken care of properly
	Parameters	Sub-carrier spacing, FFT Size, prototype filters and their overlapping factor
	Operations	QAM + S/P + pulse shaping + IFFT per group
GFDM	Basics	Applies sub-carrier filtering by pulse shaping but in a block-wise and circular manner to avoid inter burst tails, block-wise CP is added to eliminate inter-block interference in multi-path channel
	Pros	A general frame work to partition the given time/frequency resource based on specific requirements, OOB leakage can be improved by prototype filter
	Cons	No longer preserves complex-domain orthogonality, intrinsic ICI is non-negligible and will cause obvious performance loss, complicates the application of MIMO, decoding latency becomes a challenge
	Parameters	Sub-carrier spacing, FFT Size, prototype filters
	Operations	QAM + S/P + IFFT per group + CP insertion + windowing

compatibility with current MCM scheme used in LTE, *i.e.*, OFDM and DFT- spread-OFDM (DFT-s-OFDM).

In contrast, GFDM is based on a block based structure consisting of several OFDM symbols and a CP that is added at the beginning of each block instead that at the beginning of each symbol, as happens in OFDM. The sub-carriers are pulse shaped by circular filtering which makes it applicable for short burst transmission. Employing circular filter in GFDM with windowing or guard symbol insertion reduces the OOBE compared to OFDM [41]. Moreover, since a tail biting technique is used in GFDM, this makes the CP length independent of transmit and receive filters lengths [46]. This allows reducing the overhead caused by CP, thus increases spectral efficiency. The flexible frame structure of GFDM allows, by changing the number of time slots and sub-carriers in a frame, covering both conventional CP-OFDM and DFT-s-OFDM. This allows for backward compatibility with current MCM scheme used in LTE.

1.4 Motivation towards the use of different transformation tools

Based on the survey of different waveforms given in the above sections, our main focus is on two extreme waveforms from each group: CP-based OFDM and GFDM system. Here, we are going to discuss about the implementation waveforms with different transformation tools [47].

1.4.1 Use of different transformation tools in OFDM system

In 1971 Weinstein and **Ebert** *et al*. [48] proposed a modified OFDM system in which the DFT was applied to generate the orthogonal sub-carriers waveforms. Their scheme reduces the implementation complexity significantly, by making use of IDFT modules and digital-to-analog converters. Therefore, base-band signals were modulated by IDFT at the transmitter and then demodulated by DFT at the receiver.

Although OFDM has several advantages, it also presents some disadvantages that are mainly introduced by synchronization issues like high sensitivity to symbol timing offset (STO) and carrier frequency offset (CFO) [49]. CFO is due to either mismatching of transmitter and receiver oscillator's frequencies or Doppler spread while STO is caused by the discrepancy between the current sampling phase and the optimal one. The presence of CFO destroys the orthogonality among sub-carriers, generating inter-carrier interference (ICI) [50]. The presence of STO introduces phase rotations in frequency domain, within the same symbol, and inter symbol interference (ISI), between successive symbols [49].

Several approaches are available in the literature to face problems introduced by synchronization errors in OFDM systems [51]. In the presence of oscillator drifts and time-varying Doppler shifts, residual CFO and STO are still present in the received signal after the application of synchronization algorithms. In order to improve the robustness to residual CFO, an OFDM system based on the use of DFrFT was proposed by Martone in [28]. This system is analogous to the conventional OFDM one with the difference that DFT and IDFT are replaced by DFrFT and IDFrFT, respectively. As observed by Martone, in case of a time-varying frequency selective fading channel

the entire conceptual framework of frequency-domain channel partitioning, exploited by DFT-based OFDM, loses its optimality. To counteract this drawback, Martone proposed the use of the DFrFT in OFDM where orthogonal signal bases of chirp function with rate $\cot(\alpha)$, being α the 'angle parameter', are used in place of the orthogonal complex exponentials of DFT in the presence of Doppler effect. The main advantage of using orthogonal chirp function consists in the control of time-frequency partition of channel. Here, as already observed in existing literature, the same concept is used to mitigate the performance degradation introduced by the loss of orthogonality due to CFO. Moreover, concerning STO, it is here observed for the first time that DFrFT is also beneficial in terms of performance. This is demonstrated by quantifying its effect in an analytical expression of the term responsible for introducing ICI and ISI, which is part of novel contribution.

1.4.2   Use of different transformation tool in GFDM system

As it is well known, the decoding latency becomes a challenge for GFDM, as the detection process can only be started after the entire block is received. Due to large size of the block, another problem is its high receiver complexity. There have been many methods for efficient implementation of the receiver for a GFDM system in [52]- [53]. To obtain a low-complexity implementation of GFDM receiver, several techniques for different receiver architecture are proposed. In the ideal channel, low complexity can be obtained by splitting the multiplication of the receiver matrix in the frequency-domain in the place of time-domain, the implementation of frequency-domain is done by using DFT. In fact, the complexity of the DFT-based GFDM in [53] is the same as that of DGT-based GFDM [45], where GFDM transmission and reception are equivalent to a finite discrete Gabor expansion and DGT in critical sampling, respectively. Another key factor is the channel equalization that should be considered in the receiver section. Since the direct channel equalization in time domain described in [8] has a high complexity, proportional to square of total number of the data symbols in a GFDM symbol, frequency domain equalization (FDE) can be used to reduce the complexity. Here, we are going to consider, simplified GFDM waveforms based on DGT in frequency domain and transmitted GFDM signal is an inverse DGT (IDGT) [1]. According to DGT and frequency-domain IDGT format of a transmit GFDM signal, a frequency-domain DGT is proposed for GFDM signal recovery different from time-domain processing in [1].

1.5   Main contributions of Thesis

Based on the above motivations, limitations and requirements, in this Thesis, our main goal is to study the synchronization problems and evaluate performance in the presence of synchronization errors for both categories of waveforms, CP-based OFDM and GFDM system. Different transformation tools allow the efficient implementation of these waveforms and evaluate the performance of OFDM and GFDM system based on the uses of advance tools of signal transformation. Starting from this, our Thesis consists of two parts, where in part I: Synchronization problems and their impact on

performance of current cellular system based on the OFDM system; In part II: Performance evaluation of New waveform based on GFDM system.

1.5.1 CFO and STO estimations studies based on DFrFT-based chirp method

The results in this Thesis show that DFrFT-based chirp method outperforms all other methods available in literature at the cost of computational complexity. The reason for this increase in complexity is due to the fact that other methods generate timing metric by taking auto-correlation in time domain directly whereas the DFrFT-based chirp method first takes the DFrFT of received signal and then generate timing metric. We perform the mean square error (MSE) for CFO and STO estimation and compare the performance to other methods in multipath fading channel. The results presented in this Thesis shows that the DFrFT-based chirp method estimator performs better than other algorithms.

1.5.2 Performance analysis of OFDM in the presence of synchronization errors

One of the main activities of my Thesis is to derive exact symbol error probability (SEP) expressions for DFrFT-based OFDM system, when STO and CFO are present together. Then, comparing the performance of both DFT/DFrFT-based OFDM system in the presence of synchronization errors such as CFO and STO. Our results show that DFrFT-based OFDM system outperforms that based on the DFT for different values of the DFrFT 'angle parameter'. Monte Carlo simulations are used to demonstrate the correctness of the derived analytical expressions.

   The main contributions of this activity are:

1. Definition of a DFrFT-based OFDM system model for a generalized multipath channel that includes both CFO and STO effects.

2. Derivation of exact SEP expressions for a DFrFT-based OFDM system in case of simultaneous presence of CFO and STO. Analytical closed form expressions are given for BPSK, QPSK, and 16-QAM modulation formats for frequency selective Rayleigh fading channel.

3. Derivation of the closed form expression of optimal DFrFT angle parameter (α) as a function of CFO.

1.5.3 Hardware implementation of DFrFT-based OFDM system

From the performance comparison of DFT and DFrFT-based OFDM system it is visible that DFrFT-based OFDM system outperforms the conventional OFDM based on DFT. But only few works are available in the literaturerelated to DFrFT hardware implementation. Therefore, we extend this activity towards the hardware implementation of OFDM based on the use of DFrFT.

   The main contributions of this activity are:

1. We implemented the floating point to fixed point conversion of DFrFT/IDFrFT kernels.

2. We consider its implementation in Field Programmable Gate Array (FPGA).

3. To verify the design of DFrFT-based OFDM system, we use FPGA-in-the-Loop (FIL) co-simulation method to evaluate BER in presence of CFO when transmission takes place over a frequency selective Rayleigh fading channel.

1.5.4   Implementation of OFDM in LTE PHY and its limitations

After evaluating the performance analysis of OFDM system, our goal is to implement OFDM system in the framework of LTE PHY using MathWorks/Simulink Toolbox.

The main contributions of this activity are:

1. Development of FDD mode LTE PHY layer.

2. We perform the detection of primary and secondary synchronization signals.

3. We perform the estimation of carrier frequency offset, symbol timing offset and correction.

4. We also perform channel estimation.

1.5.5   Impact of pulse shaping filter in GFDM system

After studying the limitations of 4G cellular system based on LTE for future applications proposed by IMT in 2020 time-frame, we started studying of new waveforms based on filtering. First of all in part-II of Thesis, we started the activities about the impact of pulse shaping in new waveform, specially in GFDM system.

The main contributions of this activity are:

1. We propose to use improved Nyquist pulse shaping filters which have been originally introduced in the context of single-carrier modulation schemes for reducing the sensitivity to symbol timing error due to their higher eye opening and smaller maximum distortion.

2. Impact of "Better than Nyquist" pulse shaping in GFDM PHY with LTE-compatible frame structure

3. Performance evaluation of GFDM system with those pulses with different receiver architecture such as zero forcing (ZF), matched filer (MF) .

4. SER performance evaluation over different channels such as AWGN, flat fading and frequency selective fading channel.

5. We also considered the concept of wavelet for better time-frequency localization of pulse shaping filters by using the Meyer auxiliary function.

1.5.6 Implementation of GFDM system using advanced tool of signal transformation

In this activity our goal is to simplify the GFDM receiver, a relationship between a GFDM signal and DGT is investigated, where the effect of sub-symbols over the channel are also considered.

The main contributions of this activity are:

1. Implementation of GFDM system with DGT/IDGT, where the effect of channel on sub-symbols of each sub-carrier is also considered.

2. Performance evaluation of DGT based GFDM system over multi-path channel is evaluated.

3. Implementation of GFDM system with IDFrFT/DFrFT kernel is also considered.

1.5.7 Performance analysis of GFDM in the presence of synchronization errors

By extending the studies of filtered waveforms, in this activity we derive exact SEP expressions for GFDM waveform in the presence of CFO in AWGN channel and frequency selective Rayleigh fading channel. The analytical expressions of SEP are derived when matched filtering is implemented at the receiver for BPSK, QPSK, and 16-QAM in case of AWGN channel and for BPSK only in case of frequency selective Rayleigh fading channel.

The main contributions of this activity are:

1. Definition of a GFDM system model with MF receiver for a generalized multipath channel that includes the effect of CFO.

2. Derivation of exact SEP expressions for:

   - BPSK, QPSK, and 16-QAM modulation formats in case of transmission over AWGN channel.
   - BPSK modulation in case of transmission over a frequency selective Rayleigh fading channel.

3. Analysis of the impact of pulse shaping filters on the proposed SEP expressions. The investigation is limited to only those pulses that satisfy the orthogonality condition, *i.e.*, the Dirichlet shaping filter and the Gaussian pulse one, which is orthogonalized by using the isotropic orthogonal transform algorithm.

1.6 Organization of Thesis

Conceptual mapping of Thesis is given in Fig. 1.2. From Fig. 1.2, it is clearly visible that this Thesis is broadly divided in two parts. Part I of Thesis is about the performance evaluation of 4G system based on OFDM in the presence of synchronization error and its limitations, this part contains seven chapters: chapter 2 is about studies and literature
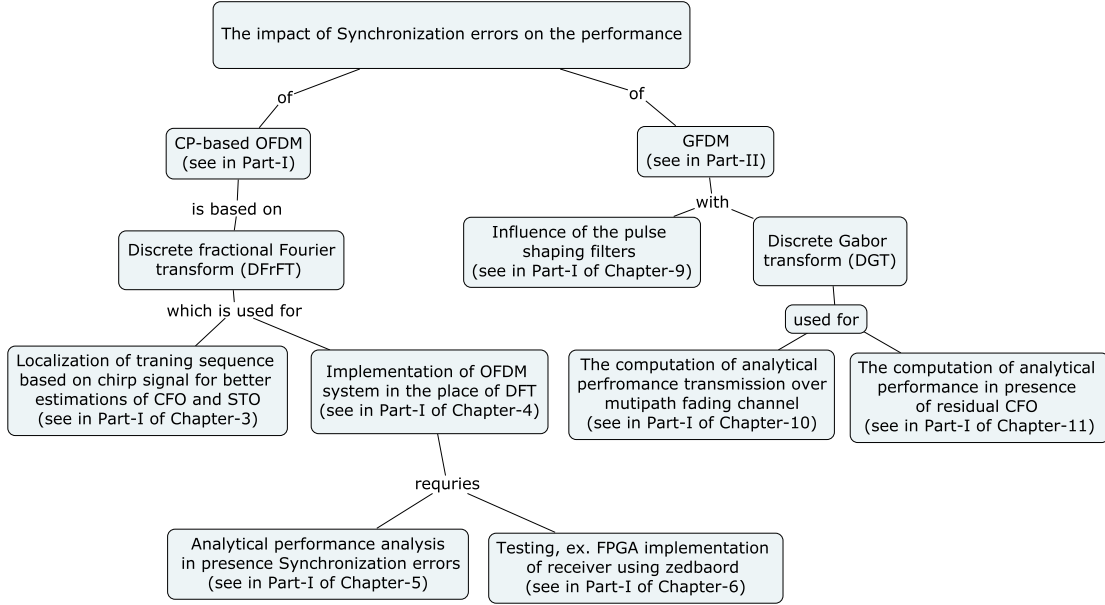
Figure 1.2: *conceptual mapping of Thesis.*

survey of different multi-carrier waveforms based on the legacy based OFDM system. Chapter 3 is about studies of synchronization problems in OFDM system. Chapter 4 contains the system model of DFrFT-based OFDM system in presence of CFO and STO and the mathematical formulation of transmitter, channel and receiver. Chapter 5 contains the derivation of exact SEP expressions for a DFrFT-based OFDM system in case of simultaneous presence of CFO and STO. Analytical closed form expressions are given for BPSK, QPSK, and 16-QAM modulation formats for frequency selective Rayleigh fading channel. In this chapter, we also consider the performance analysis of DFT/DFrFT-based OFDM system transmission over different fading environments. Chapter 6 contains the hardware implementation of DFrFT-based OFDM system. Finally, chapter 7 contains the limitation of the current cellular system and motivation for redesigning the PHY for future applications. Part II of Thesis is about the performance evaluation of new waveform based on GFDM, this part contains five chapters: chapter 8 is about the motivation and literature survey about the use of new multi-carrier waveforms based on flexible pulse shaping filters. Chapter 9 contains about the impact of pulse shaping filter on GFDM system and evaluation of its performance with different receiver architecture. Chapter 10 is about the implementation of GFDM system using DGT and also evaluated optimal ML detection over multi-path fading channel. Chapter 10 is about the analytical performance analysis of GFDM system in the presence of

synchronization errors. Finally, the conclusion and future scope of the Thesis is given in chapter 12.

The publications related to the work presented in the Thesis are listed following:

Peer-reviewed journal papers:

- Atul Kumar, Maurizio Magarini, "An Exact SER Analysis of GFDM for BPSK and QPSK Transmission over AWGN Channel with Carrier Frequency Offset," **Re-submitted** in *IEEE Transactions on Communications*, March 2018

- Atul Kumar, Maurizio Magarini, "Optimal Detection for DGT-based GFDM Transmission over Frequency Selective Channel," **Submitted** in *IEEE Communication Letter*, October 2018

- Atul Kumar, Daljeet Singh, Maurizio Magarini, Hem Dutt Joshi, and Rajiv Saxena, "Symbol Error Rate Analysis of OFDM System with CFO over TWDP Fading Channel," **Submitted** in *Wireless Personal Communications*, March 2018

- Navuday Sharma, Atul Kumar, Dushantha Nalin K. Jayakody, Maurizio Magarini, "Performance analysis of "LTE-Compatible" Non-orthogonal multicarrier waveforms (NOMA) for Aerial Base Station (UAV)," **Re-submitted** in *IEEE Transactions on Vehicular Technology*, October 2018.

- Atul Kumar, Maurizio Magarini, "Symbol Error Probability Analysis of DFrFT-based OFDM Systems with CFO and STO in Frequency Selective Rayleigh Fading Channels," in *IEEE Trans. on Vehi. Tech.*, DOI: 10.1109/TVT.2018.2881386, Nov. 2018.

- Atul Kumar, M. Magarini and S. Bregni, "Improving GFDM Symbol Error Rate Performance using "Better than Nyquist" Pulse Shaping Filters," in *IEEE Latin America Transactions*, vol. 15, no. 7, pp. 1244-1249, 2017.

- Atul Kumar, Maurizio Magarini, Hem Dutt Joshi, and Rajiv Saxena, "Exact SER Analysis of DFrFT-Based QPSK OFDM System over Frequency Selective Rayleigh Fading Channel with CFO," in *Journal of Computer Networks and Communications*, vol. 2016, Article ID 2804507, 7 pages, 2016.

- Atul Kumar *et al.*, "Exact BER analysis of FRFT-OFDM system over frequency selective Rayleigh fading channel with CFO," *Electron. Lett.*, vol. 49, no. 20, pp. 1299-1301, 2013.

- Davide Scazzoli, Atul Kumar, Navuday Sharma, Maurizio Magarini, Giacomo Verticale, "Fault Recovery in Time-Synchronized Mission Critical ZigBee-Based Wireless Sensor Networks," in *International Journal of Wireless Information Networks*, vol. 24, no. 3, pp.268–277, 2017.

Peer-reviewed conference proceedings:

- Atul Kumar, M. Magarini and S. Bregni, "Impact of "Better than Nyquist" pulse shaping in GFDM PHY with LTE-compatible frame structure, " in *IEEE 9th Latin-American Conference on Communications (LATINCOM)*, Guatemala City, pp. 1-6, 2017. doi: 10.1109/LATINCOM.2017.8240192

- Atul Kumar, M. Magarini and S. Olivieri, "Rapid prototyping and FPGA-in-the-Loop verification of a DFrFT-based OFDM system," in *25th European Signal Processing Conference (EUSIPCO)*, Kos, pp. 2526-2530 2017.

- Atul Kumar, S. Bregni and M. Magarini, "An exact SER expression for QPSK OFDM system in presence of residual CFO and STO," in 8th IEEE Latin-American Conference on Communications (LATINCOM), Medellin, pp. 1-6, 2016. doi: 10.1109/LATINCOM.2016.7811586

- Atul Kumar and M. Magarini, "Improved Nyquist pulse shaping filters for generalized frequency division multiplexing," in 8th IEEE Latin-American Conference on Communications (LATINCOM), Medellin, pp. 1-7 2016,. doi: 10.1109/LATINCOM.2016.7811588

- S. Moaveninejad, Atul Kumar, *et al.*, "BER evaluation of post-meter PLC services in CENELEC-C band," in *9th Latin-American Conference on Communications (LATINCOM)*, Guatemala City, pp. 1-6, 2017,

- Sarvraj Singh Ranhotra, Atul Kumar, Maurizio Magarin, "Performance Comparison of Blind and Non-Blind Channel Equalizers Using Artificial Neural Networks," in 9*th International Conference on Ubiquitous and Future Networks (ICUFN)*, Milan, pp. 243-248. 2017.

- D. Scazzoli, Atul Kumar, N. Sharma, M. Magarini and G. Verticale, "A novel technique for ZigBee coordinator failure recovery and its impact on timing synchronization," in *27th Annual International Symposium on Personal, Indoor, and Mobile Radio Communications (PIMRC)*, Valencia, pp. 1-5, 2016

Workshop and DEMO presentations:

- DEMO Presentation: Kumar, Atul. (2016, June). Hardware Co-simulation of Multicarrier Transmission Techniques for 5G Software Defined Radio. Poster presented at the MATLAB EXPO, Milan, Italy.

Part I

Synchronization and Performance of Current (4G) Cellular System

CHAPTER *2*

Literature Survey and Problem Formulation

THIS chapter consists of motivation towards the multi-carrier waveforms, then comparison of different multi-carrier waveforms based on legacy OFDM system. After that, mathematical formulation of waveforms and its limitations are given.

2.1 Motivation towards the multi-carrier

Single carrier modulations have been widely used in cellular systems such as global system for mobile communications (GSM), code division multiple access (CDMA) and universal mobile telecommunications system (UMTS), etc. Due to their time domain symbol sequencing, they typically provide low peak-to-average power ratio (PAPR), leading to higher PA efficiency and extended battery life. On the other hand, single carrier waveforms suffer link degradation under frequency selective channels, and typically require the use of equalizer to achieve high spectral efficiency in the presence of multi-path. Before going to the discussion, let's have a brief review of these techniques.

- The main limitation of FDMA and TDMA is the capacity. (the number of users, which can be accommodated without interference).

- The CDMA technique has been developed mainly for capacity reasons.

- CDMA techniques can potentially accommodate more users than either TDMA or FDMA.

- W-CDMA is a 3G wireless standard, evolved from CDMA to support the wide-band services at data rate as high as 2 Mbps.

- The wide band signal like DS-CDMA (Direct sequence CDMA) has a problem of frequency selective multi-path fading.

- Frequency selective multi-path fading is common in urban and indoor environment and is significant source of performance degradation.

- The performance degradation is more if the number of users increases.

- It is observed that the narrow band signals are less sensitive to ISI and frequency selective fading.

Therefore orthogonal multi-carrier modulation combined with CDMA has been used to solve the problem. It is obvious that a parallel system is capable of carrying more information than a cascaded system, simply because it uses a variety of frequency bands. When sending symbols in a parallel way, it means they are taking more time to be sent. When sending them one after another while occupying the same bandwidth, they are shorter in time. In the end it is exactly the same data rate. However, the significant advantage of OFDM is that it is robust in frequency-selective channels, which results from either multi-path fading or other communication interferences. In order to deal with frequency-selective fading, the transmitted OFDM signals are divided into many sub-channels so that those sub-channels can be considered frequency flat approximately as the number of the sub-channel N is large enough. Hence the OFDM signals will suffer less channel distortion than the conventional modulated signals.

2.2 Mathematical formulation

Multi-carrier waveforms can generally be represented as

$$y(n) = \sum_{m=-\infty}^{\infty} \sum_{k=0}^{K-1} X_m(k) \cdot p(n - mK) \cdot e^{j2\pi kF(n-mK)} \tag{2.1}$$

where $X_m(k)$ is the mth data symbol over the kth sub-carrier, $p(n)$ is the prototype filter, and $e^{j2\pi kF(n-mK)}$ represents the frequency shifter corresponding to the kth sub-carrier, m is the data symbol index within each carrier, and n is discrete time index in the digital domain.

The multi-carrier waveform can be further enhanced by inclusion of band-pass filter $b(n)$ to suppress OOB leakage shown in Fig.2.1. Here, we are going to consider only those waveforms where sub-carriers may have frequency overlap with neighbouring sub-carriers, but are actually zero at the perfect sub-carrier sampling in frequency domain. This is commonly known as legacy based OFDM waveforms. The various legacy OFDM waveforms, we are going to discuss in this Thesis are differentiated amongst themselves based on the differences of the two filters $p(n)$ and $b(n)$. The detail descriptions are:
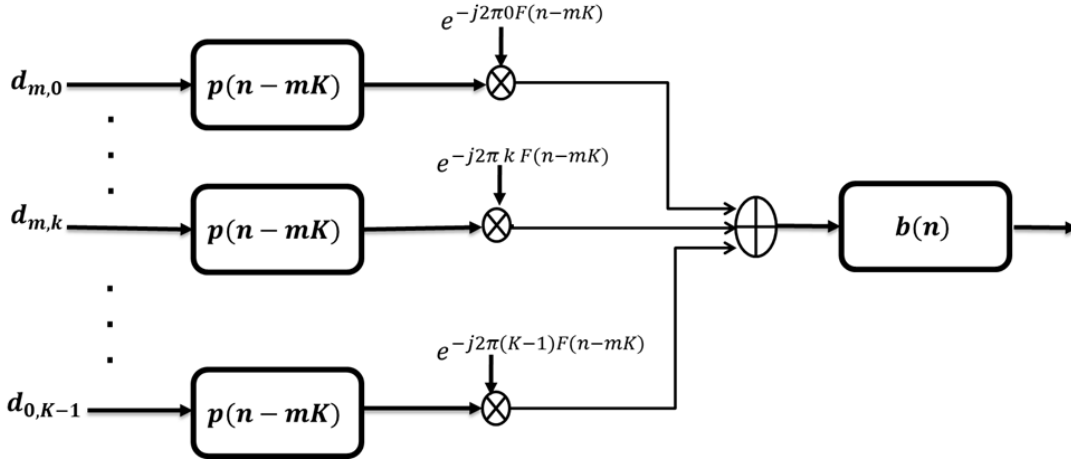
Figure 2.1: *Multi-carrier waveform analysis.*

- $p(n)$ is typically implemented through time domain windowing, which corresponds to manipulate the pulse shaping of each sub-carrier in frequency domain.

- $b(n)$ is typically implemented through time domain filtering, which corresponds to apply a frequency domain band-pass window over a block of contiguous sub-carriers.

Now, we are going to analyse different waveforms belonging to the group of legacy OFDM waveform: starting from different variants of CP-based OFDM, including W-OFDM, UFMC, and F-OFDM. Each waveform is given in detail in subsequent sections of this chapter.

2.3 CP-based OFDM

The CP-based OFDM waveform is the most widely used multi-carrier waveform in existing broadband wireless standards. To summarise the complete studies about CP-based OFDM system, this section contains: starting from the historical development of OFDM, after that mathematical formulation and finally the advantages and disadvantages are given.

2.3.1 Historical development of OFDM

As is well known **Chang** *et al*. [54] proposed the original OFDM principles in 1966, and successfully achieved a patent in January of 1970. Later on, **Saltzberg** *et al*. [55] analysed the OFDM performance and observed that the crosstalk was the severe problem in this system. Although each sub-carrier in the principal OFDM systems overlapped with the neighbourhood sub-carriers, the orthogonality can still be preserved through the staggered QAM technique. However, the difficulty will emerge when a large number of sub-carriers is required. Due to large number of sub-carriers, synchronization and coherent demodulation would induce a very complicated OFDM requiring additional
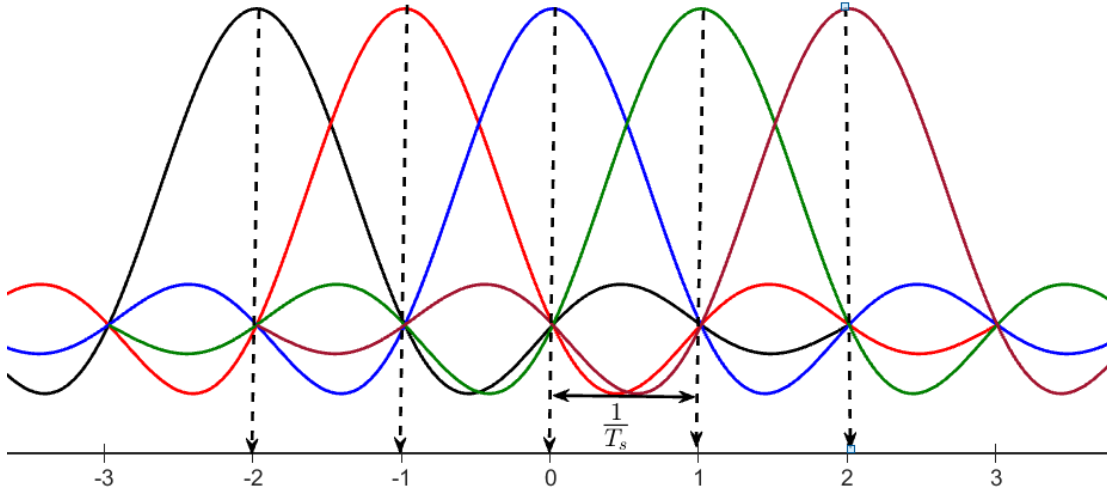
Figure 2.2: *Frequency spectrum of OFDM sub-carrier signals.*

hardware cost. In 1971, Weinstein and **Ebert** *et al.* [48] proposed a modified OFDM system in which the DFT was applied to generate the orthogonal sub-carriers wave-forms. Their scheme reduced the implementation complexity significantly, by making use of IDFT modules and the digital-to-analog converters. In their proposed model, baseband signals were modulated by IDFT at the transmitter and then demodulated by DFT at the receiver. Therefore, all the sub-carriers were overlapped with others in the frequency domain, while the DFT modulation still ensure their orthogonality, as shown in Fig. 2.2. Moreover, CP was first introduced by **Peled** and **Ruiz** *et al.* [56] for OFDM system. In their scheme, conventional null guard interval is substituted by cyclic extension for fully-loaded OFDM modulation. As a result, the orthogonality among the sub-carriers was guaranteed. With the trade-off of the transmitting energy efficiency, this new scheme can result in a phenomenal ICI reduction. In 1980, **Hirosaki** *et al.* [57] introduced an equalization algorithm to suppress both ISI and ICI. In 1985, **Cimini** *et al.* [58] introduced a pilot-based method to reduce the interference emanating from the multi-path and co-channels. In 1989, **Kalet** *et al.* [59] suggested a sub-carrier selective allocating scheme. He allocated more data through transmission of "good" sub-carriers near the centre of the transmission frequency band these sub-carriers will suffer less channel distortion. In 1990s, OFDM system was exploited for high data rate communications.

2.3.2   Mathematical formulation of CP-based OFDM

By following the eq. (2.1), CP-based OFDM waveform can be analysed as a special case when:

- Prototype filter $p(n)$ as rectangular pulse in time-domain.
- Bypassing the uses of $b(n)$ in OFDM system
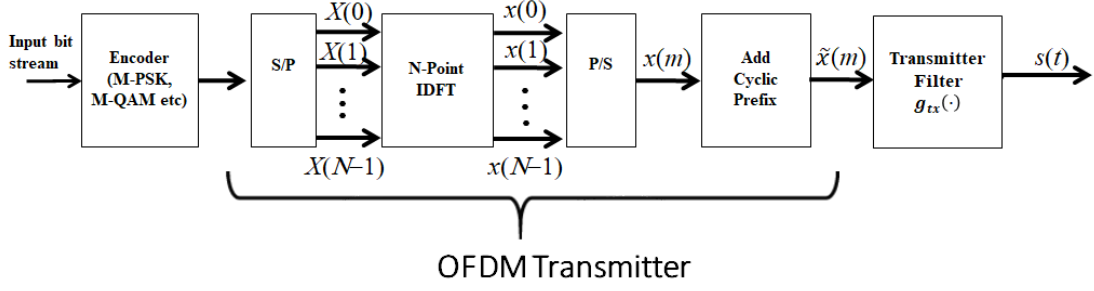
Figure 2.3: *Transmitter section of OFDM system model .*

Such simplifications allow efficient implementation of modulator and demodulator using DFT and IDFT as

Transmitter model

Figure 2.3 reports the block diagram of complex baseband equivalent model of transmitter section of OFDM system. The transmitter includes encoder block and serial-to-parallel (S/P) converter block whose role is that of splitting the high data rate stream into a number of N lower data rate parallel streams. The IDFT is computed on a block of N information symbols. These complex parallel data symbols are then modulated by a group of orthogonal sub-carriers, which satisfy the following condition of orthogonality

$$\frac{1}{T_u} \int_0^{T_u} e^{j2\pi f_k t} e^{j2\pi f_m t} = \begin{cases} 1, & k = m, \\ 0, & k \neq m. \end{cases} \tag{2.2}$$

 The complex data symbol $X(k)$ on kth sub-carrier, $k = 0, 1, 2, \ldots, N-1$, are fed into IDFT. After N-point IDFT, the mth transmitted sample is written as

$$x(m) = \frac{1}{N} \sum_{k=0}^{N-1} X(k) e^{\frac{jn\pi mk}{N}}, \quad m = 0, 1, 2, \ldots, N-1, \tag{2.3}$$

A guard band interval is usually inserted between successive OFDM symbols to avoid the ISI caused by the delay spread of multi-path channel. If a guard band interval is inserted without any signal transmission then the ISI can be eliminated almost completely. But a sudden change in waveform contains higher spectral components, resulting into ICI. Therefore the guard interval insertion technique with CP is generally used to avoid ICI. Under this condition, the linear convolution of the sequence transmitted over the channel is converted to a circular convolution. The cyclically extended sequence is first sent at the input of a continuous-time pulse shaping filter. The resulting baseband complex equivalent expression of the OFDM signal in continuous-time is

$$s(t) = \sum_{m=-N_{CP}}^{N-1} \tilde{x}(m) \, g_{tx}(t - mT), \quad 0 \leq t < T_s, \tag{2.4}$$
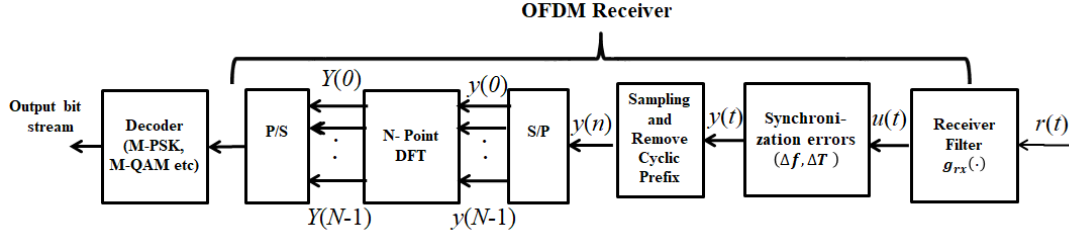
Figure 2.4: *Receiver section of OFDM system model .*

where $T_s = NT$ is the OFDM symbol interval, $g_{tx}(t)$ is transmitter filter impulse response with normalized unit energy, and

$$\tilde{x}(m) = \begin{cases} x(N+m), & m = -N_{CP}, \ldots, -1, \\ x(m), & m = 0, \ldots, N-1, . \end{cases} \tag{2.5}$$

Receiver model

Figure 2.4 reports the block diagram of complex baseband equivalent model of receiver section of OFDM system. The resulting received signal is filtered through the receiving pulse shaping filter. After sampling of received signal at output of receive pulse shaping filter, time frequency synchronization of received signal is performed. Detail of synchronization is described in next chapter of the Thesis. CP is removed and resulting samples are S/P converted and sent to DFT block. The N samples at the output of DFT are equalized, again serialized, and finally decoded to produce an estimate of the originally transmitted data.

After considering the effect of multi-path fading channel $h_l(t)$, the received signal $r(t)$ can be expressed as

$$r(t) = \sum_{l=0}^{L-1} h_l(t) s(t - lT), \tag{2.6}$$

The received signal is filtered by $g_{rx}(t)$ to give

$$u(t) = r(t) * g_{rx}(t), \tag{2.7}$$

where $*$ represent the convolution operation. In case of perfect synchronization the only distortions are introduced by multi-path channel and by the Gaussian noise. However, due to estimation errors, residual timing and frequency offsets exist. The received signal after the matched filter can be modelled as

$$y(t) = e^{j2\pi\Delta ft} u(t - \Delta T), \tag{2.8}$$

where Δf and ΔT denotes residual STO and CFO, respectively. The received signal is sampled at time instants $t = nT$. After removal of CP, resulting discrete-time signal model is

$$y(nT) = e^{\frac{j2\pi\Delta \epsilon n}{N}} \sum_{l=0}^{L-1} h_l(nT) \sum_{m=-N_{CP}}^{N-1+N_G} \tilde{x}(m) g(nT - mT - lT - \Delta T), \tag{2.9}$$

where $\Delta\epsilon = \Delta f T_s$ is the residual CFO normalized to the sub-carrier spacing $1/T_s$, and $g(t)$ is the convolution of $g_{tx}(t)$ and $g_{rx}(t)$. By omitting T, the signal after the DFT block is

$$Y(q) = \sum_{n=0}^{N-1} y(n) e^{\frac{-j2\pi qn}{N}}, \tag{2.10}$$

2.3.3 Summary

One of the main advantages of multi-carrier over single carrier is the simple equalization. Because in case of perfect equalization, single carrier system allows more frequency diversity than multi-carrier system, since the symbols are spread in frequency [10]. Moreover, another main advantage is in multiplexing of users and signals, which is particularly important for enabling flexibility in the spectrum streaming, and MIMO spatial multiplexing. Apart from these benefits, main drawback of the CP-OFDM waveform (*i.e.* without additional of windowing at the transmitter and receiver) is poor time-frequency localization due to the rectangular pulse shaping filter that results into the slowly decaying OOB leakage, causing interference to adjacent band of frequencies and also leads to in-band interference, whenever there is frequency offset remains between users. Another problem of the CP-based OFDM is CP length that is roughly 10% of the OFDM symbol length, results into large overheard. Synchronization errors are another big problem of CP-based OFDM system. The detail of synchronization errors are given in next chapter of the Thesis.

2.4 W-OFDM

CP-based OFDM with weighted overlap and add (WOLA) is commonly known as W-OFDM. In W-OFDM system more general prototype filters $p(n)$ are used in place of rectangular pulse used in CP-based OFDM. The main concern in choosing the $p(n)$ is the pulse which have soft edges (at beginning and end of the filter response), that results in faster decay of the side lobes in frequency domain.

2.4.1 Historical development of W-OFDM

As it is well know, filtering and windowing are two widely used tools to improve the capability of multi-carrier system in order to support future scenarios, especially, for asynchronous access of fragmented spectrum for MTC. In addition to CP-based OFDM waveform, the concept of WOLA was first introduced by **Qualcomm Incorporated** [22]. After that, the use of WOLA with CP-based OFDM was studied especially in case of asynchronous access [60]. Moreover, many windowing functions have been studied and compared [61] to improve the OOBE of CP-based OFDM system. However, the concept of time-domain windowing is to smooth the edges at beginning and end of OFDM signal. Due to this, these soft edges have a smooth transition between the last samples of an OFDM symbol and first samples of next OFDM symbol. The concept of wavelet tool is also important to achieve a better time-frequency localization, and, also
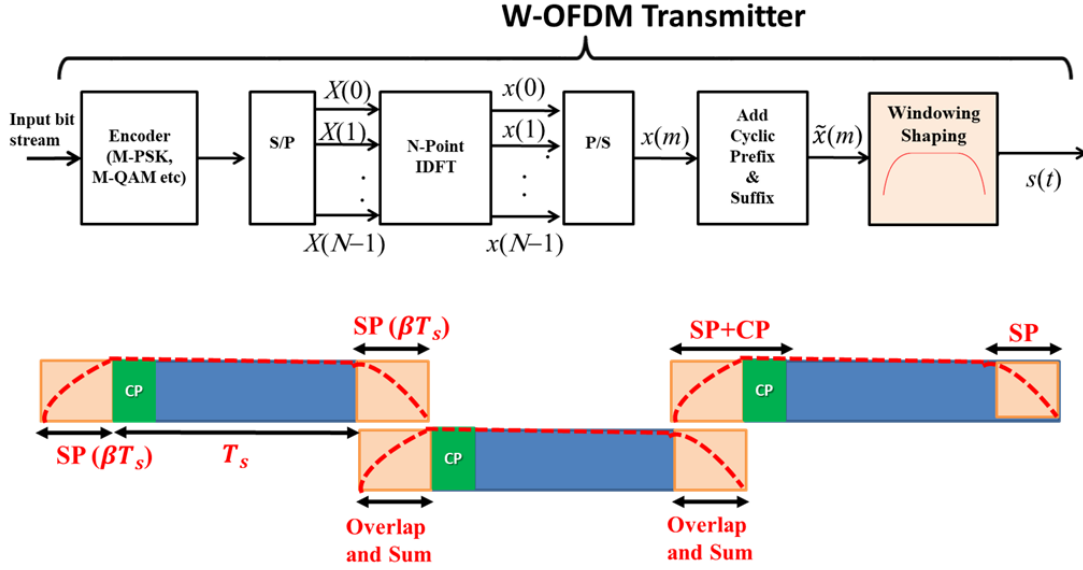
W-OFDM Transmitter

Figure 2.5: *Transmitter section of W-OFDM system model .*

to add flexibility in pulse shaping filter designing. As it is well known, the square-root Nyquist pulse has a major impact on the system design and, therefore, an alternative solution to define it in time-domain is required. This alternative solution must ensure that the derivative of designed pulse is smooth in order to confine the frequency span as much as possible. Many authors have investigated solutions based on the concept of wavelets [62]. A wavelet is a wave-like oscillation with an amplitude that begins at zero, increases, and then decreases back to zero. To ensure this smooth transition, an auxiliary function was introduced by Meyer in [63] to be used as an inner argument of different pulse shaping filters.

2.4.2   Mathematical formulation of W-OFDM

By following eq. (2.1), W-OFDM waveform can be analysed as a special case when:

- The choice of the prototype filter $p(n)$ is such that, it has better time-frequency localization than rectangular pulse.

- There is no use of $b(n)$ in W-OFDM system similar to CP-based OFDM system.

Transmitter model

Figure 2.5 reports the block diagram of complex baseband equivalent model of the transmitter section of W-OFDM system. The main difference between CP-based OFDM and W-OFDM is addition of flexible prototype pulse shaping filter in place of rectangular pulse shaping filter as in CP-based OFDM system. The main benefit of adding the flexible pulse is to smooth the edges at beginning and end of the OFDM signal.

30
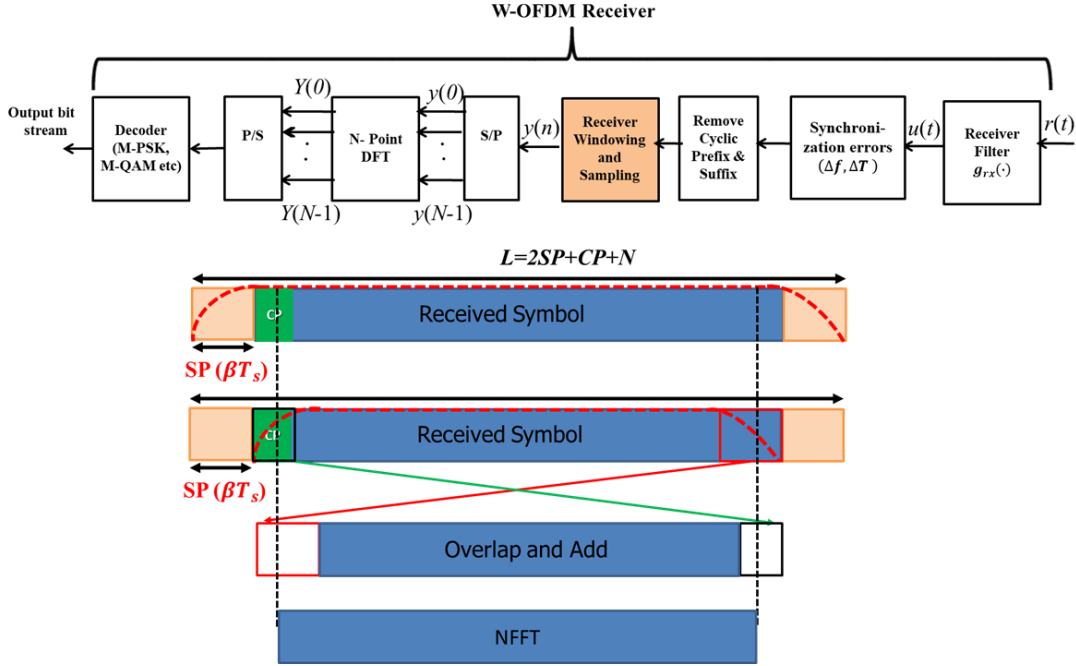
Figure 2.6: *Receiver section of the W-OFDM system model .*

The shape of window (or edge) in time domain determines the frequency response of prototype filter. Several types of windowing have been evaluated in literature [44] with different trade-offs between the width of the main lobe and suppression of the side lobes. The approach given in [64] is based on the introduction of a suffix of length N_G to take into account of the influence, at each time instant t, of the N_G symbols that precede and follow the actual one. After adding the N_G and N_{CP}, The resulting signal is written as

$$
\tilde{x}\left(m\right) = \begin{cases} x\left(N+m\right), & m = -N_{CP}, \ldots, -1, \\ x\left(m\right), & m = 0, \ldots, N-1, \\ x\left(m-N-1\right), & m = N+1, \ldots, N+N_G. \end{cases} \tag{2.11}
$$

Receiver model

In addition of applying WOLA at transmitter to reduce OOB leakage from the signal, we can also apply WOLA at the receiver to suppress other users interference as well show in Fig. 2.6. Especially in case of asynchronous access, smooth edges applied at receiver helps to reduce other user interference resulting from the mismatched FFT capture window. By using better time-frequency localization, the effect of interference from asynchronous access is suppressed.

2.4.3 Summary

By using the concept of WOLA at transmitter of CP-based OFDM system, side lobes are decayed more as compared to original CP-based OFDM. Moreover, by using WOLA

at receiver of CP-based OFDM system, better suppression of other (async) users interference is achieved. Therefore, by implementing time domain windowing, allocations of bandwidth to independent users and also easy integration with MIMO compared to CP-based OFDM system are possible.

2.5 UFMC

Similar to W-OFDM system, UFMC also aims to reduce OOBE. However, W-OFDM introduces a flexible prototype filter $p(n)$ for this, UFMC introduces a non-trivial bandpass filter $b(n)$. UFMC inserts a guard interval (GI) filled with zeros instead of CP in W-OFDM system to prevent ISI introduced due to delay of transmitter filter. After that, symbols are passed through the transmitter filter $b(n)$, and then signals are transmitted over the channel.

2.5.1 Historical development of UFMC

As it is well known, filtering and windowing are two widely used tools to improve the capability of multi-carrier system in order to support future scenarios. Therefore, to overcome the drawback of W-OFDM system, UFMC was proposed by **Vakilian**, *et al* [65]. UFMC is based on the idea of filtering operation applied to a group of consecutive sub carriers (sub-bands) shown in Fig. 2.7. Due to sub-band filtering operation, motivated by the fact that the smallest unit used by scheduling algorithm in frequency domain in LTE is a resource block (RB), which is a group of 12 carriers. Therefore, the effect of side lobes interference on immediate adjacent sub-channels are reduced. Therefore, this enhances ICI robustness and better suitability for fragmented spectrum operation. Moreover, UFMC uses shorter filter lengths compared to CP-based OFDM cyclic prefix lengths which makes it applicable for short bursts communication, but there is still a spectral efficiency loss due to time transient (tails) of the shaping filter [66]. However, UFMC does not consider the use of CP and straightforward FDE, leading to a lack of backward compatibility with OFDM and also making it more sensitive to small time misalignment

2.5.2 Mathematical formulation of UFMC

By following eq. (2.1), UFMC waveform can be analysed as a special case when:

- Prototype filter $p(n)$ is rectangular pulse followed by zero interval. The zero interval represents the guard interval between the symbols. The rectangular part corresponds to IFFT symbols..

- The tx filter $b(n)$ is carefully designed to suppress OOB interference. The filter taps for the transmitter filter $b(n)$ is usually set to be the same as GI length.

Transmitter

The transmitter section of UFMC model is shown in Figure 2.7. Symbols are generated in same way as CP-based OFDM. Instead of CP, a GI filled with zeros is introduced
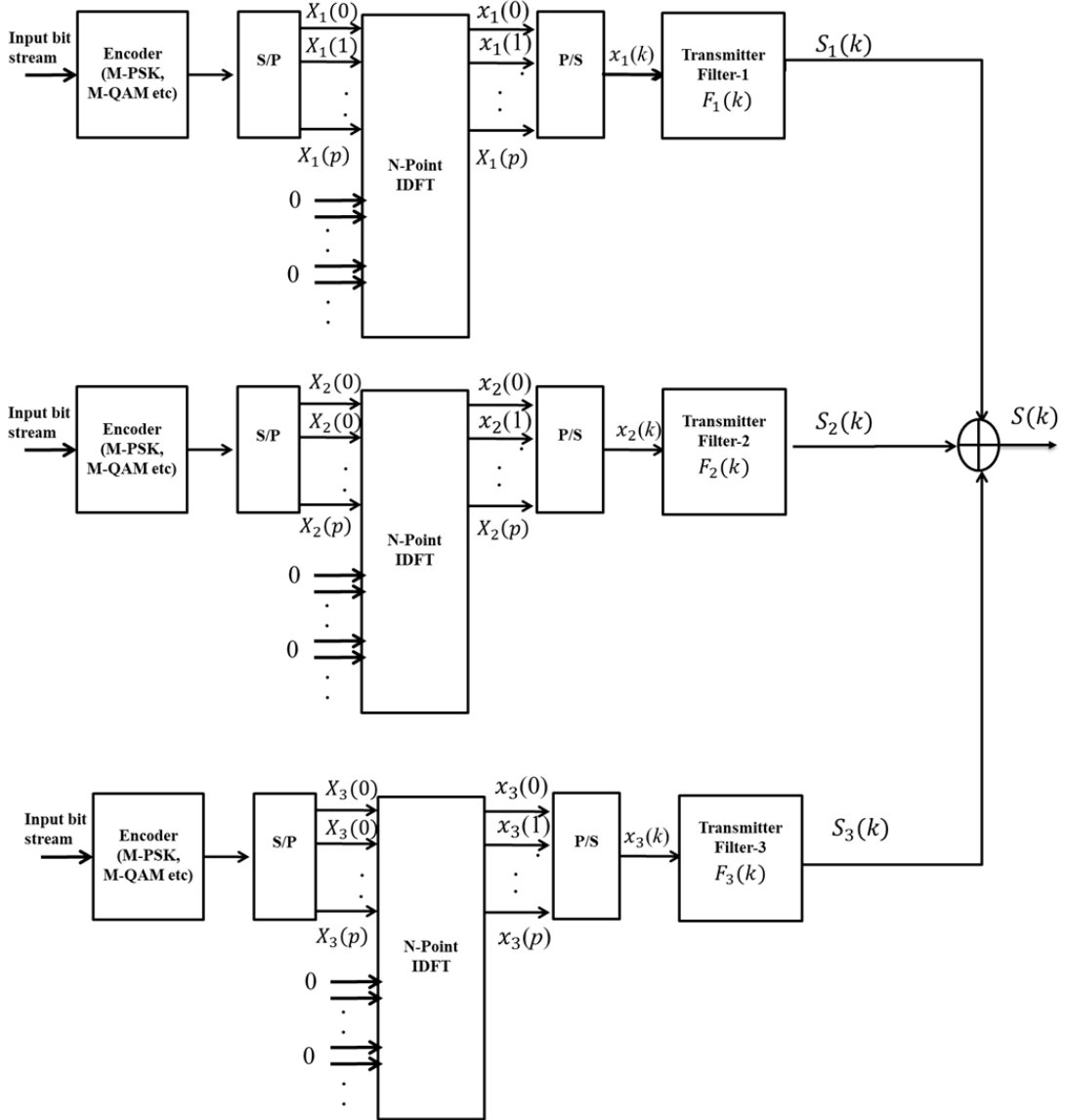
Figure 2.7: *Transmitter section of UFMC system model .*

between the IFFT symbols to prevent ISI due to transmitter filter delays. Finally, the symbols go through the transmitter filter $F(k)$, and then transmitted over the channel. Usually, the transmitter filter length is set to be the same as guard interval duration. The time domain generated signal in UFMC at a particular instant in time comprises a superposition of the filtered contributions for each of the sub-bands:

$$\boldsymbol{s} = \sum_{i=0}^{B} f_i^k \cdot F_i^N \cdot \boldsymbol{x}_i \qquad (2.12)$$

33
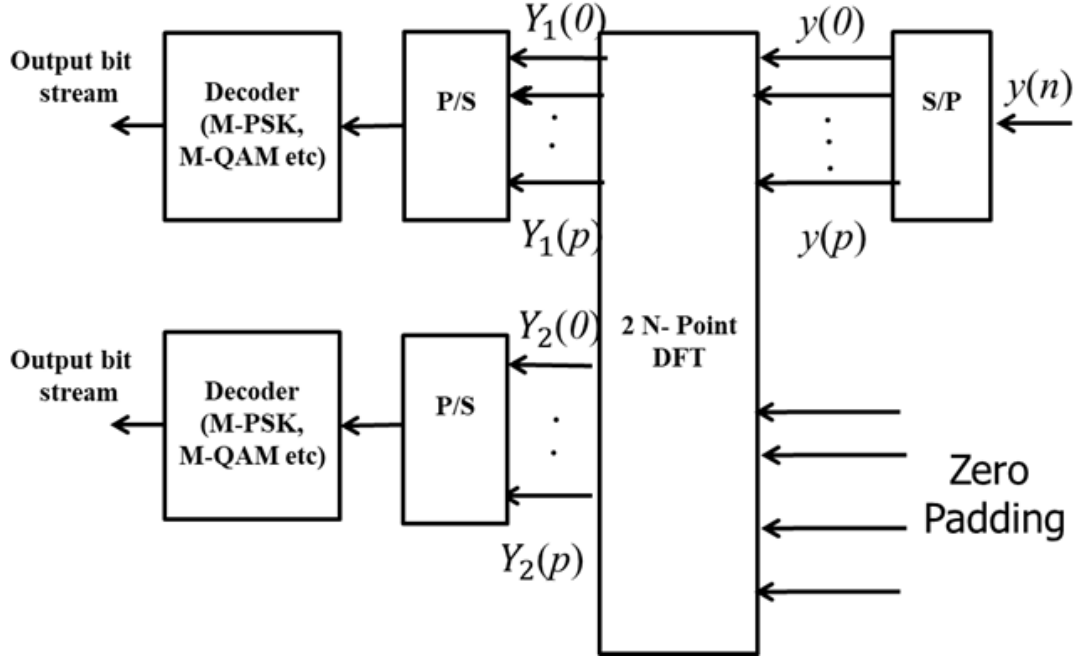
Figure 2.8: *Receiver section of UFMC system model .*

where, N is FFT length, L is sub-band time-domain filter length, we have the following terms:

- x symbols are contained in sub-band i

- B is the number of sub-bands (with index i)

- f_i^k are Toeplitz matrices containing filter impulse response for each of sub-bands (with index i), thus performing the linear convolutions.

- F_i^N are matrices including the columns of inverse Fourier transform matrix corresponding to each sub-band frequency position

Receiver

Receiver model of UFMC block diagram is shown in Fig. 2.8. Since GI is introduced instead of CP, the cyclic convolution property is not preserved in UFMC. Therefore, the receiver structure is not as simple as the one in CP-OFDM. Unlike CP-OFDM receiver which discards CP, UFMC receiver uses whole symbol including GI. For this, $2 \times$ size FFT is used at the receiver, but only the even tones of the $2 \times$ size FFT outputs are used for the detection. It is also claimed that the UFMC performance can outperform that of legacy CP-OFDM, since it fully utilizes all the received signals without discarding CP.

2.5.3 Summary

Due to transmitter filter and in the absence of a CP, we can expect that UFMC will suffer from ISI over time. Moreover, the receiver requires twice the FFT size, which increases complexity and latency of decoder. However, the OOBE is comparable to CP-OFDM with transmitter-WOLA.

2.6 F-OFDM

Similar to UFMC, F-OFDM is another waveform belonging to the group of the legacy OFDM system based on spectrum shaping technique by using filtering techniques. The main difference between UFMC and F-OFDM is in the construction of band-pass filter. In UFMC, the prototype filter $p(t)$ is rectangular pulse covering OFDM symbol as well as CP and the transmitter filter $b(t)$ is carefully designed to suppress OOB interference. However, for F-OFDM, the transmitter filter is computed as the product of ideal band pass filter and a time domain mask denoted as

$$f(n) = b_i(n) \cdot w(n) \tag{2.13}$$

where $b_i(n)$ is ideal band pass filter covering the allocated bandwidth of i-th user, and $w(n)$ is different window function with length equal to half of OFDM symbol and $f(n)$ is transmitter filter that provides good OOBE. Due to sub-band filtering there are many-folds of advantages: firstly the requirement on global synchronization is relaxed and inter-sub-band asynchronous transmission can be supported. Secondly, with proper design of filters, it is possible to suppress OOBE and also the guard band consumption can be reduced to a minimum level. Finally, within each sub-band, optimized numerology can be applied to suit the needs of certain type of services as it is major requirement of future cellular system.

2.6.1 Historical development of F-OFDM

F-OFDM was proposed first time given in [43]- [67]. F-OFDM [43]- [67], is another spectrum shaping technique based on filtering approach. Main difference between UFMC and F-OFDM is, UFMC uses short filter [65] and the filter tail does not extend to the next symbol at the transmitter. Whereas, F-OFDM normally adopts much longer filter [67]. However, the filter tails extend to the adjacent symbols to keep the system overhead same as CP-based OFDM system [67]. Due to this overlapping, system may incur more ISI and ICI than UFMC system in a scenario where a sub-band occupies small percentage of the whole bandwidth. However, the longer filter and soft overlapping among adjacent symbols in F-OFDM render the system much more robust to the adjacent-carrier interference (ACI) and the multiple-access-interference (MAI) in asynchronous systems [42]. In addition to the trade-off between overhead and performance the trade-off between complexity and performance is another important consideration in the system design of the F-OFDM given in [43].
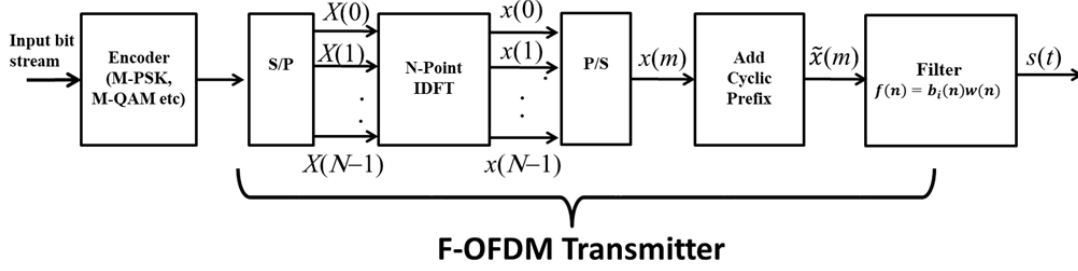
Figure 2.9: *Transmitter section of F-OFDM system model .*
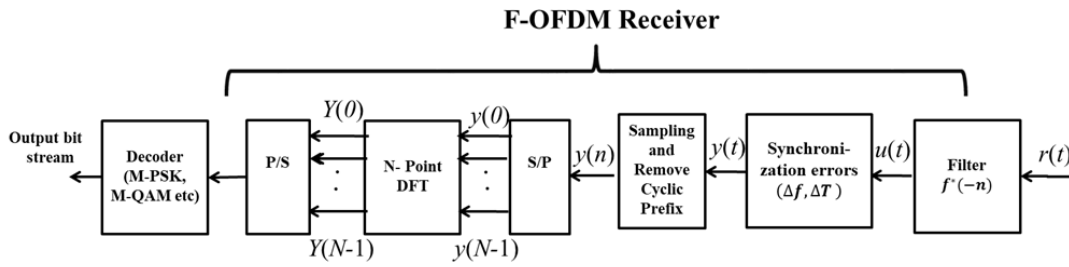
Figure 2.10: *Receiver section of F-OFDM system model .*

2.6.2 Mathematical formulation of F-OFDM

By following eq. (2.1), F-OFDM waveform can be analysed as a special case when:

- The prototype filter $p(t)$ is rectangular pulse covering OFDM symbol as well as CP.

- Transmitter filter $f(t)$ is set to be half of OFDM symbol length. To be specific, the transmitter filter is computed as the product of ideal band pass filter and a time domain mask as $f(n) = b_i(n) \cdot w(n)$

Transmitter

The transmitter section of the F-OFDM model is shown in Figure 2.9. The similar way of CP-based OFDM, symbols are generated after that F-OFDM signal $s(n)$ is then obtained by passing through an appropriately designed spectrum shaping filter $f(n)$ as

$$\tilde{s}(n) = s(n) * f(n) \tag{2.14}$$

where $f(n)$ is centred in frequency at the assigned sub-carriers, its bandwidth is equal to the total frequency width of the assigned sub-carriers, and its time duration is a portion of an OFDM symbol duration.

Receiver

At the receiver side, the received signal is first passed through the filter $f^*(-n)$, which is matched to the transmitter filter. The resulting signal is then passed through the same as CP-based OFDM receiver shown in Fig. 2.10. One should note that in F-OFDM system, the end-to-end channel is given by $f(n) * h(n) * f^*(-n)$, which is estimated and equalized by the equalization block.

2.6.3 Summary

F-OFDM is bandwidth dependent due to the band pass filter. Therefore the filters will need to be dynamically selected based on the tone allocation. Since the total filter length is fixed, the OOB suppression and ISI effect caused by the filter are also varying depending on the tone allocation. Another potential concerns of applying F-OFDM to applications is low latency, especially for TDD band and long group delay due to the long filter length.

2.7 Summary

In this chapter, the basic principles of multi carrier have been introduced, with an overview of the legacy based OFDM system: CP-based OFDM, W-OFDM, UFMC, and F-OFDM. This chapter introduces the common mathematical notation that is going to be used in remaining parts of the thesis.
Summary of this chapter is:

- Multi-carrier systems is combat multi-path fading with enhanced immunity to ISI, splitting the data into several narrow bandwidth sub-carriers.

- Mathematical formulation of multi-carrier system also given with classification of different waveforms based on legacy based OFDM.

- CP-based OFDM advantages include efficient implementation through FFT algorithms and robust performance in case of transmission over frequency selective fading channel using CP and FDE techniques

- Main disadvantages of CP-based OFDM system are: OOBE, high PAPR, and strict synchronization requirement.

- To overcome the problem related to OOBE, the concept of WOLA is proposed in the CP-based OFDM system.

- W-OFDM system achieves better side-lobe decay results. Moreover, by using WOLA at receiver of CP-based OFDM system, better suppression of other (async) users interference is achieved

- UFMC applies per sub-band filtering on OFDM signal, achieving moderated OOB reduction with shorter filter responses. UFMC is not compatible with legacy OFDM system using CP, it relies on zero padding guard interval to accommodate the filter tails.

- The literature survey related to synchronizations errors for OFDM and as well as synchronization strategies and its impact on the performance of the OFDM system will be further discussed in the remaining chapters of this Thesis

Synchronization Issues for OFDM System

THIS chapter consists of the introduction of synchronization issues in CP-based OFDM system, classification of synchronization errors in OFDM system, after that how to overcome the effect of synchronization errors by using different methods of estimators for better estimation of both CFO and STO.

3.1 Synchronization problem associated with OFDM system

Synchronization problem is one of the most challenging issues and plays a major role in PHY design of LTE-A cellular system. The goal of this chapter is to introduce the synchronization problem for CP-based OFDM system. A fundamental tool for assessing the sensitivity to time and frequency misalignments is provided. Misalignment errors in time and frequency can destroy the orthogonality and result in severe performance degradation [68], [69], and [70]. The effect of synchronization errors in OFDM receiver can be seen both in time and in frequency domain, in frequency domain CFO and phase noise are responsible for loss of orthogonality between sub-carriers and generates ICI, which results in performance degradation [68]. In time domain, STO introduces a phase rotation within the same symbol and ISI between successive symbols [68] as shown in Fig.3.1. As a consequence, the design of an efficient receiver is an important practical issue to increase robustness in the system [71]. Estimation methods for CFO and STO can be broadly categorized into two groups of data-aided approaches [71], [72] and non-data-aided approaches [73], [74], and [75]. However, in data-aided approaches, *i.e* using null sub-carriers, or special training symbols, whereas data aided approaches can allow for faster timing and frequency synchronization, requiring a smaller number
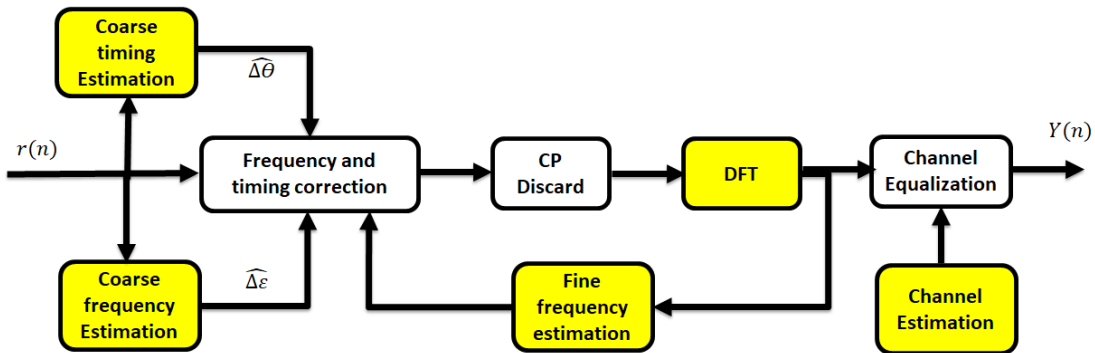
Figure 3.1: *OFDM receiver with synchronization errors and channel estimation .*

of received symbols at the cost of a reduced data rate. Moreover, in non-data-aided approaches, *i.e*, using CP periodic structure, it requires a large amount of symbols to present acceptable performance. The detail effects of STO and CFO are discussed in following sections.

3.2 Symbol timing offset

Timing synchronization is one of the major issues of OFDM system. The presence of synchronization destroys the orthogonality of sub-carriers and degrades the performance of OFDM system. Timing synchronization includes STO estimation and correction. Main benefit to estimate the correct value of timing synchronization, is to find the correct starting point of DFT window at receiver that preserves the orthogonality
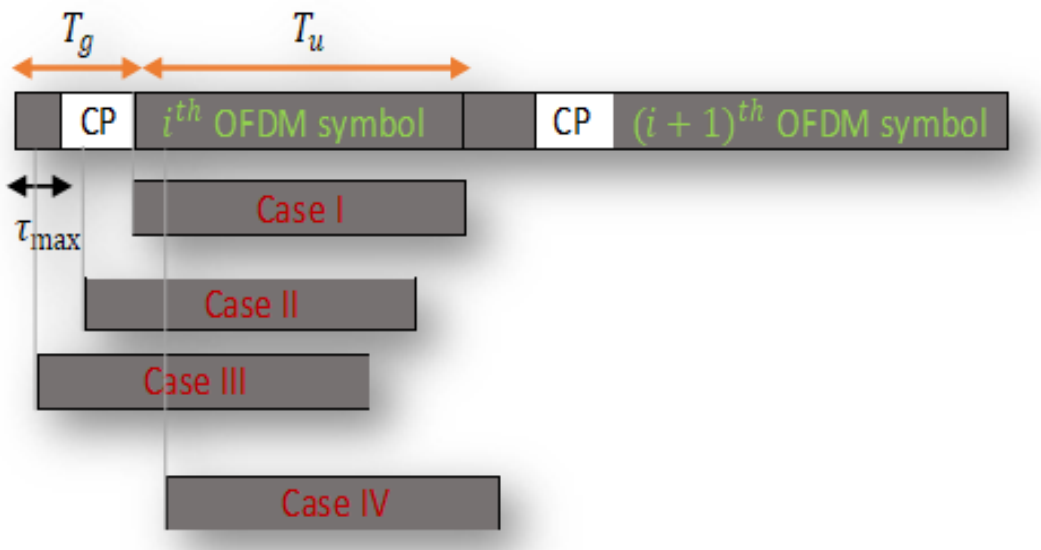
Figure 3.2: *Different cases of STO in OFDM system.*

40

among the sub-carriers. Due to wrong choice of DFT window, ICI and ISI are generated as different cases of the received signal shown in Fig. 3.2. As shown in Fig. 3.2, the effect of STO is analysed into four different cases.

Case I: When there is no timing offset error (*i.e.* timing offset $\Delta\theta = 0$). This is the case when the estimated starting point of OFDM symbol coincides with the exact timing, preserving the orthogonality among sub-carriers. Therefore the OFDM symbol can be perfectly recovered without any type of interference. In this case, the received sampled signal is possible to be recovered by just after removing the cyclic prefix.

Case II: When the estimated starting point of OFDM symbol is before the exact point. In this case, the ith symbol is not overlapped with the previous $(i-1)$th OFDM symbol, that is, without incurring any ISI by the previous symbol in this case. In order to see the effect of STO, consider the received signal in frequency domain by taking FFT of time-domain received samples given as

$$Y^i(k) = e^{j\frac{2\pi\Delta\theta n}{N}} X^i(k)\beta^i(k) + \tilde{w}(k), k = 0, \ldots, N-1, \quad (3.1)$$

where $X^i(k)$ is transmitted complex ith data symbol over kth sub-carrier, $\beta^i(k)$ is channel frequency response of ith data symbol for kth sub-carrier, $\tilde{w}(k)$ is complex AWGN with zero mean and variance per dimension $\sigma^2 = N_0/2$. From equation (3.1), it is clear that the orthogonality among sub-carriers can be completely preserved. However, there exists a phase offset which is proportional to STO ($\Delta\theta$), forcing the signal constellation to be rotated around the origin. This phase offset can be compensated by a single tap frequency domain equalizer.

Case III: When the starting point of ith OFDM symbol is estimated to exist prior to the end of (lagged) channel response of $(i-1)$th OFDM symbol, and thus, the symbol timing is too early to avoid ISI. In this case, the orthogonality among sub-carrier components is destroyed by the ISI (from the previous symbol) and furthermore, ICI occurs

Case IV when the starting point of ith OFDM symbol is estimated just after the exact point. In this case, the samples for current FFT operation interval consists of a part of the current ith OFDM symbol and a part of $(i+1)$th OFDM symbol. Therefore the received sampled signal for current FFT operation or interval can be expressed as

$$Y^i(k) = e^{j\frac{2\pi\Delta\theta n}{N}} X^i(k)\beta^i(k) + \underbrace{\sum_{q=0,q\neq k}^{N-1} X^i(q)\beta^i(q) e^{j\frac{2\pi\Delta\theta n}{N}} \left(\sum_{n=0}^{N-1-\Delta\theta} e^{\frac{j2\pi n(q-k)}{N}} \right)}_{ICI}$$

$$+ \underbrace{\sum_{q=0}^{N-1} X^{i+1}(q)\beta^{i+1}(q) e^{j\frac{2\pi(n+\Delta\theta-N_{CP}-N)}{N}} \left(\sum_{n=N-\Delta\theta}^{N-1} e^{-\frac{j2\pi nk}{N}} \right)}_{ISI} + \tilde{w}(k), \quad (3.2)$$

From equation (3.2), it is clearly visible that, first term indicates that timing offset results in phase offset. The second additive term represents ICI while the third term stands for ISI. The last term represents white Gaussian noise component. By efficient estimation and compensation of STO, it is possible to improve the performance of OFDM

system by reducing the effect of above 4 different cases. Now, in next sub-sections different estimators are described in detail and also their performance is given.

3.2.1 STO estimation

In literature, there are several methods of timing offset estimation which are based on the both non-data-aided [73] [76] [74] [77] and data-aided approaches [71] [72] [75] [78] [79] [80] [68] [81] [82] [58] [83] [84], that can be used as a basis to support the development of proper synchronization schemes. Basically non-data-aided approaches, *e.g.*, using CP periodic structure, and data-aided approaches, *e.g.*, using null sub-carriers, or special training symbols are used. Here, we are going to compare the performance of only those methods that based on the data-aided (DA) approaches. In DA methods, for timing synchronization, some training symbols or preambles are generally transmitted before the transmission of actual information data symbols. At the receiver, the concept of auto-correlation is used to detect these training symbols in incoming signal. In order to be detectable or separately identifiable within the incoming signal, these training symbols consist of some repetitive patterns or blocks. The timing estimation algorithms generally find the maxima of auto-correlation of incoming signal to detect the starting of training symbol. Now, we are going to describe only some of those methods based on the DA approach.

Schmidl and Cox

One of the most popular method for STO estimation is based on DA approach given by **Schmidl** *et.al.* [75]. This STO recovery method relies on searching for a training symbol with two identical halves in time domain. These two halves of training symbol are made identical by transmitting a pseudo noise (PN) sequence on even frequencies, while zeros are used on odd frequencies. Time domain preambles used by Schmidl and Cox as

$$Preamble = [A_{N/2} \quad A_{N/2}] \tag{3.3}$$

where A represents samples of length $N/2$ and is generated by method described above. Since, timing metric is also used to determine whether the training sequence has been received. There is a probability of either missing a training sequence and not detecting the signal or falsely detecting a training sequence. Distribution of the timing metric gives the information about the correct start of the frame. The timing metric of Schmidl and Cox is written as

$$M(d) = \frac{|P(d)|^2}{R(d)} \tag{3.4}$$

where

$$P(d) = \sum_{K=0}^{N/2-1} r^*(d+k)r(d+k+N/2) \tag{3.5}$$
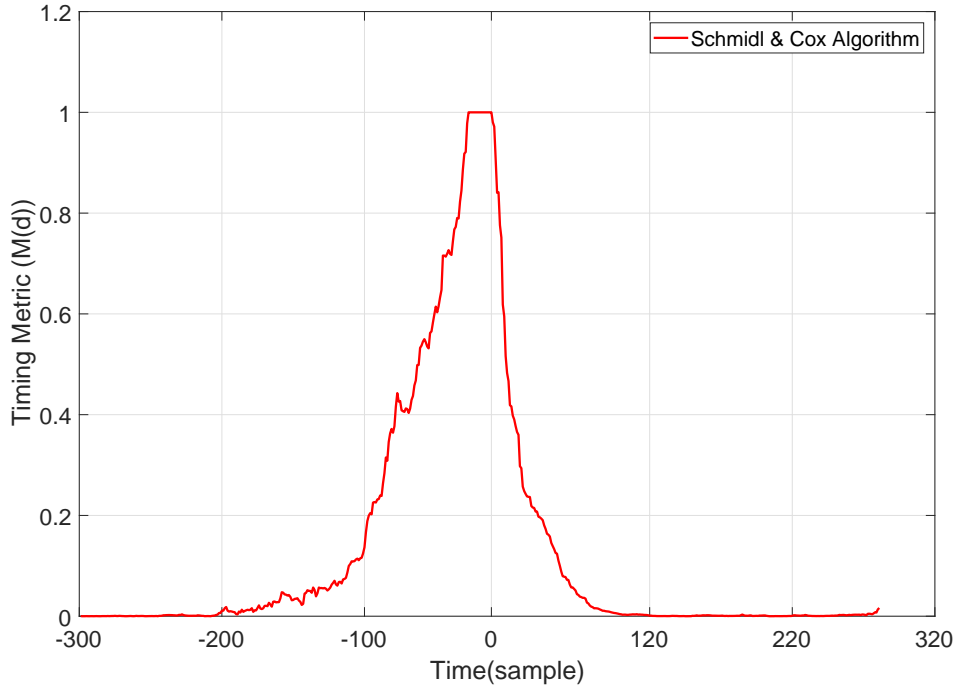
Figure 3.3: *Timing metric generated based on Schimdl and Cox estimators .*

and

$$R(d) = \sum_{k=0}^{N/2-1} |r(d + k + N/2)|^2 \tag{3.6}$$

The starting point of symbol is given by the maximum of timing metric given in eq. (3.4). From the plot of the Timing metric shown in Fig. 3.3, it is clearly visible that timing metric of Schmidl and Cox method has a large plateau. But we are looking for the exact estimate, due to large plateau an exact estimate is not possible. However, large plateau is due to the fact that the dispersive channel. The timing metric has its peak for entire interval of CP length that lead to large mean square error.

Minn's Method

In order to reduce the plateau appeared in timing metric of Schmidl Cox shown in Fig.3.3, **Minn** *et.al.* proposed method that is based on more then two identical training symbols along with flipping the signs in the last two segments to obtain a steeper roll-off trajectory at the correct timing position. The preamble of **Minn's** method is defined as

$$Preamble = [A_{N/2} \ A_{N/2} \ -A_{N/2} \ -A_{N/2}] \tag{3.7}$$

43
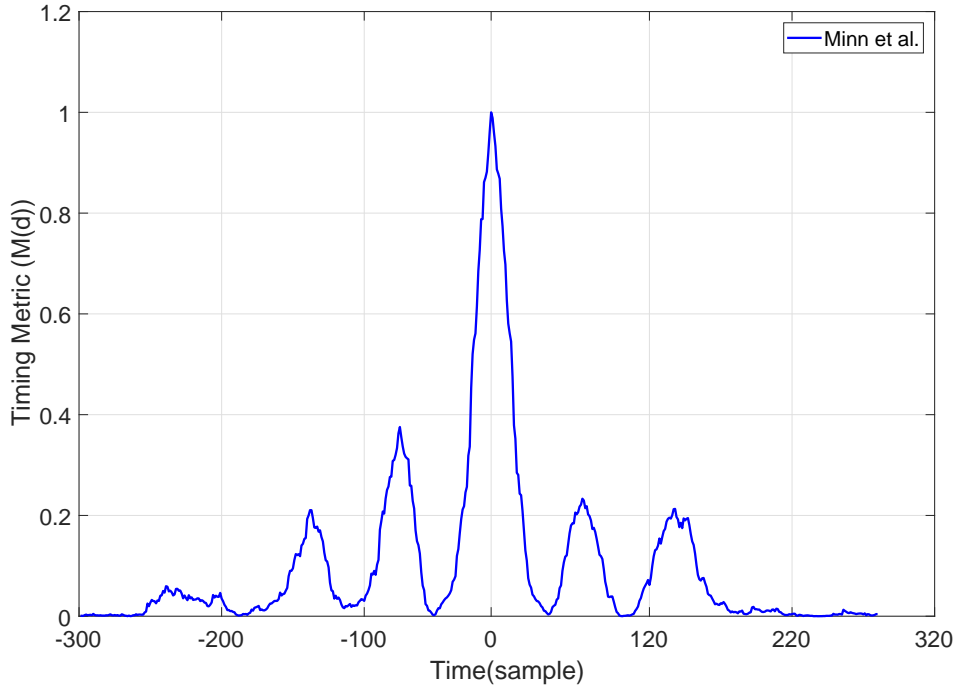
Figure 3.4: *Timing metric generated based on Minn's estimator method .*

The timing metric of **Minn's** method is written as

$$M(d) = \frac{|P(d)|^2}{R(d)} \tag{3.8}$$

where

$$P(d) = \sum_{m=0}^{1} \sum_{K=0}^{N/4-1} r^*(d + k + mN/2) r(d + k + mN/2 + N/4) \tag{3.9}$$

and

$$R(d) = \sum_{m=0}^{1} \sum_{k=0}^{N/2-1} |r(d + k + mN/2 + N/4)|^2 \tag{3.10}$$

The Minn's method has its peak at the correct starting point for OFDM symbol as shown in Fig.3.4, since correlation of some samples results in negative values. For this reason, Minn's method eliminates the peak plateau of the timing metric, hence resulting in a smaller mean square error as compared to Schmidl and cox method.

Park Method

The Park method is based on reverse autocorrelation method and performs better than Schmidl and Cox and Minn's method. The preamble of Park's method is written as

$$Preamble = [A_{N/4} \ B_{N/4} \ A^*_{N/4} \ B^*_{N/4}] \tag{3.11}$$

where, $A_{N/4}$ represents samples of length $N/4$ generated by IFFT of a PN sequence, and $A^*_{N/4}$ represents a conjugate of $A_{N/4}$. To get impulse-shaped timing metric, $B_{N/4}$ is designed to be symmetric with $A_{N/4}$. The timing metric of park method is written as

$$M(d) = \frac{|P(d)|^2}{R(d)} \tag{3.12}$$

where

$$P(d) = \sum_{k=0}^{N/2-1} r(d+k)r^*(d+k+N/2) \tag{3.13}$$

and

$$R(d) = \sum_{k=0}^{N/2-1} |r(d+k)|^2 \tag{3.14}$$

The timing metric of park method is designed such that there are $N/2$ different pairs of product between two adjacent values. It has maximum different pairs of product. Therefore, this timing metric has its peak value at the correct symbol timing, while the values are almost zero at all other positions as shown in Fig. 3.5.

DFrFT-based Localization of Chirp (DFrFT-based Chirp method)

In this method, we exploited the basic property of chirp signal which shows that it peaks in fractional Fourier domain by proper selecting the optimum DFrFT angle parameter (α_{opt}). By exploiting this characteristic of DFrFT-based on chirp signal, it can be used for searching the start of training sequence in received signal. Therefore, at receiver side, DFrFT of auto-correlation of received signal is determined and its peak is observed. Here, we consider training symbol (preamble) block containing two identical halves as

$$Preamble = [A_{N/2} \quad A_{N/2}] \tag{3.15}$$

where A is generated as a chirp signal of length N. Chirp signal is written as

$$A = x(n) = e^{j2\pi\left(a(n/N)^2+b(n/N)\right)}, \text{for } n = 0, 1, \ldots, N-1 \tag{3.16}$$

where a denote the chirp rate and b denote the central frequency signal of the chirp signal. Sliding window of N samples method is used to generate timing metric $M(d)$
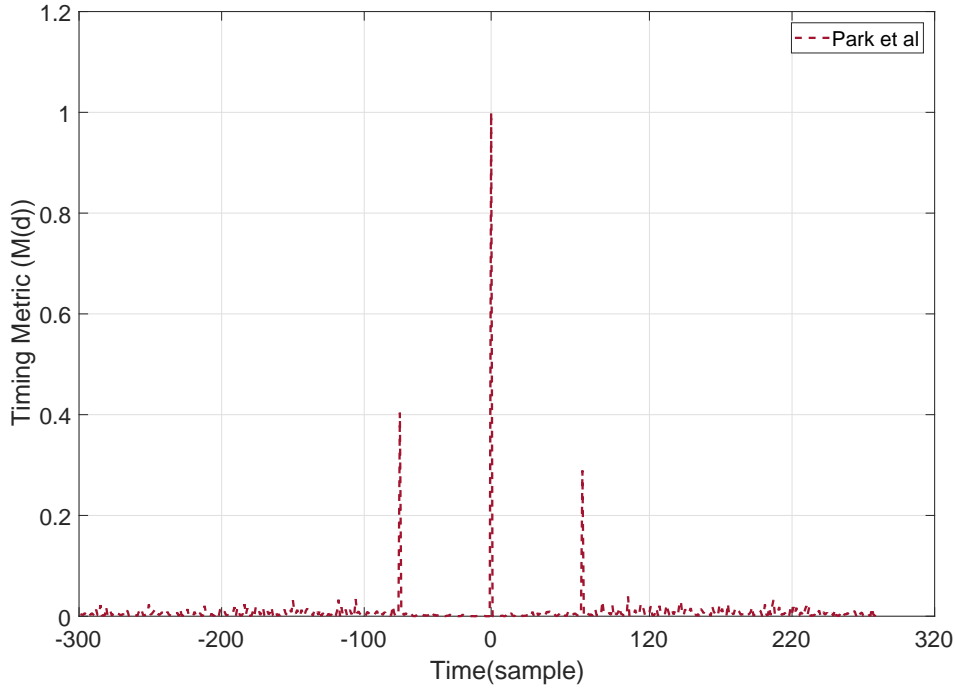
Figure 3.5: *Timing metric generated based on park estimator method .*

(where, d is a time index). First, the DFrFT of every frame or block of N samples of received signal is determined at the optimum angle α, then this DFrFT is used to calculate the $R_{xx}(u)$ given in [85]. The maximum of $|R_{xx}(u)|$ is used to give the value of timing metric defined as

$$M(d) = \underbrace{max}_{u} \left[\left| \sqrt{\frac{2\pi}{1 - jCot(\alpha)}} e^{\frac{-ju^2 Cot(\alpha)}{2}} \left(X_\alpha(u)\right)^2 \left(X_\alpha(-u)\right)^2 \right| \right] \qquad (3.17)$$

where $X_\alpha(u)$ is N point DFrFT of $x(n+d)$. The maximum of timing metric gives the starting point of training symbol. By comparing the different method of timing metric shown in Figs. 3.3, 3.4, 3.5 and 3.6, it is clearly visible that DFrFT-based chirp method performs better than other methods available in the literature.

Now, the performance comparison of different method is presented and compared with the methods available in literature. Therefore, for performance comparison we consider an OFDM system where the number of sub-carriers is 512 and length of CP is 16 the QPSK modulation scheme in case of the transmission over HIPERLAN indoor channel model given in [86]. The mean and mean square error (MSE) has been taken as performance evaluation parameter. The MSE of timing offset with all four estimators in HIPERLAN indoor channel-A shown in Fig. 3.7. It is clearly visible from Figure, due to specific channel characteristics other method gives high starting value of the STO [86]. Moreover, DFrFT-based chirp method is much better as compared to other estimators.
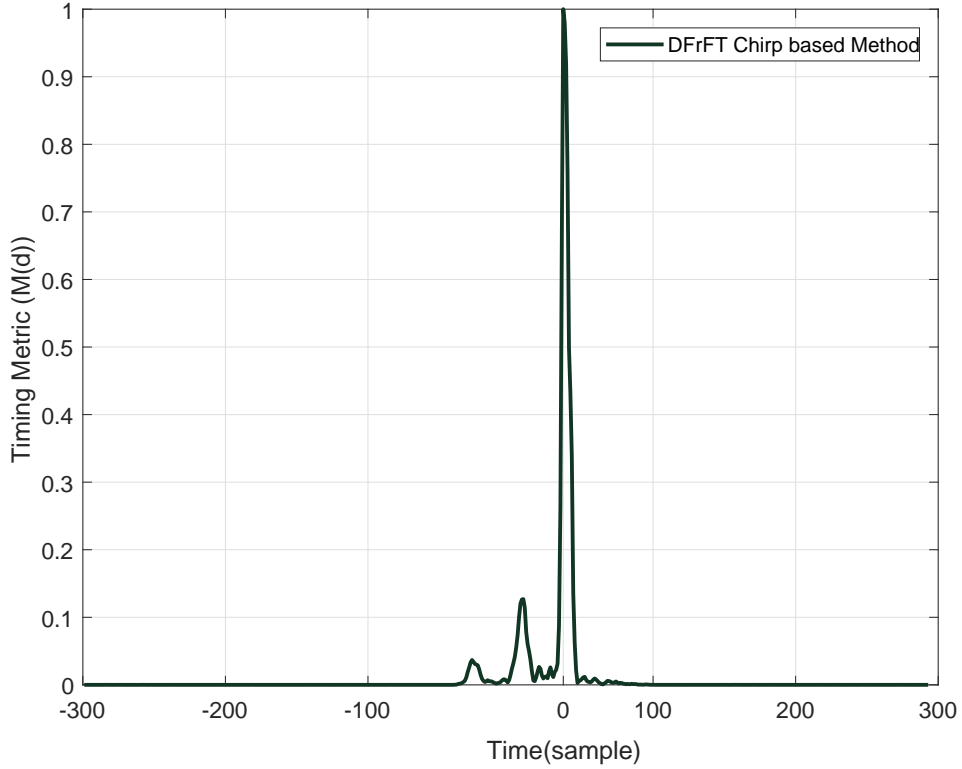
Figure 3.6: *Timing metric generated based on DFrFT-based chirp method estimator.*

DFrFT-based chirp method outperforms all other existing methods at the cost of computational complexity. The reason for this increase in complexity is due to the fact that other methods generate timing metric by taking auto-correlation in time domain directly whereas the DFrFT-based Chirp method first takes the DFrFT of received signal and then generate timing metric.

3.3 Carrier frequency offset

CFO produces a shift of received signal in the frequency domain and may result in a loss of mutual orthogonality among sub-carriers, which introduces a significant degradation of performance shown in Fig. 3.8. CFO is due to either mismatching of transmitter and receiver oscillators frequencies or Doppler spread. The presence of CFO destroys the orthogonality among sub-carriers, generating ICI. The received signal given in (3.18) has considered only the effect of multipath fading channel. Therefore, including the effect of CFO along with effects of multipath fading channel, the samples of received signal can be expressed as

$$y(n) = e^{\frac{j2\pi\Delta\varepsilon n}{K}} \sum_{i=0}^{L-1} h_i \tilde{x}(n-i) + w(n), \qquad (3.18)$$

47
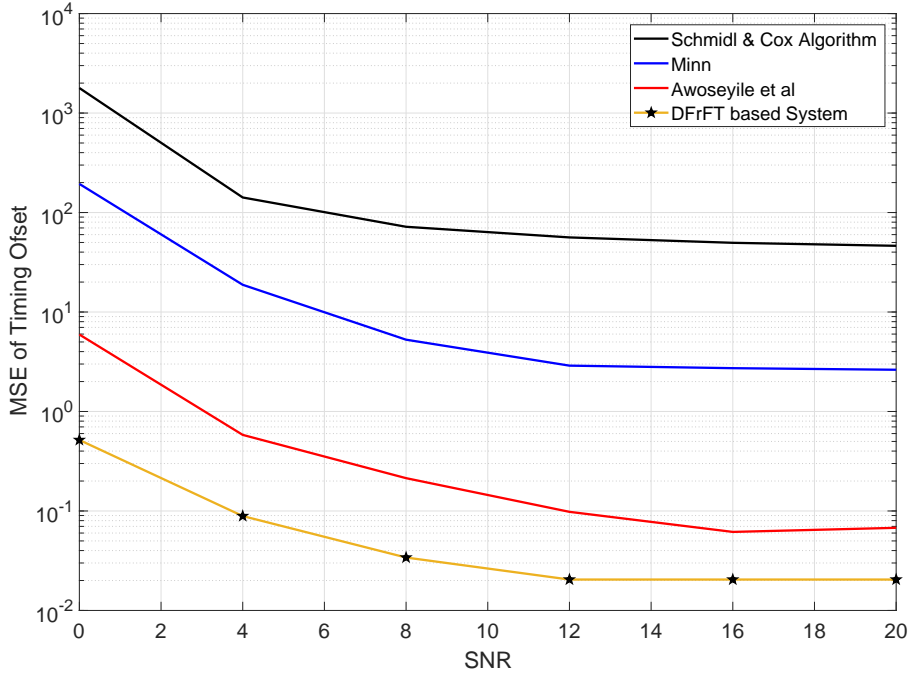
Figure 3.7: *MSE of timing offset comparison with different estimators together with DFrFT-based chirp estimator .*
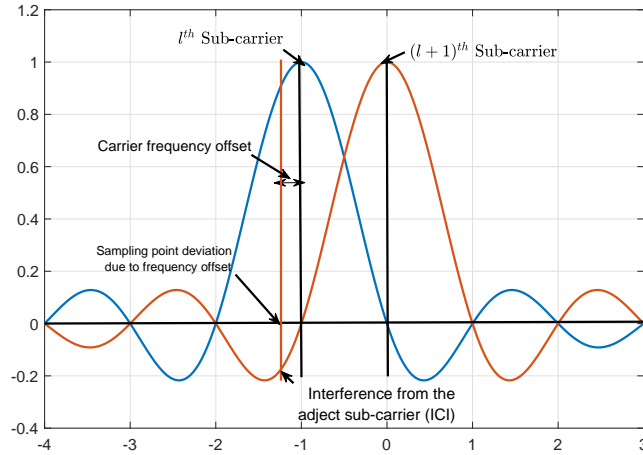
Figure 3.8: *CFO effect on sub-carriers that destroys the orthogonality among sub-carriers, generating ICI.*

where $w(n)$ represents the complex AWGN with zero mean and variance σ^2 per dimension and $\Delta\varepsilon = \Delta f M T_s$ is the residual CFO (Δf) is normalized to the sub-carrier spacing. By taking DFT of the received signal given in eq.(3.18), the received signal is

written as

$$Y(q) = \frac{1}{\sqrt{N}} \sum_{n=0}^{N-1} y(n) e^{-\frac{j2\pi qn}{N}}, \quad \text{for } q = 0, 1, \ldots, N-1. \tag{3.19}$$

After substituting the value from eq. (3.18) into eq. (3.19) as

$$Y(q) = \frac{1}{N} \sum_{n=0}^{N-1} \left\{ e^{\frac{j2\pi\Delta\epsilon n}{N}} \sum_{l=0}^{L-1} h_l(n) \sum_{m=-N_{CP}}^{N-1+N_G} \sum_{k=0}^{N-1} X(k) e^{\frac{jn\pi mk}{N}} g(n-l) + \tilde{w}(n) \right\} e^{-\frac{jn\pi qn}{N}}, \tag{3.20}$$

Symbol transmitted on the kth sub-carrier. If $k = q$, then signal will be orthogonal and desired signal will be received. If $k \neq q$ (effect on the qth sub-carrier), then signal will be non-orthogonal and interference signal will be generated. The received signal can be rewritten as

$$Y(k) = \underbrace{\underbrace{X(k)S(k)\beta(k)}_{\substack{\text{Desired Signal} \\ \text{on } k\text{th sub-carrier}}} + \underbrace{\sum_{q=0, q \neq k}^{N-1} X(q)S(<q-k>_N)\beta(q)}_{\substack{\text{ICI term} \\ \text{due to other than } k \text{ sub-carriers}}}}_{R(k)} + \tilde{w}(k), \, k = 0, \ldots, N-1, \tag{3.21}$$

where $X(q)$ is the transmitted complex data symbol over qth sub-carrier, $\beta(q)$ is channel frequency response for qth sub-carrier, and

$$S(k) = \frac{1}{N} \sum_{n=0}^{N-1} e^{j\frac{2\pi\Delta\epsilon n}{N}} \tag{3.22}$$

using trigonometric identity

$$\sum_{n=1}^{N} e^{j\theta_n} = \frac{Sin\left(\frac{n\theta}{2}\right)}{Sin(\theta/2)} e^{j\tilde{\theta}} \tag{3.23}$$

After further simplification the ICI coefficient can be written as

$$S(k) = \frac{Sin\pi(k+\Delta\epsilon)}{NSin\left(\frac{\pi(k+\Delta\epsilon)}{N}\right)} e^{j\pi\left(1-\frac{1}{N}\right)(k+\Delta\epsilon)} \tag{3.24}$$

After the studies of CFO effect, now our focus is on the development of estimation algorithms. Better estimation of CFO is to improve the robustness of the OFDM system with CFO.

3.3.1 CFO estimation

Here, we are going to describe the different estimator techniques based on the data-aided methods for frequency offset estimation. The frequency offset estimation is described into the two steps, the fractional frequency offset (FFO) estimation and integer frequency offset (IFO) estimation. Now, we are going to describe only those methods based on the data-aided approach.

Schmidl and Cox

In this method two training symbols are used with differential encoding at identical sub-carrier positions for CFO estimation. The first symbol which consists of two identical halves was used for FFO estimation, whereas IFO was estimated in frequency domain by using second symbol. The estimation range of this method was $\pm N/2$ times the sub-carrier spacing, for N-point FFT. To reduce the overhead due to second symbol in this method, several other methods have been proposed in the literature. The basic concept behind frequency offset estimation is that the two identical halves will remain identical after passing through channel, except the phase difference ϕ between them due to the frequency offset Δf. The phase difference ϕ between two halves is obtained by calculating their correlation and given as

$$\phi = \pi T_u \Delta f = \pi N T_s \Delta f \tag{3.25}$$

where T_u is the useful OFDM duration and T_s is the sampling time. This phase difference $\hat{\phi}$ can be estimated as

$$\hat{\phi} = \angle \left(P(d) \right) \tag{3.26}$$

where $P(d)$ is defined as correlation between the two halves of training symbols given in eq.(3.5), after estimation of phase frequency offset estimate, it is written as

$$\hat{\Delta f} = \underbrace{\frac{\hat{\phi}}{\pi N T_s}}_{fractional\,frequency\,offset(FFO)} + \underbrace{\frac{2\hat{\Xi}}{N T_s}}_{integer\,frequency\,offset(IFO)} \tag{3.27}$$

where $\hat{\Xi}$ is an integer frequency offset. After FFO estimation and correction, we compute DFT of both symbols taken for estimating the IFO. For IFO estimation, the second training symbol block contains a differentially encoded pseudo-noise sequence on even sub-carriers and another pseudo noise sequence on odd sub-carriers. After receiving two training symbols are $Z_1(k)$ and $Z_2(k)$ and the differentially modulated even frequencies of second training symbol $W(k)$, the sliding correlation is written as

$$B(l) = \frac{|\sum_{k \in \xi} Z_1^*(k + 2l) \cdot W(k) \cdot Z_2^*(k + 2l)|^2}{2 \left(\sum_{k \in \xi} Z_2^*(k)|^2 \right)^2} \tag{3.28}$$

where ξ is the set of indices for even frequency components, $\xi \in \{-Y, -Y+2, \cdots, Y-2, Y\}$, Y is the total number of even frequencies with PN sequence. The value of l at which $B(l)$ attains maximum value is used to calculate IFO.

Morelli Method

Morelli et.al introduced the best linear unbiased estimator (BLUE) as an extension of Schmidl and Cox method. This method consists of one training symbol with M identical parts. This algorithm can estimate FFO and IFO estimation simultaneously. In this method, by exploiting the correlations of the samples from the matched filter. The estimated CFO $\hat{\epsilon}$ is given as

$$\hat{\Delta}\epsilon = \frac{1}{2\pi/M} \sum_{m=1}^{H} \beta(m)\theta(m) \tag{3.29}$$

where H is the design parameter, and $\beta(m)$ is the mth component of β as

$$\beta = C_\theta^{-1} 1/1^T C_\theta^{-1} 1 \tag{3.30}$$

where C_θ is the covariance matrix of $\theta = [\theta(1), \theta(2), \cdots, \theta(H)]^T$ and $1 = [1, 2, \cdots, 1]^T$ is an H dimensional column vector of all ones. The angles is defined as

$$\theta(m) = [arg(R(m)) - arg(R(m-1))]_{2\pi}, \text{for } 1 \le m \le H \tag{3.31}$$

where $[\cdot]_{2\pi}$ denotes modulo-2π operation, and $arg(R(m))$ is the argument of $R(m)$ given as

$$R(m) = \frac{1}{N - mM_s} \sum_{k=mM}^{N-1} x(k)x^*(k - mM_s), \text{for } 0 \le m \le H \tag{3.32}$$

where $M_s = n/M$ is the number of samples in each section of training symbol.

Chirp Training Symbol Based Estimator

Wei et.al proposed a new method which uses chirp signal as training symbol, where training symbol blocks contains two CAZAC sequences or chirp signal. First part of the training signal is used for FFO estimation and both sequences are used for IFO estimation. The preamble is describe as

$$Preamble = [x(n, r1) \ x(n, r2)] \tag{3.33}$$

where $x(n, r1)$ and $x(n, r2)$ is defined as first and second CAZAC sequences respectively. The CAZAC sequence in time domain can be written as

$$x(n, r) = e^{j\pi rn^2/n}, \text{for } n = 0, 1, \cdots, N - 1 \tag{3.34}$$

where r is the parameter of CAZAC sequence.

The FFO estimation is same as given by Schmidl and Cox (using autocorrelation). The IFO estimation is based on the fact that DFT of a CAZAC sequence is also a CAZAC sequence. For IFO estimation, this method uses cross correlation between

known training sequence at the receiver and partially (FFO) compensated training sequence. DFT of the received signal $r(n)$ is written as

$$R_f(\Delta\epsilon - \hat{\Delta}\epsilon_f, r, \tau) = \frac{1}{N} \sum_{k=0}^{N-1} X(k-\tau)_{modN} Y^*(k) \tag{3.35}$$

where $X(k)$ is DFT of training sequence $x(n,r)$, and $Y(k)$ is DFT of received signal. After that, the normalised IFO $\hat{\epsilon}_f$ will be estimated as describe in [87].

DFrFT-based Localization of Chirp (DFrFT-based Chirp method)

Similar to STO estimation based on DFrFT-based chirp method, same approach was also adopted for CFO estimation, where chirp based training sequence are used and exploited the modulation property of DFrFT. In this method, we estimate the FFO and IFO separately and then sum up to get the overall CFO estimation. Therefore, the overall frequency offset (Δf) can be obtained as

$$\Delta f = \Delta F_{FFO} + \Delta F_{IFO} \tag{3.36}$$

FFO ΔF_{FFO} estimation method is same as given by Schmidl and Cox which is based on the chirp based training sequence in this method. After FFO estimation, DFrFT of first half of received training sequence is taken as

$$X_\alpha(u) = DFrFT\{x_1(n)\}, \text{for } n = 0, 1, \cdots, N-1. \tag{3.37}$$

However, IFO estimation is carried out by searching the peak position in DFrFT of first half of received training sequence as describe below

$$\Xi_{max} = \underbrace{argmax}_{u} [|X_\alpha(u)|] \tag{3.38}$$

Finally, to calculate the value of $\hat{\Xi}$ given by

$$\hat{\Xi} = \begin{cases} |\Xi_{max} - N/2| - 1, & \in (\hat{\phi}/N) \geq 0 \\ |\Xi_{max} - N/2|, & otherwise. \end{cases} \tag{3.39}$$

We again perform MSE for CFO estimation and compare the performance of all those methods given above. For this comparison, an OFDM system with 512 number of sub-carriers and 16 cyclic prefix with QPSK modulation in case of transmission over frequency selective fading is consider, the channel model consisting of 8 numbers of multi-path with path delays of $l = 0, 1, \cdots L - 1$ samples and an exponential power delay profile having average power of $e^{-l/L}$ is used. From Fig. 3.9 of MSE of frequency offset estimation with all estimators considered in multipath fading channel. It is clearly visible that DFrFT-based Chirp estimator performs better as compared to other discussed methods.
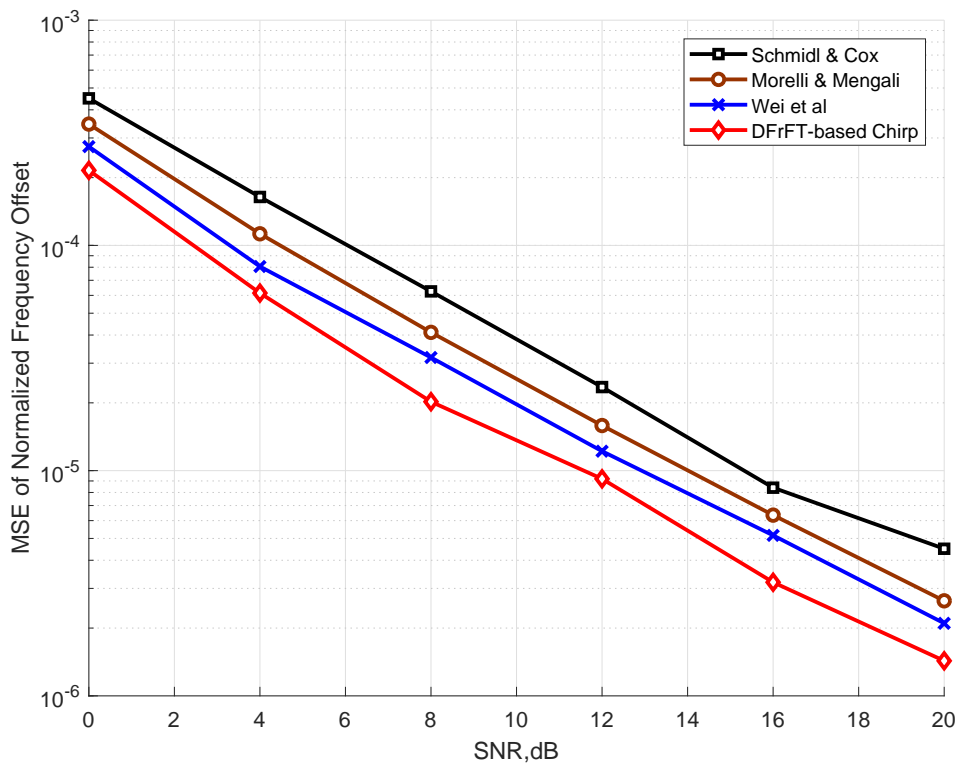
Figure 3.9: *MSE of carrier frequency offset comparison with different estimators together with DFrFT-based chirp estimator.*

3.4 Summary

Several approaches are available in literature to face the problems introduced by synchronization errors in OFDM systems [51]. Therefore, the role of the CFO and STO estimation is very important issues in the PHY. Moreover, from the results of STO and CFO estimation based on the localization of chirp signal in DFrFT domain perform better as compared to other methods available in the literature and also provides lowest MSE. However, to obtain such improvements in MSE of CFO and STO, the computational complexity increases as compared to other methods.

CHAPTER *4*

Problem Formulation and System Model

THIS chapter consists of summary of historical development of performance evaluation of OFDM system. After that system model of DFrFT-based OFDM in presence of the residual CFO and STO together in case of transmission over multi-path fading channel.

4.1 Historical development of OFDM

Taking a brief discussion about the historical development of OFDM (milestones in history). Through this initially developed OFDM, attentions of researchers moved towards the performance analysis of OFDM system. The beginning of OFDM is summarized in Table 4.1.

4.2 Literature survey of performance analysis

After the historical development of DFT-based OFDM system, researchers moved towards the problem formulation of performance analysis of OFDM system. Two methods were available for the analysis of performance degradation. Firstly, the statistical average of ICI, used as a performance measure. Secondly, the BER caused by CFO and STO, approximated by assuming ICI to be Gaussian. The performance analysis of the DFT-based OFDM system in different channel environments (flat fading, frequency selective fading, etc.) with CFO has been done by different authors in [50, 97–101, 112, 113]. Moreover, the effect of CFO and STO combinely were considered by different authors in [102, 104, 108, 109] for DFT-based OFDM system. Be-

Table 4.1: *Summary of historical development of OFDM*

1965	P. A. Bello *et al.* [88]	Initial multi-carrier (MCM) system KINEPLEX [88]
1967	M. Zimmerman *et al.* [89]	
1968	R.W. Chang *et al.* [54]	MCM employing overlapped band limited orthogonal signals.
1967	Saltzberg *et al.* [90]	MCM system employing orthogonal time staggered QAM.
1971	S.B. Weinstein *et al.* [48]	OFDM became more popular after the use of DFT to generate the orthogonal sub-carriers
1980	J.S. Chow *et al.* [91]	Suggested the use of DFT based OFDM for high speed modems
1980	Hirosiki *et al.* [92]	Suggested a system for Saltsberg' O-QAM OFDM system
1985	Cimini *et al.* [93]	Analytical and simulated results on the performance of OFDM modems
1988 and 1995	ETSI DAB standard	First OFDM based standard for digital broadcasting system

fore moving towards the problem formulation, We have discussed the brief summary of performance analysis of OFDM system given by many authors.

In 2001 the probability of error calculation of an OFDM system based on the DFT with CFO was given by **K. Sathananthan** and **C. Tellambura** [98]. They used a precise numerical technique for calculating the effect of CFO on BER/SER. The sub-carriers modulated with BPSK is solved using a series due to Beaulieu. For QPSK and 16-QAM cases, they used an infinite series expression for error function in order to express the average probability of error in terms of the two-dimensional (2D) characteristic function (CHF) of ICI. They also proposed the Gaussian approximation for approximate SNR degradation.

Later in 2005 a paper on BER of OFDM systems impaired by CFO in multi-path fading channels was given by **Luca Rugini** and **Paolo Banelli** [99]. This paper contains an analytical approach to evaluate the error probability of OFDM system subject to CFO in frequency selective channel, characterized by Rayleigh or Rician fading. By properly exploiting the Gaussian approximation of ICI, it is shown that BER for an uncoded OFDM system with QAM can be expressed by the sum of a few integrals, whose number depends on the constellation size, each integral can be evaluated numerically. In Rayleigh fading, by using a series expansion that involves generalized hyper geometric functions, each integral can be evaluated.

Table 4.2: *Summary of performance analysis of DFT and DFrFT-based OFDM system*

1990	Cases *et al.* [94]	Gave analytical and experimental results of OFDM system
1991-1993	Hara *et al.* [95]-[96]	Rayleigh frequency selective fading channel BER performance for Multicarrier Modulation Radio Transmison.
1995	T. Pollet *et al.* [97]	BER sensitivity of OFDM to CFO and Weiner phase noise
2001	K. Sathananthan *et al.* [98]	Calculated the probability of error of OFDM systems with CFO [98]
2005	Luca Rugini *et at.* [99]	Analytical approach to evaluate the error probability of OFDM systems with CFO in frequency-selective channel
2009	P. Dharmawansa *et al.* in [100]	Gave an exact error probability analysis of OFDM systems with frequency offset
2010	A.K. Chaturvedi *et al. in* [101]	Given closed form BER expressions for BPSK OFDM systems with frequency offset
2012	R. Uma Mahesh *et al* [102]	BER analysis of BPSK OFDM systems with CFO and STO in AWGN and Flat fading
2010	J. Zhang and Z. Wang *et al* [103]	ICI analysis for DFrFT-OFDM systems to frequency offset in time frequency selective fading channel
2012	Y. Wang, Z. Zhang *et al* [104]	BER analysis of BPSK OFDM systems with CFO and STO over frequency selective Rayleigh fading channels
2013	A. Kumar *et al* [105]	Closed form relations for ICI and BER in FrFT based OFDM system
2014	A. Hamza, *et al* [50]	Closed Form SER Expressions for QPSK OFDM systems CFO in Rayleigh fading channel
2015	Z. Wang *et al* [106]	BER analysis of hybrid carrier system based on WFRFT with carrier frequency offset
2015	M.R. Mousavi *et al* [107]	Hyperbolic FRFT-OFDM system BER analysis over high Doppler Rician fading channels
2015	A. Hamza, *et al* [108]	Closed-Form Expressions for the BER/SER of OFDM systems With an Integer Time Offset
2016	A. Kumar, *et al* [109]	An exact SER expression for QPSK OFDM system in presence of residual CFO and STO
2016	A.Kumar *et al* [110]	Exact SER analysis of DFrFT-based QPSK OFDM system over frequency selective Rayleigh fading channel with CFO
2016	S.Kumari *et al* [111]	Extended SEP performance evaluation to the transmission over a Nakagami-m fading channel both for BPSK and for QPSK modulation formats

Further in 2007 a paper was published on the effects of receiver windowing on OFDM performance in the presence of CFO by **Norman C. Beaulieu** and **Peng Tan** [112, 113]. The paper derived an expression for exact BER with windowing reception, and it was found that performance of OFDM in terms of BER is improved by using windowing techniques.

In 2009 a paper on exact error probability analysis of OFDM system with CFO was given by **Prathapasinghe Dharmawansa, Nandana Rajatheva**, and **Hlaing Minn** [100]. The paper also comprises all the work related to performance evaluation that was done till then. They used CHF and Beaulieu series [100] to derive exact BER expressions in the presence of ICI. They followed the procedure presented in [98] and [99] with different mathematical insight to derive the exact closed form BER/SER expressions for OFDM with ICI over AWGN, frequency selective and flat fading channel. They did not consider the Gaussian approximation of ICI, instead they consider that the probability density function of ICI is a mixture of Gaussian densities with properly selected parameters.

In 2010 a paper was published on closed form BER expressions for BPSK OFDM system with CFO by **R. Uma Mahesh** and **A. K. Chaturvedi** [101]. This paper addressed the performance degradation caused by the presence of CFO in OFDM systems. In this paper they modified the result given in [100]. The results in [100] was analyzed for lower values of CFO and there was a difference between analytical and simulated results for higher values of CFO. They modified the analytical expressions also for higher values of CFO for flat and frequency selective Rayleigh fading channels. Later on **A. Hamza**, *et al* [50] extended the SER expressions for QPSK OFDM systems.

Moreover, very few literatures studied on the effects of STO and CFO in OFDM system for BER evaluation. However, the BER performance investigations considering both CFO and STO are [102, 104, 108, 109]. Due to high sensitivity of OFDM systems to synchronization errors, they treated the ICI introduce by residual frequency and timing offsets. By Following [101], they derived BER expression with frequency and fractional timing offsets over AWGN and flat Rayleigh fading channels [102]. Furthermore, in [104] By exploiting CHF and Beaulieu series, evaluated BER expressions of BPSK impaired by residual CFO and STO transmission over frequency selective Rayleigh fading channel. Similarly the extension on above model for QPSK modulation scheme in case of transmission over frequency selective Rayleigh fading channel was given in [109]. Furthermore, **A. Hamza** *et al* [108], first time derived the analytical expressions including the CFO together with integer timing offset.

However, the mentioned above literature survey on the performance evaluation are related to DFT-based OFDM system in the presence of the CFO and STO. Moreover, as mentioned in the previous chapter by using the DFrFT as a localization tool allows to improved estimation performance of the CFO and STO. Motivated by this, we started investigation about the DFrFT-based OFDM system in the place of the one based on the DFT. Moving towards the DFrFT-based OFDM the main reference was **J. Zhang** and **Z. Wang** [103], where it was shown that in presence of CFO an OFDM system based on DFrFT allows a better tolerance to ICI than that based on the use of FFT. The DFrFT is a generalization of the ordinary FFT that allows for more flexibility in applications.

Moreover, in order to improve the robustness to residual CFO, an OFDM system based on the use DFrFT also was proposed by **Martone** *et.al.* in [28]. This system is analogous to the conventional OFDM one with the difference that DFT and inverse DFT (IDFT) are replaced by DFrFT and inverse DFrFT (IDFrFT), respectively. As observed by Martone, in case of a time-varying frequency selective fading channel the entire conceptual framework of frequency-domain channel partitioning, exploited by DFT-based OFDM, loses its optimality. To counteract this drawback, Martone proposed the use of the DFrFT in OFDM where orthogonal signal bases of chirp function with rate $\cot(\alpha)$, being α the 'angle parameter', are used in place of the orthogonal complex exponentials of DFT in the presence of Doppler effect. The main advantage of using orthogonal chirp function consists in the control of the time-frequency partition of the channel. Here, as already observed in the existing literature, the same concept is used to mitigate the performance degradation introduced by the loss of orthogonality due to CFO.

The problem of deriving closed form expressions for the symbol error probability (SEP) of a DFrFT-based OFDM system for frequency selective fading channels in presence of CFO was studied by many authors [105–107, 110, 111]. In [105], an exact BEP formula was derived for BPSK transmission over Rayleigh fading channel. For same modulation and channel model, the authors in [106] analyzed BEP for weighted-type DFrFT impaired by CFO. Always considering BPSK, in [107] the exact BEP of hyperbolic DFrFT was derived for transmission over Rician fading channel. In [110], the authors extended the work of [105] to the case of QPSK and derived an exact SEP expression for frequency selective Rayleigh fading channel. Finally, the analysis done in [111] extended SEP performance evaluation to transmission over a Nakagami-m fading channel both for BPSK and for QPSK modulation formats. However, since it happens that CFO and STO are present together in OFDM, it would be better to analyze the performance of an OFDM system when their effect is considered together instead of dealing with only CFO. Moreover, concerning STO, it is here observed for the first time in this thesis that DFrFT is also beneficial in terms of performance. This is demonstrated by quantifying its effect in an analytical expression of the term responsible for introducing ICI and ISI.

4.3 DFrFT-based OFDM system

Figure 4.1 reports the block diagram of complex baseband equivalent model of the DFrFT-based OFDM system. The transmitter includes the encoder block and the serial-to-parallel (S/P) converter block whose role is that of splitting the high data rate stream into a number of N lower data rate parallel streams. The IDFrFT is computed on a block of N information symbols. To overcome the effect of ISI, a CP is inserted between successive OFDM symbols that consists of N_{CP} samples, such that the length of the CP is at least equal to the length of the channel. Under this condition, the linear convolution of the sequence transmitted over the channel is converted to a circular convolution. The cyclically extended sequence is first sent at the input of a continuous-time pulse shaping filter and then transmitted through the multi-path Rayleigh fading channel. At the receiving side, a white Gaussian noise is added to the continuous time
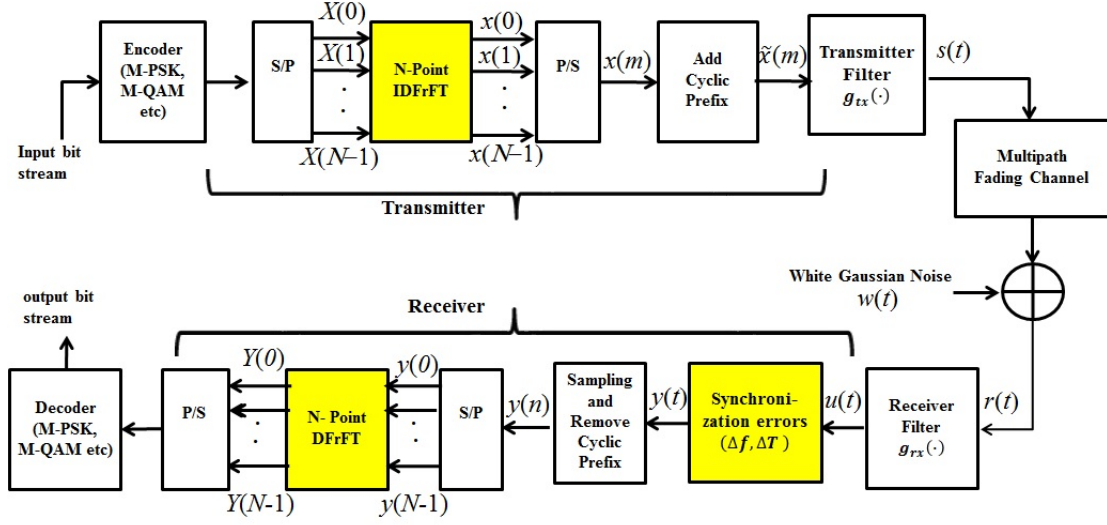
Figure 4.1: *DFrFT-based OFDM system model with multi-path fading channel.*

received signal and the resulting signal is filtered through the receiving pulse shaping filter. After sampling the signal at the output of the receive pulse shaping filter, the CP is removed and the resulting samples are S/P converted and sent to the DFrFT block. The N samples at the output of the DFrFT are equalized, again serialized, and finally decoded to produce an estimate of the originally transmitted data.

4.3.1 Transmitted Signal

The input bit stream is encoded into symbols taken from the set of complex constellation points defined by the adopted modulation scheme. After mapping bits into complex symbols, the resulting data sequence is split into groups of N symbols and sent to the S/P converter. Symbol $X(k)$, $k = 0, 1, 2, \ldots, N - 1$, are fed into the IDFrFT. After the N-point IDFrFT, the mth transmitted sample is written as

$$x(m) = \sum_{k=0}^{N-1} X(k) F_{-\alpha}(m, k), \quad m = 0, 1, 2, \ldots, N - 1, \tag{4.1}$$

where $F_{-\alpha}(m, k)$ is the IDFrFT kernel defined as

$$F_\alpha(m,k) = \sqrt{\frac{\sin\alpha + j\cos\alpha}{N}} e^{\frac{-jm^2 T^2 \cot(\alpha)}{2}} e^{\frac{-jk^2 u^2 \cot(\alpha)}{2}} e^{\frac{j2\pi mk}{N}}, \tag{4.2}$$

being u the sampling interval in the fractional Fourier domain and T the sampling interval in the time domain. The two sampling intervals are related as $u \times T = \frac{2\pi|\sin(\alpha)|}{N}$. The angle between the fractional Fourier domain and the time domain is $\alpha = a \times \frac{\pi}{2}$, with $0 \leq a \leq 1$, where a is a real number comprised between 0 and 1. For $\alpha = \frac{\pi}{2}$, that is $a = 1$, the DFrFT-based OFDM converts into DFT-based OFDM.

4.3.2 Channel Model

The L-path tapped delay line channel model defined in [114] is here considered. According to this model, the impulse response of the time-varying multi-path fading channel is defined as

$$h\left(t\right) = \sum_{l=0}^{L-1} h_l\left(t\right) \delta\left(t - \tau_l T\right), \qquad (4.3)$$

where $h_l\left(t\right)$ is the complex amplitude, or tap coefficient, at time t of the lth path associated with the propagation delay $\tau_l T$ and $\delta\left(t\right)$ is the delta Dirac function. For the coefficients of the channel, we consider a model, where $h_l(t), l = 0, 1, 2, \ldots, L - 1$, are independent and identically distributed complex random variables with Rayleigh distributed amplitude, uniform distributed phase in $[0, 2\pi)$, and average power $\sigma_l^2 = 1/L$. Therefore, $\sigma_0^2 + \sigma_1^2 + \cdots + \sigma_{L-1}^2 = 1$. In the following, we consider the case where $\tau_l = l$, which implies having delays at integer multiples of T.

The approach given in [64] is based on the introduction of a suffix of length N_G to take into account of the influence, in each time instant t, of the N_G symbols that precede and follow the actual one. Although in theory, for a raised cosine impulse responses the length of N_G should be set to infinite, in practical case we can assume for it a finite value, which depends on the considered roll-off parameter. The value of N_{CP} must be higher than L and, in general, one has $N_{CP} \geq N_G$. However, if it happens that $N_{CP} \leq N_G$ we must increase N_{CP} to N_G. Therefore, we have $N_{CP} = max(L - 1, N_G)$. The resulting baseband complex equivalent expression of the OFDM signal in the continuous-time is

$$s(t) = \sum_{m=-N_{CP}}^{N-1+N_G} \tilde{x}\left(m\right) g_{tx}\left(t - mT\right), \quad 0 \leq t < T_s, \qquad (4.4)$$

where $T_s = NT$ is the OFDM symbol interval, $g_{tx}(t)$ denotes the impulse response with normalized unit energy of the square root raised cosine transmit filter, and

$$\tilde{x}\left(m\right) = \begin{cases} x\left(N + m\right), & m = -N_{CP}, \ldots, -1, \\ x\left(m\right), & m = 0, \ldots, N - 1, \\ x\left(m - N - 1\right), & m = N + 1, \ldots, N + N_G. \end{cases} \qquad (4.5)$$

4.3.3 Received Signal

After considering the effect of the multi-path fading channel $h_l(t)$, the received signal $r\left(t\right)$ can be expressed as

$$r\left(t\right) = \sum_{l=0}^{L-1} h_l\left(t\right) s\left(t - lT\right) + w\left(t\right), \qquad (4.6)$$

where $w\left(t\right)$ represents the complex additive white Gaussian noise (AWGN) at the receiver with power spectral density N_0. The received signal in (4.6) is filtered by $g_{rx}\left(t\right)$ to give

$$u(t) = r(t) * g_{rx}(t), \tag{4.7}$$

where $*$ represent the convolution operation, which is then sampled at a rate of $1/T$.

In case of perfect synchronization the only distortions are introduced by the multipath channel and by the Gaussian noise. However, due to estimation errors, residual timing and frequency offsets exist. The received signal after the matched filter can be modeled as

$$y(t) = e^{j2\pi\Delta f t} u(t - \Delta T), \tag{4.8}$$

where Δf and ΔT denotes residual STO and CFO, respectively.

The received signal is sampled at time instants $t = nT$. After removal of the CP, resulting discrete-time signal model is

$$y(nT) = e^{\frac{j2\pi\Delta\epsilon n}{N}} \sum_{l=0}^{L-1} h_l(nT) \sum_{m=-N_{CP}}^{N-1+N_G} \tilde{x}(m)$$
$$g(nT - mT - lT - \Delta T) + \tilde{w}(nT), \tag{4.9}$$

where $\Delta\epsilon = \Delta f T_s$ is the residual CFO normalized to the sub-carrier spacing $1/T_s$, $\tilde{w}(nT) = w(nT - \Delta T)$ is the AWGN, and $g(t)$ is the convolution of $g_{tx}(t)$ and $g_{rx}(t)$, which is a raised cosine impulse response that satisfies the Nyquist condition for not having ISI. The impulse response of a raised cosine Nyquist waveform is given by

$$g(t) = \frac{\sin\frac{\pi t}{T}}{\frac{\pi t}{T}} \cdot \frac{\cos\frac{\pi\rho t}{T}}{1 - (\frac{2\rho t}{T})^2}, \tag{4.10}$$

where ρ is the roll-off. By omitting T, the signal after the DFrFT block is

$$Y(q) = \sum_{n=0}^{N-1} y(n) F_\alpha(q, n), \tag{4.11}$$

being $F_\alpha(q, n)$ the DFrFT kernel defined as

$$F_\alpha(q,n) = \sqrt{\frac{\sin\alpha - j\cos\alpha}{N}} e^{\frac{jn^2 T^2 \cot(\alpha)}{2}} e^{\frac{jq^2 u^2 \cot(\alpha)}{2}} e^{\frac{-j2\pi nq}{N}}. \tag{4.12}$$

Substituting the value of $y(n)$ given in (4.9) into (4.11) we get

$$Y(q) = \sum_{n=0}^{N-1} \left\{ e^{\frac{j2\pi\Delta\epsilon n}{N}} \sum_{l=0}^{L-1} h_l(n) \sum_{m=-N_{CP}}^{N-1+N_G} \sum_{k=0}^{N-1} X(k) \right.$$
$$\left. F_{-\alpha}(m, k) g(n - m - l - \Delta\theta) + \tilde{w}(n) \right\} F_\alpha(q, n), \tag{4.13}$$

where $\Delta\theta = \Delta T/T$ is the normalized residual fractional STO. By following [64], we apply the change of variable $n - m = p + N_{CP}$ in (4.15) to get

$$
Y(q) = \sum_{n=0}^{N-1} \left\{ e^{\frac{j2\pi\Delta\epsilon n}{N}} \sum_{k=0}^{N-1} X(k) \sum_{p=n}^{n-N+1-N_G-N_{CP}} \sum_{l=0}^{L-1} h_l(n) \right.
$$
$$
\left. g(p+N_{CP}-l-\Delta\theta)F_{-\alpha}((n-p-N_{CP})_N,k)+\tilde{w}(n) \right\} F_\alpha(q,n). \tag{4.14}
$$

Also, by using the same approximation of [64], where $g(t) \approx 0$ is assumed for $|t| \geq N_G T$, we obtain

$$
Y(q) = \sum_{n=0}^{N-1} \left\{ e^{\frac{j2\pi\Delta\epsilon n}{N}} \sum_{k=0}^{N-1} X(k)F_{-\alpha}(n,k) \sum_{l=0}^{L-1} h_l(n) \sum_{m=-N_G}^{N_{CP}} g(m-l-\Delta\theta)e^{-j\frac{2\pi}{N}km} + \tilde{w}(n) \right\} F_\alpha(q,n). \tag{4.15}
$$

In order to have a more compact notation, a matrix representation is adopted. Also, we make the assumption of block fading channel where the coefficients $h_l(n)$, with $l = 0, \ldots, L-1$, remain constant for the entire duration of the OFDM symbol, *i.e.*, $h_l(n) = h_l$. Let $\boldsymbol{X} = [X(0), X(1), \ldots, X(N-1)]^T$ be the $N \times 1$ vector transmitted symbols in the frequency domain that is applied at the input of the IDFrFT block to give the $N \times 1$ transmitted vector

$$
\boldsymbol{x} = \boldsymbol{F}_{-\alpha}\boldsymbol{X}, \tag{4.16}
$$

where $\boldsymbol{F}_{-\alpha}$ is the $N \times N$ IDFrFT kernel matrix whose element (m, k) is given in (4.2). Similarly, for $\tilde{x}(m)$, $m = -N_{CP}, \cdots, N + N_G$, we define the $N + N_G + N_{CP} \times 1$ vector

$$
\tilde{\boldsymbol{x}} = \left[\boldsymbol{x}^T(N - N_{CP} + 1 : N) \ \boldsymbol{x}^T \ \boldsymbol{x}^T(1 : N_G) \right], \tag{4.17}
$$

where $\boldsymbol{x}(n : m)$ denotes elements of vector $\boldsymbol{x}$ from n to m given by

$$
\boldsymbol{x}(n : m) = \boldsymbol{F}_{-\alpha}^{n:m,k}(n : m, k), \tag{4.18}
$$

being $\boldsymbol{F}_{-\alpha}^{n:m,k}$ the $(m - n) \times N$ matrix obtained by taking rows of $\boldsymbol{F}_{-\alpha}(n, k)$ from n to m, with $m > n$. After some mathematical manipulation we can rewrite (4.18) as

$$
\tilde{\boldsymbol{x}} = \tilde{\boldsymbol{F}}_{-\alpha}\boldsymbol{X}, \tag{4.19}
$$

where $\tilde{\boldsymbol{F}}_{-\alpha} = \left[\tilde{\boldsymbol{F}}_{-\alpha}^{(N-N_{CP}-1:N,k)} \ \boldsymbol{F}_{-\alpha} \ \boldsymbol{F}_{-\alpha}^{(1:N_G,k)} \right]$. With the introduced matrix notation, (4.9) is rewritten as the column vector

$$
\boldsymbol{y} = \boldsymbol{D}(\Delta\epsilon) \sum_{l=0}^{L-1} h_l \boldsymbol{G_l}(\Delta\theta)\tilde{\boldsymbol{x}} + \tilde{\boldsymbol{w}}, \tag{4.20}
$$

where $\boldsymbol{D}(\Delta\epsilon) = \text{diag}\left(1, e^{\frac{j2\pi\Delta\epsilon}{N}}, \cdots, e^{\frac{j2\pi\Delta\epsilon(N-1)}{N}}\right)$ is the residual CFO matrix, with $\text{diag}(\cdot)$ denoting a diagonal matrix, $\tilde{\boldsymbol{w}} = [\tilde{w}(0), \cdots, \tilde{w}(N-1)]^T$ is the $N \times 1$ noise vector, and $\boldsymbol{G_l}(\Delta\theta)$ is the time domain STO matrix. The $N \times 1$ frequency domain received signal vector can be written as

$$\boldsymbol{Y} = \boldsymbol{S}(\Delta\epsilon, \Delta\theta)\boldsymbol{H}_d\boldsymbol{X} + \tilde{\boldsymbol{W}}, \tag{4.21}$$

where $\boldsymbol{S}(\Delta\epsilon, \Delta\theta) = \boldsymbol{F}_\alpha \boldsymbol{D}(\Delta\epsilon)\boldsymbol{F}_{-\alpha}\tilde{\boldsymbol{G}}(\Delta\theta)$, $\tilde{\boldsymbol{W}} = \boldsymbol{F}_\alpha\tilde{\boldsymbol{w}}$ is the $N \times 1$ fractional Fourier domain noise, and $\tilde{\boldsymbol{G}}(\Delta\theta)$ is a diagonal matrix represented as

$$\tilde{\boldsymbol{G}}(\Delta\theta) = \text{diag}\left(\sum_{m=-N_{CP}}^{N_G} g(m-\Delta\theta)e^{\frac{-j2\pi m0}{N}},\right.$$
$$\left.\sum_{m=-N_{CP}}^{N_G} g(m-\Delta\theta)e^{\frac{-j2\pi m1}{N}}, \cdots, \sum_{m=-N_{CP}}^{N_G} g(m-\Delta\theta)e^{\frac{-j2\pi m(N-1)}{N}}\right).$$

In (4.21), $\boldsymbol{H}_d = \text{diag}(\boldsymbol{\beta})$, with $\boldsymbol{\beta} = \boldsymbol{F}_{1:L}\boldsymbol{h}$, where $\boldsymbol{h} = [h(0), \cdots, h(L-1)]^T$ is the time-domain vector of channel coefficients and $\boldsymbol{F}_{1:L}$ corresponds to the first L columns of the $N \times N$ DFT matrix. The received signal in the fractional Fourier domain on the kth sub-carrier is

$$Y(k) = \underbrace{\underbrace{X(k)S(0,k)\beta(k)}_{\substack{\text{Desired Signal} \\ \text{on the } k\text{th sub-carrier}}} + \underbrace{\sum_{q=0,q\neq k}^{N-1} X(q)S(<q-k>_N,k)\beta(q)}_{\substack{\text{ICI and ISI terms} \\ \text{due to other than } k \text{ sub-carriers}}} + \tilde{w}(k)}_{R(k)}, k = 0, \ldots, N-1,$$
$$\tag{4.22}$$

where $X(q)$ is the transmitted complex data symbol over the qth sub-carrier, $\beta(q)$ is the channel frequency response for the qth sub-carrier, $\tilde{w}(q)$ is the complex AWGN with zero mean and variance per dimension $\sigma^2 = N_0/2$, and

$$S(q-k,k) = \frac{1}{N}\sum_{n=0}^{N-1} e^{j\frac{2\pi\Delta\epsilon n}{N}}\sum_{m=0}^{N-1} e^{-j\frac{\left(m^2-n^2\right)T^2\cot(\alpha)}{2}} e^{j\frac{\left(l^2-k^2\right)u^2\cot(\alpha)}{2}} e^{j\frac{2\pi(mk-nl)}{N}} \cdot b(l+k), \tag{4.23}$$

where $b(n) = [\tilde{\boldsymbol{G}}(\Delta\theta)]_{n,n}$.

4.4 Summary

In this chapter we started with the literature survey related to the performance evaluation of the OFDM system and also discussed the different procedures for the performance analysis. After that motivation towards the DFrFT-based OFDM system have

been given in the details. Finally, the system model of the DFrFT-based OFDM system has been presented in presence of residual CFO and STO for transmission over the multi-path fading channel.

Performance Analysis of DFrFT-based OFDM

I N this chapter we derive exact SEP expressions for DFrFT-based OFDM when STO and CFO are present together. Closed form expressions are derived for BPSK, QPSK, and 16-QAM in the case of transmission over a frequency selective Rayleigh fading channel. The presented results show that the DFrFT-based OFDM system outperforms that based on the DFT for different values of the DFrFT 'angle parameter'.

5.1 Symbol Error Probability Analysis

In this section we present an exact SEP analysis of DFrFT-based OFDM system in presence of CFO and STO for BPSK, QPSK, and 16-QAM modulation formats when transmission takes place over a frequency selective Rayleigh fading channel.

5.1.1 BPSK

In the case of BPSK modulation scheme, symbols are drawn from the set $\{\pm 1\}$. As in [100], we evaluate the performance on the kth sub-carrier when $X(k) = +1$. With this assumption the received signal on the kth sub-carrier is expressed as

$$Y(k) = S(0,k)\,\beta(k) + \sum_{q=0,q\neq k}^{N-1} X(q)S(q,k)\,\beta(q) + \tilde{w}(k).\qquad(5.1)$$

The equalized signal on the kth sub-carrier, obtained by multiplying (5.1) by the complex conjugate of $\beta(k)$, denoted as $\beta^*(k)$, is given by

$$\beta^*(k)Y(k)= S(0,k)|\beta(k)|^2 + \sum_{q=0,q\neq k}^{N-1} X(q)S(q,k)\beta(q)\beta^*(k) + \tilde{w}(k)\beta^*(k).$$
(5.2)

It is worth noting that, when STO is also present, in contrast to the case of CFO only, each sub-carrier is characterized by a different SEP [64]. The SEP on the kth sub-carrier is

$$P_s(\xi_k)= \int_{\boldsymbol{\beta}} P_s(\xi_k|\boldsymbol{\beta})p_{\boldsymbol{B}}(\boldsymbol{\beta})\, d\boldsymbol{\beta},$$
(5.3)

where $P_s(\xi_k|\boldsymbol{\beta})$ is the SEP conditioned to a given $\boldsymbol{\beta}$, this latter being described by the N-dimensional joint probability density function (PDF) $p_{\boldsymbol{B}}(\boldsymbol{\beta})$. Since the evaluation of the above multi-dimensional integral is difficult, its solution can be simplified by using the following factorization

$$p_{\boldsymbol{B}}(\boldsymbol{\beta}) = p_{\boldsymbol{\beta}_k|\beta(k)}(\boldsymbol{\beta}_k|\beta(k))\, p_{\beta(k)}(\beta(k)),$$
(5.4)

where $\boldsymbol{\beta}_k=[\boldsymbol{\beta}(0:k-1)\ \boldsymbol{\beta}(k+1:N-1)]^T$, $p_{\beta(k)}(\beta(k))$ is the one dimensional PDF of $\beta(k)$, and $p_{\boldsymbol{\beta}_k|\beta(k)}(\boldsymbol{\beta}_k|\beta(k))$ is the conditional PDF of $\boldsymbol{\beta}_k$ given $\beta(k)$. By replacing (5.4) in (5.3) we obtain

$$P_s(\xi_k) = \int_0^\infty P_s(\xi_k|\beta(k))\, p_{\beta(k)}(\beta(k))\, d\beta(k),$$
(5.5)

where

$$P_s(\xi_k|\beta(k))= \int_{\boldsymbol{\beta}_k} P_s(\xi_k|\beta(k),\boldsymbol{\beta}_k)p_{\boldsymbol{\beta}_k|\beta(k)}(\boldsymbol{\beta}_k|\beta(k))d\boldsymbol{\beta}_k.$$
(5.6)

The expression of $P_s(\xi_k|\beta(k),\boldsymbol{\beta}_k)$ can be obtained by resorting to the CHF approach described in [110]. We consider the conditional CHF of the real part of the equalized received signal $\Re[\beta^*(k)Y(k)|\beta(k),\boldsymbol{\beta}_k]$ in (5.2) given by

$$\varphi_{\Re[\beta^*(k)Y(k)|\beta(k),\boldsymbol{\beta}_k]}(\omega)= E\left[e^{jw\Re[\beta^*(k)Y(k)]}|\beta(k),\boldsymbol{\beta}_k\right],$$
(5.7)

where $\Re[\cdot]$ denotes the real part and $E[\cdot]$ denotes the statistical expectation. By substituting the value $\beta^*(k)Y(k)$ from (5.2) in (5.7) and averaging over the AWGN we get

$$\varphi_{\Re[\beta^*(k)Y(k)|\beta(k),\boldsymbol{\beta}_k]}(\omega) = e^{jw\Re[S(0,k)|\beta(k)|^2]} \prod_{q=0,q\neq k}^{N-1} E\left[e^{j\omega\Re[X(k)S(q,k)\beta(q)\beta^*(k)]}\right] \cdot e^{-\frac{\omega^2\sigma_\beta^2}{2}},$$
(5.8)

where $\sigma_\beta^2=|\beta(k)|^2\sigma^2$. By computing the average over all the possible combination of symbols and by using the trigonometric identity given by [100, eq. (3)], from (5.8) we

get

$$\varphi_{\Re[\beta^*(k)Y(k)|\beta(k),\boldsymbol{\beta}_k]}(\omega) = e^{j\omega\Re[S(0,k)|\beta(k)|^2]} \cdot e^{-\frac{\omega^2\sigma_\beta^2}{2}}$$

$$\frac{1}{2^{N-1}} \sum_{q=0,q\neq k}^{2^{N-2}} e^{j\omega\Re[\beta^*(k)\boldsymbol{e}_q^T\boldsymbol{\Lambda}\boldsymbol{\beta}_k]} + e^{-j\omega\Re[\beta^*(k)\boldsymbol{e}_q^T\boldsymbol{\Lambda}\boldsymbol{\beta}_k]}, \tag{5.9}$$

where $\boldsymbol{\Lambda} = \text{diag}(S(1,k), S(2,k), \ldots, S(N-1,k))$ and $\boldsymbol{e}_q$ is an $N\times1$ vector corresponding to the binary codeword of the number $2^{N-1} - q$, in which zeros have been substituted with -1s. After some straightforward mathematical passages, (5.9) can be rewritten as

$$\varphi_{\Re[\beta^*(k)Y(k)|\beta(k),\boldsymbol{\beta}_k]}(\omega) = \frac{1}{2^{N-1}} \cdot e^{-\frac{\omega^2\sigma_\beta^2}{2}}$$

$$\sum_{q=0}^{2^{N-2}-1} e^{j\omega\left(\Re[S(0,k)|\beta(k)|^2]+\Re[\beta^*(k)\boldsymbol{e}_q^T\boldsymbol{\Lambda}\boldsymbol{\beta}_k]\right)} + \sum_{q=0}^{2^{N-2}-1} e^{j\omega\left(\Re[S(0,k)|\beta(k)|^2]-\Re[\beta^*(k)\boldsymbol{e}_q^T\boldsymbol{\Lambda}\boldsymbol{\beta}_k]\right)}.$$
$$\tag{5.10}$$

It can be observed that (5.10) represents the CHF of a mixture of Gaussian densities [100]. Now, an error will occur only if $\Re[\beta^*(k)Y(k)|\beta(k)\boldsymbol{\beta}_k] < 0$. The probability of this event can be computed as

$$P_s(\xi_k|\beta(k),\boldsymbol{\beta}_k) = \int_{-\infty}^0 f_{\Re[\beta^*(k)Y(k)|\beta(k),\boldsymbol{\beta}_k]}(x)\,dx, \tag{5.11}$$

where $f_{\Re[\beta^*(k)Y(k)|\beta(k),\boldsymbol{\beta}_k]}(\cdot)$ is the conditional PDF obtained from the inverse Fourier transform of the CHF given in (5.10). The solution of (5.11) gives the following expression of the resulting conditional SEP

$$P_s(\xi_k|\beta(k),\boldsymbol{\beta}_k) = \frac{1}{2^{N-1}} \sum_{q=0}^{2^{N-2}-1} Q\left(\frac{|\beta(k)|^2\Re[S(0,k)]+b_q^k}{\sigma_\beta}\right) + Q\left(\frac{|\beta(k)|^2\Re[S(0,k)]-b_q^k}{\sigma_\beta}\right), \tag{5.12}$$

where $b_q^k = \Re[\beta^*(k)\boldsymbol{e}_q^T\boldsymbol{\Lambda}\boldsymbol{\beta}_k]$. The expression of $P_s(\xi_k|\beta(k))$ can now be obtained by replacing (5.12) in (5.6) and averaging over conditional Gaussian PDF $p_{\boldsymbol{\beta}_k|\beta(k)}(\boldsymbol{\beta}_k|\beta(k))$, with mean $E[\boldsymbol{\beta}_k|\beta(k)]$ and covariance $C_{\boldsymbol{\beta}_k|\beta(k)}$ [100, eq. (27)]. The resulting expression is

$$P_s(\xi_k|\beta(k)) = \frac{1}{2^{N-1}} \sum_{q=0}^{2^{N-2}-1} Q\left(\frac{\beta(k)\left(\Re[S(0,k)]+z_q^k\right)}{\sigma\sqrt{1+\frac{a_q^k}{2\sigma^2}}}\right) Q\left(\frac{\beta(k)\left(\Re[S(0,k)]-z_q^k\right)}{\sigma\sqrt{1+\frac{a_q^k}{2\sigma^2}}}\right), \tag{5.13}$$

where z_q^k and a_q^k are related to the mean and to the variance of the conditional random variable $(b_q^k|\beta(k))$ as [105]

$$z_q^k = \frac{E[b_q^k|\beta(k)]}{|\beta(k)|^2} = C_{\beta(k)\beta(k)}^{-1}\Re[(\boldsymbol{e}_q^T\boldsymbol{\Lambda})C_{\boldsymbol{\beta}_k\beta(k)}] \tag{5.14}$$

and

$$a_q^k = 2\frac{\text{var}\left[b_q^k|\beta(k)\right]}{|\beta(k)|^2} = \left(e_q^T \Lambda\right) C_{\beta_k|\beta(k)} \left(e_q^T \Lambda\right)^H,\tag{5.15}$$

respectively. In (5.14) and (5.15) we have $C_{\beta_k\beta(k)} = E\left[\beta_k\beta^*(k)\right]$, $C_{(\beta_k|\beta(k))} = C_{\beta_k\beta_k} - C_{\beta(k)\beta(k)}^{-1}C_{\beta_k\beta(k)}C_{\beta_k\beta(k)}^H$, $C_{(\beta_k\beta_k)} = F_{1:L}hF_{1:L}^H$, being $(\cdot)^H$ the Hermitian transpose conjugation. In order to calculate the overall SEP we first introduce the change of variable $\gamma_k = |\beta(k)|^2/N_0$, which allows us to express (5.13) as a function of the instantaneous signal-to-noise ratio (SNR) γ_k on the kth sub-carrier, and then we average (5.5) over all the sub-carriers as

$$P_s(\xi) = \frac{1}{N}\sum_{k=0}^{N-1}P_s(\xi_k) = \frac{1}{N}\sum_{k=0}^{N-1}\int_0^\infty P_s(\xi_k|\gamma_k)\,p_{\gamma_k}(\gamma_k)\,d\gamma_k,\tag{5.16}$$

where

$$p_{\gamma_k}(\gamma_k) = \bar{\gamma}_k^{-1}e^{\frac{\gamma_k}{\bar{\gamma}_k}}\tag{5.17}$$

is the PDF of Rayleigh fading with average SNR $\bar{\gamma}_k = E\left[|\beta(k)|^2\right]/N_0$.

In what follows we adopt the polar form definition given in [114] for the Q-function in (5.13). The overall SEP is computed by applying the moment generating function (MGF) approach in (5.16) as

$$P_s(\xi) = \frac{1}{\pi N2^{N-1}}\sum_{q=0}^{2^{N-2}-1}\sum_{k=0}^{N-1}\int_0^{\frac{\pi}{2}}\left\{\underbrace{\int_0^\infty\exp\left(-\frac{\gamma_k\left(\Re\left[S(0,k)\right]+z_q^k\right)^2}{\left(1+\frac{a_q^k}{2\sigma^2}\right)\sin^2\theta}\right)p_{\gamma_k}(\gamma_k)d\gamma_k}_{M_{\gamma_k}(s_1)}\right.$$

$$\left.+\underbrace{\int_0^\infty\exp\left(-\frac{\gamma_k\left(\Re\left[S(0,k)\right]-z_q^k\right)^2}{\left(1+\frac{a_q^k}{2\sigma^2}\right)\sin^2\theta}\right)p_{\gamma_k}(\gamma_k)d\gamma_k}_{M_{\gamma_k}(s_2)}\right\},\tag{5.18}$$

where $M_{\gamma_k}(s)$ is used to denote the scaled Laplace transform of $p_{\gamma_k}(\gamma_k)$, which is known as MGF. The analytical expression of the MGF for the Rayleigh distribution is given by

$$M_{\gamma_k}(s) = \left(1 - s\bar{\gamma}_k\right)^{-1}.\tag{5.19}$$

The computation of $P_s(\xi)$ is done by using (1.8) and (5.6) of [114]. The resulting analytical expression is

$$P_s(\xi) = \frac{1}{2} - \frac{1}{N2^N}\sum_{q=1}^{2^{N-2}-1}\sum_{k=0}^{N-1}\left\{f_1\sqrt{\frac{\bar{\gamma}_kC_{\beta(k)\beta(k)}(\Re\left[S(0,k)\right]+z_q^k)^2}{1+\bar{\gamma}_k(C_{\beta(k)\beta(k)}(\Re\left[S(0,k)\right]+z_q^k)^2+a_q^k)}}\right.$$

$$\left.+f_2\sqrt{\frac{\bar{\gamma}_kC_{\beta(k)\beta(k)}(\Re\left[S(0,k)\right]-z_q^k)^2}{1+\bar{\gamma}_k(C_{\beta(k)\beta(k)}(\Re\left[S(0,k)\right]-z_q^k)^2+a_q^k)}}\right\},\tag{5.20}$$

where $f_1 = \text{sgn}(\Re[S(0,k)] + z_q^k)$ and $f_2 = \text{sgn}(\Re[S(0,k)] - z_q^k)$, being $\text{sgn}(\cdot)$ the signum function. Substituting $\alpha = \pi/2$ in $S(q,k)$ and $C_{\beta(k)\beta(k)} = 2\sigma^2$, we get the final expression of SEP for BPSK OFDM system based on DFT given by (13) of [105]. This is conform to the fact that OFDM system based on DFrFT is a generalization of conventional OFDM system.

5.1.2 QPSK

For QPSK modulation the symbols are drawn from the set $\{1+j, 1-j, -1+j, -1-j\}$. Without loosing generality, as done in Sec. 5.1.1, we make the assumption that the symbol transmitted on the kth sub-carrier is $X(k) = 1+j$. By following [110] we can write the conditional probability of correct decision as

$$P_c(\beta^*(k)Y(k) \in D_1 | X(k) = 1+j, \Re[\beta^*(k)R(k)], \Im[\beta^*(k)R(k)])$$
$$= Q\left(-\frac{\Re[\beta^*(k)R(k)]}{\sigma_\beta}\right) Q\left(-\frac{\Im[\beta^*(k)R(k)]}{\sigma_\beta}\right), \qquad (5.21)$$

which corresponds to the probability that the random variable defined by the equalized signal $\beta^*(k)Y(k)$ given $X(k) = 1+j$, that is $\beta^*(k)R(k)|X(k) = 1+j$ falls in D_1, the first quadrant of the complex plane. In (5.21) $\Im[\cdot]$ denotes the imaginary part.

The probability of correct decision is obtained by averaging (5.21) over the joint 2D PDF defined by the real and imaginary parts of $\beta^*(k)R(k)|X(k) = 1+j$, which is given by inverse Fourier transform (IFT) of the CHF as

$$\varphi_{\Re[\beta^*(k)R(k)|\beta(k),\boldsymbol{\beta}_k], \Im[\beta^*(k)R(k)|\beta(k),\boldsymbol{\beta}_k]}(\omega_I, \omega_Q) =$$
$$e^{j|\beta(k)|^2\left(\omega_I(\Re[S(0,k)] - \Im[S(0,k)]) + \omega_Q(\Im[S(0,k)] + \Re[S(0,k)])\right)}$$
$$\prod_{\substack{q=0 \\ q \neq k}}^{N-1} \cos\left(\omega_I \Re[S(q,k)\beta^*(k)\beta(q)] + \omega_Q \Im[S(q,k)\beta^*(k)\beta(q)]\right)$$
$$\cos\left(\omega_I \Im[S(q,k)\beta^*(k)\beta(q)] - \omega_Q \Re[S(q,k)\beta^*(k)\beta(q)]\right). \qquad (5.22)$$

By following [110], the resulting 2D PDF is

$$p(\Re[\beta^*(k)R(k)], \Im[\beta^*(k)R(k)]) = \frac{1}{2^{2N-2}} \sum_{q=0}^{2^{N-2}-1} \sum_{n=0}^{2^{N-2}-1} \sum_{m=1}^{4}$$
$$\delta\left[\Re(\beta^*(k)R(k)) - |\beta(k)|^2(D_A + \varphi_{q,n}[1,m])\right] \delta\left[\Im(\beta^*(k)R(k)) - |\beta(k)|^2(D_B + \varphi_{q,n}[2,m])\right], \qquad (5.23)$$

where $D_A = \Re[S(0,k)] - \Im[S(0,k)]$, $D_B = \Re[S(0,k)] + \Im[S(0,k)]$ and $\varphi_{q,n}[r,c]$ is the entry (r, c) of the 2×4 matrix $\boldsymbol{G} = [(\boldsymbol{g}_A + \boldsymbol{g}_B) \quad (-\boldsymbol{g}_A - \boldsymbol{g}_B) \quad (\boldsymbol{g}_A - \boldsymbol{g}_B) \quad (-\boldsymbol{g}_A + \boldsymbol{g}_B)]$ with

$$\boldsymbol{g}_A = \left[\Re\left[\beta^*(k)\boldsymbol{e}_q^T \boldsymbol{\Lambda}\boldsymbol{\beta}_k\right] \quad \Im\left[\beta^*(k)\boldsymbol{e}_n^T \boldsymbol{\Lambda}\boldsymbol{\beta}_k\right]\right]^T,$$

$$\boldsymbol{g}_B = \begin{bmatrix} \Im\left[\beta^*(k)\boldsymbol{e}_q^T\boldsymbol{\Lambda}\boldsymbol{\beta}_k\right] & -\Re\left[\beta^*(k)\boldsymbol{e}_n^T\boldsymbol{\Lambda}\boldsymbol{\beta}_k\right] \end{bmatrix}^T.$$

The expression of the conditional probability of correct decision $P_c(\beta^*(k)R(k)\in D_1|\beta(k),\boldsymbol{\beta}_k)$ is therefore obtained by averaging (5.21) over the 2D PDF in (5.23). The conditional SEP on the kth sub-carrier is obtained by subtracting the corresponding conditional probability of correct decision from 1 as

$$P_s\left(\xi_k|\beta\left(k\right),\boldsymbol{\beta}_k\right) = 1 - P_c\left(\beta^*(k)R(k) \in D_1|\beta(k),\boldsymbol{\beta}_k\right)$$

$$=1-\frac{1}{N2^{2N-2}}\sum_{q=0}^{2^{N-2}-1}\sum_{n=0}^{2^{N-2}-1}\sum_{m=1}^{4}Q\left(-\frac{|\beta\left(k\right)|^2(D_A+\varphi_{q,n}\left[1,m\right])}{\sigma_\beta}\right)$$

$$Q\left(-\frac{|\beta\left(k\right)|^2\left(D_B+\varphi_{q,n}\left[2,m\right]\right)}{\sigma_\beta}\right). \tag{5.24}$$

As seen in Sec. 5.1.1, computing $P_s(\xi_k|\beta(k),\boldsymbol{\beta}_k)$ requires the solution of a multi-dimensional integral. Therefore, first we need to average $P_s(\xi_k|\beta\left(k\right),\boldsymbol{\beta}_k)$ over $p_{\boldsymbol{\beta}_k|\beta(k)}(\boldsymbol{\beta}_k|\beta\left(k\right))$, then the expression of $P_s\left(\xi_k|\beta\left(k\right)\right)$ is obtained by using the mean $|\beta\left(k\right)|^2\vartheta_{q,n}\left[i,m\right]$ and variance $|\beta\left(k\right)|^2\nu_{q,n}\left[m\right]/2$ of the conditional Gaussian random variable $\varphi_{q,n}\left[i,m\right]|\beta\left(k\right)$ as

$$P_s\left(\xi_k|\beta\left(k\right)\right) = 1 - \frac{1}{N2^{2N-2}}\sum_{q=0}^{2^{N-2}-1}\sum_{n=0}^{2^{N-2}-1}\sum_{m=1}^{4}$$

$$Q\left(\frac{|\beta(k)|(D_A+\vartheta_{q,n}[1,m])}{\sigma\sqrt{1+\frac{\nu_{q,n}[m]}{2\sigma^2}}}\right)Q\left(\frac{|\beta\left(k\right)|(D_B+\vartheta_{q,n}\left[2,m\right])}{\sigma\sqrt{1+\frac{\nu_{q,n}[m]}{2\sigma^2}}}\right), \tag{5.25}$$

where

- $\vartheta_{q,n}\left[i,m\right]$ is the entry (i,m) of the 2×4 matrix
  $\boldsymbol{W} = [(\boldsymbol{w}_A+\boldsymbol{w}_B)\,(-\boldsymbol{w}_A-\boldsymbol{w}_B)\,(\boldsymbol{w}_A-\boldsymbol{w}_B)\,(-\boldsymbol{w}_A+\boldsymbol{w}_B)]$ with

$$\boldsymbol{w}_A = C_{\beta(k)\beta(k)}^{-1}\left[\Re\left[\boldsymbol{e}_q^T\boldsymbol{\Lambda}\boldsymbol{C}_{\boldsymbol{\beta}_k\beta(k)}\right]\quad\Im\left[\boldsymbol{e}_q^T\boldsymbol{\Lambda}\boldsymbol{C}_{\boldsymbol{\beta}_k\beta(k)}\right]\right]^T,$$

$$\boldsymbol{w}_B = C_{\beta(k)\beta(k)}^{-1}\left[\Im\left[\boldsymbol{e}_n^T\boldsymbol{\Lambda}\boldsymbol{C}_{\boldsymbol{\beta}_k\beta(k)}\right] - \Re\left[\boldsymbol{e}_n^T\boldsymbol{\Lambda}\boldsymbol{C}_{\boldsymbol{\beta}_k\beta(k)}\right]\right]^T,$$

  being $\boldsymbol{C}_{\boldsymbol{\beta}_k|\beta(k)}$ the channel auto-covariance matrix given in [105];

- $\nu_{q,n}\left[m\right]$ is the entry m of the 1×4 vector $\boldsymbol{\nu} = [\nu_1\ \nu_2\ \nu_3\ \nu_4]$, where $\nu_i = \boldsymbol{\zeta}_i^T\boldsymbol{\Lambda}\boldsymbol{C}_{\boldsymbol{\beta}_k\beta(k)}\boldsymbol{\Lambda}\boldsymbol{\zeta}_i$ and $\boldsymbol{\zeta}_1 = \boldsymbol{e}_q+\boldsymbol{e}_n$, $\boldsymbol{\zeta}_2 = -\boldsymbol{e}_q-\boldsymbol{e}_n$, $\boldsymbol{\zeta}_3 = \boldsymbol{e}_q-\boldsymbol{e}_n$, $\boldsymbol{\zeta}_4 = -\boldsymbol{e}_q+\boldsymbol{e}_n$.

We convert the multiplication of the two Q-functions in (5.25) into the sum of two Q-functions, which is given in equation (4.8) of [114]. Then, we apply the polar form definition of the Q-function in (5.25) and introduce the same change of variable $\gamma_k=|\beta(k)|^2/N_0$ used in Sec. 5.1.1 to express the instantaneous SNR on kth sub-carrier. As

done in (5.16) the resulting SEP is obtained by averaging over all the sub-carriers as

$$P_s(\xi) = 1 - \frac{1}{2\pi N 2^{N-2}} \sum_{k=0}^{N-1} \sum_{q=0}^{2^{N-2}-1} \sum_{n=0}^{2^{N-2}-1} \sum_{m=1}^{4}$$

$$\left\{ \underbrace{\int_0^{\frac{\pi}{2}-\tan^{-1}\left(\frac{D_B+\vartheta_{q,n}[2,m]}{D_A+\vartheta_{q,n}[1,m]}\right)} \int_0^{\infty} \exp\left(-\frac{\gamma_k(D_A+\vartheta_{q,n}[1,m])^2}{\left(1+\frac{\nu_{q,n}[m]}{2\sigma^2}\right)\sin^2\theta}\right) p_{\gamma_k}(\gamma_k) d\gamma_k}_{M_{\gamma_k}(s_1)} + \right.$$

$$\left. \underbrace{\int_0^{\tan^{-1}\left(\frac{D_B+\vartheta_{q,n}[2,m]}{D_A+\vartheta_{q,n}[1,m]}\right)} \int_0^{\infty} \exp\left(\frac{\gamma_k(D_B+\vartheta_{q,n}[2,m])^2}{\left(1+\frac{\nu_{q,n}[m]}{2\sigma^2}\right)\sin^2\theta}\right) p_{\gamma_k}(\gamma_k) d\gamma_k}_{M_{\gamma_k}(s_2)} \right\}. \tag{5.26}$$

The above equation can be further simplified by using [114, eq. (1.8)] and by using MGF of Rayleigh fading, given in (5.19), as

$$P_s(\xi) = 1 - \frac{1}{2\pi N 2^{N-2}} \sum_{k=0}^{N-1} \sum_{q=0}^{2^{N-2}-1} \sum_{n=0}^{2^{N-2}-1} \sum_{m=1}^{4}$$

$$\left\{ \int_0^{\frac{\pi}{2}-\tan^{-1}\left(\frac{D_B+\vartheta_{q,n}[2,m]}{D_A+\vartheta_{q,n}[1,m]}\right)} \left(1+\frac{\gamma_k\left(D_A+\vartheta_{q,n}[1,m]\right)^2}{\left(1+\frac{\nu_{q,n}[m]}{2\sigma^2}\right)\sin^2\theta}\right)^{-1} \right.$$

$$\left. + \int_0^{\tan^{-1}\left(\frac{D_B+\vartheta_{q,n}[2,m]}{D_A+\vartheta_{q,n}[1,m]}\right)} \left(1+\frac{\gamma_k\left(D_B+\vartheta_{q,n}[2,m]\right)^2}{\left(1+\frac{\nu_{q,n}[m]}{2\sigma^2}\right)\sin^2\theta}\right)^{-1} \right. . \tag{5.27}$$

The integral in (5.27) can be solved using (5.102) of [114]. After some mathematical passages, the SEP expression is given by

$$P_s(\xi) = \frac{3}{4} - \frac{1}{N 2^{2N-1}} \sum_{k=0}^{N-1} \sum_{q=0}^{2^{N-2}-1} \sum_{n=0}^{2^{N-2}-1} \sum_{m=1}^{4} \sqrt{\frac{C_{\beta(k)\beta(k)}\bar{\gamma}_k \Psi^2_{q,n}[1,m]}{2+\bar{\gamma}_k\nu_{q,n}[m]+C_{\beta(k)\beta(k)}\bar{\gamma}_k \Psi^2_{q,n}[1,m]}}$$

$$\left(\frac{1}{2}+\frac{1}{\pi}\text{atan}\left\{\sqrt{\frac{C_{\beta(k)\beta(k)}\bar{\gamma}_k \Psi^2_{q,n}[2,m]}{2+\bar{\gamma}_k\nu_{q,n}[m]+C_{\beta(k)\beta(k)}\bar{\gamma}_k \Psi^2_{q,n}[1,m]}}\right\}\right)$$

$$+\sqrt{\frac{C_{\beta(k)\beta(k)}\Psi^2_{q,n}[2,m]\bar{\gamma}_k}{2+\bar{\gamma}_k\nu_{q,n}[m]+C_{\beta(k)\beta(k)}\bar{\gamma}_k \Psi^2_{q,n}[2,m]}}$$

$$\left(\frac{1}{2}+\frac{1}{\pi}\text{atan}\left\{\sqrt{\frac{C_{\beta(k)\beta(k)}\bar{\gamma}_k \Psi^2_{q,n}[1,m]}{2+\bar{\gamma}_k\nu_{qn}[m]+C_{\beta(k)\beta(k)}\bar{\gamma}_k \Psi^2_{q,n}[2,m]}}\right\}\right), \tag{5.28}$$

where $\Psi_{q,n}[i,m]$ is the entry (i,m) of the 2×4 matrix $\mathbf{\Phi} = \mathbf{D} \otimes \mathbf{1}_{1\times 4} + \mathbf{W}$, in which $\otimes$ is the Kronecker product, $\mathbf{1}_{1\times 4}$ is a 1×4 vectors of 1s, and $\mathbf{D} = [D_A \, D_B]^{\mathrm{T}}$.

Similarly, substituting $\alpha = \pi/2$ in $S(q, k)$ and $C_{\beta(k)\beta(k)} = 2\sigma^2$ in (5.28) we get the SEP expression of QPSK for conventional OFDM system given by (16) of [50].

5.1.3 16-QAM

As done for BPSK and for QPSK, here symbols are drawn from the set $\{\pm 1 \pm j, \pm 1 \pm 3j, \pm 3 \pm j, \pm 3 \pm 3j\}$. We assume that symbol $X(k)$ transmitted on the kth sub-carrier is drawn from the subset of symbols $\{1+j, 1+3j, 3+j, 3+3j\}$ belonging to the first quadrant D_1. We consider first that transmitted symbol is $X(k) = 1 + j$ and evaluates the probability that the equalized received signal lies in the region $D_{s1} = \{a + bj | 2 \geq a \geq 0, 2 \geq b \geq 0\}$ of the complex plane. Thus, the conditional probability of making a correct decision given $X(k) = 1 + j$ is

$$P_{c,1}(\beta^*(k)Y(k) \in D_{s1} | X(k) = 1+j, \Re[\beta^*(k)R(k)], \Im[\beta^*(k)R(k)])$$

$$= \int_0^2 \frac{1}{\sqrt{2\pi}\sigma} e^{-\frac{(x - \Re[\beta^*(k)R(k)])^2}{2\sigma^2}} dx \int_0^2 \frac{1}{\sqrt{2\pi}\sigma} e^{-\frac{(y - \Im[\beta^*(k)R(k)])^2}{2\sigma^2}} dy$$

$$= \left[Q\left(\frac{-\Re[\beta^*(k)R(k)]}{\sigma_\beta}\right) - Q\left(\frac{2 - \Re[\beta^*(k)R(k)]}{\sigma_\beta}\right) \right]$$

$$\left[Q\left(\frac{-\Im[\beta^*(k)R(k)]}{\sigma_\beta}\right) - Q\left(\frac{2 - \Im[\beta^*(k)R(k)]}{\sigma_\beta}\right) \right]$$

$$= Q\left(\frac{-\Re[\beta^*(k)R(k)]}{\sigma_\beta}\right) Q\left(\frac{-\Im[\beta^*(k)R(k)]}{\sigma_\beta}\right) - Q\left(\frac{-\Re[\beta^*(k)R(k)]}{\sigma_\beta}\right)$$

$$Q\left(\frac{2 - \Im[\beta^*(k)R(k)]}{\sigma_\beta}\right) - Q\left(\frac{2 - \Re[\beta^*(k)R(k)]}{\sigma_\beta}\right) Q\left(\frac{-\Im[\beta^*(k)R(k)]}{\sigma_\beta}\right)$$

$$+ Q\left(\frac{2 - \Re[\beta^*(k)R(k)]}{\sigma_\beta}\right) Q\left(\frac{2 - \Im[\beta^*(k)R(k)]}{\sigma_\beta}\right). \tag{5.29}$$

The probability of correct decision is obtained by averaging (5.29) over the joint 2D PDF of $\beta^*(k)R(k)$ as

$$P_{c,1\,avg}(\beta^*(k)Y(k) \in D_{s1} | X(k) = 1+j) = \int_{-\infty}^{\infty} \int_{-\infty}^{\infty}$$

$$P_{c,1}(\beta^*(k)Y(k) \in D_{s1} | X(k) = 1+j, \Re[\beta^*(k)R(k)], \Im[\beta^*(k)R(k)])$$

$$p(\Re[\beta^*(k)R(k)], \Im[\beta^*(k)R(k)] | X(k) = 1+j)\, d\Re[\beta^*(k)R(k)] d\Im[\beta^*(k)R(k)]. \tag{5.30}$$

The expression of $p(\Re[\beta^*(k)R(k)], \Im[\beta^*(k)R(k)] | X(k) = 1+j)$ to compute the 2D CHF is given in [115]. Following [110], after substituting the value of the equalized signal $\beta^*(k)R(k)$ and after some simplifications, the 2D-CHF can be written as

$$\varphi_{\Re[\beta^*(k)R(k)|\beta(k),\boldsymbol{\beta}_k], \Im[\beta^*(k)R(k)|\beta(k),\boldsymbol{\beta}_k]}(\omega_I, \omega_Q) = E\left[e^{j|\beta(k)|^2 (\Omega^T \boldsymbol{S_a}(0,k)\Re[X(k)] - \Omega^T \boldsymbol{S_b}(0,k)\Im[X(k)])} \right]$$

$$\prod_{\substack{q=0 \\ q \neq k}}^{N-1} E\left[e^{j\left(\beta^*(k)\beta(q)\Omega^T \boldsymbol{S_a}(q,k)\Re[X(q)] - \beta^*(k)\beta(q)\Omega^T \boldsymbol{S_b}(q,k)\Im[X(q)]\right)} \right], \tag{5.31}$$
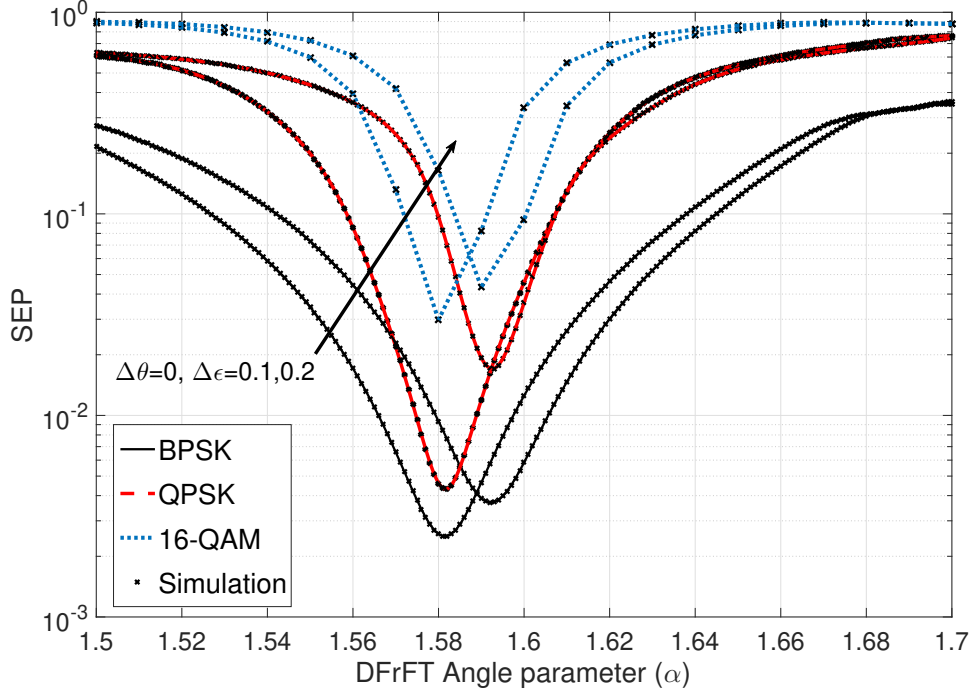
Figure 5.1: *Analytical and simulated SEP versus DFrFT angle parameter α at normalized CFO $\Delta\epsilon = 0.1, 0.2$ in case of 8-point DFrFT-based OFDM for BPSK, QPSK, and 16-QAM for transmission over frequency selective Rayleigh fading channel with 2-tap equal power delay profile at $\bar{\gamma}_k = 25$ dB.*

where $\boldsymbol{S_a}(q,k) = [\Re[S(q,k)] \ \Im[S(q,k)]]^T$, $\boldsymbol{S_b}(q,k) = [\Im[S(q,k)] \ -\Re[S(q,k)]]^T$ and $\Omega^T = [\omega_I \ \omega_Q]$,. By substituting the value of $X(k) = 1 + j$ in (5.31) and after simplification interms of real and imaginary parts we get

$$
\varphi_{\Re[\beta^*(k)R(k)|\beta(k),\boldsymbol{\beta}_k],\Im[\beta^*(k)R(k)|\beta(k),\boldsymbol{\beta}_k]}(\omega_I, \omega_Q)
$$

$$
= E\left[e^{\left[j|\beta(k)|^2\{\omega_I\left(\Re[S(0,k)]-\Im[S(0,k)]+\omega_Q(\Im[S(0,k)]+\Re[S(0,k)])\}\right]}\right]
$$

$$
\prod_{\substack{q=0 \\ q\neq k}}^{N-1}\cos(\omega_I\Re[S(q,k)\beta^*(k)\beta(q)]+\omega_Q\Im[S(q,k)\beta^*(k)\beta(q)])
$$

$$
\cos(2\omega_I\Re[S(q,k)\beta^*(k)\beta(q)]+2\omega_Q\Im[S(q,k)\beta^*(k)\beta(q)])
$$

$$
\cos(\omega_I\Im[S(q,k)\beta^*(k)\beta(q)]-\omega_Q\Re[S(q,k)\beta^*(k)\beta(q)])
$$

$$
\cos(2\omega_I\Im[S(q,k)\beta^*(k)\beta(q)]-2\omega_Q\Re[S(q,k)\beta^*(k)\beta(q)]). \tag{5.32}
$$

The resulting 2D PDF is obtained by computing IFT of (5.32) and it is written as

$$
p_{(\Re[\beta^*(k)R(k)],\Im[\beta^*(k)R(k)])} = \frac{1}{2^{4(N-2)}}\sum_{q=0}^{2^{N-2}-1}\sum_{l=0}^{2^{N-2}-1}\sum_{m=0}^{2^{N-2}-1}\sum_{n=0}^{2^{N-2}-1}\sum_{f=1}^{16}\delta\Big[\Re[\beta^*(k)R(k)]-
$$

$$
\left(|\beta(k)|^2\left(D_A+\boldsymbol{\zeta}_{q,l,m,n}[1,f]\right)\right)\Big]\delta\Big[\Im[\beta^*(k)R(k)]-\left(|\beta(k)|^2\left(D_B+\boldsymbol{\zeta}_{q,l,m,n}[2,f]\right)\right)\Big], \tag{5.33}
$$
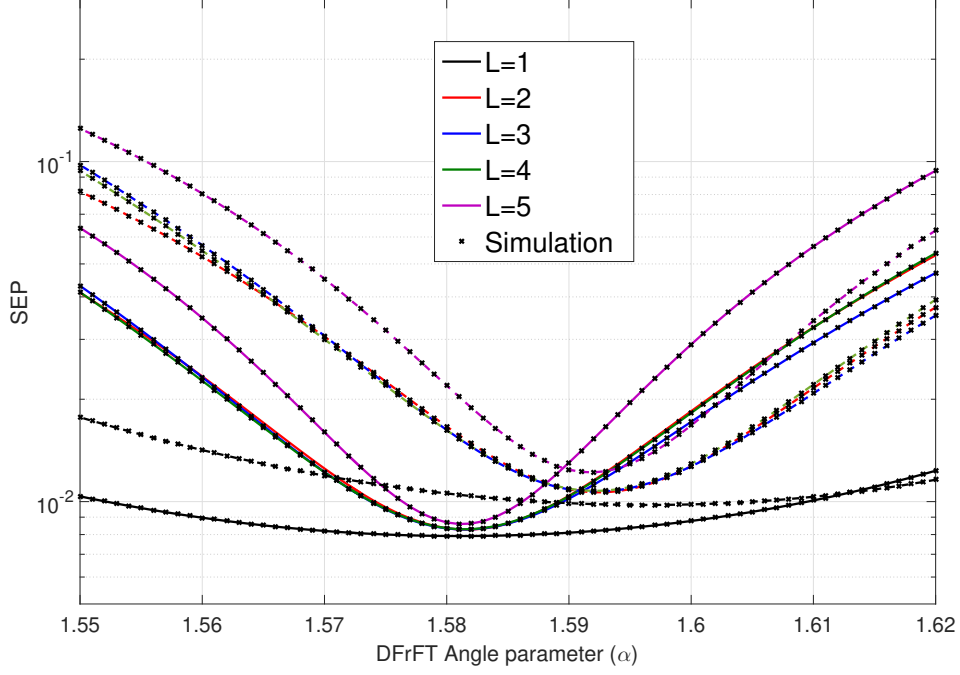
Figure 5.2: *Analytical and simulated SEP versus DFrFT angle parameter α at $\Delta\epsilon = 0.1, 0.2$ for 8-point DFrFT-based OFDM in the case of BPSK transmission over frequency selective Rayleigh fading channel with different values of L at $\bar{\gamma}_k = 25$ dB.*

where $\zeta_{q,l,m,n}[p,q]$ is the entry of the 2×16 matrix of

$$
\boldsymbol{G} = \Big[(\boldsymbol{g}_A + \boldsymbol{g}_B + \boldsymbol{g}_C + \boldsymbol{g}_D) \ (\boldsymbol{g}_A + \boldsymbol{g}_B + \boldsymbol{g}_C - \boldsymbol{g}_D) \ (\boldsymbol{g}_A + \boldsymbol{g}_B - \boldsymbol{g}_C + \boldsymbol{g}_D)
$$
$$
(\boldsymbol{g}_A + \boldsymbol{g}_B - \boldsymbol{g}_C - \boldsymbol{g}_D) \ (-\boldsymbol{g}_A - \boldsymbol{g}_B + \boldsymbol{g}_C + \boldsymbol{g}_D) \ (-\boldsymbol{g}_A - \boldsymbol{g}_B + \boldsymbol{g}_C - \boldsymbol{g}_D)
$$
$$
(-\boldsymbol{g}_A - \boldsymbol{g}_B - \boldsymbol{g}_C + \boldsymbol{g}_D) \ (-\boldsymbol{g}_A - \boldsymbol{g}_B - \boldsymbol{g}_C - \boldsymbol{g}_D) \ (\boldsymbol{g}_A - \boldsymbol{g}_B + \boldsymbol{g}_C + \boldsymbol{g}_D)
$$
$$
(\boldsymbol{g}_A - \boldsymbol{g}_B + \boldsymbol{g}_C - \boldsymbol{g}_D) \ (\boldsymbol{g}_A - \boldsymbol{g}_B - \boldsymbol{g}_C + \boldsymbol{g}_D) \ (\boldsymbol{g}_A - \boldsymbol{g}_B - \boldsymbol{g}_C - \boldsymbol{g}_D)
$$
$$
(-\boldsymbol{g}_A + \boldsymbol{g}_B + \boldsymbol{g}_C + \boldsymbol{g}_D) \ (-\boldsymbol{g}_A + \boldsymbol{g}_B + \boldsymbol{g}_C - \boldsymbol{g}_D) \ (-\boldsymbol{g}_A + \boldsymbol{g}_B - \boldsymbol{g}_C + \boldsymbol{g}_D)
$$
$$
(-\boldsymbol{g}_A + \boldsymbol{g}_B - \boldsymbol{g}_C - \boldsymbol{g}_D) \Big]
$$

with

$$
\boldsymbol{g}_A = \big[\Re\left[\beta^*(k) \boldsymbol{\Lambda} \boldsymbol{\beta}_k e_q^T \right] \quad \Im\left[\beta^*(k) \boldsymbol{\Lambda} \boldsymbol{\beta}_k e_q^T \right] \big]^T,
$$
$$
\boldsymbol{g}_B = \big[2\Re\left[\beta^*(k) \boldsymbol{\Lambda} \boldsymbol{\beta}_k e_l^T \right] \quad 2\Im\left[\beta^*(k) \boldsymbol{\Lambda} \boldsymbol{\beta}_k e_l^T \right] \big]^T,
$$
$$
\boldsymbol{g}_C = \big[\Im\left[\beta^*(k) \boldsymbol{\Lambda} \boldsymbol{\beta}_k e_m^T \right] \quad -\Re\left[\beta^*(k) \boldsymbol{\Lambda} \boldsymbol{\beta}_k e_m^T \right] \big]^T,
$$
$$
\boldsymbol{g}_D = \big[2\Im\left[\beta^*(k) \boldsymbol{\Lambda} \boldsymbol{\beta}_k e_n^T \right] \quad -2\Re\left[\beta^*(k) \boldsymbol{\Lambda} \boldsymbol{\beta}_k e_n^T \right] \big]^T.
$$
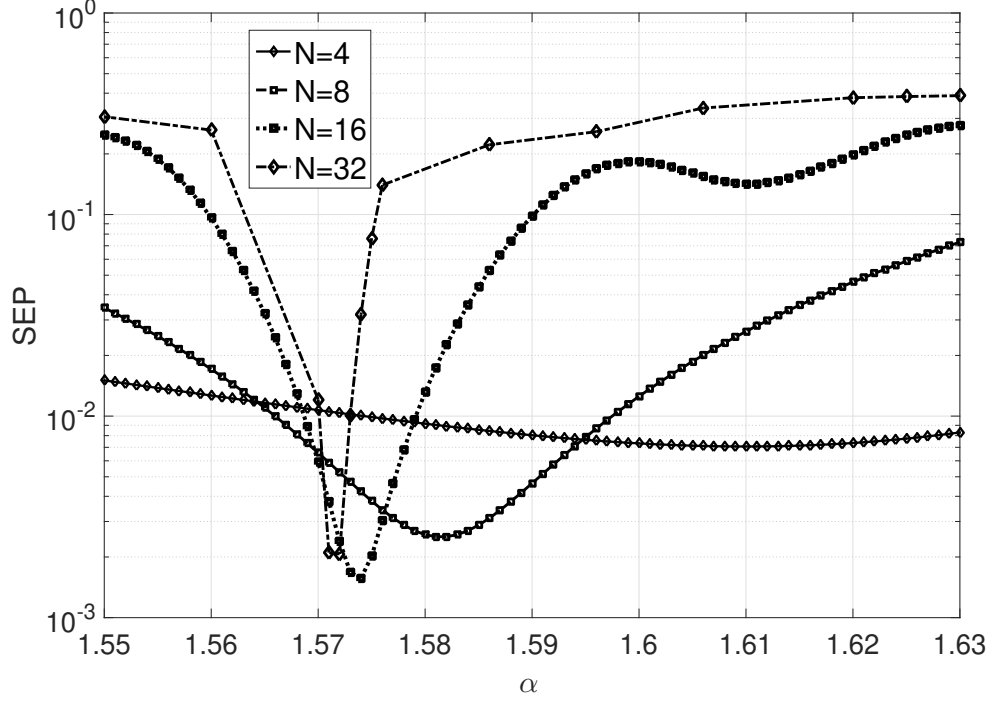
Figure 5.3: *Comparison of SEP versus α for different values of N in the case of BPSK transmission over a 2-tap Rayleigh fading channel with equal power delay profile, $\Delta\epsilon = 0.1$, and $\bar{\gamma}_k = 25\,dB$.*

The PDF given in (5.33) is a function of $\boldsymbol{\beta}$ and, by substituting in (5.30), we get

$$
P_{c,\text{lavg}}(\beta^*(k)Y(k)\in D_{s1}|\beta(k),\boldsymbol{\beta}_k)=\frac{1}{2^{4(N-2)}}\sum_{q=0}^{2^{N-2}-1}\sum_{l=0}^{2^{N-2}-1}\sum_{m=0}^{2^{N-2}-1}\sum_{n=0}^{2^{N-2}-1}\sum_{f=1}^{16}
$$

$$
Q\!\left(\frac{-\left(|\beta(k)|^2 D_A + \zeta_{q,l,m,n}[1,f]\right)}{\sigma_\beta}\right)Q\!\left(\frac{-\left(|\beta(k)|^2 D_B + \zeta_{q,l,m,n}[2,f]\right)}{\sigma_\beta}\right)
$$

$$
-Q\!\left(\frac{-\left(|\beta(k)|^2 D_A + \zeta_{q,l,m,n}[1,f]\right)}{\sigma_\beta}\right)Q\!\left(\frac{2-\left(|\beta(k)|^2 D_B + \zeta_{q,l,m,n}[2,f]\right)}{\sigma_\beta}\right)
$$

$$
-Q\!\left(\frac{2-\left(|\beta(k)|^2 D_A + \zeta_{q,l,m,n}[1,f]\right)}{\sigma_\beta}\right)Q\!\left(\frac{-\left(|\beta(k)|^2 D_B + \zeta_{q,l,m,n}[2,f]\right)}{\sigma_\beta}\right)
$$

$$
+Q\!\left(\frac{2-\left(|\beta(k)|^2 D_A + \zeta_{q,l,m,n}[1,f]\right)}{\sigma_\beta}\right)Q\!\left(\frac{2-\left(|\beta(k)|^2 D_B + \zeta_{q,l,m,n}[2,f]\right)}{\sigma_\beta}\right). \tag{5.34}
$$

When symbol $X(k) = 1 + 3j$ is considered, a correct decision is taken when the equalized received signal lies in the region $D_{s2}=\{a + bj|2 \geq a \geq 0, b \geq 2\}$. By repeating the same considerations done for symbol $X(k) = 1+j$, probability of correct
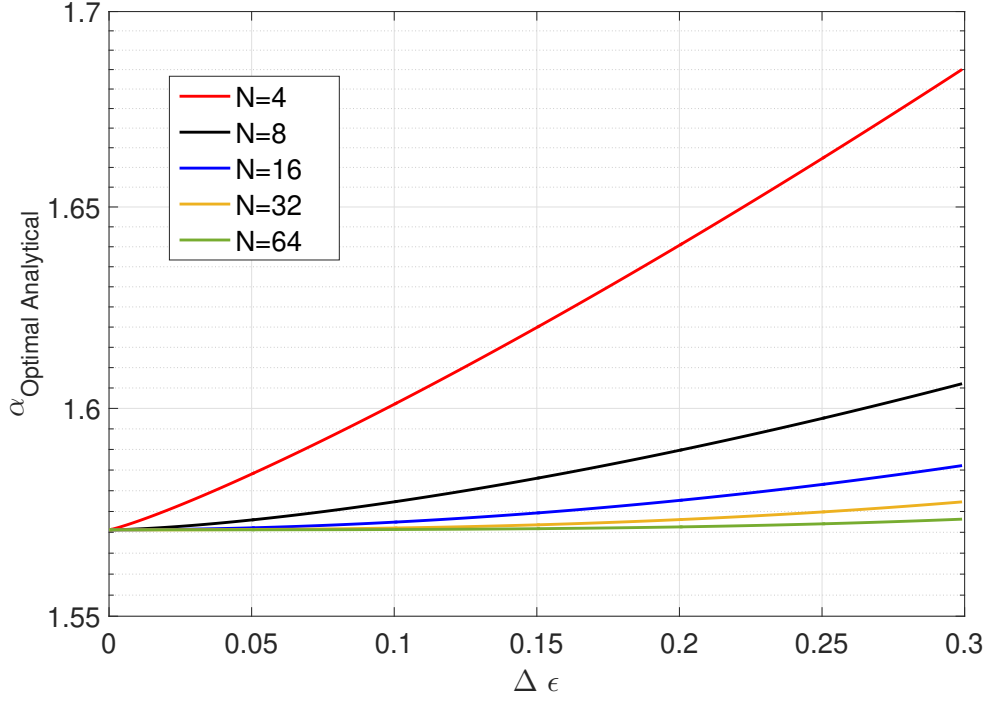
Figure 5.4: *Optimal DFrFT angle parameter for DFrFT-based OFDM and BPSK modulation.*

decision conditioned to the transmission of symbol $X(k) = 1 + 3j$ as

$$
P_{c,2avg}\left(\beta^*(k)Y(k) \in D_{s2}|\beta(k),\boldsymbol{\beta}_k\right) = \frac{1}{2^{4(N-2)}} \sum_{q=0}^{2^{N-2}-1}\sum_{l=0}^{2^{N-2}-1}\sum_{m=0}^{2^{N-2}-1}\sum_{n=0}^{2^{N-2}-1}\sum_{f=1}^{16}
$$

$$
\mathrm{Q}\left(\frac{-\left(|\beta(k)|^2 D_A + \boldsymbol{\zeta}_{q,l,m,n}[1,f]\right)}{\sigma_\beta}\right)\mathrm{Q}\left(\frac{2-\left(|\beta(k)|^2 D_B + \boldsymbol{\zeta}_{q,l,m,n}[2,f]\right)}{\sigma_\beta}\right)
$$

$$
-\mathrm{Q}\left(\frac{2-\left(|\beta(k)|^2 D_A + \boldsymbol{\zeta}_{q,l,m,n}[1,f]\right)}{\sigma_\beta}\right)\mathrm{Q}\left(\frac{2-\left(|\beta(k)|^2 D_B + \boldsymbol{\zeta}_{q,l,m,n}[2,f]\right)}{\sigma_\beta}\right). \tag{5.35}
$$

Similarly, for transmitted symbol $X(k) = 3 + j$, the correct decision lies in the region $D_{s3} = \{a + bj | a \geq 2, 2 \geq b \geq 0\}$

$$
P_{c,3avg}\left(\beta^*(k)Y(k) \in D_{s3}|\beta(k),\boldsymbol{\beta}_k\right) = \frac{1}{2^{4(N-2)}} \sum_{q=0}^{2^{N-2}-1}\sum_{l=0}^{2^{N-2}-1}\sum_{m=0}^{2^{N-2}-1}\sum_{n=0}^{2^{N-2}-1}\sum_{f=1}^{16}
$$

$$
\mathrm{Q}\left(\frac{2-\left(|\beta(k)|^2 D_A + \boldsymbol{\zeta}_{q,l,m,n}[1,f]\right)}{\sigma_\beta}\right)\mathrm{Q}\left(\frac{-\left(|\beta(k)|^2 D_B + \boldsymbol{\zeta}_{q,l,m,n}[2,f]\right)}{\sigma_\beta}\right)
$$

$$
-\mathrm{Q}\left(\frac{2-\left(|\beta(k)|^2 D_A + \boldsymbol{\zeta}_{q,l,m,n}[1,f]\right)}{\sigma_\beta}\right)\mathrm{Q}\left(\frac{2-\left(|\beta(k)|^2 D_B + \boldsymbol{\zeta}_{q,l,m,n}[2,f]\right)}{\sigma_\beta}\right). \tag{5.36}
$$
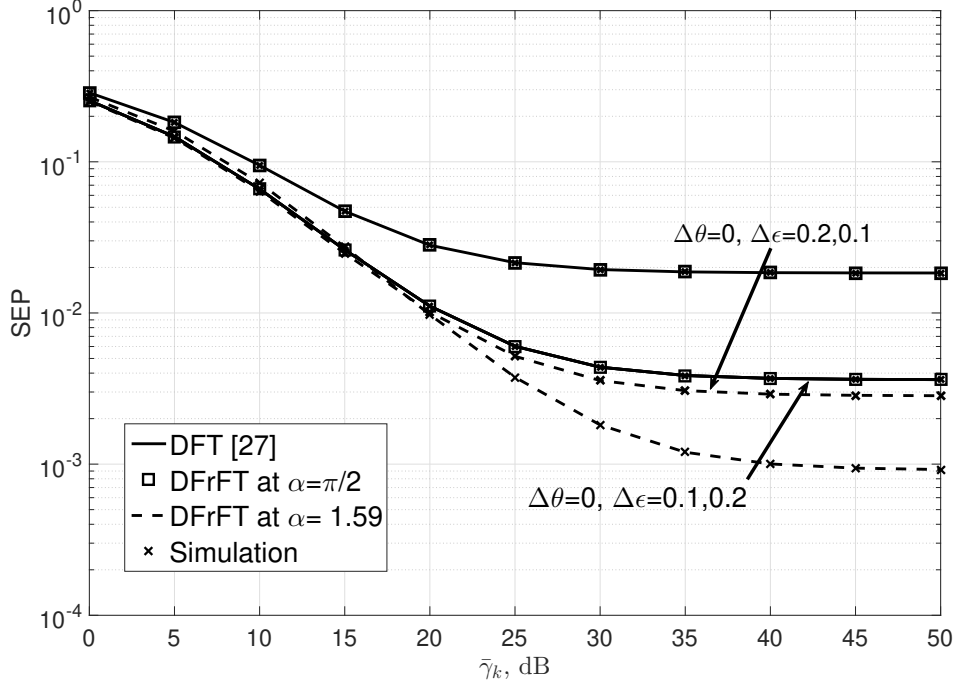
Figure 5.5: *Comparison of SEP versus $\bar{\gamma}_k$ for 8-point DFT- and DFrFT-based OFDM in case of BPSK modulation and transmission over an equal power delay 2-tap frequency selective Rayleigh fading channel at $\alpha = 1.59$ when $\Delta\epsilon = 0.1, 0.2$ and $\Delta\theta=0$.*

Finally, for transmitted symbol $X(k) = 3 + 3j$, the correct decision lies in the region $D_{s4}=\{a + bj | a \geq 2, b \geq 2\}$

$$P_{c,4avg}\left(\beta^*(k)Y(k)\in D_{s4}|\beta(k),\boldsymbol{\beta}_k\right)=\frac{1}{2^{4(N-2)}}\sum_{q=0}^{2^{N-2}-1}\sum_{l=0}^{2^{N-2}-1}\sum_{m=0}^{2^{N-2}-1}\sum_{n=0}^{2^{N-2}-1}\sum_{f=1}^{16}$$

$$Q\left(\frac{2-\left(|\beta(k)|^2 D_A+\boldsymbol{\zeta}_{q,l,m,n}[1,f]\right)}{\sigma_\beta}\right)Q\left(\frac{2-\left(|\beta(k)|^2 D_B+\boldsymbol{\zeta}_{q,l,m,n}[2,f]\right)}{\sigma_\beta}\right). \tag{5.37}$$

By taking into account the symmetry of the 16-QAM modulation, the average probability of correct decision given in (5.63) is obtained by dividing the individual probabilities of correct decision given in (5.34), (5.35), (5.36), and (5.37) by 4. From (5.63) it is clearly visible that the dependence on $(\beta(k), \boldsymbol{\beta}_k)$ is implicit in $\boldsymbol{\zeta}_{q,l,m,n}[1,f]$ and $\boldsymbol{\zeta}_{q,l,m,n}[2,f]$. The analytical expression of the SEP given $(\beta(k), \boldsymbol{\beta}_k)$ is given by

$$P_s\left(\xi_k|\beta(k),\boldsymbol{\beta}_k\right) \triangleq P_s(\beta^*(k)Y(k)\notin D_{s1}|\beta(k),\boldsymbol{\beta}_k)$$
$$= 1 - P_c(\beta^*(k)Y(k)\in D_{s1}|\beta(k),\boldsymbol{\beta}_k) \tag{5.64}$$

It is worth observing that $P_s\left(\xi_k|\boldsymbol{\beta}_k\beta(k)\right)$ involves the computation of an N-dimensional integral and, therefore, it is difficult to evaluate. By following (5.6), the analytical expression of $P_s\left(\xi_k|\beta(k)\right)$ given in (5.65) is obtained by using the conditional mean
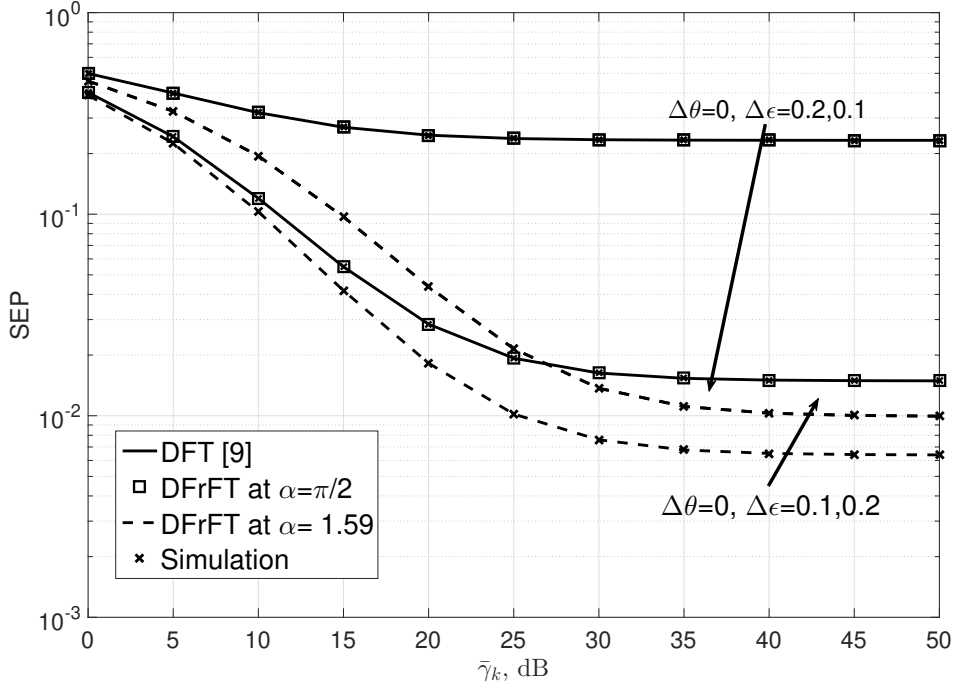
Figure 5.6: *Comparison of SEP versus $\bar{\gamma}_k$ between an 8-point DFT- and DFrFT-based OFDM system for QPSK in the case of the transmission over frequency selective Rayleigh fading channel with 2-tap of equal power delay profile at differnt $\Delta\epsilon$ by considering the $\alpha = 1.59$.*

$|\beta(k)|^2 \vartheta_{q,l,m,n}[i,m]|\beta(k)$ and the conditional variance $|\beta(k)|^2 \nu_{q,l,m,n}[m]/2|\beta(k)$ of the conditional Gaussian random variable $\boldsymbol{\zeta}_{q,l,m,n}[i,f]|\beta(k)$, $i = 1,2$, where

- $\vartheta_{q,l,m,n}[i,m]$ is the entry (i,m) of the 2×16 matrix of $\boldsymbol{W} =$

$$
\begin{aligned}
\Big[& (\boldsymbol{w}_A + \boldsymbol{w}_B + \boldsymbol{w}_C + \boldsymbol{w}_D) \; (\boldsymbol{w}_A + \boldsymbol{w}_B + \boldsymbol{w}_C - \boldsymbol{w}_D) \; (\boldsymbol{w}_A + \boldsymbol{w}_B - \boldsymbol{w}_C + \boldsymbol{w}_D) \\
& (\boldsymbol{w}_A + \boldsymbol{w}_B - \boldsymbol{w}_C - \boldsymbol{w}_D) \; (-\boldsymbol{w}_A - \boldsymbol{w}_B + \boldsymbol{w}_C + \boldsymbol{w}_D) \; (-\boldsymbol{w}_A - \boldsymbol{w}_B + \boldsymbol{g}_C - \boldsymbol{w}_D) \\
& (-\boldsymbol{w}_A - \boldsymbol{w}_B - \boldsymbol{w}_C + \boldsymbol{w}_D) \; (-\boldsymbol{w}_A - \boldsymbol{w}_B - \boldsymbol{w}_C - \boldsymbol{w}_D) \; (\boldsymbol{w}_A - \boldsymbol{w}_B + \boldsymbol{w}_C + \boldsymbol{w}_D) \\
& (\boldsymbol{w}_A - \boldsymbol{w}_B + \boldsymbol{w}_C - \boldsymbol{w}_D) \; (\boldsymbol{w}_A - \boldsymbol{w}_B - \boldsymbol{w}_C + \boldsymbol{w}_D) \; (\boldsymbol{w}_A - \boldsymbol{w}_B - \boldsymbol{w}_C - \boldsymbol{w}_D) \\
& (-\boldsymbol{w}_A + \boldsymbol{w}_B + \boldsymbol{w}_C + \boldsymbol{w}_D) \; (-\boldsymbol{w}_A + \boldsymbol{w}_B + \boldsymbol{w}_C - \boldsymbol{w}_D) \; (-\boldsymbol{w}_A + \boldsymbol{w}_B - \boldsymbol{w}_C + \boldsymbol{w}_D) \\
& (-\boldsymbol{w}_A + \boldsymbol{w}_B - \boldsymbol{w}_C - \boldsymbol{w}_D) \Big],
\end{aligned}
$$

with

$$
\begin{aligned}
\boldsymbol{w}_A &= C_{\beta(k)\beta(k)}^{-1} \left[\Re\left[\boldsymbol{e}_q^T \boldsymbol{\Lambda} \boldsymbol{C}_{\boldsymbol{\beta}_k \beta(k)} \right] \; \Im\left[\boldsymbol{e}_q^T \boldsymbol{\Lambda} \boldsymbol{C}_{\boldsymbol{\beta}_k \beta(k)} \right] \right]^T \\
\boldsymbol{w}_B &= C_{\beta(k)\beta(k)}^{-1} \left[2\Re\left[\boldsymbol{e}_l^T \boldsymbol{\Lambda} \boldsymbol{C}_{\boldsymbol{\beta}_k \beta(k)} \right] \; 2\Im\left[\boldsymbol{e}_l^T \boldsymbol{\Lambda} \boldsymbol{C}_{\boldsymbol{\beta}_k \beta(k)} \right] \right]^T \\
\boldsymbol{w}_C &= C_{\beta(k)\beta(k)}^{-1} \left[\Im\left[\boldsymbol{e}_m^T \boldsymbol{\Lambda} \boldsymbol{C}_{\boldsymbol{\beta}_k \beta(k)} \right] \; -\Re\left[\boldsymbol{e}_m^T \boldsymbol{\Lambda} \boldsymbol{C}_{\boldsymbol{\beta}_k \beta(k)} \right] \right]^T \\
\boldsymbol{w}_D &= C_{\beta(k)\beta(k)}^{-1} \left[2\Im\left[\boldsymbol{e}_n^T \boldsymbol{\Lambda} \boldsymbol{C}_{\boldsymbol{\beta}_k \beta(k)} \right] \; -2\Re\left[\boldsymbol{e}_n^T \boldsymbol{\Lambda} \boldsymbol{C}_{\boldsymbol{\beta}_k \beta(k)} \right] \right]^T
\end{aligned}
$$
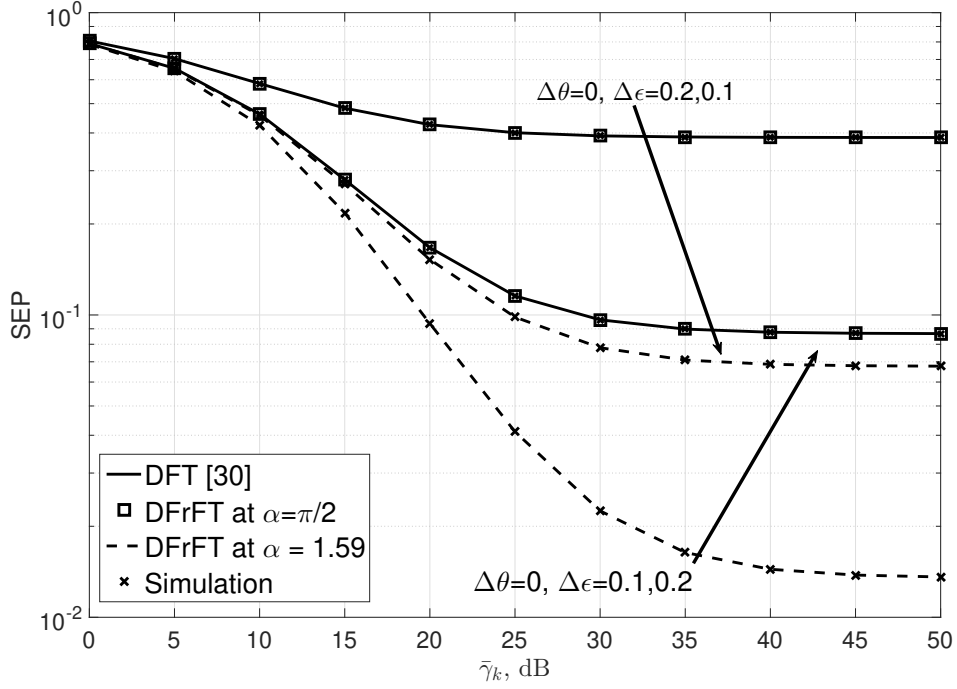
Figure 5.7: *Comparison of SEP versus $\bar{\gamma}_k$ between 8-point DFT- and DFrFT-based OFDM for 16-QAM modulation scheme transmission over frequency selective Rayleigh fading channel of 2-tap with equal power delay profile at $\Delta\epsilon = 0.1, 0.2$ and $\Delta\theta$=0 by considering $\alpha = 1.59$.*

being $\boldsymbol{C}_{\boldsymbol{\beta}_k|\beta(k)}$ the channel auto-covariance matrix given in [105];

- $\nu_{q,l,m,n}[m]$ is the mth element of the 1×16 vector $\boldsymbol{\nu} = [\nu_1 \ \ \nu_2 \ \ \cdots \ \ \nu_1 6\,]$, where $\nu_i = \boldsymbol{\zeta}_i^T \boldsymbol{\Lambda} \boldsymbol{C}_{\boldsymbol{\beta}_k\beta(k)} \boldsymbol{\Lambda} \boldsymbol{\zeta}_i$ and $\boldsymbol{\zeta}_1 = \boldsymbol{e}_q + \boldsymbol{e}_l + \boldsymbol{e}_m + \boldsymbol{e}_n$, $\boldsymbol{\zeta}_2 = \boldsymbol{e}_q + \boldsymbol{e}_l + \boldsymbol{e}_m - \boldsymbol{e}_n$, $\boldsymbol{\zeta}_3 = \boldsymbol{e}_q + \boldsymbol{e}_l - \boldsymbol{e}_m + \boldsymbol{e}_n$, $\boldsymbol{\zeta}_4 = \boldsymbol{e}_q + \boldsymbol{e}_l - \boldsymbol{e}_m - \boldsymbol{e}_n$, $\boldsymbol{\zeta}_5 = -\boldsymbol{e}_q - \boldsymbol{e}_l + \boldsymbol{e}_m + \boldsymbol{e}_n$, $\boldsymbol{\zeta}_6 = -\boldsymbol{e}_q - \boldsymbol{e}_l + \boldsymbol{e}_m - \boldsymbol{e}_n$, $\boldsymbol{\zeta}_7 = -\boldsymbol{e}_q - \boldsymbol{e}_l - \boldsymbol{e}_m + \boldsymbol{e}_n$, $\boldsymbol{\zeta}_8 = -\boldsymbol{e}_q - \boldsymbol{e}_l - \boldsymbol{e}_m - \boldsymbol{e}_n$, $\boldsymbol{\zeta}_9 = \boldsymbol{e}_q - \boldsymbol{e}_l + \boldsymbol{e}_m + \boldsymbol{e}_n$, $\boldsymbol{\zeta}_{10} = \boldsymbol{e}_q - \boldsymbol{e}_l + \boldsymbol{e}_m - \boldsymbol{e}_n$, $\boldsymbol{\zeta}_{11} = \boldsymbol{e}_q - \boldsymbol{e}_l - \boldsymbol{e}_m + \boldsymbol{e}_n$, $\boldsymbol{\zeta}_{12} = \boldsymbol{e}_q - \boldsymbol{e}_l - \boldsymbol{e}_n - \boldsymbol{e}_n$, $\boldsymbol{\zeta}_{13} = -\boldsymbol{e}_q + \boldsymbol{e}_l + \boldsymbol{e}_m + \boldsymbol{e}_n$, $\boldsymbol{\zeta}_{14} = -\boldsymbol{e}_q + \boldsymbol{e}_l + \boldsymbol{e}_m + \boldsymbol{e}_n$, $\boldsymbol{\zeta}_{15} = -\boldsymbol{e}_q + \boldsymbol{e}_l - \boldsymbol{e}_m + \boldsymbol{e}_n$, $\boldsymbol{\zeta}_{16} = -\boldsymbol{e}_q + \boldsymbol{e}_l - \boldsymbol{e}_m - \boldsymbol{e}_n$.

By following the same analysis developed in Sec. 5.1.2, the computation of the SEP can be performed by replacing the polar form definition of the Q-function in (5.65). Moreover, by following [114], the expression of unconditional SEP is given in (5.66), where $\Gamma_{[1,f]}(a) = a - |\beta(k)|(D_A + \vartheta_{q,l,m,n}[1,f])$, $\Gamma_{[2,f]}(a) = a - |\beta(k)|(D_B + \vartheta_{q,l,m,n}[2,f])$ and $\Upsilon[m] = \left(1 + \frac{\nu_{q,l,m,n}[m]}{2\sigma^2}\right)$.

In order to solve the integral given in (5.66), first we need to apply the identity that converts the multiplication of the two Q-functions into the sum of two Q-functions given in equation (4.8) of [114]. After that, the integral mentioned in (5.66) can be solved using (5.102) of [114]. The expression of the resulting SEP $P_s(\xi)$ is given in (5.68). Substituting $\alpha = \pi/2$ in $S(q,k)$ and $C_{\beta(k)\beta(k)} = 2\sigma^2$ in (5.20) we get the SEP expression of 16-QAM for conventional OFDM system given by (51) of [108].
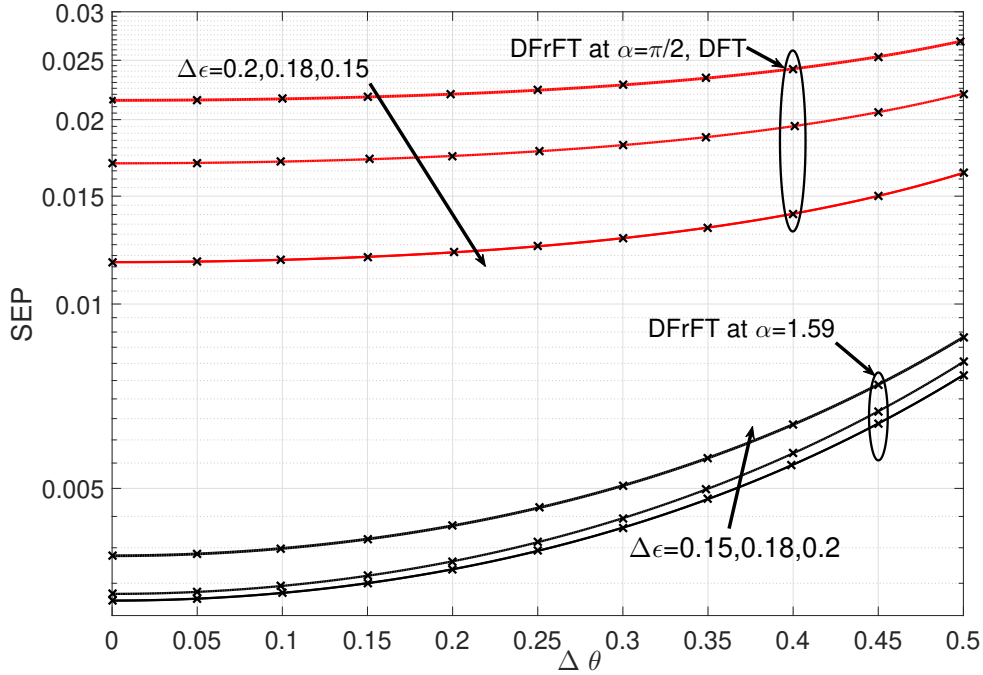
Figure 5.8: *Comparison of SEP versus $\Delta\theta$ between 8-point DFT- and DFrFT- based OFDM BPSK in the case of transmission over frequency selective Rayleigh fading channel with 2-tap of equal power delay profile at $\Delta\epsilon = 0.15, 0.18, and 0.2$ and $\bar{\gamma}_k = 25\,dB$ for DFrFT angle parameter $\alpha = 1.59$.*

5.2 Optimal DFrFT Angle Parameter

From Fig. 5.1 it is clearly visible that for a given $\Delta\epsilon$ the optimal value of the DFrFT angle parameter α is independent from the modulation scheme. The reason of this independency can be easily explained from (4.22), which gives the model of the received signal used to derive all the analytical expressions of the SEP. From such an equation we observe that the first term, which denotes the desired signal, and the second term, which is responsible for the introduction of ICI and ISI, consist of a scaling of the symbols transmitted on different sub-carriers by $S(0, k)$ and $S(l, k)$, with $l = q-k$, where $q \neq k$, respectively, since this function includes the effect of α, $\Delta\epsilon$ and $\Delta\theta$. Therefore, all the derived expressions of SEP given in (5.20), (5.28), and (5.68) have the same minimum for a given value of $\Delta\epsilon$. After having observed this, one can argue that a strategy to find an expression for the optimal value of α consists in taking the most manageable SEP expression and look for its minimization. Hence, in our approach, we consider the SEP expression for BPSK given in (5.20) with respect to α. In order to minimize $P_s(\xi)$ given in (5.20), we proceed with the calculation of the partial derivative $\partial P_s(\xi)/\partial\alpha$ as reported in Appendix A. The result is given in (5.67). The derivation of the closed form expression of the optimal α can be obtained by considering the following remarks:

Remark 1: Figure 5.2 reports the SEP versus α at $\gamma_k = 25\,dB$ with $\Delta\theta = 0$

Figure 5.9: *Comparison of SEP versus $\Delta\theta$ between 8-point DFT- and DFrFT- based OFDM for QPSK transmission over frequency selective Rayleigh fading channel of 2-tap with equal power delay profile at normalized CFOs $\Delta\epsilon = 0.15, 0.18, and 0.2$ and $\bar{\gamma}_k = 25\,dB$ for DFrFT angle parameter $\alpha = 1.59$.*

for an 8-point DFrFT-based OFDM system in case of BPSK transmission over multi-path Rayleigh fading channel having number of channel coefficients $L = 1, \ldots, 5$ with equal power delay profile when $\Delta\epsilon = 0.1, 0.2$. From Fig. 5.2 it can be observed that the optimal α, for a fixed $\Delta\epsilon$, is independent of channel coefficients L, besides being independent of the modulation schemes. With the above observation, we can say that the optimal α is independent of the channel co-variance, meaning that it does not depend on z_q^k and a_q^k and on the respective partial derivatives $\partial z_q^k/\partial\alpha$ and $\partial a_q^k/\partial\alpha$ defined in Appendix A. Hence, the two partial derivatives $\partial z_q^k/\partial\alpha$ and $\partial a_q^k/\partial\alpha$ are set to zero in (5.67), which can be therefore rewritten as (5.69). The following variables $\tilde{C} = \sqrt{f_+(\alpha)}$, $\tilde{D} = \sqrt{f_-(\alpha)}$, $Z = \bar{\gamma}_k a_q^k + 1$, $GG = \sqrt{A\tilde{C}^2/1 + A\tilde{C}^2 + \bar{\gamma}_k a_q^k}$ and $FF = \sqrt{A\tilde{D}^2/1 + A\tilde{D}^2 + \bar{\gamma}_k a_q^k}$ have been introduced in (5.69).

Remark 2: From Remark 1, it descends that when $\partial z_q^k/\partial\alpha$ and $\partial a_q^k/\partial\alpha$ are equal to zero it happens that $\tilde{C} = \tilde{D}$ and, therefore, we have $YY = ZZ$ and $WW = XX$ in (5.69), which can be rewritten as

Figure 5.10: *Comparison of SEP versus $\Delta\theta$ between 8-point DFT- and DFrFT based OFDM for 16-QAM transmission over frequency selective Rayleigh fading channel of 2-tap with equal power delay profile at $\Delta\epsilon$ = 0.15, 0.18 and 0.2 and at $\bar{\gamma}_k$ = 25dB for DFrFT angle parameter $\alpha = 1.59$.*

$$\frac{\partial P_s(\xi)}{\partial\alpha} = \frac{2}{N2^N}\sum_{q=1}^{2^{N-2}-1}\sum_{k=0}^{N-1}YY - \frac{2}{N2^N}\sum_{q=1}^{2^{N-2}-1}\sum_{k=0}^{N-1}WW. \tag{5.70}$$

From (5.70) we observe that to have $\partial P_s(\xi)/\partial\alpha = 0$ both the two terms at the RHS must be equal to zero individually:

- $\sum_{q=1}^{2^{N-2}-1}\sum_{k=0}^{N-1}YY = 0$

- $\sum_{q=1}^{2^{N-2}-1}\sum_{k=0}^{N-1}WW = 0.$

Based on both above points, this condition can be satisfied only when $\partial S(0,k)/\partial\alpha = 0$.

Remark 3: In Fig. 5.3, we plotted the SEP versus α at $\bar{\gamma}_k = 25$dB for different values of N in case of BPSK transmission over an equal power delay profile frequency selective Rayleigh fading channel with 2 taps when $\Delta\epsilon = 0.1$ and $\Delta\theta = 0$. From the figure it is clearly visible that the optimal α for fixed $\Delta\epsilon$ is a function of N. By using **Remarks 1**, **2**, and **3** and following the derivation reported in the Appendix, it is now possible to compute the optimal α expression by setting $\partial S(0,k)/\partial\alpha = 0$. After

Figure 5.11: *Comparison of SEP versus $\bar{\gamma}_k$ between 8-point DFT- and DFrFT based OFDM for BPSK modulation techniques transmission over frequency selective Rayleigh fading channel with different number of channel coefficients L at $\Delta\epsilon$ = 0.1 and $\Delta\theta = 0$.*

some mathematical manipulations and after substituting $\Delta\theta = 0$, the final closed form expression of the optimal α is given by

$$\alpha_{opt} = 10 \left| arccoth\left(2 \cdot \log\left(-\exp\left(\frac{j(\Delta\epsilon)^a \pi}{b} \right) \right) \right) \right|, \quad (5.71)$$

where $a = 0.7 N^{0.3664}$ and $b = -25.22 N^{-0.5943} + 14.62$.

Finally, to confirm that the derived optimal expression for α gives a minimum, we computed the second partial derivative and evaluated its sign. The expression of the second order partial derivative is not reported due to the lack of space. By replacing the optimal value of α for different $\Delta\epsilon$ we got a positive sign, thus confirming that a minimum of SEP was achieved. The optimal α as a function of $\Delta\epsilon$ is reported in Fig. 5.4. From the results reported in the figure it is confirmed that the derived closed form expression of the optimal α matches with the one we are getting form the SEP performance given in Fig. 5.1

5.3 Theoretical and Simulation Results

In order to verify the correctness of the analysis done in Sec. 5.1, SEP results obtained from Monte Carlo (MC) simulations, marked as ($\times$), are compared to those given in
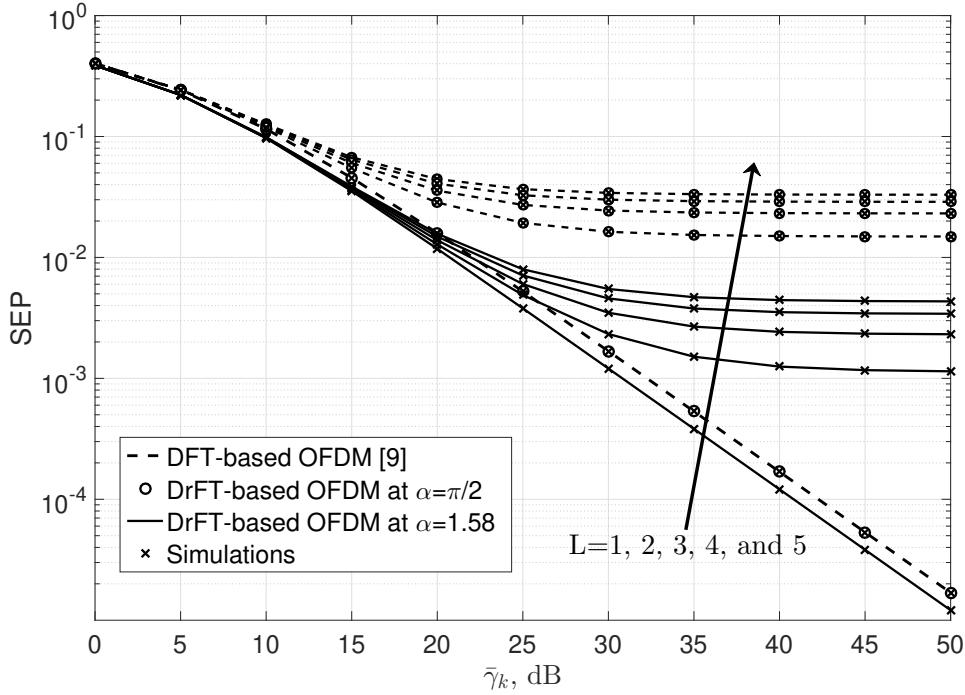
Figure 5.12: *Comparison of SEP versus $\bar{\gamma}_k$ between 8-point DFT- and DFrFT based OFDM for QPSK modulation techniques transmission over frequency selective Rayleigh fading channel with different number of channel coefficients L at $\Delta\epsilon$ = 0.1 and $\Delta\theta = 0$.*

equations (5.20), (5.28) and (5.68) by considering the roll-off $\rho = 0.1$. First of all, the impact of the DFrFT angle parameter α is numerically evaluated to find its optimal value that minimizes the SEP for different values of the normalized CFO $\Delta\epsilon$ versus $\bar{\gamma}_k$ with $\Delta\theta = 0$. The analytical and MC simulation results, obtained for $\Delta\epsilon = 0.1, 0.2$ at $\bar{\gamma}_k = 25$ dB with $N = 8$ in case frequency selective Rayleigh fading channel with $L = 2$ are shown in Fig. 5.1. From Fig. 5.1 it is clearly visible that the optimal value of α is independent of the modulation order for a given value of $\Delta\epsilon$. The optimal value of the angle parameter α_{opt} depends only on the normalized carrier frequency offset $\Delta\epsilon$. From the figures it is clearly viable that simulation results confirm the derived analytical expressions. The choice of $\bar{\gamma}_k = 25$ dB represents a value that is about in the middle of the range of SNR values considered for measuring SEP performance, as it will be shown in Figs. 5.5, 5.6, and 5.7. However, the SEP performance is analyzed by considering the $\alpha = 1.59$ for both the two values of the CFOs, $\Delta\epsilon = 0.1, 0.2$, and the STO $\Delta\theta = 0$. Obviously, in the results presented in this section $\alpha = \pi/2$ converts to the DFT-based OFDM. In Fig. 5.5 the SEP performance analysis is done in the case of BPSK modulation scheme for the DFrFT-based OFDM system with two different values of CFOs, *i.e.*, $\Delta\epsilon = 0.1, 0.2$. The analytical expression of the SEP given in (5.20) is confirmed by MC simulation in the case of transmission over the Rayleigh fading channel with $L = 2$. Moreover, by substituting $\alpha = \pi/2$, the proposed expression given in (5.20) converts into the DFT-based OFDM and at $\alpha = 1.59$ is the same for both the values of
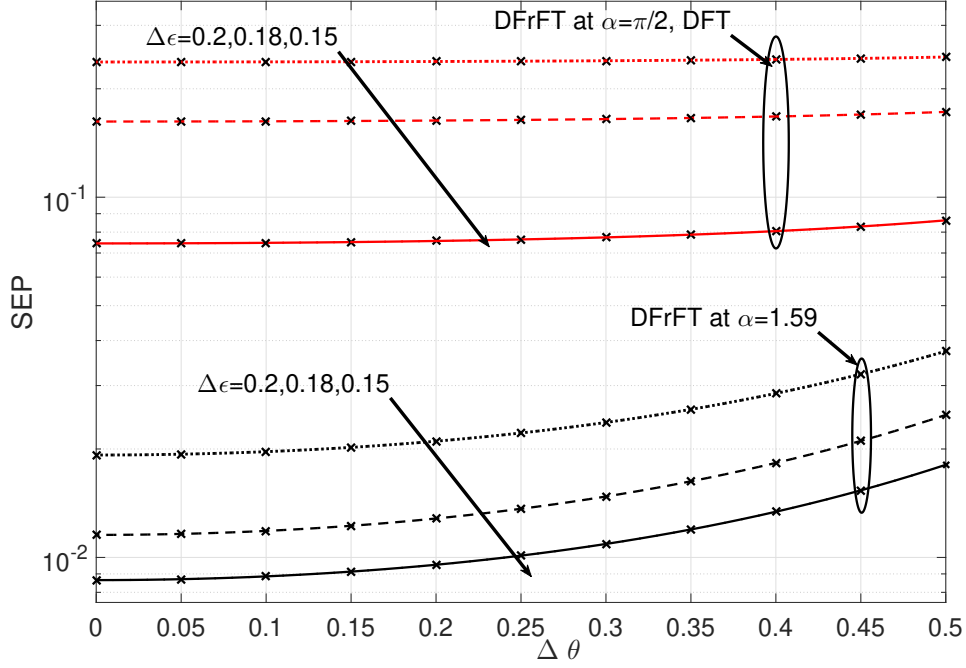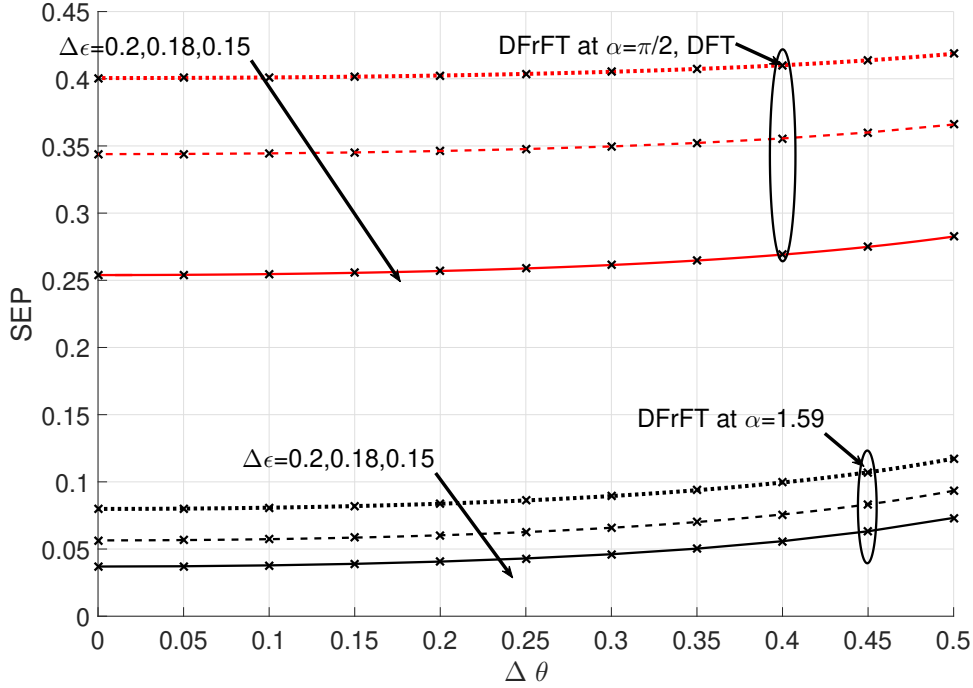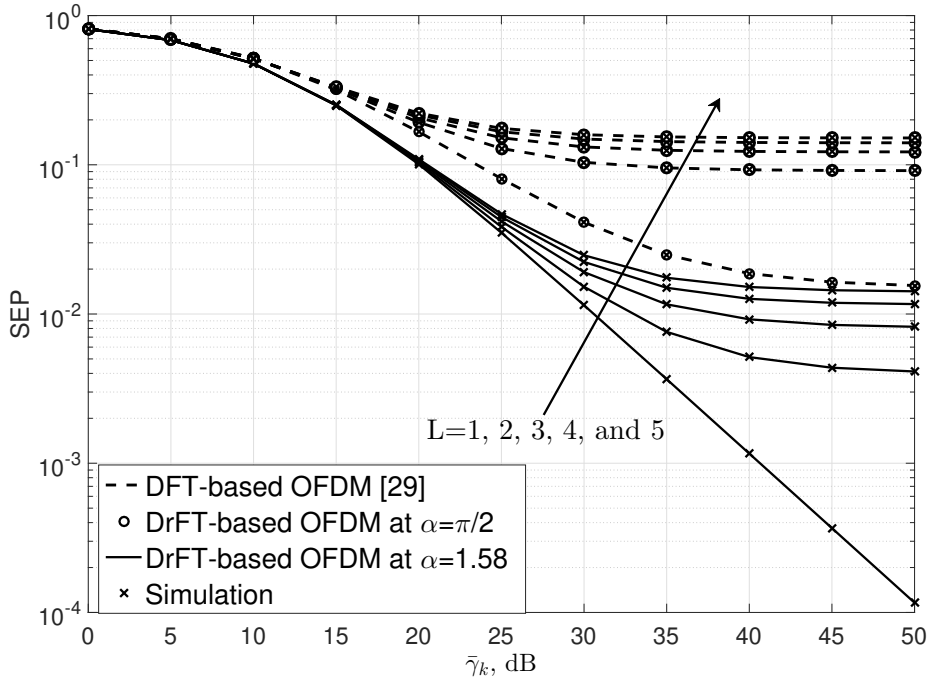
Figure 5.13: *Comparison of SEP versus $\bar{\gamma}_k$ between 8-point DFT and DFrFT-based OFDM 16-QAM transmission over frequency selective Rayleigh fading channel with different number of channel taps L at $\Delta\epsilon$=0.1 and $\Delta\theta$=0*

CFO, $\Delta\epsilon = 0.1, 0.2$. Similarly, Figs. 5.6 and 5.7 reports the SEP performance for QPSK and 16-QAM, respectively, considering the same parameters used above. As it can be observed from Figs. 5.5, 5.6, and 5.7, the performance of the DFrFT-based OFDM system with $\alpha = 1.59$ overcomes that of the DFT-based one and simulation results perfectly match analytical ones for different values of $\Delta\epsilon$ and $\Delta\theta = 0$. Furthermore, the analysis of the STO effect on SEP performance for DFrFT-based OFDM system using the same value of the DFrFT angle parameter $\alpha = 1.59$ and for $\alpha = \pi/2$ at $\bar{\gamma}_k = 25\,\text{dB}$ is given in Figs. 5.8, 5.9, and 5.10. In Fig. 5.8 the SEP performance obtained from the analytical expression given in (5.20), which holds for BPSK, is plotted for different values of the CFO, $\epsilon = 0.15, 0.18, 0.2$. From Fig. 5.8, it is clearly visible that DFrFT-based OFDM system for $\alpha = 1.59$ is more robust to STO than that based on DFT. Moreover, it can be observed that DFrFT-based OFDM is more robust to STO as well as to CFO as compared to DFT-based OFDM. Similarly, Figs. 5.9 and 5.10 reports SEP performance of the QPSK and 16-QAM, respectively, for the same values of CFO considered above. As it is clearly visible form Figs. Figs. 5.8, 5.9, and 5.10, by increasing values of the $\Delta\theta$ SEP performance degrades significantly, rate of the degradation rate DFrFT is larger as compare to DFT. This is because we fixed the values of the DFrFT angle parameter to $\alpha = 1.59$ and evaluated over the different $\Delta\theta$. By increasing the value of $\Delta\theta$ for fixed α the term $S(q, k)$, which is responsible for ICI and ISI in (23), increases. Due to the fixed value of $\alpha = 1.59$, the rate of the degradation in SEP performance in
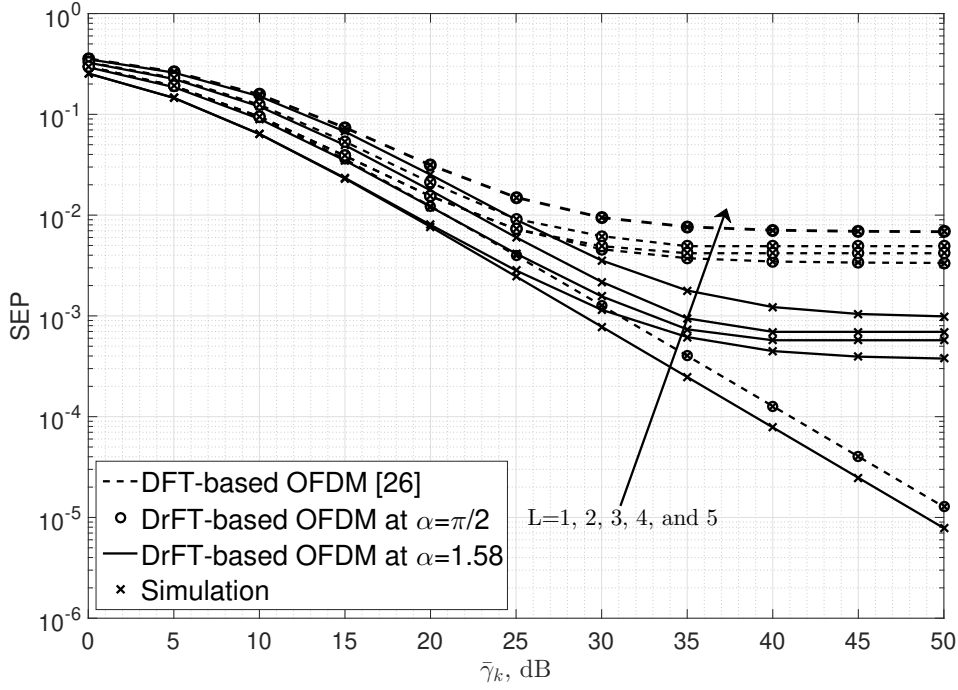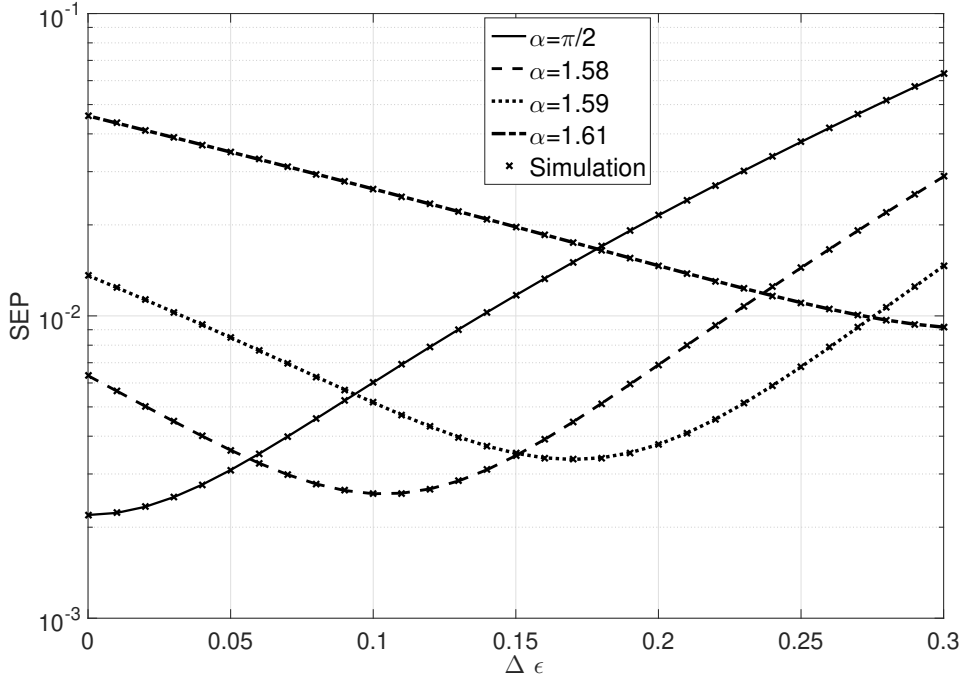
Figure 5.14: *Comparison of SEP versus $\Delta\epsilon$ between 8-point DFrFT-based OFDM for BPSK modulation techniques transmission over frequency selective Rayleigh fading channel with 2-taps for different α and at $\bar{\gamma}_k$ = 25dB.*

DFrFT is larger as compared to the one based on DFT. Our results show that DFrFT-based OFDM system guarantees more robustness that DFT-based OFDM system when the effect of CFO and STO are considered together by proper selection of the DFrFT angle value α.

Figure 5.11 reports the SEP versus $\bar{\gamma}_k$ for different values of the multi-path Rayleigh fading channel coefficients L for BPSK. In the figure, we compare the SEP performance for 8-point DFrFT- and DFT-based OFDM system for different values of L with equal power delay profile frequency selective Rayleigh fading channel when $\Delta\epsilon = 0.1$ and $\Delta\theta = 0$. From Fig. 5.11, it is clearly visible that the performance of the DFrFT-based OFDM system is always better than that of the DFT-based one for any value of L. Also, at $\alpha = \pi/2$ and $\Delta\theta = 0$ derived results have perfect match with the results given in literature when only CFO is present. Similarly, with the same parameters of Fig. 5.11. In Fig. 5.12 reports similar result of SEP versus $\bar{\gamma}_k$ for QPSK is reported. From Fig. 5.12 it is clearly visible that at $\alpha = \pi/2$ and $\Delta\theta = 0$ a perfect match with the results given in [50] is observed. Finally, similar confirmation can also be obtained for 16-QAM. The result for 16-QAM is shown in Fig. 5.13 and at $\alpha = \pi/2$ and $\Delta\theta = 0$ derived results have perfect match with the results given in [108]. Therefore, the results confirm the superiority of DFrFT-based OFDM compared to DFT-based OFDM when the optimal angle parameter is set for the given value of $\Delta\epsilon$.

The optimality of α was verified by drawing the SEP versus CFO in case of trans-
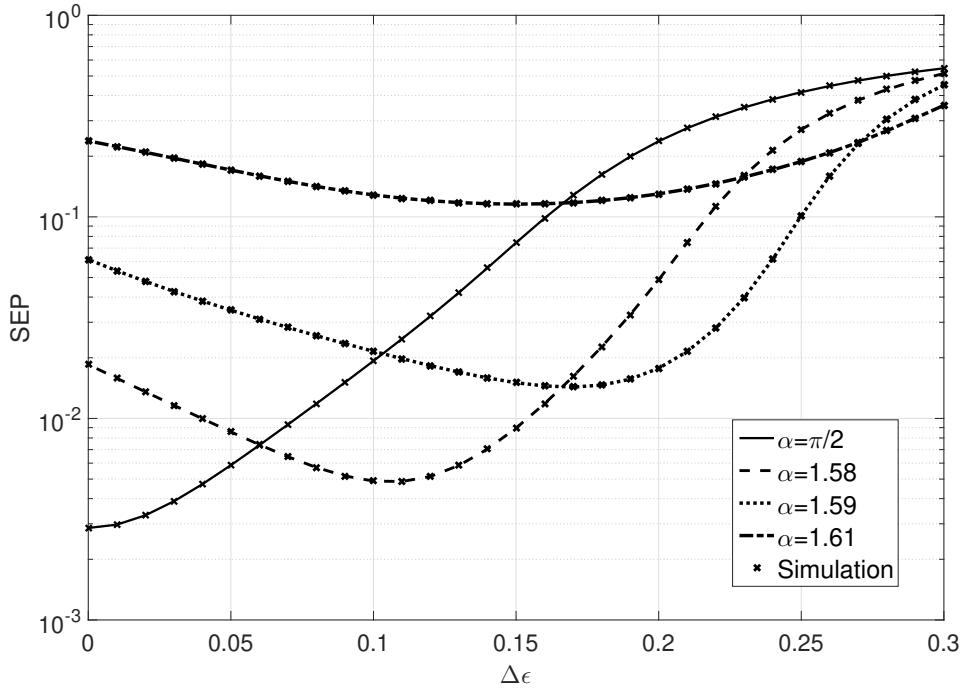
Figure 5.15: *Comparison of SEP versus $\Delta\epsilon$ between 8-point DFrFT-based OFDM for QPSK modulation techniques transmission over frequency selective Rayleigh fading channel with 2-tap for different α and at $\bar{\gamma}_k = 25dB$.*

mission over a 2-tap frequency selective Rayleigh fading channel. In Fig. 5.14, we plotted the SEP versus $\Delta\epsilon$ by considering the fixed value of $\bar{\gamma}_k = 25dB$ and $\Delta\theta = 0$ with 8-point BPSK DFrFT-based OFDM system at $\alpha = \pi/2, 1.584, 1.591,$ and 1.61. The chosen values of α are the optimal ones for $\Delta\epsilon = 0.1, 0.2,$ and 0.3, respectively. From Fig. 5.14 we observe that the best SEP performance is always better at the $\Delta\epsilon$ value that defines α_{opt} and that as we move away from both sides of the $\Delta\epsilon$ giving α_{opt}, the performance degrades. With the same parameters as given in Fig. 5.14, Fig. 5.15 reports the SEP versus $\Delta\epsilon$ for QPSK. From Fig. 5.15 we can observe similar behavior in the SEP performance to $\Delta\epsilon$. Finally, similar behavior can be observed for 16-QAM, the result for 16-QAM is shown in Fig. 5.16.

5.4 Summary

This chapter provides SEP analysis of DFrFT-based OFDM systems with CFO and STO in frequency selective Rayleigh fading channels. It is well known that DFrFT-based OFDM systems allow to improve the performance of the DFT-based one over doubly dispersive fading channels by properly choosing the optimal value of the DFrFT angle parameter α_{opt}. Derivation of exact SEP expressions for DFrFT-based OFDM system in case of BPSK, QPSK, and 16-QAM modulation scheme for frequency selective Rayleigh fading channel in presence of STO and CFO at the same time. From the presented results, it came out for the first time that DFrFT based OFDM system is also
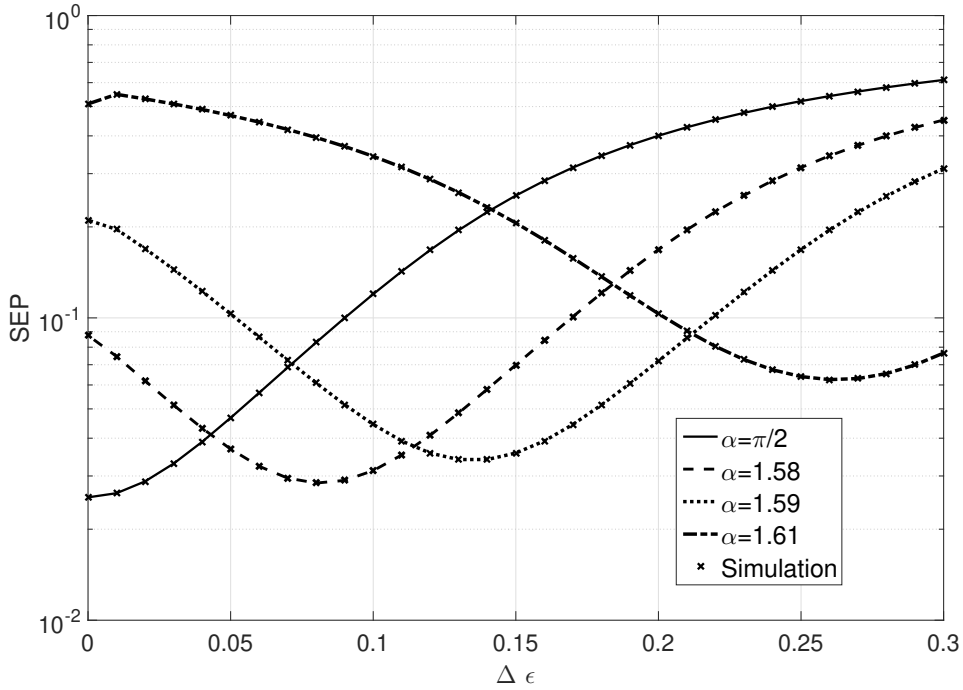
Figure 5.16: *Comparison of SEP versus $\Delta\epsilon$ between 8-point DFrFT-based OFDM for 16-QAM in case of transmission over frequency selective Rayleigh fading channel with 2-taps with different α and at $\bar{\gamma}_k$ = 25dB.*

more robust to STO ($\Delta\theta$) as well as the CFO ($\Delta\epsilon$) at α_{opt}. In order to get the confirmation of the α_{opt} for particular CFO values, in this chapter we also derived the closed form expression of the α_{opt} as a function of the $\Delta\epsilon$. The correctness of the derived analytical expressions has been demonstrated by comparing them to SEP obtained by means of Monte Carlo simulations. Our results demonstrate that at optimal value of the angle parameter α_{opt} the DFrFT-based OFDM system overcomes DFT-based OFDM one because the lower sensitive to the STO as well as the CFO. For $\alpha = \pi/2$ DFrFT-based OFDM system converts to DFT-OFDM system.

$$P_c(\xi_k|\beta(k),\boldsymbol{\beta}_k)=\frac{1}{4\times2^{4(N-2)}}\sum_{q=0}^{2^{N-2}-1}\sum_{l=0}^{2^{N-2}-1}\sum_{m=0}^{2^{N-2}-1}\sum_{n=0}^{2^{N-2}-1}\sum_{f=1}^{16}\ Q\left(\frac{-\left(|\beta(k)|^2D_A+\boldsymbol{\zeta}_{q,l,m,n}[1,f]\right)}{\sigma_\beta}\right)$$

$$Q\left(\frac{-\left(|\beta(k)|^2D_B+\boldsymbol{\zeta}_{q,l,m,n}[2,f]\right)}{\sigma_\beta}\right)-Q\left(\frac{-\left(|\beta(k)|^2D_A+\boldsymbol{\zeta}_{q,l,m,n}[1,f]\right)}{\sigma_\beta}\right)Q\left(\frac{2-\left(|\beta(k)|^2D_B+\boldsymbol{\zeta}_{q,l,m,n}[2,f]\right)}{\sigma_\beta}\right)$$

$$-Q\left(\frac{2-\left(|\beta(k)|^2D_A+\boldsymbol{\zeta}_{q,l,m,n}[1,f]\right)}{\sigma_\beta}\right)Q\left(\frac{-\left(|\beta(k)|^2D_B+\boldsymbol{\zeta}_{q,l,m,n}[2,f]\right)}{\sigma_\beta}\right)+Q\left(\frac{2-\left(|\beta(k)|^2D_A+\boldsymbol{\zeta}_{q,l,m,n}[1,f]\right)}{\sigma_\beta}\right)$$

$$Q\left(\frac{2-\left(|\beta(k)|^2D_B+\boldsymbol{\zeta}_{q,l,m,n}[2,f]\right)}{\sigma_\beta}\right)+Q\left(\frac{-\left(|\beta(k)|^2D_A+\boldsymbol{\zeta}_{q,l,m,n}[1,f]\right)}{\sigma_\beta}\right)Q\left(\frac{2-\left(|\beta(k)|^2D_B+\boldsymbol{\zeta}_{q,l,m,n}[2,f]\right)}{\sigma_\beta}\right)$$

$$-Q\left(\frac{2-\left(|\beta(k)|^2D_A+\boldsymbol{\zeta}_{q,l,m,n}[1,f]\right)}{\sigma_\beta}\right)Q\left(\frac{2-\left(|\beta(k)|^2D_B+\boldsymbol{\zeta}_{q,l,m,n}[2,f]\right)}{\sigma_\beta}\right)+Q\left(\frac{2-\left(|\beta(k)|^2D_A+\boldsymbol{\zeta}_{q,l,m,n}[1,f]\right)}{\sigma_\beta}\right)$$

$$Q\left(\frac{-\left(|\beta(k)|^2D_B+\boldsymbol{\zeta}_{q,l,m,n}[2,f]\right)}{\sigma_\beta}\right)-Q\left(\frac{2-\left(|\beta(k)|^2D_A+\boldsymbol{\zeta}_{q,l,m,n}[1,f]\right)}{\sigma_\beta}\right)Q\left(\frac{2-\left(|\beta(k)|^2D_B+\boldsymbol{\zeta}_{q,l,m,n}[2,f]\right)}{\sigma_\beta}\right)$$

$$+Q\left(\frac{2-\left(|\beta(k)|^2D_A+\boldsymbol{\zeta}_{q,l,m,n}[1,f]\right)}{\sigma_\beta}\right)Q\left(\frac{2-\left(|\beta(k)|^2D_B+\boldsymbol{\zeta}_{k,l,m,n}[2,f]\right)}{\sigma_\beta}\right),\tag{5.63}$$

$$P_s(\xi_k|\beta(k))=1-\frac{1}{2^{2(2N-3)}}\sum_{q=0}^{2^{N-2}-1}\sum_{l=0}^{2^{N-2}-1}\sum_{m=0}^{2^{N-2}-1}\sum_{n=0}^{2^{N-2}-1}\sum_{f=1}^{16}\ Q\left(\frac{-|\beta(k)|(D_A+\vartheta_{q,l,m,n}[1,f])}{\sigma\sqrt{1+\frac{\nu_{q,l,m,n}[m]}{2\sigma^2}}}\right)$$

$$Q\left(\frac{-|\beta(k)|(D_B+\vartheta_{q,l,m,n}[2,f])}{\sigma\sqrt{1+\frac{\nu_{q,l,m,n}[m]}{2\sigma^2}}}\right)-Q\left(\frac{-|\beta(k)|(D_A+\vartheta_{q,l,m,n}[1,f])}{\sigma\sqrt{1+\frac{\nu_{q,l,m,n}[m]}{2\sigma^2}}}\right)Q\left(\frac{2-|\beta(k)|(D_B+\vartheta_{q,l,m,n}[2,f])}{\sigma\sqrt{1+\frac{\nu_{q,l,m,n}[m]}{2\sigma^2}}}\right)$$

$$-Q\left(\frac{2-|\beta(k)|(D_A+\vartheta_{q,l,m,n}[1,f])}{\sigma\sqrt{1+\frac{\nu_{q,l,m,n}[m]}{2\sigma^2}}}\right)Q\left(\frac{-|\beta(k)|(D_B+\vartheta_{q,l,m,n}[2,f])}{\sigma\sqrt{1+\frac{\nu_{q,l,m,n}[m]}{2\sigma^2}}}\right)+Q\left(\frac{2-|\beta(k)|(D_A+\vartheta_{q,l,m,n}[1,f])}{\sigma\sqrt{1+\frac{\nu_{q,l,m,n}[m]}{2\sigma^2}}}\right)$$

$$Q\left(\frac{2-|\beta(k)|(D_B+\vartheta_{q,l,m,n}[2,f])}{\sigma\sqrt{1+\frac{\nu_{q,l,m,n}[m]}{2\sigma^2}}}\right)+Q\left(\frac{-|\beta(k)|(D_A+\vartheta_{q,l,m,n}[1,f])}{\sigma\sqrt{1+\frac{\nu_{q,l,m,n}[m]}{2\sigma^2}}}\right)Q\left(\frac{2-|\beta(k)|(D_B+\vartheta_{q,l,m,n}[2,f])}{\sigma\sqrt{1+\frac{\nu_{q,l,m,n}[m]}{2\sigma^2}}}\right)$$

$$-Q\left(\frac{2-|\beta(k)|(D_A+\vartheta_{q,l,m,n}[1,f])}{\sigma\sqrt{1+\frac{\nu_{q,l,m,n}[m]}{2\sigma^2}}}\right)Q\left(\frac{2-|\beta(k)|(D_B+\vartheta_{q,l,m,n}[2,f])}{\sigma\sqrt{1+\frac{\nu_{q,l,m,n}[m]}{2\sigma^2}}}\right)+Q\left(\frac{2-|\beta(k)|(D_A+\vartheta_{q,l,m,n}[1,f])}{\sigma\sqrt{1+\frac{\nu_{q,l,m,n}[m]}{2\sigma^2}}}\right)$$

$$Q\left(\frac{-|\beta(k)|(D_B+\vartheta_{q,l,m,n}[2,f])}{\sigma\sqrt{1+\frac{\nu_{q,l,m,n}[m]}{2\sigma^2}}}\right)-Q\left(\frac{2-|\beta(k)|(D_A+\vartheta_{q,l,m,n}[1,f])}{\sigma\sqrt{1+\frac{\nu_{q,l,m,n}[m]}{2\sigma^2}}}\right)Q\left(\frac{2-|\beta(k)|(D_B+\vartheta_{q,l,m,n}[2,f])}{\sigma\sqrt{1+\frac{\nu_{q,l,m,n}[m]}{2\sigma^2}}}\right)$$

$$+Q\left(\frac{2-|\beta(k)|(D_A+\vartheta_{q,l,m,n}[1,f])}{\sigma\sqrt{1+\frac{\nu_{q,l,m,n}[m]}{2\sigma^2}}}\right)Q\left(\frac{2-|\beta(k)|(D_B+\vartheta_{q,l,m,n}[2,f])}{\sigma\sqrt{1+\frac{\nu_{q,l,m,n}[m]}{2\sigma^2}}}\right),\tag{5.65}$$

$$P_s(\xi) = 1 - \frac{1}{2^{2(2N-3)}} \sum_{q=0}^{2^{N-2}-1} \sum_{l=0}^{2^{N-2}-1} \sum_{m=0}^{2^{N-2}-1} \sum_{n=0}^{2^{N-2}-1} \sum_{k=0}^{N-1} \sum_{f=1}^{16} \frac{1}{\pi^2} \int_0^\infty \left\{ \int_0^{\frac{\pi}{2}} \exp\left(-\frac{(\Gamma_{[1,f]}(0))^2}{2\sigma^2 \Upsilon[m]\sin^2\theta} \right) \right.$$

$$\left. \int_0^{\frac{\pi}{2}} \exp\left(-\frac{(\Gamma_{[2,f]}(0))^2}{2\sigma^2 \Upsilon[m]\sin^2\theta} \right) \right\} p_{\gamma_k}(\gamma_k) d\gamma_k - \frac{1}{\pi^2} \int_0^\infty \left\{ \int_0^{\frac{\pi}{2}} \exp\left(-\frac{(\Gamma_{[1,f]}(0))^2}{2\sigma^2 \Upsilon[m]\sin^2\theta} \right) \int_0^{\frac{\pi}{2}} \exp\left(-\frac{(\Gamma_{[2,f]}(2))^2}{2\sigma^2 \Upsilon[m]\sin^2\theta} \right) \right\} p_{\gamma_k}(\gamma_k) d\gamma_k$$

$$-\frac{1}{\pi^2} \int_0^\infty \left\{ \int_0^{\frac{\pi}{2}} \exp\left(-\frac{(\Gamma_{[1,f]}(2))^2}{2\sigma^2 \Upsilon[m]\sin^2\theta} \right) \int_0^{\frac{\pi}{2}} \exp\left(-\frac{(\Gamma_{[2,f]}(0))^2}{2\sigma^2 \Upsilon[m]\sin^2\theta} \right) \right\} p_{\gamma_k}(\gamma_k) d\gamma_k - \frac{1}{\pi^2} \int_0^\infty \left\{ \int_0^{\frac{\pi}{2}} \exp\left(-\frac{(\Gamma_{[1,f]}(2))^2}{2\sigma^2 \Upsilon[m]\sin^2\theta} \right) \right.$$

$$\left. \int_0^{\frac{\pi}{2}} \exp\left(-\frac{(\Gamma_{[2,f]}(2))^2}{2\sigma^2 \Upsilon[m]\sin^2\theta} \right) \right\} p_{\gamma_k}(\gamma_k) d\gamma_k + \frac{1}{\pi^2} \int_0^\infty \left\{ \int_0^{\frac{\pi}{2}} \exp\left(-\frac{(\Gamma_{[1,f]}(0))^2}{2\sigma^2 \Upsilon[m]\sin^2\theta} \right) \int_0^{\frac{\pi}{2}} \exp\left(-\frac{(\Gamma_{[2,f]}(2))^2}{2\sigma^2 \Upsilon[m]\sin^2\theta} \right) \right\} p_{\gamma_k}(\gamma_k) d\gamma_k$$

$$-\frac{1}{\pi^2} \int_0^\infty \left\{ \int_0^{\frac{\pi}{2}} \exp\left(-\frac{(\Gamma_{[1,f]}(2))^2}{2\sigma^2 \Upsilon[m]\sin^2\theta} \right) \int_0^{\frac{\pi}{2}} \exp\left(-\frac{(\Gamma_{[2,f]}(2))^2}{2\sigma^2 \Upsilon[m]\sin^2\theta} \right) \right\} p_{\gamma_k}(\gamma_k) d\gamma_k + \frac{1}{\pi^2} \int_0^\infty \left\{ \int_0^{\frac{\pi}{2}} \exp\left(-\frac{(\Gamma_{[1,f]}(2))^2}{2\sigma^2 \Upsilon[m]\sin^2\theta} \right) \right.$$

$$\left. \int_0^{\frac{\pi}{2}} \exp\left(-\frac{(\Gamma_{[2,f]}(0))^2}{2\sigma^2 \Upsilon[m]\sin^2\theta} \right) \right\} p_{\gamma_k}(\gamma_k) d\gamma_k - \frac{1}{\pi^2} \int_0^\infty \left\{ \int_0^{\frac{\pi}{2}} \exp\left(-\frac{(\Gamma_{[1,f]}(2))^2}{2\sigma^2 \Upsilon[m]\sin^2\theta} \right) \int_0^{\frac{\pi}{2}} \exp\left(-\frac{(\Gamma_{[2,f]}(2))^2}{2\sigma^2 \Upsilon[m]\sin^2\theta} \right) \right\} p_{\gamma_k}(\gamma_k) d\gamma_k$$

$$+\frac{1}{\pi^2} \int_0^\infty \left\{ \int_0^{\frac{\pi}{2}} \exp\left(-\frac{(\Gamma_{[1,f]}(2))^2}{2\sigma^2 \Upsilon[m]\sin^2\theta} \right) \int_0^{\frac{\pi}{2}} \exp\left(-\frac{(\Gamma_{[2,f]}(2))^2}{2\sigma^2 \Upsilon[m]\sin^2\theta} \right) \right\} p_{\gamma_k}(\gamma) d\gamma_k, \tag{5.66}$$

$$\frac{\partial P_s(\xi)}{\partial \alpha} = -\frac{1}{N2^N} \sum_{q=1}^{2^{N-2}-1} \sum_{k=0}^{N-1} \left\{ \frac{sign(\tilde{C})}{\sqrt{\frac{A\tilde{C}^2}{1+A\tilde{C}^2+\bar{\gamma}_k a_q^k}}} \frac{AZ\tilde{C}\left(\frac{\partial \Re[S(0,k)]}{\partial \alpha} + \frac{\partial z_q^k}{\partial \alpha} \right) - A\bar{\gamma}_k \tilde{C}^2 \frac{\partial a_q^k}{\partial \alpha}}{\left(1+A\tilde{C}^2+\bar{\gamma}_k a_q^k \right)^2} + 4\sqrt{\frac{A\tilde{C}^2}{1+A\tilde{C}^2+\bar{\gamma}_k a_q^k}} \right.$$

$$\tilde{C}\delta\left(\tilde{C} \right)\left(\frac{\partial \Re[S(0,k)]}{\partial \alpha} + \frac{\partial z_q^k}{\partial \alpha} \right) + \frac{sign(\tilde{D})}{\sqrt{\frac{A\tilde{D}^2}{1+A\tilde{D}^2+\bar{\gamma}_k a_q^k}}} \frac{AZ\tilde{D}\left(\frac{\partial \Re[S(0,k)]}{\partial \alpha} - \frac{\partial z_q^k}{\partial \alpha} \right) - A\bar{\gamma}_k \tilde{D}^2 \frac{\partial a_q^k}{\partial \alpha}}{\left(1+A\tilde{D}^2+\bar{\gamma}_k a_q^k \right)^2}$$

$$\left. +4\sqrt{\frac{A\tilde{D}^2}{1+A\tilde{D}^2+\bar{\gamma}_k a_q^k}} \tilde{D}\delta\left(\tilde{D} \right)\left(\frac{\partial \Re[S(0,k)]}{\partial \alpha} - \frac{\partial z_q^k}{\partial \alpha} \right) \right\} \tag{5.67}$$

$$P_s(\xi) = \frac{3}{4} - \frac{1}{2^{4(N-2)}} \sum_{q=0}^{2^{N-2}-1} \sum_{l=0}^{2^{N-2}-1} \sum_{m=0}^{2^{N-2}-1} \sum_{n=0}^{2^{N-2}-1} \sum_{k=0}^{N-1} \sum_{f=1}^{16} \Xi_1^1(0)\Psi_0^1[1,f] \left(\frac{1}{2} + \frac{1}{\pi}\text{atan}\left\{\Xi_1^1(0)\Psi_0^1[2,f]\right\}\right)$$

$$+ \Xi_2^1(0)\Psi_0^1[2,f]\left(\frac{1}{2}+\frac{1}{\pi}\text{atan}\{\Xi_2^1(0)\Psi_0^1[1,f]\}\right) - \Xi_1^1(0)\Psi_0^1[1,f]\left(\frac{1}{2}+\frac{1}{\pi}\text{atan}\{\Xi_1^1(0)\Psi_2^1[2,f]\}\right)$$

$$- \Xi_2^1(2)\Psi_2^1[2,f]\left(\frac{1}{2}+\frac{1}{\pi}\text{atan}\{\Xi_2^1(2)\Psi_0^1[1,f]\}\right) - \Xi_1^1(2)\Psi_2^1[1,f]\left(\frac{1}{2}+\frac{1}{\pi}\text{atan}\left\{\Xi_1^1(2)\Psi_0^1[2,f]\right\}\right)$$

$$- \Xi_2^1(0)\Psi_0^1[2,f]\left(\frac{1}{2}+\frac{1}{\pi}\text{atan}\left\{\Xi_2^1(0)\Psi_2^1[1,f]\right\}\right) + \Xi_1^1(2)\Psi_2^1[1,f\left(\frac{1}{2}+\frac{1}{\pi}\text{atan}\{\Xi_1^1(2)\Psi_2^1[2,f]\}\right)$$

$$+\Xi_2^1(2)\Psi_2^1[2,f]\left(\frac{1}{2}+\frac{1}{\pi}\text{atan}\{\Xi_2^1(2)\Psi_2^1[1,f]\}\right) + \Xi_1^2(0)\Psi_0^2[1,f]\left(\frac{1}{2}+\frac{1}{\pi}\text{atan}\{\Xi_1^2(0)\Psi_2^2[2,f]\}\right)$$

$$+ \Xi_2^2(2)\Psi_2^2[2,f]\left(\frac{1}{2}+\frac{1}{\pi}\text{atan}\{\Xi_2^2(a)\Psi_0^2[1,f]\}\right) + \Xi_1^2(2)\Psi_2^2[1,f]\left(\frac{1}{2}+\frac{1}{\pi}\text{atan}\{\Xi_1^2(2)\Psi_2^2[2,f]\}\right)$$

$$+ \Xi_2^2(2)\Psi_2^2[2,f]\left(\frac{1}{2}+\frac{1}{\pi}\text{atan}\{\Xi_2^2(2)\Psi_2^2[1,f]\}\right) + \Xi_1^3(2)\Psi_2^3[1,f]\left(\frac{1}{2}+\frac{1}{\pi}\text{atan}\{\Xi_1^3(2)\Psi_0^3[2,f]\}\right)$$

$$+\Xi_2^3(0)\Psi_0^3[2,f]\left(\frac{1}{2}+\frac{1}{\pi}\text{atan}\{\Xi_2^3(0)\Psi_2^3[1,f]\}\right) - \Xi_1^3(2)\Psi_2^3[1,f]\left(\frac{1}{2}+\frac{1}{\pi}\text{atan}\left\{\Xi_1^3(2)\Psi_2^3[2,f]\right\}\right)$$

$$- \Xi_2^3(2)\Psi_2^3[2,f]\left(\frac{1}{2}+\frac{1}{\pi}\text{atan}\{\Xi_2^3(2)\Psi_2^3[1,f]\}\right) + \Xi_1^4(2)\Psi_2^4[1,f]$$

$$\left(\frac{1}{2}+\frac{1}{\pi}\text{atan}\{\Xi_1^4(2)\Psi_2^4[2,f]\}\right)+\Xi_2^4(2)\Psi_2^4[2,f]\left(\frac{1}{2}+\frac{1}{\pi}\text{atan}\{\Xi_2^4(2)\Psi_2^4[1,f]\}\right). \tag{5.68}$$

where $\Xi_1^i(a) = \sqrt{\dfrac{C_{\beta(q)\beta(k)}\bar{\gamma}_k}{5+\bar{\gamma}_k\nu_{q,l,m,n}[m]+C_{\beta(k)\beta(k)}\bar{\gamma}_k\left(\Psi_a^i[1,f]\right)^2}}$, $\Psi_a^i[1,f] = \left[D^i\left(1\right)+\vartheta_{q,l,m,n}[1,f]-a\right]$

and $\Xi_2^i(a) = \sqrt{\dfrac{C_{\beta(q)\beta(k)}\bar{\gamma}_k}{5+\bar{\gamma}_k\nu_{q,l,m,n}[m]+C_{\beta(k)\beta(k)}\bar{\gamma}_k\left(\Psi_a^i[2,f]\right)^2}}$, $\Psi_a^i[2,f] = \left[D^i\left(2\right)+\vartheta_{q,l,m,n}[2,f]-a\right]$.

being $\boldsymbol{D}^1 = [1\ 1]$, $\boldsymbol{D}^2 = [1\ 3]$, $\boldsymbol{D}^3 = [3\ 1]$ and $\boldsymbol{D}^4 = [3\ 3]$

$$\frac{\partial P_s(\xi)}{\partial\alpha} = \frac{-1}{N2^N}\sum_{q=1}^{2^{N-2}-1}\sum_{k=0}^{N-1}\left\{\underbrace{\frac{\text{sign}(\tilde{C})AZ\tilde{C}\left(\frac{\partial\Re[S(0,k)]}{\partial\alpha}\right)}{GG\left(1+A\tilde{C}^2+\bar{\gamma}_ka_q^k\right)^2}}_{YY}+\underbrace{4GG\tilde{C}\delta(\tilde{C})\left(\frac{\partial\Re[S(0,k)]}{\partial\alpha}\right)}_{WW}\right.$$

$$\left.+\underbrace{\frac{\text{sign}(\tilde{D})AZ\tilde{D}\left(\frac{\partial\Re[S(0,k)]}{\partial\alpha}\right)}{FF\left(1+A\tilde{D}^2+\bar{\gamma}_ka_q^k\right)^2}}_{ZZ}+\underbrace{4FF\tilde{D}\delta(\tilde{D})\left(\frac{\partial\Re[S(0,k)]}{\partial\alpha}\right)}_{XX}\right\} \tag{5.69}$$

Hardware Implementation of DFrFT-based OFDM

I n this chapter hardware implementation of the DFrFT-based OFDM system is considerd. It is well known that DFrFT-based OFDM has higher robustness to synchronization errors. Only few works are available in the literature that concern with DFrFT hardware implementation. In this chapter we consider its implementation in a Field FPGA. To verify the design of the DFrFT-based OFDM system, we use FIL co-simulation method to evaluate BER in presence of CFO.

6.1 Survey related to DFrFT computational complexity

It is worth noting that the higher tolerance to CFO and STO of DFrFT-based OFDM systems is achieved without any increase in implementation complexity compared to FFT efficient implementation of DFT. However, in the literature several discrete versions of DFrFT algorithms have been proposed [116]. These proposed discrete versions belongs to four different categories: eigenvector decomposition-based method [117], weighted summation-based method [118], linear combination-based method [119], and sampling-based method [120]. By following [116], we observe that when the block of length N is a power of 2, the run time complexity of DFrFT computation is in the order of $O(N^2)$ for the eigenvector decomposition and the weighted summation-based method. In contrast, the complexity is in the order of $O(Nlog_2N)$ for sampling method and linear-based method, which is the same as that of FFT. As shown in Table I of [116], the complexity mainly depends on the constraints set on the discrete implementations of different DFrFT algorithms. Concerning with the use of DFrFT algorithm in OFDM,

Table 6.1: *Computation of max percentage quantization error on the different values of the word length.*

Word length	Test Input	TE	MAE	MPQE	*Average MPQE over input*
18	1st	0.0392-0.0129i	1.451	2.8518	2.31
	2nd	-0.0019+0.007i	1.0236	0.711	
	3rd	$0.0352 - 0.0285i$	1.579	2.8514	
	4th	$0.0144 - 0.0268i$	1.0645	2.85	
14	1st	$0.0395 - 0.0126i$	1.451	2.851	2.28
	2nd	$-0.0014 + 0.006i$	1.0236	0.693	
	3rd	$0.0355 - 0.028i$	1.579	2.866	
	4th	$0.0143 - 0.0269i$	1.0645	2.867	
12	1st	$0.0364 - 0.0126i$	1.451	2.6	1.62
	2nd	$-0.004 + 0.005i$	1.0236	0.65	
	3rd	$0.038 - 0.027i$	1.579	2.95	
	4th	$0.0039 + .003i$	1.0645	2.914	
8	1st	$0.0550 + 0.0412i$	1.451	4.73	3.28
	2nd	$0.0018 + 0.038i$	1.0236	4.15	
	3rd	$0.0318 + 0.05i$	1.579	3.9	
	4th	$-0.019 - 0.025i$	8.5	0.37	

the most important property that must be satisfied is the reversibility in the IDFrFT computation, which also satisfies Hermitian property. For this reason, we focus on the closed-form type form of sampling-based method since it has the same order of complexity as that of FFT and also ensures reversibility property [121]. The complexity of the sampling-based method is in the order of $O(Nlog_2N)$, which can be achieved by the Pei's algorithm [122]. This algorithm can be further optimized via a novel sub-linear algorithm for DFT named sparse Fourier transform (SFT) developed by Haitham *et al.* [123]. When the input data have a large size with a sparse spectrum, this algorithm reduces the complexity of DFT to $O(log_2N \cdot \sqrt{kNlog_2N})$, where k stands for the number of large coefficients in the frequency domain. Similarly, Liu *et al.* [121] proposed the sparse DFrFT (SDFrFT) to achieve fast computation. These recent results about low complexity implementation of the DFrFT are the main motivation towards hardware implementations as, for example, those described in [124].

6.2 Description of the DFrFT-based OFDM System

The block diagram of the DFrFT-based OFDM system is shown in 4.1. From the figure it is clearly visible that the IDFrFT kernel is used at the transmitter side while DFrFT kernel used at the received side. In this section, we are going to describe about the mathematical details of the IDFrFT and DFrFT kernels and it equivalent Simulink of the kernels are given.

6.2.1 IDFrFT kernel at the transmitter

The block of N transmitted symbols is applied to the input of the IDFrFT kernel. After N-point IDFrFT computation, the expression of the mth transmitted sample is written as

$$x(m) = \sum_{k=0}^{N-1} X(k) F_{-\alpha}(m, k), \quad m = 0, 1, \ldots, N-1, \tag{6.1}$$

where $X(k)$ is the symbol transmitted on the kth sub-carrier and $F_-(m,k)$ is the IDFrFT kernel given by

$$F_{-\alpha}(m, k) = \underbrace{\sqrt{\frac{\sin(\alpha) + j\cos(\alpha)}{N}}}_{\text{Constant\_A}} \underbrace{e^{\frac{-jm^2 T_s^2 \cot(\alpha)}{2}}}_{\text{1st\_Term\_Kernel}} \underbrace{e^{\frac{-jk^2 u^2 \cot(\alpha)}{2}}}_{\text{2nd\_Term\_Kernel}} \underbrace{e^{\frac{j2\pi mk}{N}}}_{\text{3rd\_Term\_Kernel}},$$

$$\tag{6.2}$$

In order to get an efficient receiver implementation, a full fixed-point data type FPGA prototyping is addressed in this chapter. The IDFrFT kernel given in (6.2) has many floating-point operations: square root, exponential and trigonometric functions. There are many hardware efficient algorithms for representing a floating-point function into its fixed-point form. Among these, the set of shift-add algorithms, known as for COordinate Rotation DIgital Computer (CORDIC), can be employed for computing a wide range of trigonometric, hyperbolic, linear, and logarithmic functions [125]. The IDFrFT kernel contains the following floating-point functions: square root, exponential, sin(·), cos(·), and cot(·). First, we need to convert into fixed-point functions using the CORDIC algorithms. While the CORDIC implementations of sin(·), cos(·), and exp(·) functions are already available, there is no direct implementation available for cot(·), which is present in the exponent of (6.1). By using the trigonometric property of cot(·)=cos(·)/sin(·), implementation becomes possible. After the implementation of CORDIC algorithms, the Simulink model of the IDFrFT kernel is shown in Fig. 6.1. Each factor in the mathematical expression of the IDFrFT kernel in eq. (6.1) is reported as a sub-block in the Simulink model. It is worth observing that HDL Coder will be used in the following to automatically generate the VHDL code for the FPGA. As given in eq. 6.1, the IDFrFT kernel has two variables, m, k, both taking values from 0 to $N-1$. So, after computation of "1st_Term" and "2nd_Term" of the kernel is given in (6.2), their product is obtained as matrix multiplication. This is because HDL

97
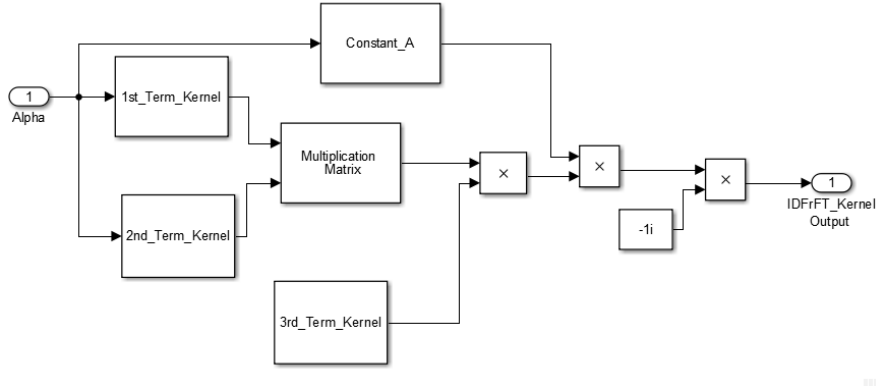
Figure 6.1: *Simulink model of the implemented IDFrFT and DFrFT kernels*

Coder does not support matrix multiplication operation. Hence, to perform the required "Matrix Multiplication", we had to develop our own block implementing element wise multiplication.

6.2.2   DFrFT kernel at the receiver

At the receiving side, after DFrFT computation, the received signal on the q-th subcarrier is

$$y\left(q\right) = \sum_{n=0}^{N-1} r(n)\, F_\alpha\left(q, n\right), \qquad q = 0, 1, \dots, N-1, \tag{6.3}$$

where $r(n)$ is the received signal before the DFrFT block and $F_\alpha(q,n)$ is the kernel given by

$$F_\alpha\left(q, n\right) = \underbrace{\sqrt{\frac{\sin\left(\alpha\right) - j\cos\left(\alpha\right)}{N}}}_{\text{Constant\_A}} \quad \underbrace{e^{\frac{jn^2 T_s^2 \cot(\alpha)}{2}}}_{\text{1st\_Term\_Kernel}} \underbrace{e^{\frac{jq^2 u^2 \cot(\alpha)}{2}}}_{\text{2nd\_Term\_Kernel}} \underbrace{e^{\frac{-j2\pi nq}{N}}}_{\text{3rd\_Term\_Kernel}}.$$

$$\tag{6.4}$$

The Hermitian property of the DFrFT kernel makes almost identical to that of ID-FrFT and, therefore, the same considerations also hold for the DFrFT kernel as well.

6.3   FPGA-in-the-Loop co-simulation of Receiver with equalization of DFrFT-based OFDM

As an example of Simulink model that implements a DFrFT-based OFDM system, we consider the case of transmission of a video signal as shown in Fig. 6.2. The video signal is captured from a generic webcam and FIL co-simulation is run both to verify the correctness of the FPGA implementation and to accelerate the simulation at
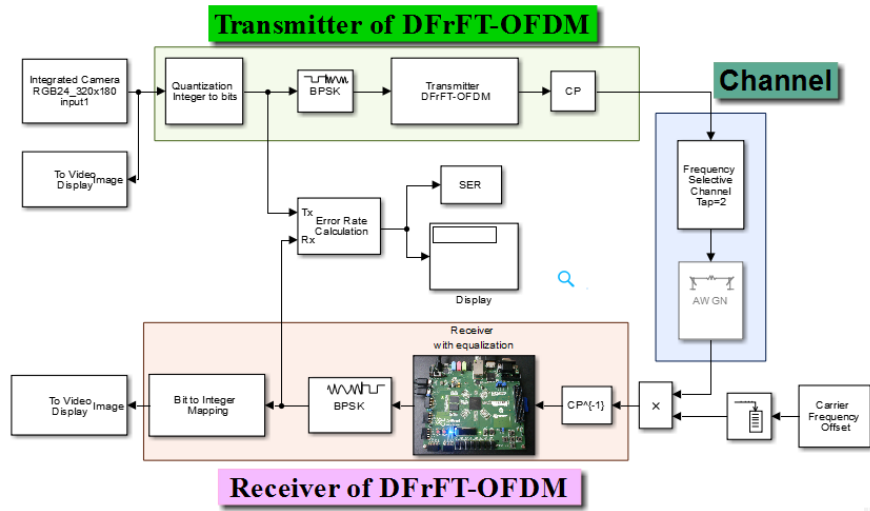
Figure 6.2: *Simulink model of the FIL receiver co-simulation of the DFrFT-based OFDM system*
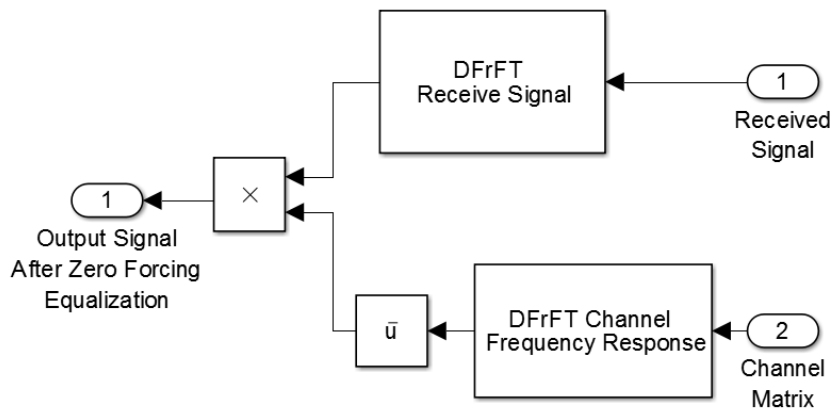
Figure 6.3: *Simulink model of receiver with zero-forcing equalization*

Figure 6.4: *Comparing the floating-point and fixed-point output of fixed-point converted ID-FrFT kernel by applying the random input*

the receiver. Since the receiver of the DFrFT-based system includes also zero forcing equalization, its overall complexity turns out to be higher than that at the transmitter and, therefore, the possibility of performing its rapid is more challenging. The Simulink setup of the receiver with zero forcing equalization of the DFrFT-based OFDM system is given in Fig. 6.3. As a figure of merit we analyse the quality of the reproduced video by comparing the output of DFrFT-based OFDM system with that of the conventional one based on the DFT for different CFO

6.3.1   Receiver with zero-forcing equalization of the DFrFT-based OFDM system

Zero forcing equalization is implemented by assuming ideal knowledge of the channel. We compute the frequency response of the channel and use it to divide sub-carrier by sub-carrier the received signal after the DFrFT block.

6.3.2   Floating-point to fixed-point conversion

The FPGA implementation requires conversion from floating-point to fixed-point data type. However, conversion from floating-point to fixed-point is very challenging and time consuming, typically demanding from 25 to 50% of the total design and implementation time. The conversion process introduces quantization errors that depend on the word and the fractional lengths that, in turn, impacts on the FPGA hardware resources. The optimization of the word length is an iterative process that is carried out using the Fixed Point Toolbox, available in Simulink, with the goal of achieving the best possible performance.

Here, we compare floating-point and fixed-point results for the implementation of the IDFrFT/DFrFT kernels. Figure 5 shows an example of the output of the IDFrFT kernel for floating-point and for fixed-point with word length of 12 bits. Steps for the design are repeated several times using different random inputs to average over different fixed-point outputs. In Fig. 6.4 the average quantization error due to the conversion from floating-point to fixed-point for different values of word length is shown. The average quantization errors obtained for different values of the word length are shown in Fig. 6.5. Similarly, the results for floating- and fixed-point outputs of the fixed-point DFrFT kernel are shown in Fig. 6.6. Those for the average quantization error obtained for different values of the word length are shown in Fig. 6.7.

The average quantization error $e_c(n)$ for fixed-point representation with codeword length of c bits is defined as

$$e_c\left(n\right) = \frac{1}{B}\sum_{i=1}^{B}\left|e_{c,i}\left(n\right)\right|, \qquad n = 1,\ldots,N \qquad (6.5)$$

where B is the number of input blocks containing the N samples to be transformed and $e_{c,i}(n)$ is the quantization error the i-th input block given by

$$e_{c,i}\left(n\right) = \left|\left|floting\ point_i\left(n\right)\right| - \left|fixed\ point_{c,i}\left(n\right)\right|\right|$$

with $i=1,\ldots,B$.

Based on the definition of $e_c(n)$, we consider the fixed-point implementation of the model by selecting the proper word length values from Table 6.1 and then we perform the floating-point and fixed-point simulation of the model and compare the results of IDFrFT/DFrFT kernels, as reported in Figs. 6.4 and 6.6, respectively. The computation of the average quantization error shown in Figs. 6.5 and 6.7. After computation of the average quantization error, we have also computed the maximum percentage quantization error (MPQE) as

$$\text{MPQE} = 100 \times \frac{|TE|}{MAE}, \qquad (6.6)$$

where top error (*TE*) = max (maximum positive error, maximum negative error) and maximum absolute value *MAE* = max (abs (floating-point value)). Based on the definition of MPQE, we simulated the model by applying four different inputs as a test bench into our IDFrFT kernel. The computation results of MPQE for each input is given in the corresponding column of Table 6.1. We also performed the average of MPQE over the different inputs for fixed word lengths. Results for the average MPQE are reported in Table 6.1 from which it is clear that our system performs better if we select word length =12.

6.3.3 Code Conversion (from. mdl and .m file to VHDL)

After fixed-point implementation of the kernels, we have used HDL Coder to generate the VHDL code. The HDL workflow advisor available in HDL Coder guides through the conversion of the Simulink model to VHDL code.
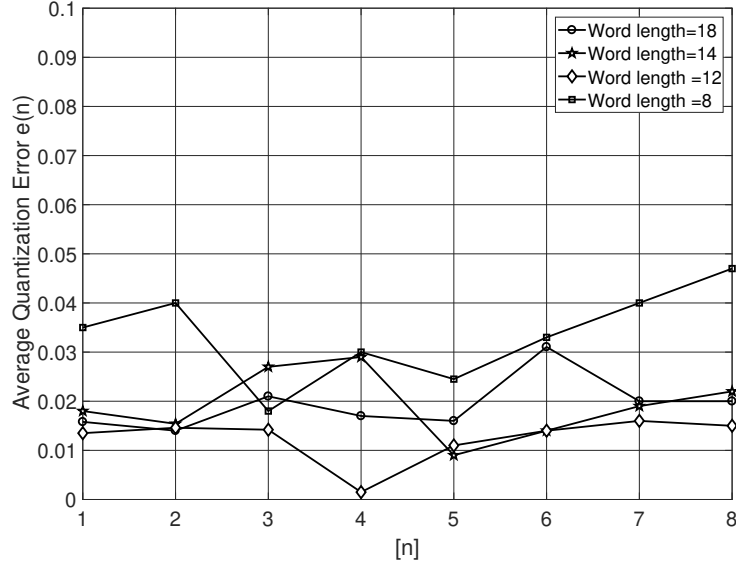
Figure 6.5: *Average absolute quantization error versus index of the sample for different value of the word length for IDFrFT fixed-point block*

6.3.4 FPGA-in-the-Loop co-simulation

For verification purposes, HDL Verifier was used to run FIL co-simulation of the DFrFT-based OFDM receiver along with equalization. Our goal was to run both the receiver and the equalizer on the FPGA board, in order to increase the simulation speed as well as get rapid development of these algorithms in FPGA. Validation of the FIL co-simulation was done through a comparison with the theoretical analysis given in [124].

6.3.5 Implementation Results

First, the correctness of DFrFT-based OFDM system is verified by substituting $\alpha = \pi/$ in order to get conventional OFDM-based DFT. An 8-point implementation of the DFrFT-based OFDM is considered. Transmission takes place over a multi-path Rayleigh fading channel with 2-tap equal power delay profile in presence of a normalized carrier frequency offset $\Delta\epsilon = 0.1$ As shown in Fig. 6.9, BER performance of the DFrFT-based OFDM system performs better than the one based on DFT in presence of CFO. In the Monte Carlo simulation of DFrFT-based OFDM system, implementation of the IDFrFT/DFrFT block is given by the floating-point model.

Considering the conversion of the floating-point Simulink model of IDFrFT/DFrFT kernel into fixed point, we have optimized the fixed-point model by using the proper value of the word length based on what reported in Table 6.1. We also computed the quantization error from floating to fixed-point for given word lengths. Figure 5 shows the results for floating and for fixed-point output of IDFrFT kernel at word length of 12. The computation of the quantization error was done for different values of the word

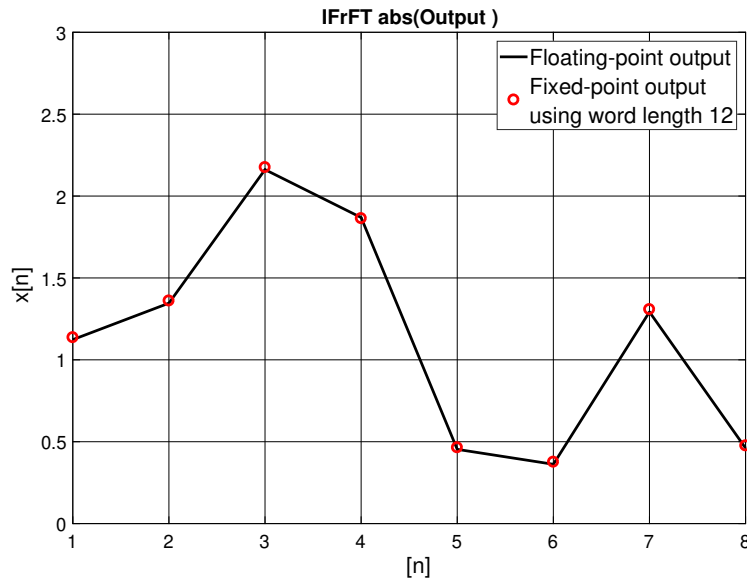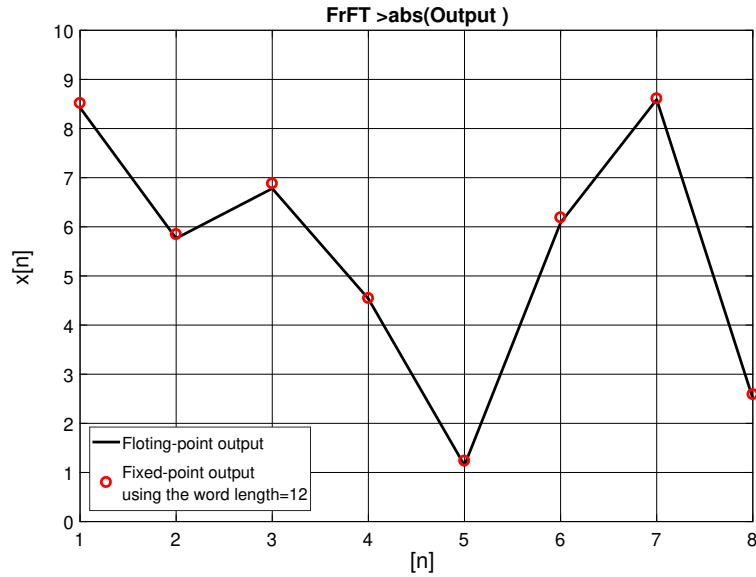**Figure 6.6:** *Comparing the floating and fixed point output of fixed-point converted DFrFT kernel by applying the random input*

length, so that we were able to analyze the impact of word length on the quantization conversion error as given in Fig. 6.5. Similarly, results for the DFrFT kernel output and for the quantization error are given in Fig. 6.7 and Fig. 6.8, respectively.

A summary of the Average max percentage quantization error for different inputs at different word lengths is reported in Table 6.1. After fixed-point conversion, we run simulations based on the fixed-point model. In Fig. 6.9, a perfect match is observed with Monte Carlo simulations (marked as $\times$). The figure reports BER versus versus signal-to-noise ratio per bit E_b/N_0, where E_b is the received signal energy per bit and N_0 is the power spectral density of AWGN. After that, the VHDL code of the kernels was generated and optimized. In order to validate our design on the hardware, we generated the bit stream for programming the FPGA on the ZedBoard using Xilinx ISE design suite, that is integrated in HDL Coder. ZedBoard is a complete prototyping development kit for Xilinx Zynq®-7000 all programmable SoC family. Xilinx ISE compiles and generates the bit stream file which is then loaded into the FPGA using JTAG via the USB connection. After generation of the bit stream, we were able to run the FIL co-simulation and verify the correctness of our model. A Perfect match is observed between FIL co-simulation (marked as $\times$), compared with the fixed-point implementation (marked as $\square$) and also with the Monte Carlo simulation shown in the Fig. 6.9.
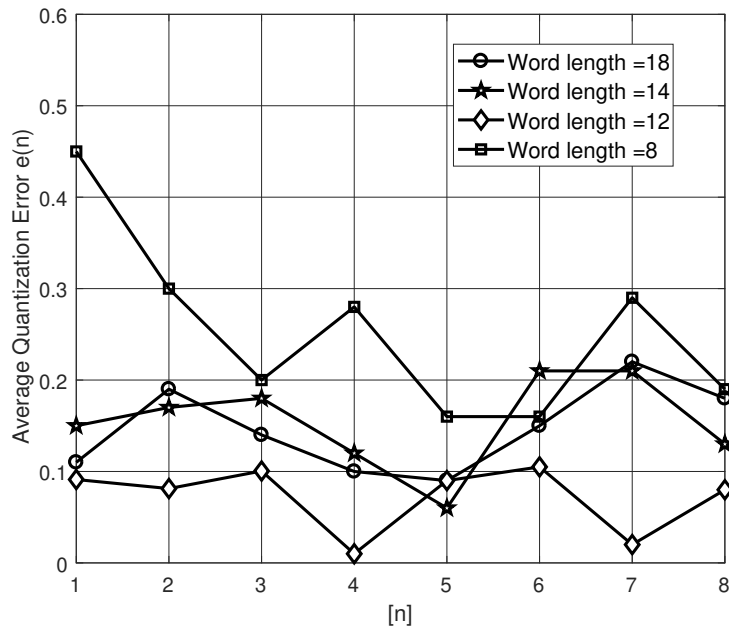
Figure 6.7: *Average absolute quantization error versus index of the sample for different value of the word length for DFrFT fixed-point block*

6.4 Summary

In this chapter rapid prototyping of the receiver for a DFrFT-based OFDM system has been considered by adopting a Model-Based Design approach with the help of MAT-LAB and Simulink. Iterative verification of each step was done starting from floating-point to fixed-point representation, HDL code generation and, finally, hardware co-simulation. We have considered FIL co-simulation of the receiver with the implementation of the equalization of DFrFT-based OFDM system for BPSK transmission over a frequency selective Rayleigh fading channel in presence of CFO. Simulation results clearly demonstrate that the FPGA implementation of a DFrFT-based OFDM system in presence of CFO has the same performance as that obtained from Monte Carlo simulation. Also, the performance is validated with the fixed-point model of the DFrFT-based OFDM. The approach described in this chapter constitutes an efficient way to convert the floating-point model into a fixed-point one to be run in an FPGA and then verify its correctness through FIL co-simulation.
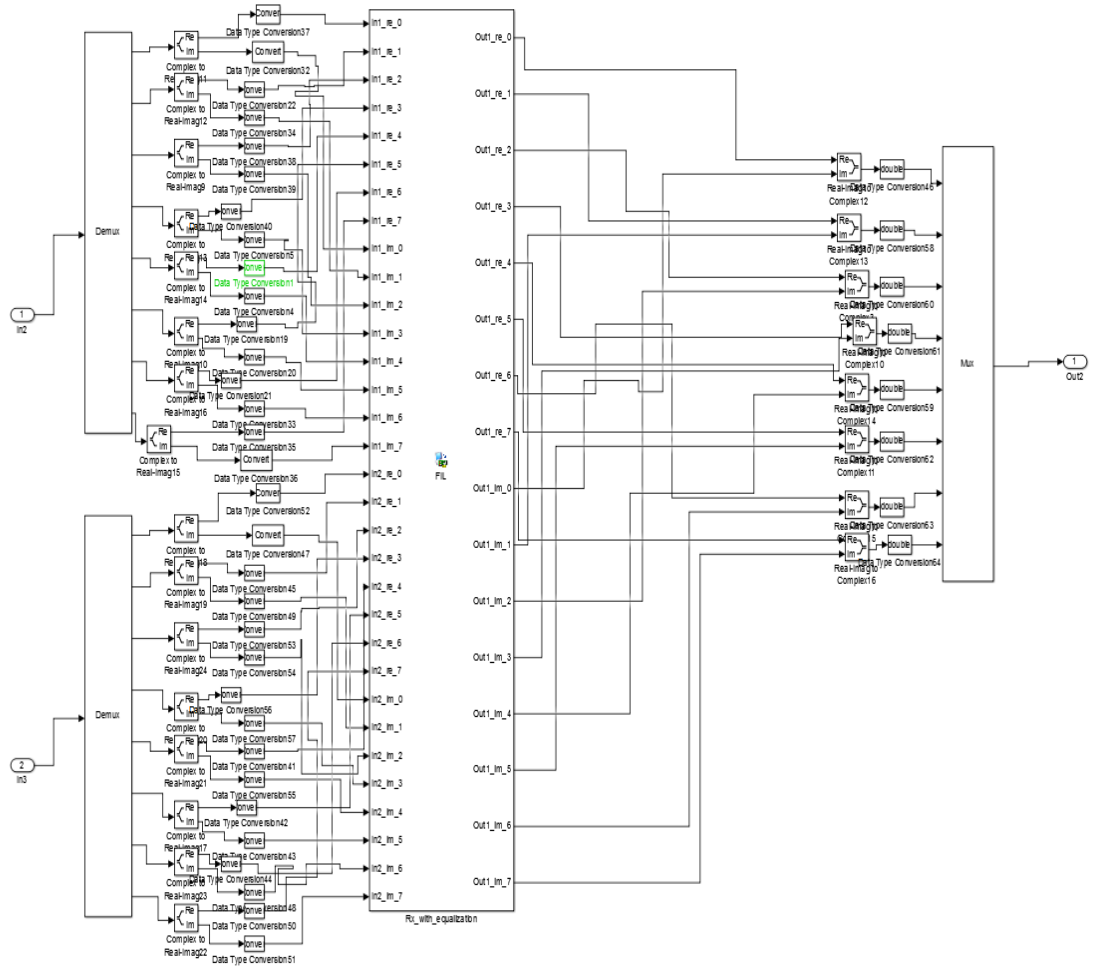
Figure 6.8: *FPGA-in-the-LOOP of Receiver with Equalization of FrFT -based OFDM system .*
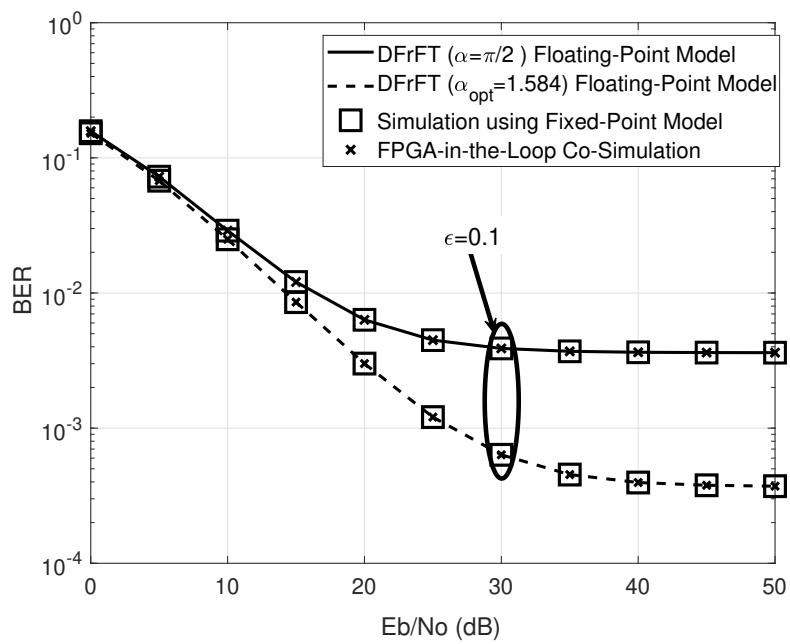
Figure 6.9: *BER comparison for DFT- and DFrFT-based OFDM BPSK transmission over a 2-tap equal power delay profile frequency selective Rayleigh fading channel at CFO = 0.1.*

Implementation of OFDM in LTE PHY and Its Limitations

I N this chapter we described the implementation of OFDM system in the framework of LTE PHY design using MathWorks/Simulink Toolbox. We perform the estimation of CFO and channel estimation by following LTE frame structure and also perform the detection of primary and secondary synchronization signal. Finally limitations of LTE PHY are also given.

7.1 Introduction

Starting from "3GPP Releases 8" specification, we develop the Simulink model of LTE downlink at 20MHz by following the frame structure of FDD shown in Fig. 7.1. The detail frame structure of FDD is given in Fig. 7.1. It only shows the structure of radio frame. Description of radio frame as:

- Time duration of radio frame is 10 ms.

- Number of samples in radio frame (10 ms) is 307200 (307.200 K) samples. This means that the number of samples per second is 307200 x 100 = 30.72 M samples/sec.

- Number of sub-frames in radio frame is 10.

- Number of slots in one sub-frames is 2. This means that we have 20 slots within radio frame.
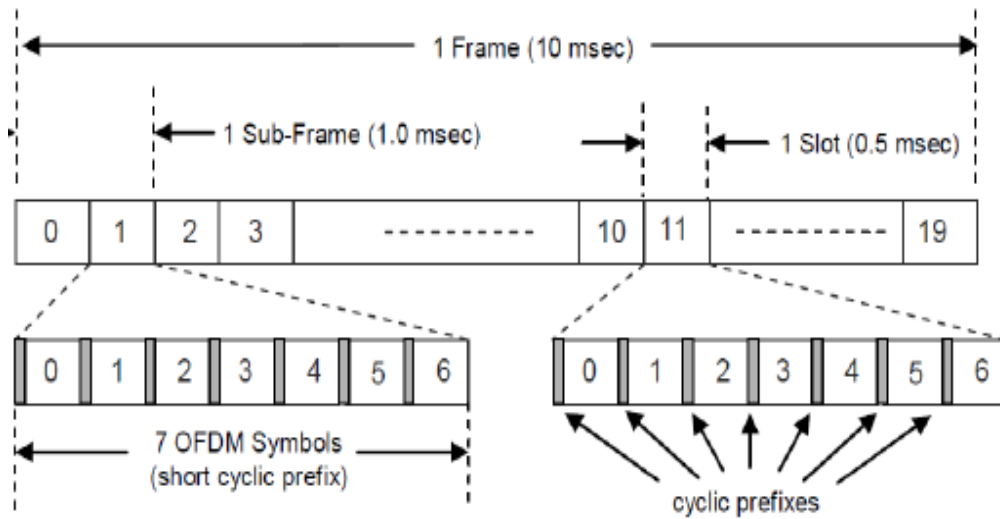
Figure 7.1: *Frame structure of LTE in FDD mode.*

In first slot of the radio frame there are 7 OFDM symbols. A detailed description of the slot is shown in Figure 7.2

7.2   Resource grid generation

By following the same Frame structure of FDD mode, a Simulink model of the 1st sub-frame of 1st slot of resource grid is developed. The detail resource grid of first sub-frame is shown in Fig. 7.3. After the generation of the resource grid, our goal is to generate the corresponding signal such as reference signal, primary synchronization signal, secondary synchronization signal and data. After generation of these signals filling of corresponding signals into resource grid is done. A detailed description of these signals are given below.

Five types of downlink reference signals are defined:

- Cell-specific reference signals (CRS)

- MBSFN reference signals

- UE-specific reference signals (DM-RS)

- Positioning reference signals (PRS)

- CSI reference signals (CSI-RS)

Figure 7.2: *1st slot of LTE radio frame.*
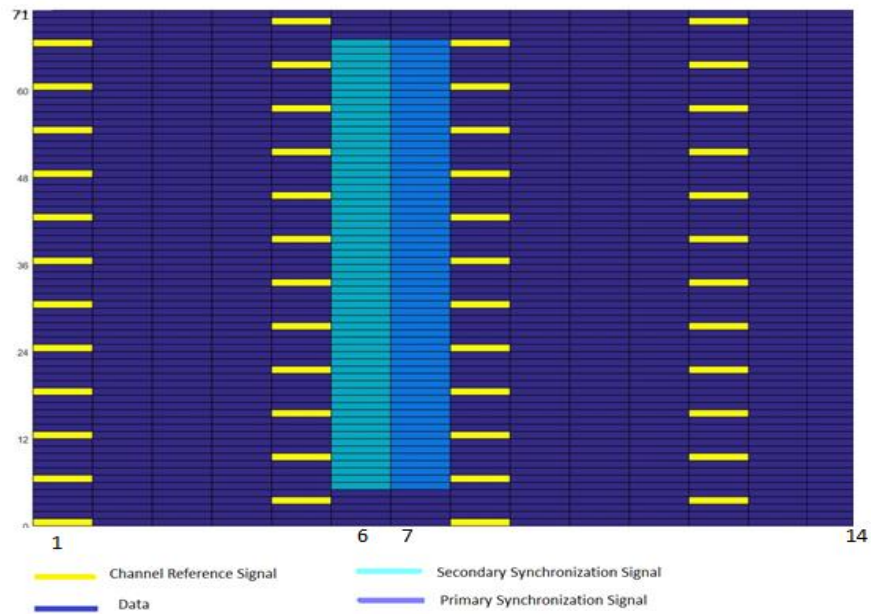
Figure 7.3: *Resource grid of 1st slot of radio frame.*

109
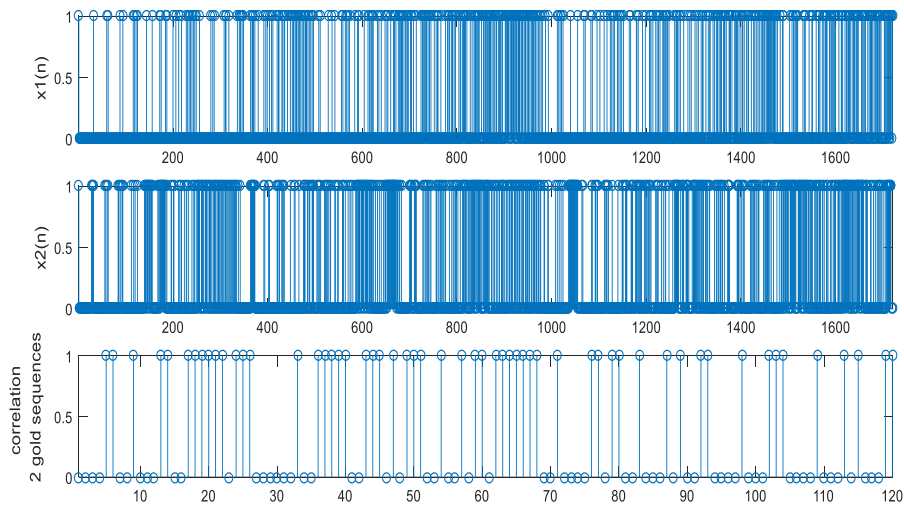
Figure 7.4: *Cell-specific reference signals.*

7.2.1 Cell-specific reference signals

The cell specific reference signal is transmitted in all downlink sub-frames. These signals are transmitted on one or more then one antenna ports ranging 0 to 3 in the LTE. In this chapter, we are considered only single antenna port. The cell-specific reference signal is a kind of Gold sequence known as pseudo random sequence. Reference signal is generated by combining the two Gold Sequences. Generation of two gold sequence represented as $x_1(n)$ and $x_2(n)$ and correlation of $x_1(n)$ and $x_2(n)$ results into gold sequences shown in Fig. 7.4, to be used as a cell- specific reference [91].

7.2.2 Primary synchronization signal

Primary synchronization signal (PSS) is a specific physical layer signal that is used for frame synchronization with the following characteristics:

- Mapped to 72 sub-carriers (6 resource blocks), centered on DC sub-carrier.

- PSS equation generation using Zadoff-Chu Sequence.

- Used for Downlink Frame Synchronization

- Used for determining physical Cell ID

110
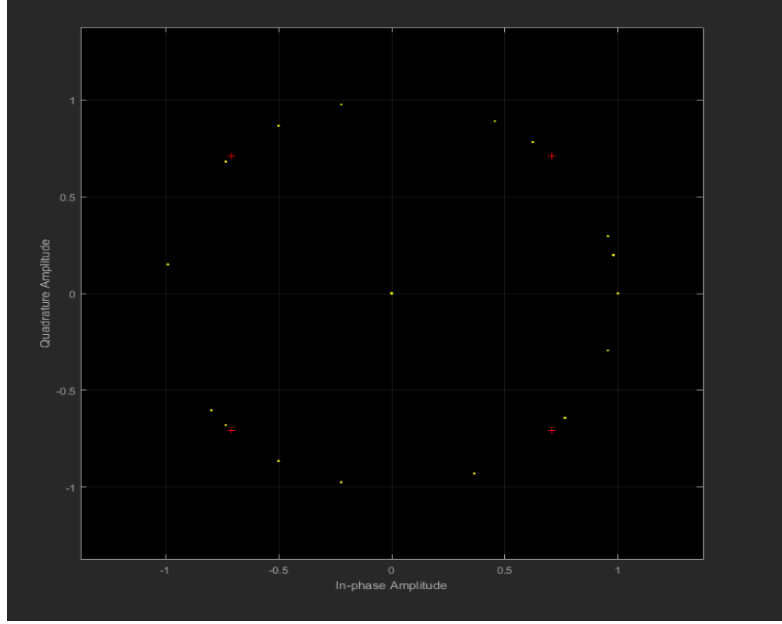
Figure 7.5: *Zadoff-Chu mapping on* 62 *sub-carriers and centered on DC sub-carrier.*

The sequence $d(n)$ used for the PSS generated from a frequency-domain Zadoff-Chu sequence according to

$$
d(n) = \begin{cases}
e^{\frac{-j\pi u n(n+1)}{63}}, & n = 0, \ldots, 30 \\
e^{\frac{-j\pi u (n+1)(n+2)}{63}}, & n = 31, \ldots, 61,
\end{cases}
\tag{7.1}
$$

where u is the root sequence index (root: 25, 29 and 34) of Zadoff-Chu. The constellation diagram of the PSS sequence is shown in Fig. 7.6 After generation of PSS sequence we need to perform the correlation between the different roots such as 25, 29 and 34. The results of correlation are shown in Figure 7.6.

7.2.3 Secondary synchronization signal

Secondary synchronization signal (SSS) is a specific physical layer signal also used for frame synchronization and for finding the group ID with the following characteristics:

- Mapped to 72 sub-carriers (6 resource blocks), centered around the sub-carrier

- The sequence of SSS in sub-frame 0 and the one in sub-frame 5 are different from each other

- Made up of 62 Scrambling Sequence (based on m-sequence)

- The value in odd indexed resource element and the one in even indexed resource elements generated by different equations

111
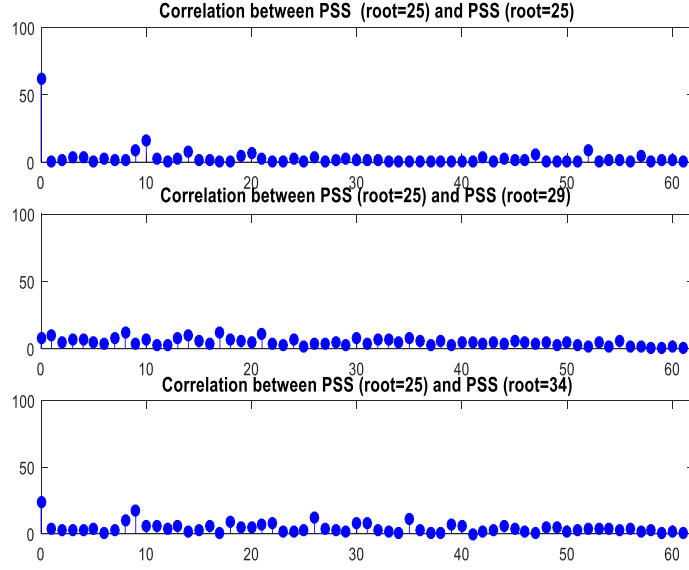
Figure 7.6: *Correlation between the different roots.*

The sequence $d(0), \ldots, d(61)$ used for the second synchronization signal is an interleaved concatenation of two length-31 binary sequences. The concatenated sequence is scrambled with a scrambling sequence given by the PSS. The combination of two length-31 sequences defining the secondary synchronization signal differs between sub-frame 0 and sub-frame 5 according to

$$d(2n) = \begin{cases} S_0^{m_0}(n)c_0(n), & \text{in sub-frame } 0 \\ S_1^{m_1}(n)c_0(n), & \text{in sub-frame } 5, \end{cases} \quad (7.2)$$

$$d(2n+1) = \begin{cases} S_1^{m_1}(n)c_1(n)z_1^{m_0}(n), & \text{in sub-frame } 0 \\ S_1^{m_1}(n)c_0(n)z_1^{m_1}(n), & \text{in sub-frame } 5, \end{cases} \quad (7.3)$$

where $0 \leq n \leq 30$. The indices m_0 and m_1 are derived from the physical-layer cell identity and two sequences $s_0^{m_0}(n)$ and $S_1^{m_1}(n)$ are defined as two different cyclic shifts of the m-sequence. Figure 7.7, we can see that left plot of constellation diagram and right plot of SSS generated by a kind of scrambling sequence (based on m-sequence). After the generation of PSS, SSS sequences and cell-specific reference signals, we mapped these sequences along with the data in resource grid as shown in Fig. 7.5.

7.3 Development of TTI frame using Simulink

After mapping of synchronization signal, reference signal, data, we developed the Simulink model of LTE for 1st sub-frame. The complete Simulink model of LTE is shown in Figure 7.8.
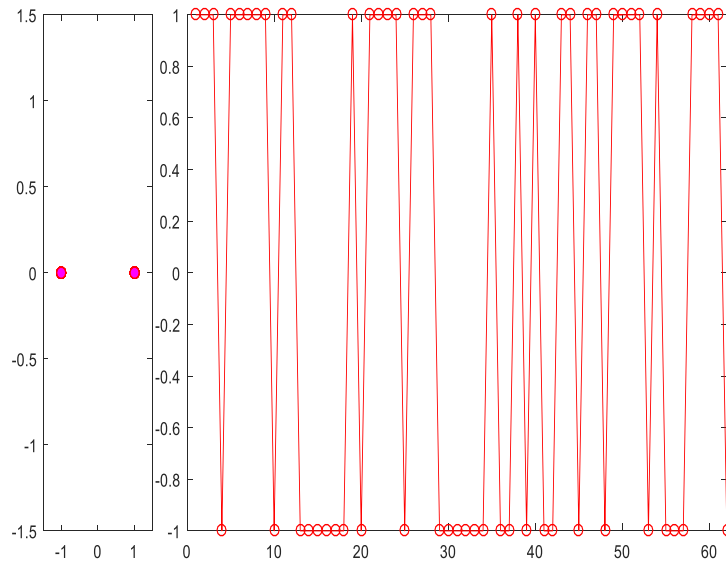
Figure 7.7: *SSS signal of 62 symbols.*
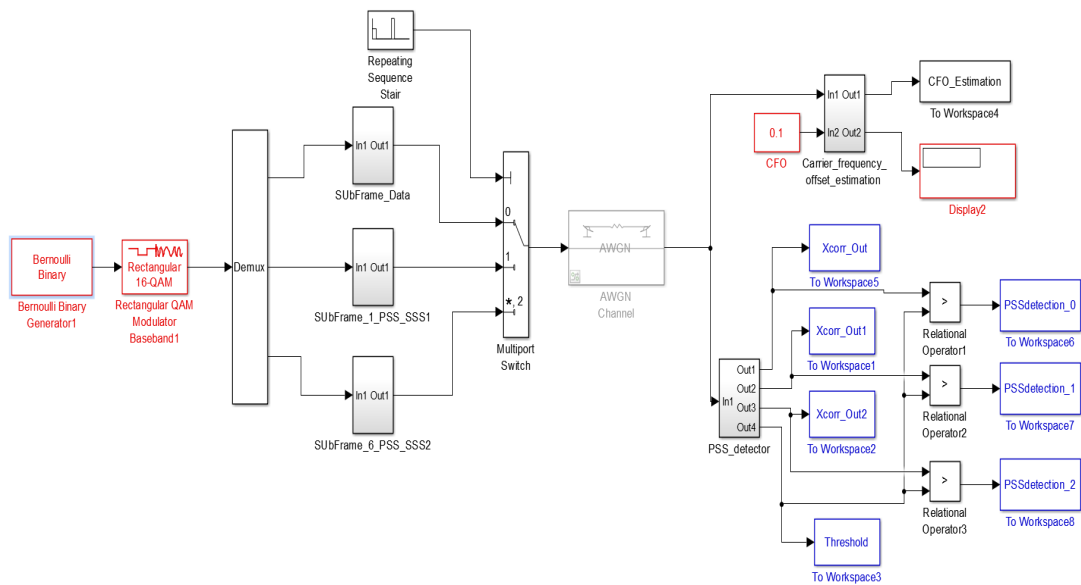
Figure 7.8: *Simulink model of LTE for 1st sub-frame.*

113

After the development of Simulink model of LTE for FDD, our goal is to address the three major synchronization aspects in LTE using Primary and Secondary synchronization signal:

- Symbol and frame timing acquisition, to determine the correct symbol start position.

- Carrier frequency synchronization, which is required to reduce or compensate the effect of frequency errors arising from a mismatch of local oscillators between transmitter and the receiver and due to Doppler shift.

- Sampling clock synchronization.

7.3.1   Symbol Start Position

Incorrect Symbol timing synchronization is one of the synchronization problems that LTE system needs to solve. Because the receiver does not know the correct starting position of the OFDM symbol. Symbol timing synchronization is used to find the correct starting position of OFDM symbol. Due to the presence of the CP, LTE system on symbol synchronization requirements is not as stringent as other communication systems.

As long as the starting point for the FFT window falls into the range of CP, the receiver can demodulate received data correctly and does not cause inter-symbol interference. Symbol timing synchronization algorithms can be broadly divided intoe two categories: first, that is based on the data aided algorithm of training sequence, that is, the transmitting end inserts some known pilot frequency information in the transmitted data frame to the receiving end and the known signal correlation operation will complete the synchronization. The second is to use CP with blind estimation algorithm. Therefore, it is also known as synchronization algorithm algorithms which is based on CP. In our case we follow the CP based synchronization. The correct symbol starting position is shown in Figure 7.9. From Fig. 7.9, it is clearly visible that if we consider one OFDM symbol of length 2048, so peak is started from 2048 and finished at 2192 because we added the CP of length 144. Therfore, starting point of the DFT window lies on the length of CP part for correct OFDM symbol start.

7.3.2   PSS Sequence Detection

PSS detection is time-based, because the complexity of this method does not allow to go in frequency domain for each inter-correlation phase. The PSS detection subsystem is split into three further subsystems:

- Cross Correlation,

- Peak Detection,

- Determine Cell-ID and Offset
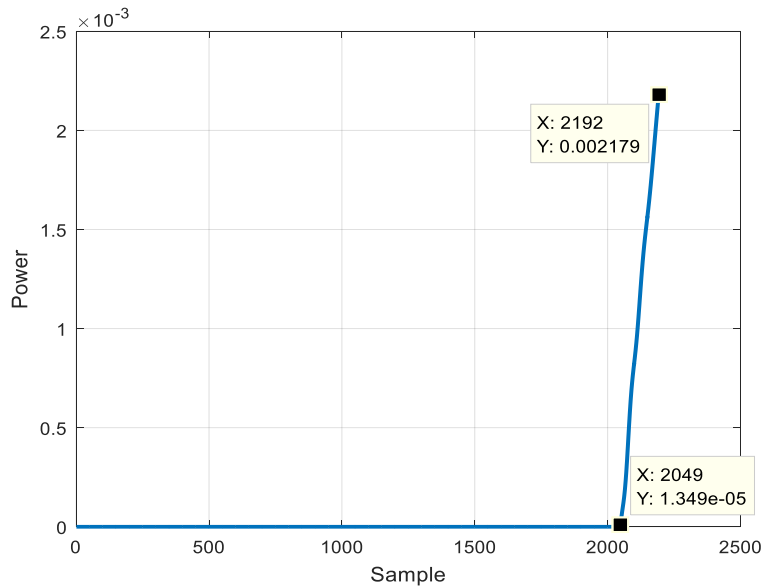
Figure 7.9: *Finding of correct symbol start position known as coarse timing synchronization.*

Cross correlation

The Cross correlation subsystem is shown in Figure 7.10. Furthermore, the received signal is decimated with 16 factor before being buffered, thus dividing the number of processed samples by the same number. The sampling frequency changes from 30.72 MHz (the maximum sample frequency) to 1.92 MHz because the PSS sequence occupies only 945 kHz (63 sub-carriers using a 15 kHz spacing), no spectral aliasing will be noticed. Cross correlates the received signal with each of the three possible time domain PSS sequences with diffent root, i.e. 25, 29, and 34. After computing the square magnitude of each of the cross-correlations. Because the primary sequence detection is done without a priori knowledge of the channel, the system uses a non-coherent correlator.

$$y(m) = \sum_{i=0}^{N-1} Y(i+m)S^*(i) \tag{7.4}$$

where m is time offset, $N = \max\left(size(y(i)), size(s(i)), Y(i)\right)$ is the decimated signal value and $S(i)$ is the PSS sequence in time domain with different roots.

Peak Detection

The peak detection is done by comparing the value of inter-correlation, between the received signal and PSS sequence, with a threshold. The peak detection subsystem checks if the cross-correlation output from each of the three exceeds the threshold value

After the correlation the result is compared with a threshold and if correlation output is higher than the threshold then peak is detected. From Fig. 7.12, it gives the detection

115
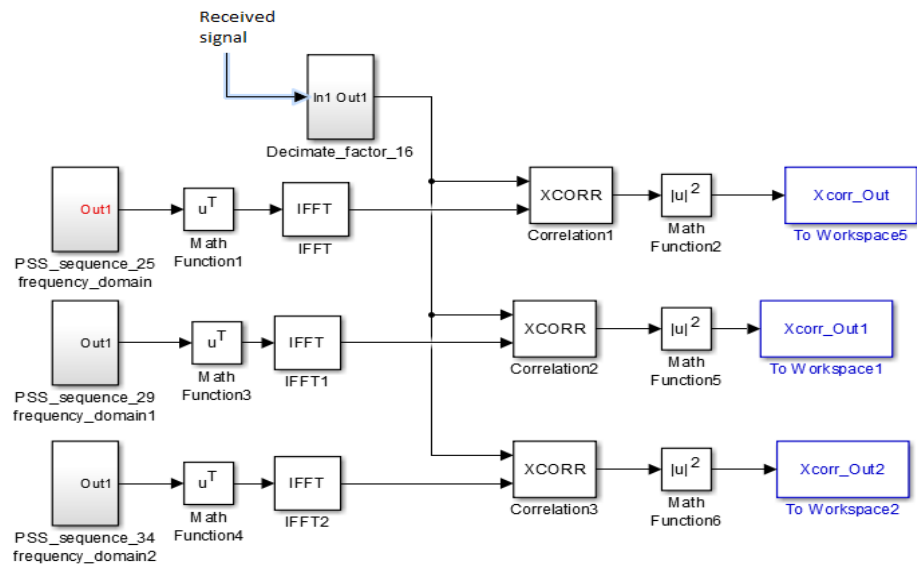
Figure 7.10: *Simulink model of cross correlation between the different root PSS sequence.*
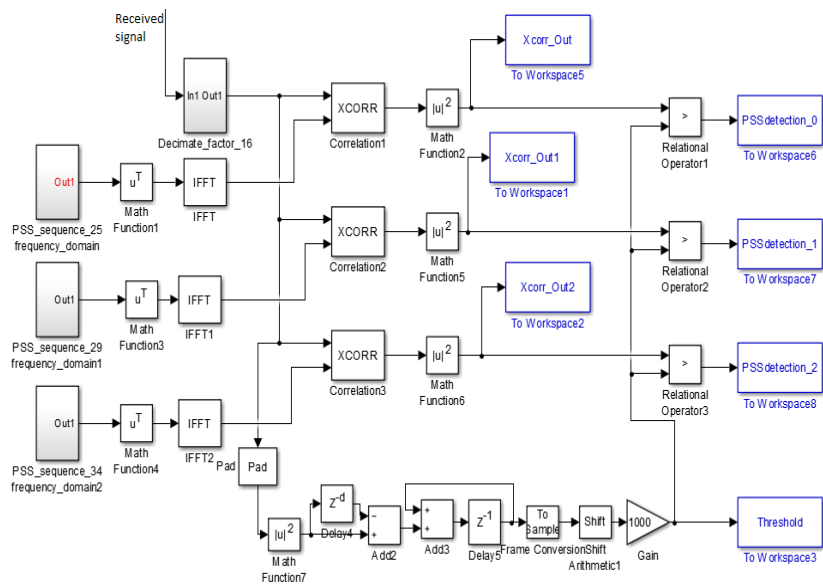
Figure 7.11: *Simulink model of cross correlation between the different root PSS sequence and corresponding peak detection.*

116

Figure 7.12: *Simulink model of cross correlation between the PSS sequence of root* 25 *at transmitter and receiver.*

of peak.

Figure 7.15 shows the output of the PSS detection, in power plot of cross-correlation of the received signal with the detected PSS sequence over time. The average threshold signal is also plotted to illustrate the identification process. The visible peaks which exceed the threshold indicate that this PSS sequence has been detected.

Carrier Frequency Offset Estimation:

The frequency offset is measured by exploiting the CP of OFDM signal. The CP correlator sub-system generates a complex valued correlation signal which has peak magnitude at the end of each OFDM symbol. The phase angles of the correlation signal at peak is proportional to the frequency offset. The correlation signal is converted to magnitude and angle values by the using rectangular to polar sub-system. The angle of maximum sub-system searches for maximum correlation magnitude and records the corresponding phase angle every 960 samples. Finally, the phase angles are filtered with a simple IIR low pass filter to smooth the result, generating the final frequency estimate as shown in Fig. 7.16.

7.4 Problem associated with OFDM based LTE PHY

New waveforms for new generation have been designed to overcome some restrictions in previous technology or increase the spectrum efficiency. It is likely that the new waveform will overcome a restriction of current 4th generation waveform based on
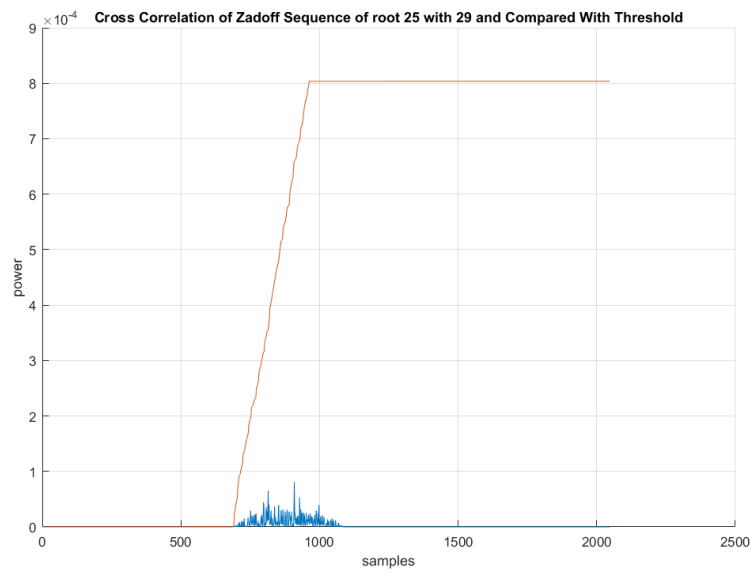
Figure 7.13: *Cross correlation between the PSS sequence of root* 25 *at transmitter with* 29 *at receiver.*
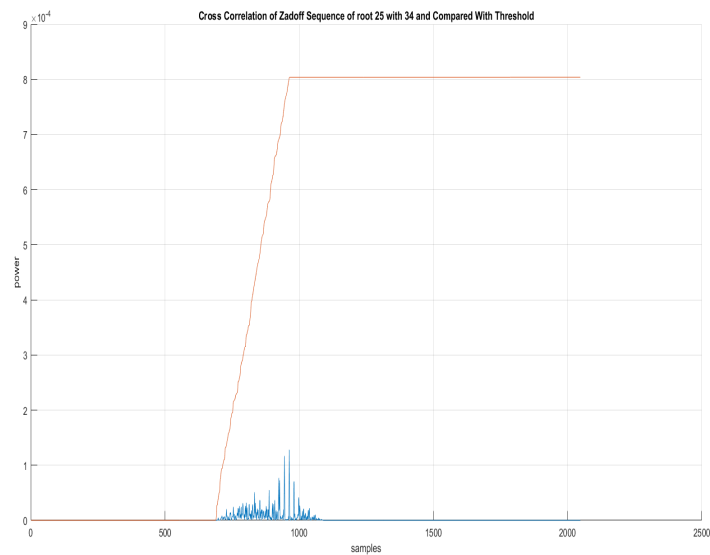
Figure 7.14: *Cross correlation between the PSS sequence of root* 25 *at transmitter with* 34 *at receiver.*

Figure 7.15: *PSS sequence detection and determination of Cell-ID without presence of Noise.*
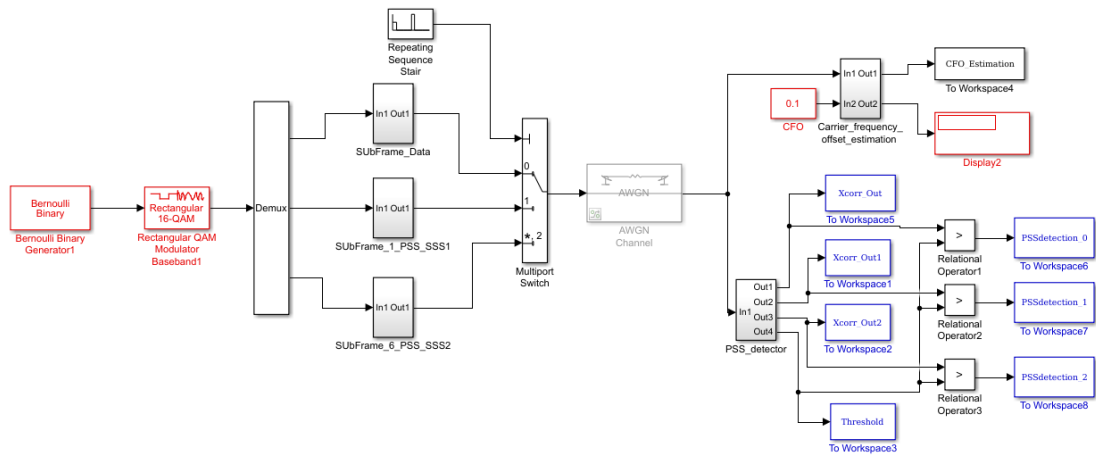
Figure 7.16: *Simulink model for cross correlation along with CFO estimation and companions*
.
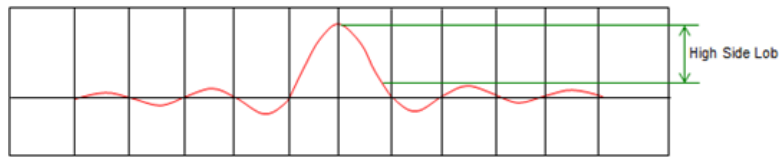
Figure 7.17: *Side lobe of OFDM sub-carrier.*

OFDM and possibly improve spectral efficiency as well. The major problem of current LTE Waveform is listed below.

- Cyclic prefix overhead

- Less tolerance to inter sub-carrier interference

- Large PAPR (peak to average power ratio)

- High out of band side lobe

7.4.1 Cyclic prefix overhead

In terms of symbol structure of LTE downlink, one LTE radio frame is made up of 20 slots. As we know every OFDM symbol has its own CP. Even though this CP plays important roles in current LTE strictly speaking it is a kind of overhead. Just by simple calculation at 20 MHz, you would notice the overhead is around 7.2% (160/(160+2048)) in case of first OFDM in a slot and is around 6.5 % (144/(144+2048)) in other OFDM symbols. Some of future waveform candidates tries to completely remove it, but many of the candidates still use the CP with various lengths.

7.4.2 Less tolerance to inter sub-carrier interference

Currently LTE OFDM is based on the assumption that all the sub-carries are strictly orthogonal to each other. There would be serious performance degradation when the orthogonality is disturbed between the sub-carriers.

7.4.3 Peak to average power ratio

Due to this problem, it requires high linearity for output power amplifier. This reduces UE power amplifier efficiency and increase energy consumption.

7.4.4 High out of band side lobe

As we know, the current OFDM symbol is made up of sub carriers. The first problem of this sub-carrier is that it has big side lobes as shown in Figure 7.17. This is a kind of leakage and this leakage can act as source of interference to neighbouring sub-carriers. To reduce the effect of interference of a sub carrier, it is strictly required that the space
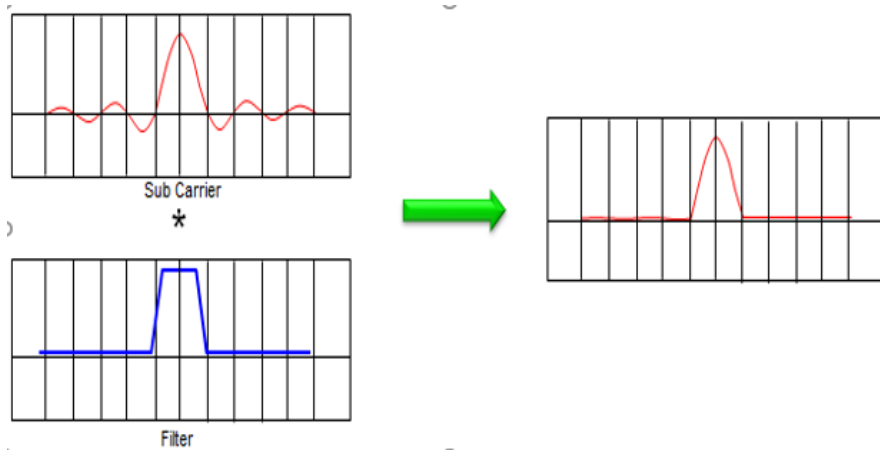
Figure 7.18: *Reduction in the side lob after the filtering of the received signal.*

between the sub-carriers need to be strictly determined in such a way that each sub-carrier is orthogonal to each other. As long as the orthogonality is maintained, we can minimize the interference between sub carriers. There have been several different techniques that would reduce these problems. The most common concept is to design a specific filter and perform filtering to each sub carrier or a group of sub carriers (sub-band) as shown in Fig. 7.18.

7.5 Summary

In this chapter we have studied about the development of the Simulink model based on the LTE PHY design. In this, we study about the primary and secondary synchronization signal and also found the correct starting position of OFDM symbol at each symbol on the frame. Moreover, also developed the estimator for CFO estimation. Finally, we have discussed about the detail of the problem associated with LTE PHY design and motivation towards the new waveforms which is based on filtering technique.

Part II

Performance Evaluation of New Waveform Based on GFDM System

Literature Survey and Problem Formulation

T HIS chapter consists of motivation towards the new waveforms, then details of FBMC and GFDM starting from the historical development of these waveforms after that mathematical formulation of these waveforms and its limitations. A Final survey related to synchronization issues in GFDM system is given.

8.1 Motivation towards the New Waveforms

Currently, ITU has categorized the usage scenarios IMT into three main groups [3]- [4]: eMBB [6], mMTC [7], and URLLC [8]. These scenarios require massive connectivity with low round-trip latency and high reliability with high system throughput and improved spectral efficiency for the implementation of future cellular networks [3]- [4].

However, 4G cellular transmission schemes based on LTE use OFDM in PHY design, where in PHY design a fixed set of waveform parameters, including sub-carrier spacing and length of CP, is uniformly applied across the entire system bandwidth [6]. A main issue of such a fixed design is the lack of flexibility to support mixed services with different waveform parameters within one carrier, which is a key requirements of PHY design of future cellular networks [3,4,7,13,126]. Additionally, OOB emission in frequency-domain (FD) is introduced by time-domain (TD) rectangular pulse shaping filter [41]. Also, OFDM signal with one CP per symbol may have a prohibitive low spectral efficiency and also increase the OFDM symbol duration [13].

For this reason, we look for new waveforms that are able to support variable and customizable pulse shaping filters in order to achieve a better trade-off between time-

domain and frequency-domain localization, which is one of the research priorities [126]. To this aim, in March 2016, a study item was approved by *3GPP* to investigate the potential technologies for 5th generation new radio (NR) [127]. The main reason of naming it "new radio" is that this air interface will not be backward compatible with any 4G standards such as LTE-Advanced-pro. This new radio interface can be deployed stand-alone, *i.e.*, an independent network not relying on other networks. NR can also be deployed in non-stand-alone fashion, *i.e.*, along with LTE-Advanced-pro, since LTE evolution is also considered as a part of 5G. At the physical layer, potential technical areas of NR include multiple access, waveform, channel coding, frame structure, MIMO, device-to-device (D2D), vehicle-to-vehicle (V2V), unlicensed spectrum, etc. This study item of NR under *(Phase 1)* is concluded by March 2017, followed by the work item stage *(Phase 2)*. Phase 1 aims to specify basic functionalities of NR that can partially fulfill the performance requirements of 5G. Its specification work was completed by June 2018 and this would make it possible to deploy the first 5G network by around 2020. It became clear that not all the technologies can be specified in Phase 1, because some of features are not considered as so urgent until 2020.

The waveforms discussed in this Thesis are broadly classified into two categories [4]: legacy OFDM transceivers supported [19] and new transceivers required [9,20,21]. In part-I of Thesis, we focused on the **legacy OFDM transceivers** system model, now in Part-II, we are going to focus on the **new transceiver structures** that are different from CP-based OFDM. The waveforms in this category include FBMC [24] and GFDM [8].

8.2 FBMC

FBMC is one of the well-known multi-carrier modulation schemes in the literature which is also discussed as a future wireless cellular system. FBMC offers a great advantage of pulse shaping on each sub-carrier and facilitates flexible use of spectral resources along with meeting various system requirements, *e.g.*, low latency, multiple access, etc. This is also an advantage for making signal robust against channel effects, *i.e.*, dispersion in time and frequency domain. However, pulse shaping is one of the important choices to use in this kind of waveforms. Many other pulse shaping filters are also investigated to cope with various effects of channel and provide a reliable system design based on different scenarios [128].

8.2.1   Historical development of FBMC

FBMC technique was first developed in mid-1960s by **Chang** *et.al.* [129], for signaling a parallel set of PAM symbol sequences through a bank of overlapping filters within a minimum bandwidth. To transmit PAM symbols in a bandwidth-efficient manner, **Chang** *et.al.* proposed vestigial sideband signaling for sub-carrier sequences. Furthermore, **Saltzberg** *et.al.* [130] extended for transmission of QAM symbols in a double-sideband modulated format. In order to have efficient bandwidth utilization, **Saltzberg** *et.al.* mentioned that the in-phase and quadrature components of each QAM
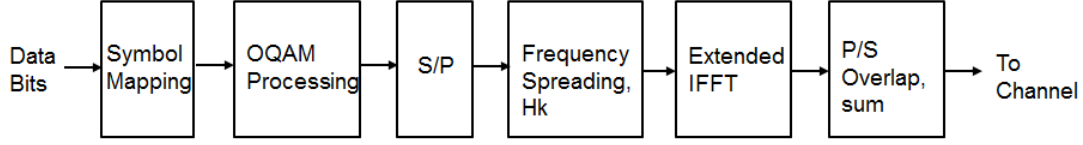
Figure 8.1: *Transmitter section of FBMC system model .*

symbol should be time staggered by half a symbol interval. Moreover, implementation of [130] through polyphase structures was first introduced in [131]. Another key development proposed in [132] is that method given in [129], [130] could be adopted to match channel variations in doubly dispersive channels and, hence, minimized ISI and ICI. However, **Saltzberg***et.al.* [130] method has received a broad attention in the literature and has been given different names. Most authors have used the name off-set QAM (OQAM) to reflect the fact that the in-phase and quadrature components are transmitted with a time offset with respect to each other. Moreover, to emphasize the multi-carrier feature of the method, the suffix OFDM has been added, hence, the name OQAM-OFDM. Others have chosen to call it staggered QAM (SQAM), equivalently SQAM-OFDM. Finally, we can say there are three type of FBMC systems:

1. CMT: based on original idea given by **Chang** *et.al.* [129];

2. SMT: based on the extension made by **Saltzberg** *et.al.* [130]

3. FMT: based on the conventional method FDM [133].

8.2.2 Mathematical formulation of FBMC

In this sub-section, the mathematical details of FBMC transmitter and receiver are given.

Transmitter model

Figure 8.1 reports the block diagram of complex FBMC filter. The prototype filter is the one used for the zero frequency carrier and is the basis for other sub-carrier filters. At the transmitter side, the discrete time FBMC signal is written as

$$s(m) = \sum_{m=0}^{M-1} \sum_{n \in Z} a_{k,n} g[m - nM/2] e^{j\frac{2\pi}{M}k(M-D/2)} e^{j\phi_{k,n}}, \quad (8.1)$$

where M is an odd number of sub-carriers, $g[m]$ is the prototype filter taking values in real field, $D/2$ is the delay term which depends on the length L_g of $g[m]$. We have $D = KM - 1$ and $L_g = KM$, where K is the overlapping factor. The transmitted symbols $< a_{k,n} >$ are the real or the imaginary parts of QAM symbols. The additional phase term $\phi_{k,n}$ is given by

$$\phi_{k,n} = \frac{\pi}{2}(n + k) - \pi nk \quad (8.2)$$
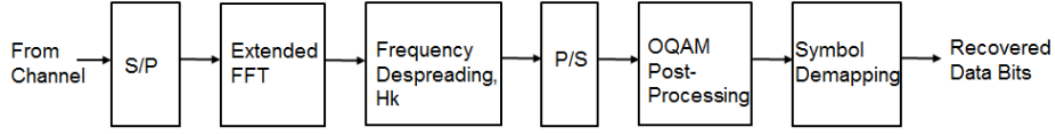
Figure 8.2: *Receiver section of FBMC system model .*

The current FBMC implementation uses frequency spreading. It uses an $M \times K$ length IFFT with symbols overlapped with a delay of $N/2$, where N is the number of sub-carriers.

Receiver model

The receiver implements a basic FBMC demodulator as shown in Fig. 8.2 for the chosen configuration in the absence of a channel. The processing includes matched filtering followed by OQAM separation to form the received data symbols. These are demapped to bits and the resultant bit error rate is determined. In the presence of a channel, linear multi-tap equalizers may be used to mitigate the effects of frequency-selective fading. Receiver side implementation applies dual operations with respect to the ones performed by the constituent blocks of the transmitter. The IFFT must be replaced by an FFT as shown in Figure 8.2. If $r(k)$ is the received signal and $\hat{s}_n(m)$ are the recovered PAM symbols, then we can written as

$$u_n(m) = \sum_{l=0}^{K-1} g(k + lM)r(k + M/2(2l + n)) \tag{8.3}$$

$$U_n(m) = C_n(m) \sum_{k=0}^{M-1} u_n(m)e^{j2\pi \frac{km}{M}} \tag{8.4}$$

$$\hat{s}_n(m) = \Re\left(\phi_{k,n}^* U_n(m)\right) \tag{8.5}$$

where $*$ represents the complex conjugate operation, and $C_n(m)$ is zero forcing (ZF) equalizer coefficient to compensate the impairments introduced by the channel.

8.2.3 Summary

In FBMC modulation the use of a prototype pulse shaping filter on each sub-carrier is proposed to minimize OOB emission. Several works in the literature focus on the design of the pulse shaping filters for FBMC with the aim of minimizing the OOB emission and improving spectral efficiency [46, 134]. However, FBMC is not suitable for short burst transmissions because the length of pulse shaping filter is quite long, which cause interference into its neighbouring sub-carriers and also higher complexity

and latency [40]. Apart from these challenges, one of the main drawback of FBMC is that it does not provide backward compatibility with current MCM schemes used in LTE, *i.e.*, OFDM and DFT-s-OFDM.

8.3 GFDM

GFDM is based on a block based structure consisting of several OFDM symbols and a CP that is added at the beginning of each block instead at the beginning of each symbol, as happens in OFDM. The sub-carriers are pulse shaped by circular filtering which makes it applicable for short burst transmission. Employing circular filter in GFDM with windowing or guard symbol insertion reduces the OOB emissions compared to OFDM [41]. Moreover, since a tail biting technique is used in GFDM, this makes the CP length independent of transmit and receive filters lengths [46]. This allows reducing the overhead caused by the CP, thus increasing the spectral efficiency. The flexible frame structure of GFDM allows, by changing the number of time slots and sub-carriers in a frame, covering both conventional CP-OFDM and DFT-s-OFDM. This allows for backward compatibility with current MCM scheme used in LTE [8].

8.3.1 Historical development of GFDM

A flexible multi-carrier modulation scheme, named GFDM, has also been proposed for the air interface [135]. GFDM provides the promising solution due to its flexibility with different scenario requirements. In case of the real-time applications, the signal length must be reduced to fulfill certain latency requirements [136]. Due to its block based structure of GFDM with MK samples, where K sub-carriers and each sub-carrier carry M sub-symbols, it is possible to design the time frequency structure to match the time constraints [135]. GFDM provides flexibility in the choice of pulse-shaping filter and its impact on the OOB emissions and the SER performance. GFDM also allows flexibility in their frequency and time characteristics. Thus, the scheme retains all main benefits of OFDM at the cost of some additional implementation complexity. The overhead is kept small by adding a single CP for an entire block that contains multiple sub-symbols. This benefit can be used to improve the spectral efficiency of the system or it can be traded for an additional cyclic suffix (CS), which allows to relax the synchronization requirements of multiple users in an MTC scenario due to plateau effect in the autocorrelation, which introduces ambiguity and reduces the precision of the technique. Furthermore, all major synchronization algorithms developed for OFDM [84] can be adopted for GFDM. Hence GFDM aims at combining the flexibility and simplicity of OFDM with stronger interference reduction mechanisms

8.3.2 Mathematical formulation of GFDM

In this sub-section, mathematical detail of transmitter and receiver of the GFDM waveforms are given.
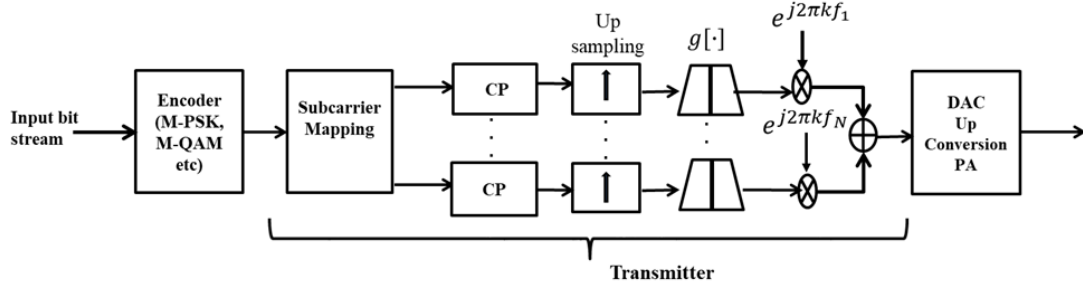
Figure 8.3: *Transmitter section of GFDM system model .*

Transmitter model

Figure 8.3 reports the block diagram of complex baseband equivalent model of transmitter section of GFDM system. The data vector $\mathbf{d}$ can be decomposed into K groups of M symbols according to

$$\mathbf{d} = \left[(\boldsymbol{d}_0)^T, (\mathbf{d}_1)^T, \ldots\ldots, (\mathbf{d}_{K-1})^T \right]^T \tag{8.6}$$

with

$$\mathbf{d}_k = [d_{k,0}, d_{k,1}, \ldots\ldots, d_{k,M-1}]^T \tag{8.7}$$

where $d_{k,m}$ corresponds to the QAM symbol transmitted on the kth subcarrier and mth subsymbol of the block and $(\cdot)^T$ denotes transposition. The time-duration of each data block $\mathbf{d}_k$ is MT_s and the sub-carrier spacing is equal to $1/MT_s$. In GFDM modulator, each $d_{k,m}$ is transmitted with corresponding pulse shaping filter

$$g_{k,m}[n] = g\left[(n-mk) \bmod N\right] e^{\frac{-j\,2\,\pi\,k\,n}{K}}, \tag{8.8}$$

where $g[n]$ is a prototype discrete-time impulse response and n is the sampling index. Note that, each $g_{k,m}[n]$ corresponds to a time and frequency shifted version of $g[n]$, where the complex exponential performs the shifting operation in frequency domain. The n-th entry of $MK \times 1$ transmitted vector $\mathbf{x}$ is given by

$$x[n] = \sum_{k=0}^{K-1} \sum_{m=0}^{M-1} d_{k,m} g_{k,m}[n], \quad n = 0, 1, \ldots\ldots\ldots KM-1. \tag{8.9}$$

Receiver model

The receiver system model of GFDM is shown in Fig. 8.4. In the literature, several standard receiver options for GFDM demodulator, the overall GFDM transceiver equation can be written as

$$\boldsymbol{y}_{eq} = \boldsymbol{H}^{-1}\boldsymbol{H}\boldsymbol{A}\boldsymbol{d} + \boldsymbol{H}^{-1}\boldsymbol{w} = \boldsymbol{A}\boldsymbol{d} + \tilde{\boldsymbol{w}} \tag{8.10}$$

130

Figure 8.4: *Receiver section of GFDM system model .*

as the received signal after channel equalization, linear demodulation of the signal can be expressed as

$$\widehat{d} = \mathbf{B}\boldsymbol{y}_{eq}, \tag{8.11}$$

where $\boldsymbol{y}_{eq}$ is the equalized signal in time-domain and **B** denotes the demodulator matrix for different receiver given below:

- **ZF**: $\boldsymbol{B}_{\text{ZF}} = \boldsymbol{A}^{-1}$ on the contrary completely removes any self-interference at the cost of enhancing the noise.

- **MF**: $\boldsymbol{B}_{\text{MF}} = \boldsymbol{A}^{H}$ maximizes the signal-to-noise ratio (SNR) per sub-carrier, but with the effect of introducing self-interference when a non-orthogonal transmit pulse is applied.

- **MMSE**: $\boldsymbol{B}_{\text{MMSE}} = (R_2(w) + \boldsymbol{A}^{H}\boldsymbol{H}^{H}\boldsymbol{H}\boldsymbol{A})^{-1}\boldsymbol{A}^{H}\boldsymbol{H}^{H}$ makes a trade-off between self-interference and noise enhancement. Here, $R_2(w)$ denotes the covariance matrix of the noise.

8.4 Survey of Synchronization issues in GFDM

The impact of synchronization errors, *i.e.*, CFO and STO, on MCM schemes under study for future cellular systems still remain that need to be investigated [137]. As it is well known, CFO corresponds to a mismatch between frequencies of local oscillators of transmitter and receiver. Its main consequence is the introduction of ICI, which significantly degrades the performance. Considering STO, which is caused by a sampling phase offset at the receiver, its main impairment is a phase rotation in the frequency domain that introduces ISI between subsequent OFDM symbols [138].

Several works available in literature are related to the performance analysis of GFDM system in the presence of synchronization errors [139]- [140]. In [139], Choi *et al.*, studied the effect of timing offset and CFO on the signal-to-interference ratio (SIR) for GFDM transmission over the AWGN channel through Monte Carlo simulations only. In [141], Gaspar *et al.* presented, for the first time, an analytical expression of the SER for the GFDM system with zero forcing receiver considering the same synchronization errors of [139] for BPSK modulation in case of transmission over the multipath

131

Rayleigh fading channel. Finally, in [140], Lim *et al.* extended [139] by including the effect phase noise and derived an analytical expression of the SIR performance for the AWGN channel. Motivated by this, in part II of thesis, we derive for the first time exact SEP expressions for GFDM system. We consider the case where matched filter (MF) is used at the receiver in the presence of CFO for transmission over AWGN and frequency selective Rayleigh fading channels.

Despite the above mentioned advantages of GFDM, another issues is the need of equalization, implemented by block-based processing in time or frequency domain, that is required even in the case of transmission over an ideal channel [8]. For an efficient implementation of GFDM receiver in time-domain, a relationship between the GFDM signal and DGT was proposed in [31]. In particular, it was shown that GFDM transmission and reception are equivalent to a finite discrete Gabor expansion and DGT in critical sampling, respectively. According to such a DGT interpretation, when the circular pulse shaping filters used at transmitter and receiver satisfy the Wexler-Raz condition, the transmitted signal and symbols of a GFDM signal define a DGT and IDGT pair. The Gabor interpretation allows for an efficient computation of the ZF and minimum mean-squared error receiving filters without resorting to matrix inversion. An optimal symbol-by-symbol detector can be used after the DGT-based receiver in case of ideal channel. An equivalent interpretation of the DGT receiver in frequency-domain was given in [1], which allows for signal recovery with lower complexity compared to the time-domain approach.

8.5 summary

In this chapter, we have discussed about the motivation towards the introduction of new waveforms, *i.e.*, FBMC and GFDM. As is well know that, GFDM is a block based multi-carrier modulation scheme that relies on the use of circular pulse shaping filters. GFDM is a block based multi-carrier modulation scheme that relies on the use of circular pulse shaping filters. This novel waveforms that provide the flexibility in the choosing of waveform design parameters so that different applications can be addressed by a single solution. This flexibility includes the partitioning of time and frequency resources.

CHAPTER 9

Impact of the Pulse Shaping

I_N this chapter we use improved Nyquist pulse shaping filters in the GFDM system. We also focus on the integration of GFDM in the time-frequency grid of the LTE-A system and then we analyze the impact of "Better than Nyquist" pulse shaping filters on OOB emission and SER. Moreover, we also considered the concept of the wavelet for better time-frequency localization of the pulse shaping filters by using the Meyer auxiliary function.

9.1 System Model

The block diagram of the considered GFDM transmission scheme is shown in Fig. 9.1. In this scheme the transmitter part includes several blocks. By using a matrix notation, the vector of input bits $\mathbf{b}$ is applied at the input of the encoder. The encoder splits the high bit-rate stream into a number of lower bit-rate streams and forms the encoded vector $\mathbf{b}_c$. The vector $\mathbf{b}_c$ is applied at the input of the mapper which gives at its output an $N \times 1$ data vector $\mathbf{d}$ whose elements take values from a complex constellation, *e.g.*, QAM. The data vector $\mathbf{d}$ is then applied at the input of the GFDM modulator that contains N elements. In the GFDM modulator, each $d_{k,m}$ is transmitted with the corresponding pulse shaping filter

$$g_{k,m}\left[n\right] = g\left[\left(n-mk\right)\ \mathrm{mod}\ N\right] e^{\frac{-j\ 2\ \pi\ k\ n}{K}},\qquad(9.1)$$

where $g\left[n\right]$ is a prototype discrete-time impulse response and n is the sampling index. Note that, each $g_{k,m}\left[n\right]$ corresponds to a time and frequency shifted version of $g\left[n\right]$,
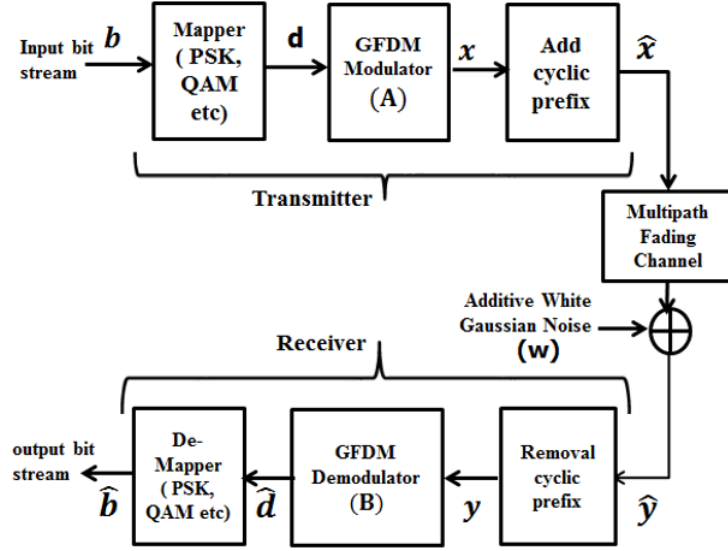
Figure 9.1: *System model of the GFDM system.*
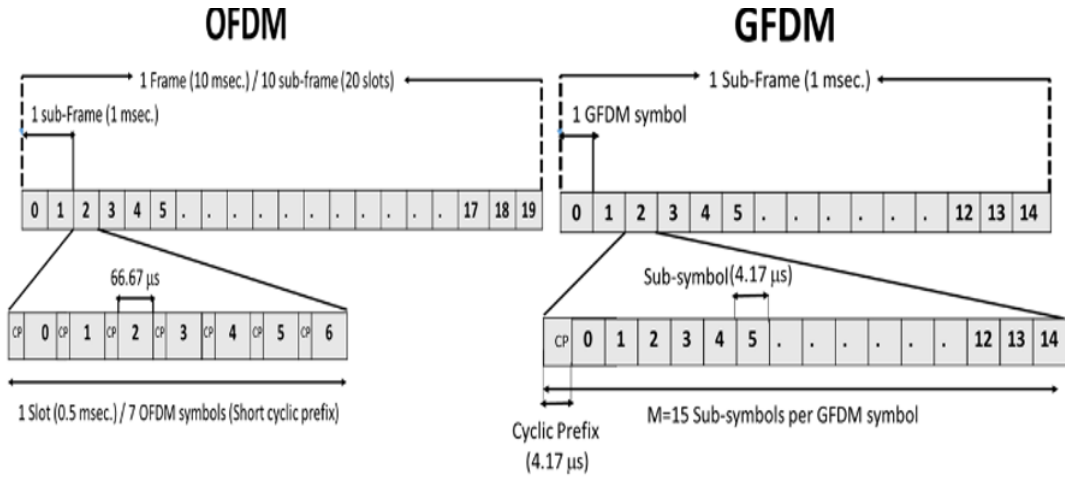
Figure 9.2: *GFDM frame aligned with LTE.*

where the complex exponential performs the shifting operation in the frequency domain. The n-th entry of the $MK \times 1$ transmitted vector $\mathbf{x}$ is given by

$$x[n] = \sum_{k=0}^{K-1} \sum_{m=0}^{M-1} d_{k,m} g_{k,m}[n], \quad n = 0, 1, \ldots \ldots KM-1. \tag{9.2}$$

Pulse shaping filter samples in the $KM \times 1$ vector $\mathbf{g}_{k,m} = [g_{k,m}[0], g_{k,m}[1], \cdots, g_{k,m}[MK-1]]^T$, allows to represent eq. (9.2) in matrix form as

$$\mathbf{x} = \mathbf{A}\mathbf{d} \tag{9.3}$$

Table 9.1: *Parameters for GFDM approach aligned with LTE grid.*

Parameter	Normal Mode
Sub-frame duration	1ms or 30,720 sample
GFDM symbol duration	$66.67\mu s$ or 2048 sample
Sub-symbol duration	$4.17\mu s$ or 128 sample
Sub-carrier spacing	240kHz
Sub-carrier bandwidth	240kHz
Sampling Freq. (Clock)	30.72MHz
Sub-carrier K	128
# active sub-carrier K_{on}	75
# sub-symbol per GFDM symbol M	15
# GFDM symbol per sub-frame	15
CP length	$4.17\mu s$ or 128 samples

where $\mathbf{A}$, a $KM \times KM$ matrix known as *GFDM modulation matrix*.

$$\mathbf{A} = \begin{bmatrix} \boldsymbol{g}_{0,0} \cdots \boldsymbol{g}_{K-1,0} \; \boldsymbol{g}_{0,1} \cdots \cdots \cdot \boldsymbol{g}_{K-1,1} & \boldsymbol{g}_{0,M-1} \cdots \boldsymbol{g}_{K-1,M-1} \end{bmatrix}. \qquad (9.4)$$

Before transmission a CP of length N_{CP} is added to form the vector
$\widehat{\boldsymbol{x}} = \left[\mathbf{x} \left(N - N_{CP} : N - 1 \right)^T, \mathbf{x}^T \right]^T.$

Transmission takes place over a multi-path channel defined by the following impulse response

$$h[n] = \sum_{k=0}^{L-1} h_k \delta[n-k], \qquad (9.5)$$

where h_k is the k-th complex coefficient and $L \geq 1$ denotes the length. At the receiver, we assume that the length of CP is higher than the maximum delay spread of the multi-path channel, that is, $L \leq N_{CP}$. Let $\mathbf{h}$ be a $(N \times 1)$ vector where the L first elements represent the channel impulse response and the last $N-L$ elements are zero. Under these assumptions, the received signal vector after removal of the CP is written as

$$\mathbf{y} = \mathbf{Hx} + \mathbf{w}, \qquad (9.6)$$

where $\mathbf{H}$ is an $N \times N$ circulant matrix built from $\mathbf{h}$ and $\mathbf{w}$ is the $N \times 1$ noise vector in which each entry is an i.i.d. zero mean complex Gaussian random variable with variance σ_w^2.
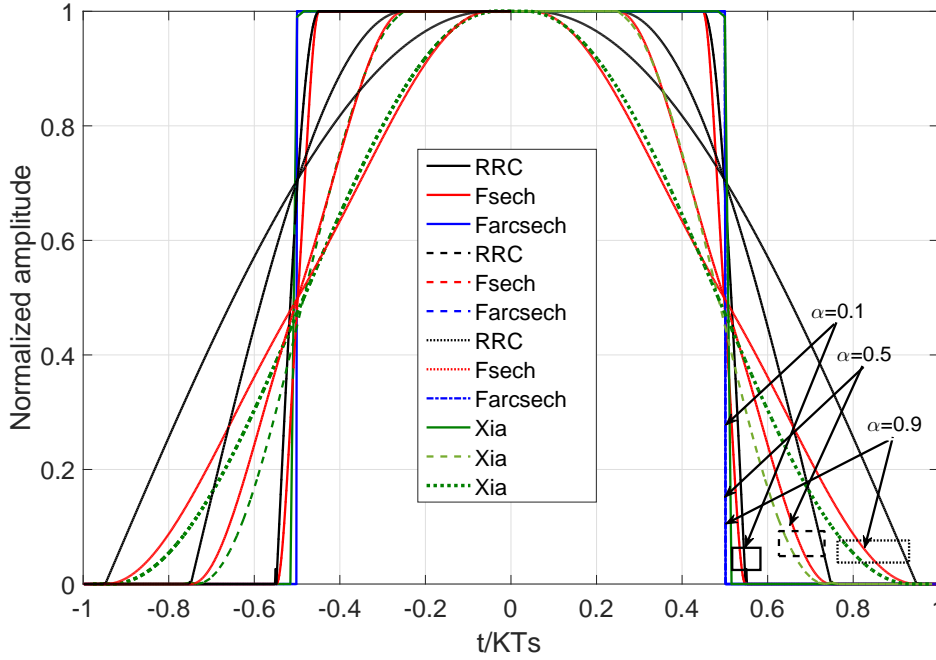
Figure 9.3: *Time-domain function of different pulse shaping filters.*

The estimated data vector after equalization is written as

$$\widehat{\mathbf{d}} = \mathbf{B}_{ZF} \boldsymbol{y}_{eq} = \mathbf{B}_{ZF}\mathbf{A}\mathbf{d} + \mathbf{B}_{ZF}\mathbf{H}^{-1}\mathbf{w}, \tag{9.7}$$

where $\boldsymbol{y}_{eq}$ is the equalized signal in time-domain. From the eq. (9.7) we observe that the ZF receiver completely removes self-interference at the cost of noise enhancement. The *noise enhancement factor* (NEF) ξ determines the SNR reduction when using the ZF receiver. It is defined as

$$\xi = \sum_{n=0}^{MK-1} |[B_{ZF}]\,k,n|^2, \tag{9.8}$$

9.2 Pulse shaping filter

GFDM is derived from the filter bank approach, is based on a block filtered MCM scheme. The data transmission on each block is distributed in time and frequency and each sub-carrier is pulse-shaped. Reduction of OOB emission is obtained in GFDM by using different time-domain pulse shaping filters other than the conventional rectangular one used in CP-OFDM [142]. Moreover, the tail biting technique used in GFDM makes the CP length to be independent of transmit and receive filters length [143]. This allows to reduce the overhead caused by the CP, thus increasing the spectral efficiency.

136

The choice of the discrete-time pulse shaping impulse response g[n] strongly influences the spectral properties of the GFDM signal. A classical approach for choosing the discrete-time impulse response is to sample at the rate of the sampling frequency of the continuous-time impulse response $g(t)$ windowed given as

$$g_w\left(t\right) = \begin{cases} \text{g}_{\text{wdown}}\left(\text{t}\right), & 1 \leq t \geq KT_s \\ \text{g}_{\text{wup}}, & (MK - K)T_s \leq t \geq MKT_s, \end{cases} \tag{9.9}$$

where $g_{wup}(t) = g_{pulse}(t)$, $g_{wdown}(t) = 1 - g_{pulse}(t)$ and T_s symbol interval, being $g_{pulse}(t)$ one of the different types of pulse shaping filters reported below. As is well known, Nyquist impulse responses have periodic zero values in time-domain at multiples of the symbol period. When we move in the frequency domain this condition turns into a vestigial symmetry [144]. This means that their spectrum exhibits odd symmetry around the cut-off frequency, which is half the symbol rate. Hence, Nyquist filters can be defined by imposing an odd symmetry to the frequency coefficients around the cut-off frequency. In digital communication systems, the global Nyquist filter is generally split into two parts, a square-root Nyquist filter in the transmitter and a square-root Nyquist filter in the receiver. Then, the symmetry condition is satisfied by the squares of the frequency coefficients. In order to design a proper Nyquist filter to be used in GFDM, the principles of odd symmetry need to be applied from a time-domain perspective by interchanging the role of the frequency independent variable with that of the time independent variable in the analytical function defining the Nyquist pulse. The advantage deriving from this formal exchange between the two independent variables is the elimination of the time-domain overlapping with consequent reduction of interference.

The concept of wavelet is also included here to achieve a better time-frequency localization [145, 146], and, also to add flexibility in the design of the pulse shaping filter. As is well known, the square-root Nyquist pulse has a major impact on the system design and, therefore, an alternative solution to define it in the time-domain is required. This alternative solution must ensure that the derivative of the designed pulse is smooth in order to confine the frequency span as much as possible. Many authors have investigated solutions based on the concept of wavelets [145, 146]. A wavelet is a wave-like oscillation with an amplitude that begins at zero, increases, and then decreases back to zero. To ensure this smooth transition, an auxiliary function was introduced by Meyer in [147] to be used as an inner argument of different pulse shaping filters. The *Meyer auxiliary function* is defined as

$$v\left(x\right) = x^4\left(35 - 84x + 70x^2 - 20x^3\right), \tag{9.10}$$

Therefore, in our results we will consider the impact of improved Nyquist pulse shaping filters with and without Meyer auxiliary function on the SER performance of the GFDM system.

9.2.1 Root raised cosine (RRC)

This category of pulse shaping filters is defined by the well-known raised cosine (RC) and root raised cosine (RRC) functions in time-domain for a given roll-off factor α.

Here, we consider the time-domain expression that results by interchanging the independent frequency variable with the time variable

$$
g_{RC}(t) = \begin{cases} 1, & |t| \leq \frac{(1-\alpha)T}{2} \\ \frac{1}{2}\left[1+cos\left(\pi P_{RC}(t)\right)\right], & \frac{(1-\alpha)T}{2} < |t| \leq \frac{(1+\alpha)T}{2} \\ 0, & otherwise, \end{cases}
\tag{9.11}
$$

where $P_{RC}(t)$ is the inner argument of the cosine written as

$$
P_{RC}(t) = \left(\frac{|t| - \left(\frac{(1-\alpha)T}{2}\right)}{\alpha\,T} \right).
\tag{9.12}
$$

By introducing the Meyer auxiliary function $v(x)$, the inner argument of the cosine must be modified as

$$
P_{RC}(t) = v\left(\frac{|t| - \left(\frac{(1-\alpha)T}{2}\right)}{\alpha\,T} \right).
\tag{9.13}
$$

The RRC pulse shaping filter is defined as

$$
g_{RRC}(t) = \sqrt{g_{RC}(t)}.
\tag{9.14}
$$

9.2.2 Xia pulses

A family of pulses, termed Xia pulses, is considered in [148]. The main property of this family is that of satisfying the Nyquist condition for inter-symbol interference free transmission with and without matched filtering, thus providing better robustness to timing jitter. The time-domain expression of Xia pulse shaping filter is

$$
g(t) = \begin{cases} 1\,, & |t| \leq \frac{(1-\alpha)KT_s}{2} \\ \frac{1}{2}\left(1+e^{j\,\pi\;P_{1Xia}(t)}\right), & \frac{(1-\alpha)KT_s}{2} < |t| \leq \frac{(1+\alpha)KT_s}{2}, \\ 0, & \frac{(1+\alpha)KT_s}{2} < |t|\,, \end{cases}
\tag{9.15}
$$

where

$$
P_{1Xia}(t) = \left(\frac{|t| - \left(\frac{(1-\alpha)KT_s}{2}\right)}{\alpha\,T} \right).
\tag{9.16}
$$

Using the concept of the Meyer auxiliary function $v(x)$ we get

$$
P_{1Xia}(t) = v\left(\frac{|t| - \left(\frac{(1-\alpha)KT_s}{2}\right)}{\alpha\,T} \right).
\tag{9.17}
$$

9.2.3 Flipped-hyperbolic secant (Fsech)

This improved Nyquist pulse shaping filter is proposed in [148]. By following [148], we consider first the flipped-hyperbolic secant (Fsech) pulse shaping filters. The time-domain expression is obtained by interchanging independent frequency variable with the time variable is given by

$$
g\left(t\right) = \begin{cases} 1, & |t| \leq \frac{(1-\alpha)T}{2} \\ 1 - sech\left(\rho P_{1Fsech}\left(t\right)\right), & \frac{(1-\alpha)T}{2} < |t| \leq \frac{T}{2} \\ sech\left(\rho P_{2Fsech}\left(t\right)\right), & \frac{T}{2} < |t| \leq \frac{(1+\alpha)T}{2} \\ 0, & \frac{(1+\alpha)T}{2} < |t|, \end{cases} \tag{9.18}
$$

where $sech$ is the hyperbolic secant function, $\rho = ln\left(\sqrt{3}+2\right)/\alpha \times \frac{T}{2}$, $P_{1Fsech}\left(t\right)$ and $P_{2Fsech}\left(t\right)$ is the inner arguments of the hyperbolic secant function written as

$$
P_{1Fsech}\left(t\right) = \left(\left(\frac{(1+\alpha)T}{2}\right) - |t|\right), \tag{9.19}
$$

and

$$
P_{2Fsech}\left(t\right) = \left(|t| - \left(\frac{(1-\alpha)T}{2}\right)\right). \tag{9.20}
$$

When we introduces the Meyer auxiliary function $v\left(x\right)$, inner arguments of the hyperbolic secant function $P_{1Fsech}\left(t\right)$ and $P_{2Fsech}\left(t\right)$ must be modified as

$$
P_{1Fsech}\left(t\right) = v\left(\left(\frac{(1+\alpha)T}{2}\right) - |t|\right), \tag{9.21}
$$

and

$$
P_{2Fsech}\left(t\right) = v\left(|t| - \left(\frac{(1-\alpha)T}{2}\right)\right). \tag{9.22}
$$

9.2.4 Flipped-inverse hyperbolic secant (Farcsech)

Another improved Nyquist pulse shaping filter proposed in [148] is the flipped-inverse hyperbolic secant (Farcsech). The time-domain expression of Farcsech pulse shaping filter is obtained by interchanging independent frequency variable with the time variable as

$$
g\left(t\right) = \begin{cases} 1, & |t| \leq \frac{(1-\alpha)T}{2} \\ arcsech\left(\frac{1}{\rho} P_{1Farcsech}\left(t\right)\right), & \frac{(1-\alpha)T}{2} < |t| \leq \frac{T}{2} \\ 1 - arcsech\left(\frac{1}{\rho} P_{2Fsech}\left(t\right)\right), & \frac{T}{2} < |t| \leq \frac{(1+\alpha)T}{2} \\ 0, & \frac{(1+\alpha)T}{2} < |t|, \end{cases} \tag{9.23}
$$
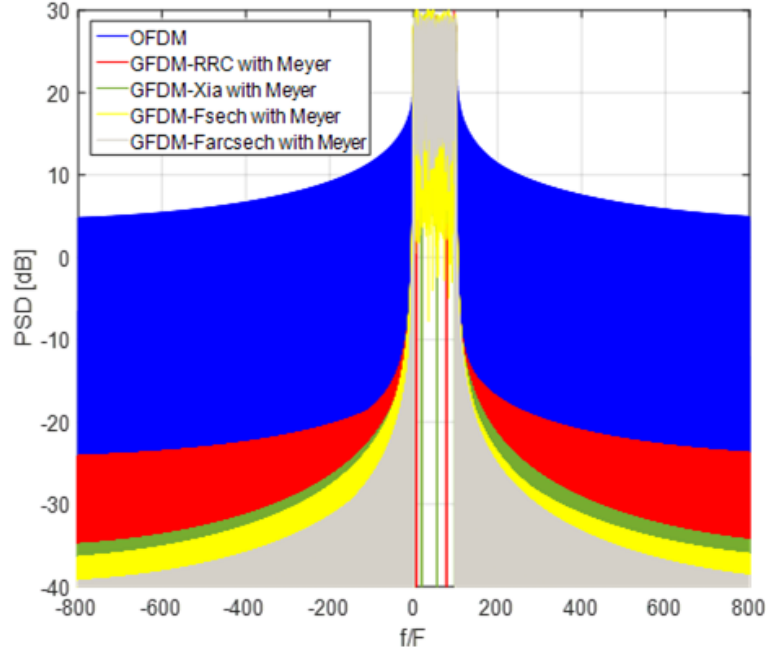
Figure 9.4: *PSD comparison of OFDM along with GFDM with different pulse shaping filters at roll-off= 0.1.*

where $arcsech$ is the inverse hyperbolic secant function, $P_{1Farcsech}(t)$ and $P_{2Fsech}(t)$ is the inner arguments of the inverse hyperbolic secant function written as

$$P_{1Farcsech}(t) = \left(|t| - \left(\frac{(1-\alpha)T}{2}\right)\right),$$ (9.24)

and

$$P_{2Fsech}(t) = \left(\left(\frac{(1+\alpha)T}{2}\right) - |t|\right).$$ (9.25)

By introducing the concept of the Meyer auxiliary function $v(x)$, the inner arguments Farcsech pulse shaping filters $P_{1Farcsech}(t)$ and $P_{2Fsech}(t)$ are modified as

$$P_{1Farcsech}(t) = v\left(\left(\frac{(1+\alpha)T}{2}\right) - |t|\right),$$ (9.26)

and

$$P_{2Farcsech}(t) = v\left(|t| - \left(\frac{(1-\alpha)T}{2}\right)\right)$$ (9.27)
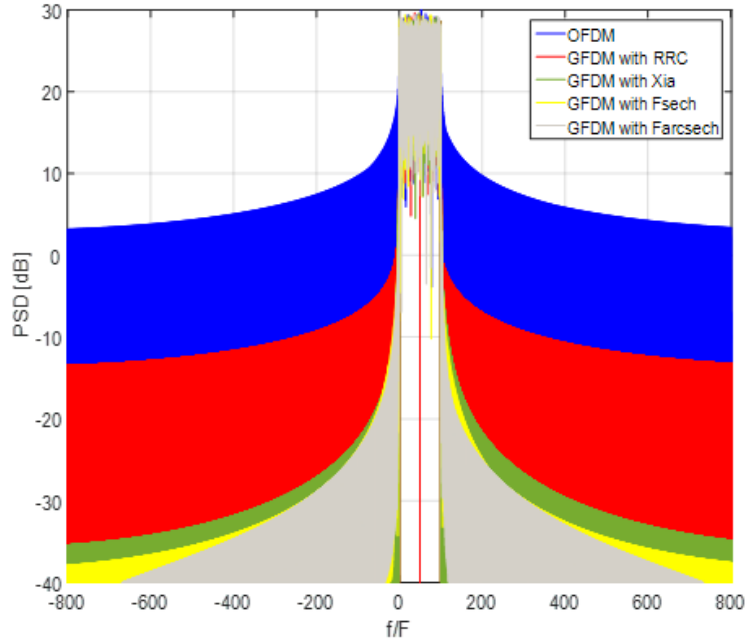
Figure 9.5: *PSD comparison of OFDM along with GFDM with different pulse shaping filters at roll-off= 0.1.*

9.3 OOB Emissions

One of the main characteristics of GFDM is the flexible time-domain pulse shaping, which allows to reduce the OOB emissions. However, the abrupt transitions between the GFDM blocks limit the overall reduction that can be achieved in OOB emission. In the literature, there are two methods available for reducing the effect of this issue [16]. The first method is based on the use of guard sub-symbols while the second one on the use of time windowing. In this paper, we employ the time-windowing method for further reduction of the OOB emission. The analysis of the OOB emission is based on the computation of the power spectral density (PSD) [8]. As shown in [8], the PSD of the baseband signal can be computed as

$$P(f) = \lim_{T \to \infty} \left(\frac{1}{T} E\left[|x_T(t)|^2 \right] \right), \qquad (9.28)$$

where $x_T(t)$ is the transmitted signal and F_N is the N-points DFT matrix. Here, we are integrating the GFDM signal into the LTE-A time-frequency grid. Hence, according to Table 1, we have to concatenate the multiple GFDM blocks. After concatenation, the GFDM signal $x_T(t)$ is represented as

$$x_T(t) = \sum_{v,m,k} d_{v,m,k} g_{k,m}(t - vMT_S) e^{-j2\pi vMT_s f} \qquad (9.29)$$

where T_s is the time duration of one sub-symbol, v is the block index, and k, m range over all allocated sub-carrier and sub-symbol. By following [8], we substitute (9.29)
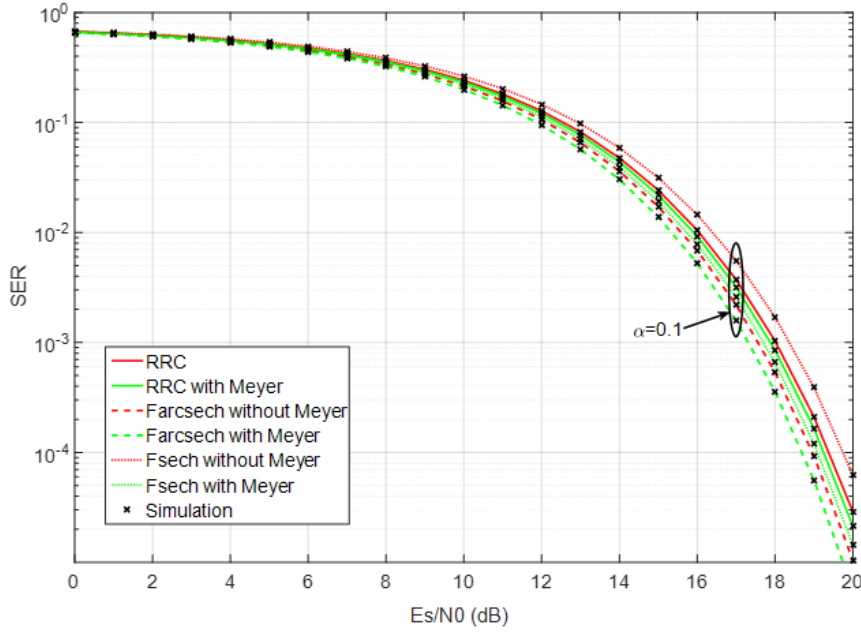
Figure 9.6: *SER performance of different pulse shaping filter in the case of the transmission over the AWGN channel at roll-off= 0.1.*

in (9.28) and assume that $d_{v,m,k}$ data symbols are i.i.d. with unit variance. After the computation of the Fourier transform, the PSD is written as

$$P(f) = \frac{1}{MT_s} \sum_{m,k} |G_m \left(f - \frac{k}{T_s} \right)|^2 \tag{9.30}$$

where $G_m(\cdot)$ is the frequency response of $g(\cdot)$.

9.4 SER Analysis

In this section we analyze the performance of the GFDM transmission over AWGN, static-FSC, and TVC. By following the same frame structure of LTE-A shown in Fig.9.2, we introduce improved Nyquist pulse shaping filters with and without using Meyer auxiliary functions. As previously mentioned, the performance is evaluated by employing ZF receiver. The parameters used in our simulations are presented in Table 9.1.

9.4.1 AWGN

The general expression of SER for QAM transmission over the AWGN channel is

$$P_{\text{AWGN}} = 2 \left(\frac{\kappa - 1}{\kappa} \right) erfc\left(\sqrt{\rho}\right) - \left(\frac{\kappa - 1}{\kappa} \right) erfc^2\left(\sqrt{\rho}\right), \tag{9.31}$$
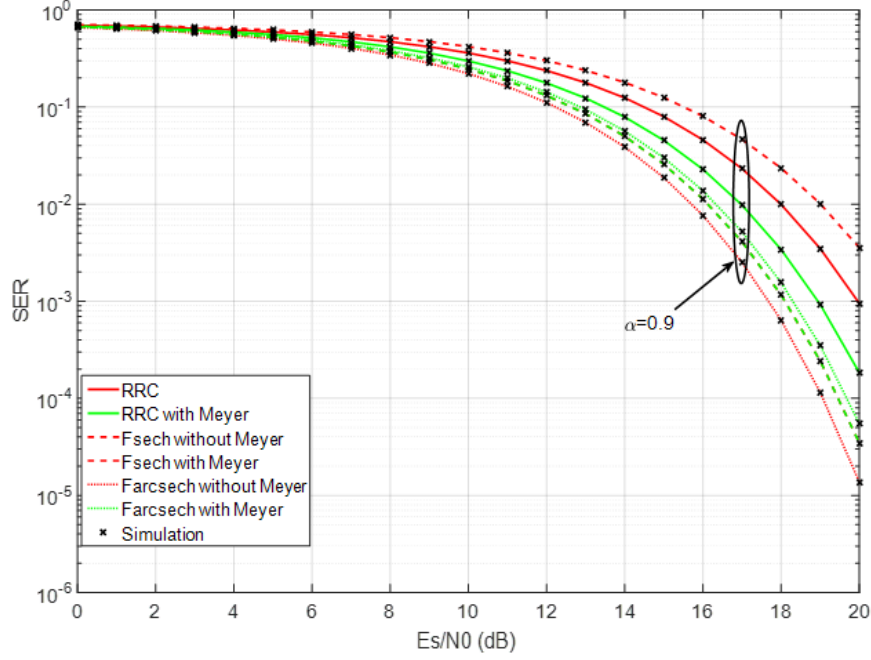
Figure 9.7: *SER performance of different pulse shaping filter in the case of the transmission over the AWGN channel at roll-off= 0.9.*

where $\kappa=\sqrt{2^\mu}$, with μ being the number of bits per symbol, and $\rho=\frac{3R_T}{2(2^\mu-1)}\frac{E_s}{\xi N_o}$. being E_s and $N_o= 2\sigma_w^2$ be the average energy per symbol and the noise power spectral density of complex AWGN, respectively, and $R_T=\frac{KM}{KM+N_{cp}+N_{cs}}$, with N_{cp} and N_{cs} the length of CP and guard symbol, respectively and ξ is the noise enhancement factor (NEF) the determines the SNR reduction when using the ZF receiver. The NEF is given in eq.(9.8).

9.4.2 Static frequency selective channel

The SER performance over static-FSC is an important requirement for multicarrier modulations. Here, we consider the static-FSC with L=16 defined as

$$\boldsymbol{h}_{FSC} = \left(10^{\frac{-\left(\frac{2}{3}\right)l}{20}}\right), \qquad l = 0, 1, \ldots, 15, \qquad (9.32)$$

The corresponding SER is written as

$$P_{FSC} = 2\left(\frac{\kappa-1}{\kappa K}\right)\sum_{l=0}^{K-1} erfc\left(\sqrt{\rho_l}\right) - \frac{1}{K}\left(\frac{\kappa-1}{\kappa}\right)\sum_{l=0}^{K-1} erfc^2\left(\sqrt{\rho_l}\right) \qquad (9.33)$$

where $\rho_l = \frac{3R_T}{2(2^\mu-1)}\frac{E_s}{\xi_l N_o}$, $\xi_k = \frac{1}{MK}\sum_{k=0}^{MK-1}\left|\frac{G_{R_{k,0}}[-k]}{H[k]}\right|^2$ and $G_{R_{k,0}}[k]$ is the frequency response of the filter for the k-th sub-carrier and the first sub-symbol, and ξ_k is the cor-
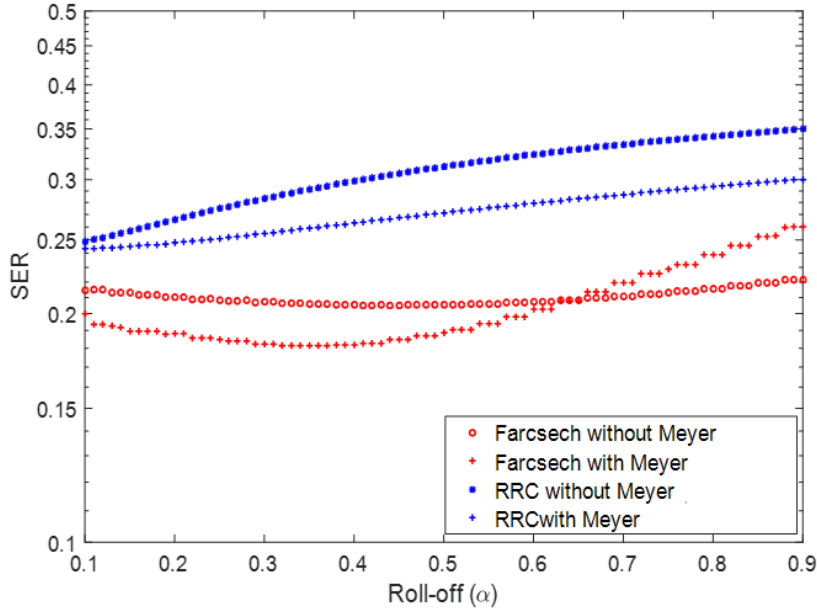
Figure 9.8: *SER comparison of RRC and Farcsech with an without Meyer at* 10 *dB SNR.*

responding NEF for the *k*-th subcarrier is varies with the receiver filter and the channel frequency response.

9.4.3 Time-variant frequency flat fading channel

The SER performance in the case of TVC can be obtained by assuming that the channel coherence time is larger than one GFDM block. Here, we are considering

$$\boldsymbol{h}_{TVC} = h, \qquad h \sim \mathcal{CN}\left(0, 1\right). \tag{9.34}$$

For the case of TVC, the SER expression for QAM is written as

$$P_{TVC} = 2\left(\frac{\kappa-1}{\kappa K}\right)\left(1 - \sqrt{\frac{\rho_l}{1+\rho_l}}\right) - \left(\frac{\kappa-1}{\kappa K}\right)^2 \left[1 - \frac{4}{\pi}\sqrt{\frac{\rho_l}{1+\rho_l}}\ \mathrm{atan}\left(\sqrt{\frac{\rho_l}{1+\rho_l}}\right)\right] \tag{9.35}$$

where

$$\rho_l = \frac{3\sigma_r^2 R_T}{(2^\mu - 1)} \frac{E_s}{\xi N_o},$$

9.5 Simulation Results

Figure 9.3 gives a pictorial description of the different time-domain Nyquist pulse shaping filters for different values of roll-off. The analytical expressions are obtained by
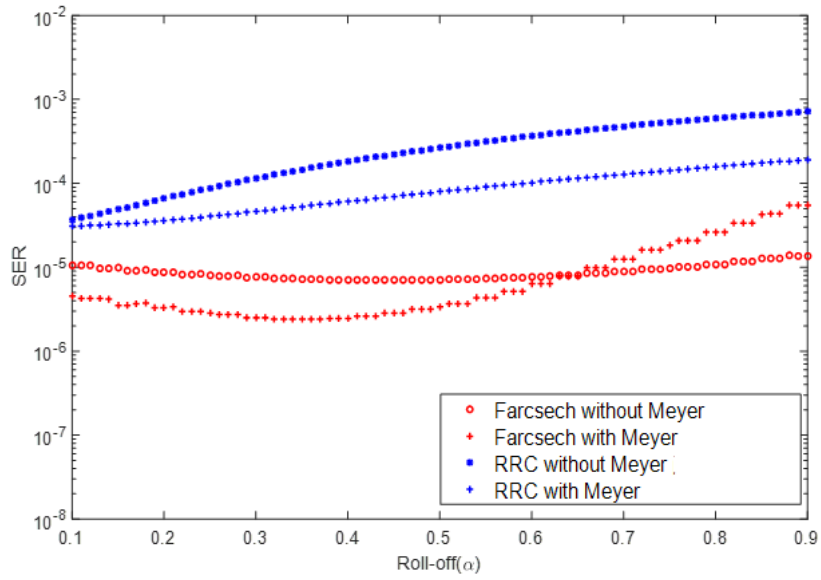
Figure 9.9: *SER comparison of RRC and Farcsech with an without Meyer at* 20 *dB SNR.*
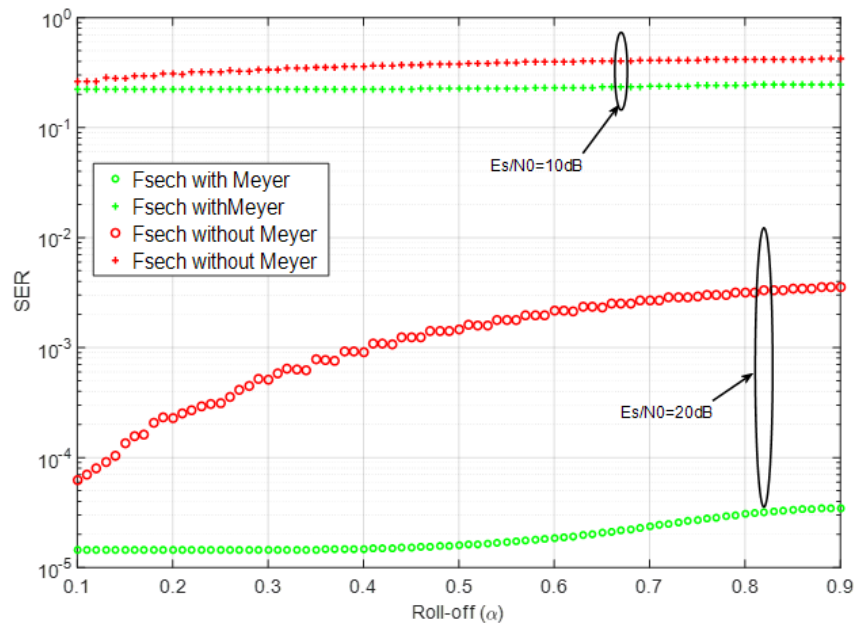
Figure 9.10: *SER comparison of Fsech with and without Meyer at* 10 *and* 20 *dB SNR.*
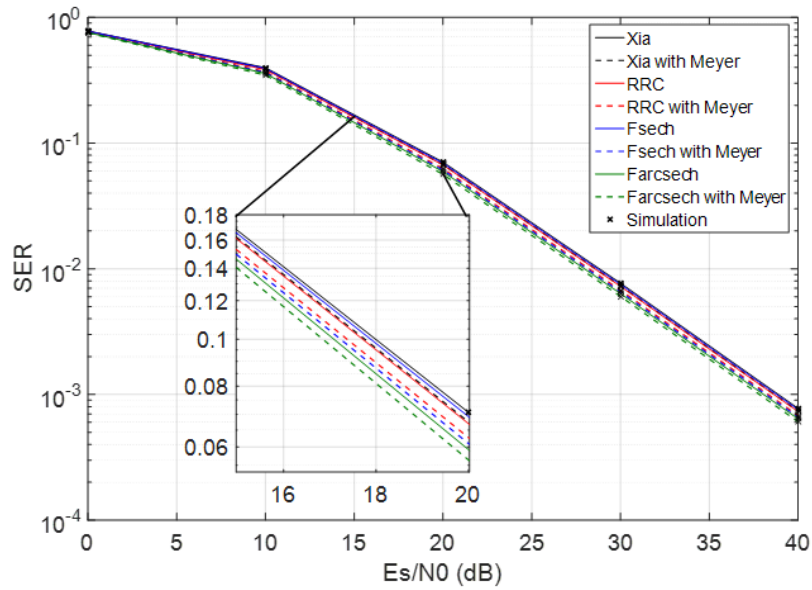
Figure 9.11: *SER performance of different pulse shaping filter with and without Meyer auxiliary function in the TVC chnnel at roll-off=0.1.*
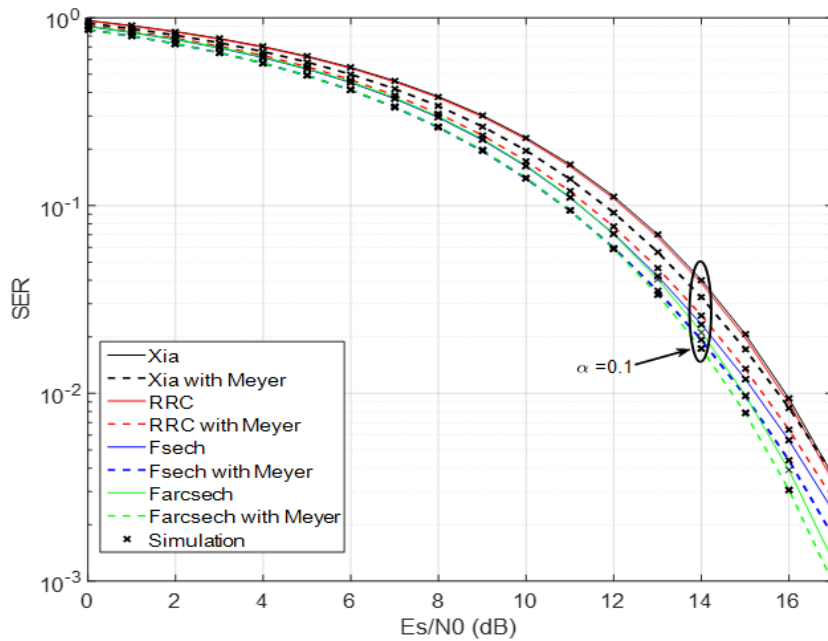
Figure 9.12: *SER performance of different pulse shaping filter with and without Meyer auxiliary function in the static FSC at roll-off=0.1.*

interchanging the frequency independent variable with the time one. After such an interchange of the independent variables, the resulting time-domain expressions are those given in Sec. 9.4. From Fig. 9.3, it is clearly visible that by increasing the value of α we have larger spread but in the case of Farcsech pulse shaping filter we have almost the same spread at different values of α. Now, we are computing the OOB emission of the GFDM system for the different pulse shaping filters. The OOB emission is studied by evaluating the PSD of the GFDM transmitted signal.

From Fig. 9.4 we see that "Better than Nyquist" pulse shaping filters significantly reduce OOB emission. In addition, by introducing the concept of wavelet a smooth transition is guaranteed. After considering the Meyer with pulse shaping, further reduction in the OOB emission is observed for RRC pulse, while for Xia, Fsech pulses there is no improvement and for Farcsech there is little degradation in OOB emission as shown in Fig. 9.5 with different pulse shaping filters at roll-off(α)= 0.1.

Figure 9.6 shows the comparison of SER performance verses E_s/N_0 of 16-QAM with different pulse shaping filters with and without Meyer auxiliary function for GFDM transmission over the AWGN channel. Here, a number of 64 sub-carriers is considered and each sub-carrier contains 7 sub-symbols with $\alpha = 0.1$. It is clearly visible from the graphs that at $\alpha = 0.1$, Farcsech pulse shaping filter is the optimal one in comparison with the RRC and with Fsech pulse shaping filter. Furthermore, if we apply the concept of Meyer auxiliary function on these filters a further improvements in terms of SER is observed as compared to without Meyer auxiliary function. The same type of comparison done in Fig. 9.7 for $\alpha = 0.9$. It is clearly evident from the graphs that at $\alpha = 0.9$, Farcsech pulse shaping filter is the optimal one as compared to the RRC and Fsech pulse shaping filters but when we apply the Meyer auxiliary function on the Farcsech pulse shape filter it results in a higher SER, as compared with that without Meyer.

To investigate the effect of Meyer auxiliary function on the Farcsech pulse shaping filter, in Figs. 9.8 and 9.9 we have considered two fixed values of the E_s/N_0 at 10 and 20 dB respectively. Then, we have plotted SER versus different values roll-off (α). It can be observed that at low values of α Farcsech with Meyer auxiliary function performs better than without it. At higher values of α starting from $\alpha = 0.65$ Farcsech without Meyer auxiliary function performs better than with using it. Similarly, in Fig. 9.10 it is shown SER verses roll-off for the Fsech pulse shape filter with and without Meyer auxiliary function at 10 and 20 dB of E_s/N_0. In this case for Fsech pulse shaping filter Meyer function always provides an improvement in comparison to Fsech pulse shaping filter.

Figure 9.11 shows the SER performance of transmission over the time-varying frequency flat fading channel. The amplitude is modeled as a Rayleigh random variable with variance $\sigma_r^2 = 0.5$ and phase uniformly distributed between 0 and 2π. It is assumed that the channel remains static during the transmission of one GFDM symbol. From Fig. 9.11 we observe that also for this case use of "Better than Nyquist" pulse shaping allows to almost same SER performance compare to RRC pulse. Again, the use of Meyer auxiliary function allows achieving better performance

Figure 9.12 shows the SER performance of transmission over the static frequency

selective fading channel. It is clearly visible from Fig. 9 that by using the "Better than Nyquist" pulse shaping there is an improvement in the SER performance as compared to RRC and Xia pulses, which is furtherer improved by introducing the Meyer auxiliary function.

9.6 Summary

We consider the four LTE resource blocks to fit three GFDM sub-carriers and 15 GFDM symbols into one sub-frame. After having integrated of the GFDM into the frame structure of LTE system, we have analyzed the impact of the "Better than Nyquist" on the OOB emission. The GFDM system with low OOB emission guarantees low interference in the LTE signals. We have also consider different pulses and also together with concept of wavelet with Meyer auxiliary function for better time-frequency localization in the GFDM system and analyze the SER performance in the case of transmission over AWGN, static FSC, and TVC for the 16-QAM modulation scheme with ZF receiver. From the presented results in this Thesis shows that when we include the Meyer auxiliary function in the improved Nyquist pulse shaping filters a further improvement in terms of SER is achieved

Discrete Gabor Transform-based GFDM

THIS chapter deals with the problem of optimal detection for DGT-based GFDM system in case of transmission over a frequency selective channel. Here, we consider the implementation of GFDM in the concept GT and at the receiver a time-domain maximum likelihood (ML) detection approach is developed to optimally decide transmitted symbols when the synthesis function, *i.e.* pulse shaping filter, and the analysis function, *i.e.* receiving filter, satisfy the *Wexler-Raz* identity. Choosing functions that satisfy the Wexler-Raz condition allows for optimal symbol-by-symbol detection after DGT-based receiver in case of ideal channel. However, when transmission takes place over a frequency selective channel symbol-by-symbol detection of sub-symbols is not longer optimal due to inter-sub-symbol interference (ISSI) generated bysub-symbols transmitted over the same sub-carrier.

10.1 Introduction to DGT-based GFDM

Despite the above mentioned advantages of GFDM compared to OFDM, a main issue is the need of equalization, implemented by block-based processing in time or frequency domain, that is required even in the case of transmission over an ideal channel [8]. For an efficient implementation of GFDM receiver in time-domain, a relationship between the GFDM signal and DGT was proposed in [31]. In particular, it was shown that GFDM transmission and reception are equivalent to a finite discrete Gabor expansion and DGT in critical sampling, respectively. According to such a DGT interpretation, when the circular pulse shaping filters used at transmitter and receiver satisfy the

Wexler-Raz condition, the transmitted signal and symbols of a GFDM signal define a DGT and IDGT pair.

The Gabor interpretation allows for an efficient computation of the ZF and minimum mean-squared error receiving filters without resorting to matrix inversion. An optimal symbol-by-symbol detector can be used after the DGT-based receiver in case of ideal channel. An equivalent interpretation of the DGT receiver in frequency-domain was given in [1], which allows for signal recovery with lower complexity compared to the time-domain approach.

However, it is worth observing that when transmission over a frequency-selective channel is considered the DGT interpretation with critical sampling looses its validity. In this case, to restore the condition required to use the DGT at the receiver, the effect of the channel must be taken into account in the equalization of the whole GFDM symbol. This aspect was considered in [1], where it can be observed that the performance of the proposed low complexity frequency-domain equalization approach for the DGT-based GFDM system is close to that of ODFM for a low number of sub-symbols transmitted over each sub-carrier is low. However, when this number increases the resulting SIR is much lower than that of OFDM with a rapid degradation in the performance. This degradation of performance is due to the ISSI that arises from the sub-symbols transmitted on the same sub-carrier, which is not properly considered in [1]. The main contribution of this chapter consists in the implementation of a time-domain ML detector that is able to take into account ISSI and, thus, provides the optimal decision for the transmitted symbols.

10.2   DGT-based GFDM System Model

With reference to one GFDM symbol, the block of transmitted bits is applied to the input of a mapper that gives at its output an $M \times K$ data matrix $\mathbf{X}$ whose $N = MK$ elements take values from a complex constellation [149]. The data matrix $\mathbf{X}$ is sent to the GFDM modulator, based on K sub-carriers, where each sub-carrier is used to transmit M sub-symbols. After pulse shape filtering, the nth sample of the transmitted GFDM signal is written as

$$x(n) = \sum_{k=0}^{K-1}\sum_{l=0}^{M-1} X_k(l) g_{k,l}[n] = \sum_{k=0}^{K-1}\sum_{l=0}^{M-1} X_k(l) g\left[\langle n - lK\rangle_N\right] e^{\frac{j2\pi kn}{K}}, \qquad (10.1)$$

where $n = 0, 1, \cdots, N-1$, is the sampling index and $\langle\cdot\rangle_N$ denotes the modulo N operation that implements the circular shifting of the periodic prototype discrete-time impulse response $g[n]$ of length N.

10.2.1   Transmission over an Ideal Channel

As first observed in [31], equation (10.1) can be interpreted as the IDGT, where $g[n]$ represents the synthesis function whose time-domain translations and frequency-domain shiftings $g_{q,m}[n]$ are weighted by transmitted symbols. With this interpretation, in case

of transmission over an ideal channel the symbols $X_q(m)$ can be recovered from $x(n)$ at the receiver by applying DGT as

$$X_q(m) = \sum_{n=0}^{N-1} \gamma_{q,m}^*[n]x(n), \tag{10.2}$$

where $\gamma_{q,m}$ is a periodic discrete function with period N, which is defined as the analysis function obtained from time and frequency shifts of an analysis window $\gamma[n]$ as

$$\gamma_{q,m}[n] = \gamma\left[\langle n - mK\rangle_N\right] e^{\frac{j2\pi qn}{K}}. \tag{10.3}$$

Note that, the identity defined by (10.2) holds only when the synthesis function $g[n]$ and the analysis function $\gamma[n]$ satisfy the *Wexler-Raz* identity given in [1, eq. (11)]. If this condition is not satisfied interference arises both from symbols transmitted on other sub-carriers and from sub-symbols transmitted on the same sub-carrier.

10.2.2 Transmission over a Frequency-selective Channel

When transmission takes place over a frequency-selective channel, the effect of ISI introduced by the time spread of the channel can be mitigate by inserting a CP, which consists of N_{CP} samples such that the length of the CP is at least equal to that of the channel. The CP-extended signal is written as

$$\tilde{x}(n) = \begin{cases} x(N+n), & n = -N_{CP}, \ldots, -1, \\ x(n), & n = 0, \ldots, N-1. \end{cases} \tag{10.4}$$

We consider here the same L-path tapped delay line channel model defined in [150]. According to this model, the continuous-time impulse response of the multi-path fading channel is defined as

$$h(t) = \sum_{i=0}^{L-1} h_i \delta(t - \tau_i), \tag{10.5}$$

where h_i is the complex amplitude, or tap coefficient, of the ith path associated with the propagation delay τ_i and $\delta(t)$ is the delta Dirac function. When $L = 1$ we get the flat fading Rayleigh channel model. For the particular case where h_0 is constant and equal to 1 we have the ideal channel. In the following, for simplicity, we consider the case where $\tau_i = i$, with $i = 0, \ldots, L-1$. The tap coefficients h_i, $i = 0, 1, 2, \ldots, L-1$, are modeled as independent and identically distributed zero mean complex random variables with average power $\sigma_i^2 = 1/L$, uniform distributed phase in $[0, 2\pi)$, and Rayleigh distributed amplitude. According to such a model we have $\sigma_0^2 + \sigma_1^2 + \cdots + \sigma_{L-1}^2 = 1$.

After passing through the channel the received signal is written as

$$y(n) = \sum_{i=0}^{L-1} h_i \tilde{x}(n-i) + w(n), \tag{10.6}$$

where $w(n)$ represents the complex AWGN with zero mean and variance σ^2 per dimension. Under the assumption $N_{CP} \geq L - 1$, by removing the effect of the cyclic prefix and by replacing (10.1) in (10.6) we get

$$y(n) = \sum_{i=0}^{L-1} h_i \sum_{k=0}^{K-1} \sum_{l=0}^{M-1} X_k(l) g[\langle n - i - lK \rangle_N] e^{\frac{j2\pi k(n-i)}{K}} + w(n) . \qquad (10.7)$$

In order to recover the transmitted symbols, the DGT defined in (10.2) is applied to the received signal as

$$Y_q(m) = \sum_{n=0}^{N-1} \gamma_{q,m}^*[n] y(n) = \sum_{n=0}^{N-1} \gamma^*[\langle n - mK \rangle_N] y(n) e^{-\frac{j2\pi qn}{K}}$$

$$= \sum_{k=0}^{K-1} \sum_{l=0}^{M-1} X_k(l) \sum_{i=0}^{L-1} h_i P_{(q-k)M}[(m-l)K, i] e^{-\frac{j2\pi ki}{K}} + W_q(m) , \qquad (10.8)$$

where $W_q(m)$ is the DGT of the AWGN and

$$P_{kM}[l, i] = \sum_{n=0}^{N-1} \gamma^*[n] g[\langle n - i + lK \rangle_N] e^{-\frac{j2\pi kn}{K}}$$

$$= \frac{1}{N} \sum_{q=0}^{N-1} \Gamma_q^* G_{\langle q+kM \rangle_N} e^{-\frac{j2\pi(q+kM)(i-lK)}{N}}$$

$$= \left(\frac{1}{N} \sum_{q=0}^{N-1} \Gamma_q^* G_{\langle q+kM \rangle_N} e^{\frac{j2\pi ql}{M}} e^{-\frac{j2\pi qi}{N}} \right) e^{-\frac{j2\pi ki}{K}} \qquad (10.9)$$

with Γ_q and G_q corresponding to the N-points DFT of $\gamma[n]$ and $g[n]$, respectively.

As function satisfying the Wexler-Raz identity with critical sampling in what follows we consider a Dirichlet pulse, also referred *discrete sinc*, which is characterized by a DFT that is a rectangular pulse

$$G_k^D = \begin{cases} 1, & \left(0 \leq k \leq \lceil \frac{M}{2} \rceil - 1\right) \bigcup \left(N - \lfloor \frac{M}{2} \rfloor \leq k \leq N-1\right), \\ 0 & otherwise, \end{cases} \qquad (10.10)$$

where $\lceil \cdot \rceil$ and $\lfloor \cdot \rfloor$ denote the nearest upper and lower integer, respectively. With the use of Dirichlet function we have $\gamma[n] = g[n]$, and the filtering implemented at the receiver with the analysis function $\gamma[n]$ can be therefore interpreted as satisfying the matched and ZF condition at the same time. By setting $G_k = G_k^D$ in (10.9) we get

$$P_{kM}[lK, i] = \delta[k] \frac{1}{N} \frac{\sin\left(\frac{\pi(i-lK)}{K}\right)}{\sin\left(\frac{\pi(i-lK)}{N}\right)} e^{\frac{j\pi(i-lK)(1+(-1)^M)}{2N}} , \qquad (10.11)$$

where $\delta[k]$ denotes the Kronecher delta. In the special case $i = 0$, (10.11) converts into eq. (14) of [1], for which we obtain the Wexler-Raz identity

$$P_{kM}[lK, 0] = \frac{1}{N} \sum_{q=0}^{N-1} \Gamma_q^* G_{\langle q+kM \rangle_N} e^{\frac{j2\pi ql}{M}} = \delta[k]\delta[l],$$
$$0 \leq k \leq K - 1, \text{ and } 0 \leq l \leq M - 1. \qquad (10.12)$$

By substituting $P_{kM}[lK, i]$ given in (10.11) into the (10.8), after some mathematical manipulation (10.8) can we rewritten as

$$Y_q(m) = \sum_{l=0}^{M-1} X_q(l) \sum_{i=0}^{L-1} h_i \frac{\sin\left(\frac{\pi(i-(m-l)K)}{K}\right)}{\sin\left(\frac{\pi(i-(m-l)K)}{N}\right)} e^{-\frac{j2\pi qi}{K}} + W_q(m)$$
$$= \sum_{l=0}^{M-1} X_q(l) \bar{H}_{qM}((m-l)K) + W_q(m), \qquad (10.13)$$

where the even property of the periodic Dirichlet sinc function has been used. The above equation shows that in case of Dirichlet function the interference is generated only by sub-symbols transmitted on the same sub-carrier and not from sub-symbols transmitted on other sub-carriers. The "windowed" channel is given by

$$\bar{H}_q(m) = \sum_{i=0}^{N-1} h_i^{(ZP)} w_{\langle i-m \rangle_N} e^{\frac{-j2\pi qi}{N}}, \qquad (10.14)$$

where $w_{\langle i-m \rangle_N}$ corresponds to a shifting of m samples of the periodic windowing function

$$w_n = \frac{\sin\left(\frac{\pi n}{K}\right)}{\sin\left(\frac{\pi n}{N}\right)}, \qquad n = 0, \dots, N-1,$$

and

$$h_i^{(ZP)} = \begin{cases} h_i & i = 0, \dots, L-1, \\ 0 & i = L, \dots, N-1. \end{cases} \qquad (10.15)$$

Equation (10.14) can be rewritten

$$\bar{H}_q(m) = H_q \otimes_N W_q e^{-j\frac{2\pi mq}{N}}, \qquad (10.16)$$

which is the circular convolution between the DFT of the channel and the DFT of the shifted windowing function, where $W_q = G_q^D$. According to the definition of G_k^D given in (10.10), eq. (10.16) realizes a weighted average of M frequency domain values of H_k around $k = q$, where the weights are obtained from the complex exponential for a given m. The M samples H_k involved in the average are $k = \langle q - \lfloor \frac{M}{2} \rfloor \rangle, \dots, q - 1 \rangle_N$ and $k = \langle q, \dots, q + \lceil \frac{M}{2} \rceil - 1 \rangle_N$, which define the M points around q taking into account

of the periodic nature of H_k. After some straightforward mathematical manipulations, (10.8) can be rewritten as

$$Y_q(m) = \underbrace{X_q(m)\bar{H}_{qM}(0)}_{\substack{m\text{th sample received} \\ \text{on the } q\text{th sub-carrier}}} + \underbrace{\sum_{l=0,l\neq m}^{M-1} X_q(l)\bar{H}_{qM}((m-l)K)}_{\substack{\text{Interference induced by sub-symbols} \\ \text{other than } X_q(m) \text{ transmitted} \\ \text{on the } q\text{th sub-carrier}}} + \underbrace{W_q(m)}_{\text{AWGN Noise}}, \qquad (10.17)$$

where it appears that the mth sub-symbol transmitted on the qth sub-carrier $X_q(m)$ is

- scaled by the term $\bar{H}_{qM}(0)$;

- impaired by the interference generated by the mth sub-symbol transmitted on the same sub-carrier through the term $\bar{H}_{qM}(l-m)K$, $l \neq m$;

- distorted by the AWGN term $W_q(m)$.

Remark To confirm the flexibility of the GFDM system from eq. (10.13), the two extreme cases of GFDM system are:

- OFDM, when $M = 1$ in which each sub-carrier is used to transmit only one symbol and $K = N$. We get the conventional OFDM where $P_k[0,i] = \delta_k$, $\forall i$.

- DFT-s-OFDM when $N = M$, which corresponds to single-carrier transmission where $P_0[l,i] = \delta_N[i-l]$, $\forall l, i$, which is periodic Kronecher δ with period N.

10.3 Maximum Likelihood Detection (MLD)

The model of the received signal is

$$\mathbf{Y}_q = \bar{\mathbf{H}}_{qM}\mathbf{x}_q + \mathbf{W}_q, \quad q = 1, \ldots, K-1. \qquad (10.18)$$

Thanks to the model of the received signal given in (10.17) it is possible to implement the optimal maximum likelihood (ML) detection principle [151] by applying it to decide the M symbols transmitted on the same sub-carrier. The ML detection principle reads as

$$\hat{\mathbf{X}}_q = \arg \min_{\mathbf{x} \in \mathcal{X}^M} \left\| \mathbf{Y}_q - \bar{\mathbf{H}}_{qM}\mathbf{x} \right\|^2,$$

where $\| \cdot \|$ denotes the norm, $\mathcal{X}$ is space defined by alphabet of input symbols, $\mathbf{Y}_q = [Y_q(0), Y_q(1), \ldots, Y_q(M-1)]$, and

$$\bar{\mathbf{H}}_{qM} = \begin{bmatrix} \bar{H}_{qM}(0) & \bar{H}_{qM}(N-K) & \cdots & \bar{H}_{qM}(N-(M-1)K) \\ \bar{H}_{qM}(N-(M-1)K) & \bar{H}_{qM}(0) & \cdots & \bar{H}_{qM}(N-K) \\ \vdots & \ddots & \ddots & \vdots \\ \bar{H}_{qM}(N-K) & \bar{H}_{qM}(N-2K) & \cdots & \bar{H}_{qM}(0) \end{bmatrix} \qquad (10.19)$$

10.4 Simulation Results

In order to verify the correctness of the proposed optimal MLD detection technique implemented at the receiver side of the GFDM system and performance the monte carlo simulation for analyze the SER verses Es/No performance in the case of the transmission over the Frequency selective Rayleigh fading channel. First of all, to confirm the flexibility of our optimal MLD detection techiques in DGT-based GFDM system by comparing them with two special cases such as OFDM and DFT-s-OFDM, by changing the number of time slots and of sub-carriers in a frame.

In the Fig. 10.1 we compare the SER performance for DGT-based GFDM system with optimal MLD detection techique implemented at the receiver with OFDM and DFT-s-OFDM system. For $M = 1$ GFDM system converted in the OFDM system with $K = 32$, and for $M = 16$ and $K = 2$, GFDM converted into the DFT-s-OFDM system with $M = 32$, for BPSK modulation technique in the case of the transmission over the frequency selective Rayleigh fading channel with 9-taps for Dirichlet pulse shaping filter. Moreover, from the Fig. 10.1, it is clearly visible that proposed optimal
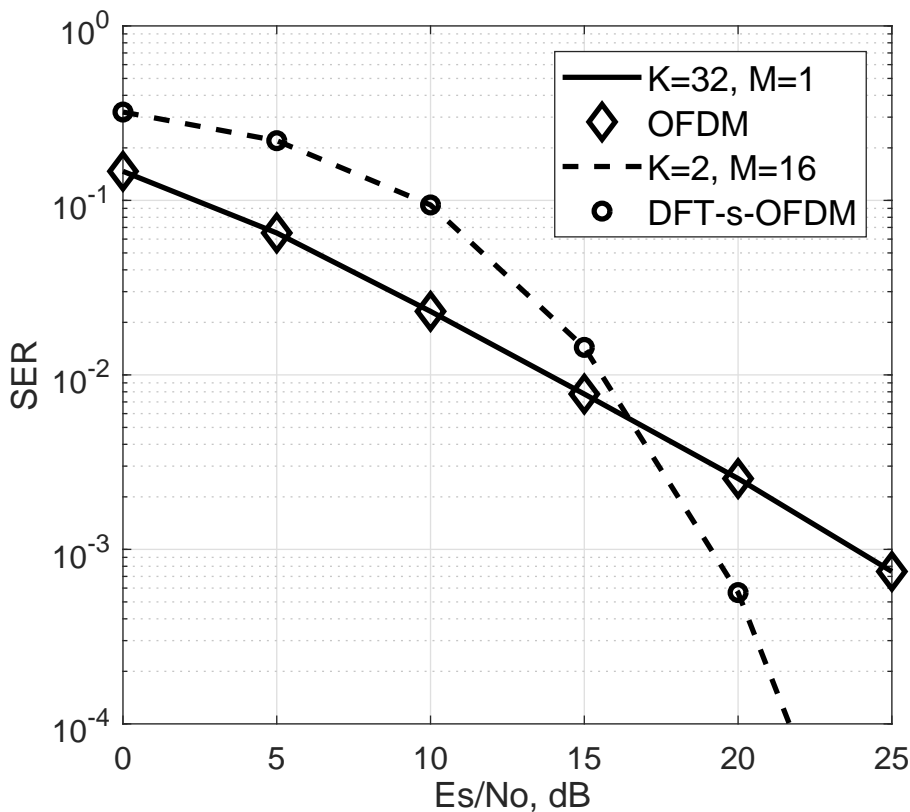
Figure 10.1: *Compare the SER performance of BPSK, GFDM with $M = 1$ and OFDM for $K = 32$, and, GFDM with $M = 16$ and $K = 2$ and with DFT-s-OFDM for $M = 16$ and $K = 2$, in frequency selective Rayleigh fading channel with 9-taps for Dirichlet pulse shaping filter.*
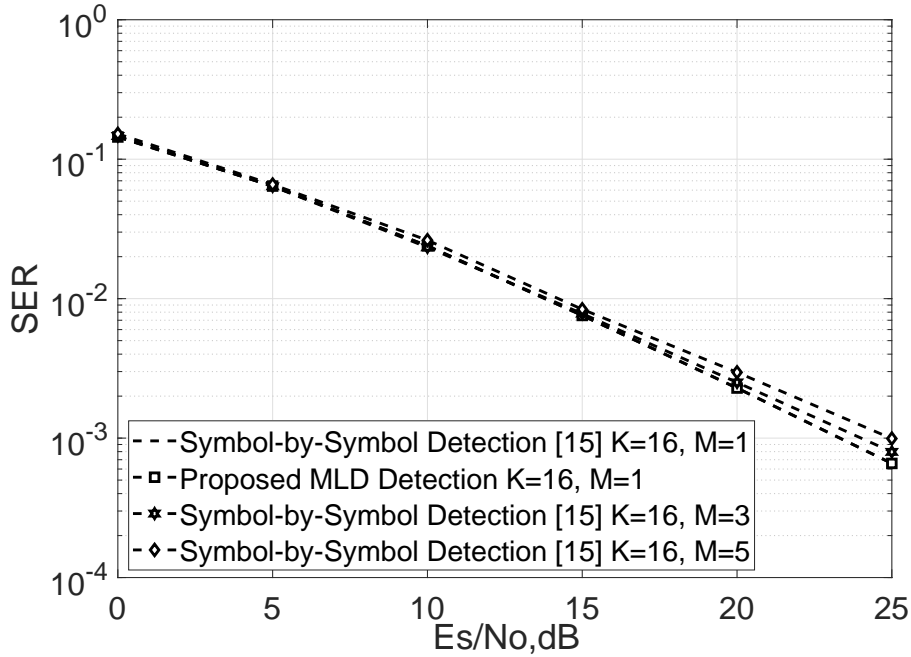
Figure 10.2: *Comparison of the SER performance between the proposed schema and with symbol-by sysmbol scheme given in [1] for BPSK GFDM in frequency selective Rayleigh fading channel with Dirichlet pulse shaping filter.*

MLD detection techniques in this letter is compatible with the two extreme case of GFDM and verify the performance with the benchmark results given in the literature for CP-based OFDM and DFT-s-OFDM.

Figure 10.2 reports the SEP versus Es/No for BPSK DGT-based GFDM system with symbol-by-symbol detection techniques implemented at the receiver given in [1] for different values of M and also compare the performance with proposed optimal MLD detection techniques implemented at the receiver for $M = 1$ for fixed K with frequency selective Rayleigh fading channel of 9-taps for Dirichlet pulse shaping filter.From the reults, it is clearly visible that for $M = 1$ proposed scheme and system-by symbol methode gives the same performance. Moreover, Fig. 10.2 confirm the limitation of the symbol-by symbol detector methode gien in [1], is that of not taking into account the sub-symbols transmitted with the same sub-carrier, thus introducing ISSI that degrades the SER performance.

To improve this, In this letter, we proposed the optimal MLD detector for DGT-based GFDM system. In the fig. 10.3 SER vurse Es/No performance for DGT-based GFDM system with optimal MLD detection techique implemented at the receiver are given for different values of M and fixed K for BPSK modulation technique in the case of the transmission over the frequency selective Rayleigh fading channel with 9-taps for Dirichlet pulse shaping filter. The result shows that by increasing the values of the M, the proposed optimal MLD detection technique implemented at the receiver of the DGT-based GFDM system performance better than symbol-by symbol methode.

156
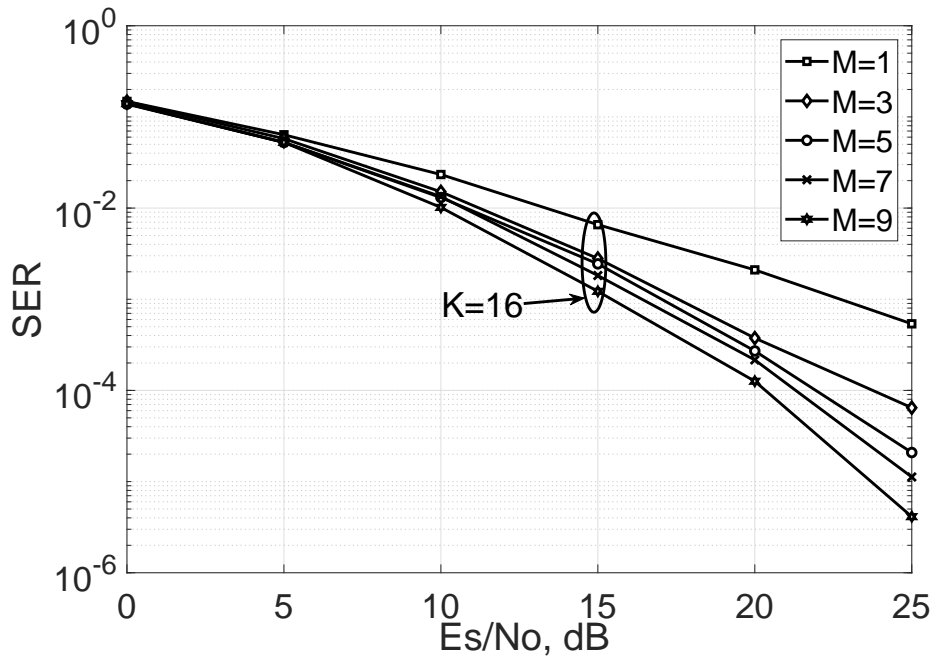
Figure 10.3: *SER verses SER of BPSK GFDM in frequency selective Rayleigh fading channel with Dirichlet pulse shaping filter with different values of M for same value of the bandwidth for $K = 16$.*

10.5 Summary

In this chapter, SER performance of the GFDM system with Dirichlet pulse shaping filter for BPSK has been given by taking into the account interference introduces by the sub-symbols on each sub-carrier. For SER performance evaluation at the receiver side we implemented the maximum likelihood detection. As expected, by increasing the values of the sub-symbols on each sub-carrier, the performance of GFDM degrades. As is well known, the flexible frame structure of GFDM allows, by changing the number of sub-symbols and of sub-carriers in a frame, covering both conventional CP-OFDM and DFT-s-OFDM.

CHAPTER *11*

Performance Evaluation of GFDM System

IN this chapter we derive exact SEP expressions for GFDM transceiver in the presence of CFO in AWGN channel and frequency selective Rayleigh fading channel. The analytical expressions of SEP are derived when matched filtering is implemented at the receiver for BPSK, QPSK, and 16-QAM in case of AWGN channel. In case of frequency selective Rayleigh fading channel the analytical expression is derived for BPSK.

11.1 Literature survey related to performance analysis

Several works available in the literature are related to the performance analysis of the GFDM system in the presence of synchronization errors [139]- [140]. In [139], **Choi** *et al.*, studied the effect of timing offset and CFO on the signal-to-interference ratio (SIR) for GFDM transmission over the AWGN channel through Monte Carlo simulations only. In [141], **Gaspar** *et al.* presented, for the first time, an analytical expression of the SER for the GFDM system with zero forcing receiver considering the same synchronization errors of [139] for BPSK modulation in case of transmission over the multipath Rayleigh fading channel. Finally, in [140], **Lim** *et al.* extended [139] by including the effect phase noise and derived an analytical expression of the SIR performance for the AWGN channel. Motivated by this, in this chapter we derive for the first time exact SEP expressions for GFDM system. We consider the case where MF is used at the receiver in the presence of CFO for transmission over AWGN and frequency selective Rayleigh fading channels.
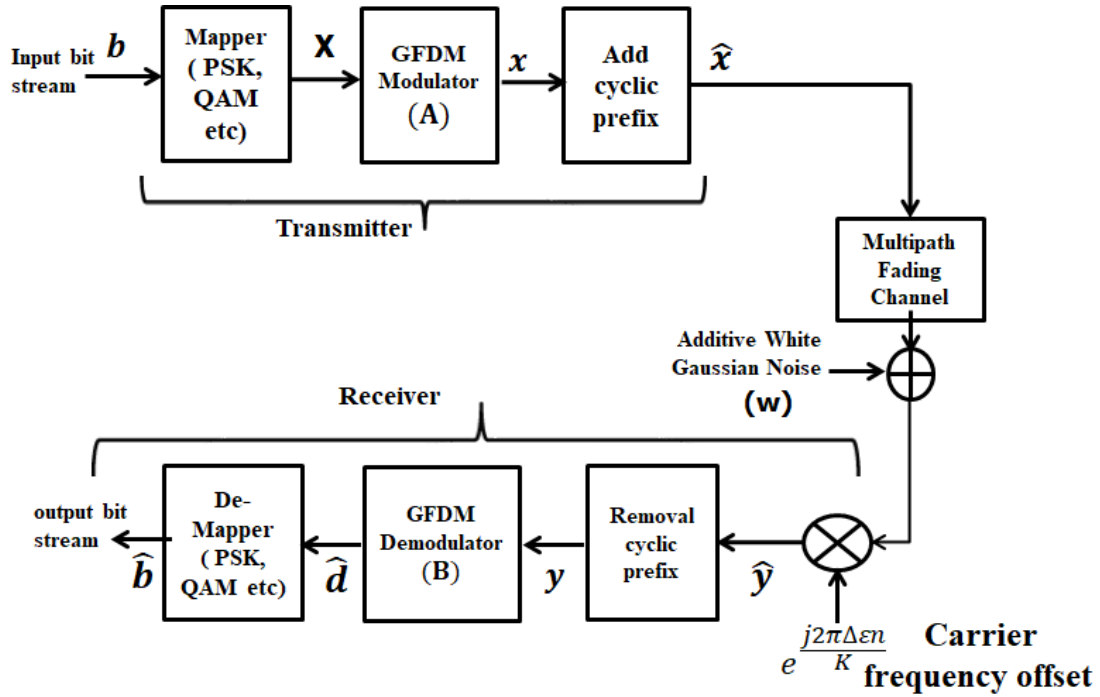
Figure 11.1: *System model of the GFDM system in presence of CFO.*
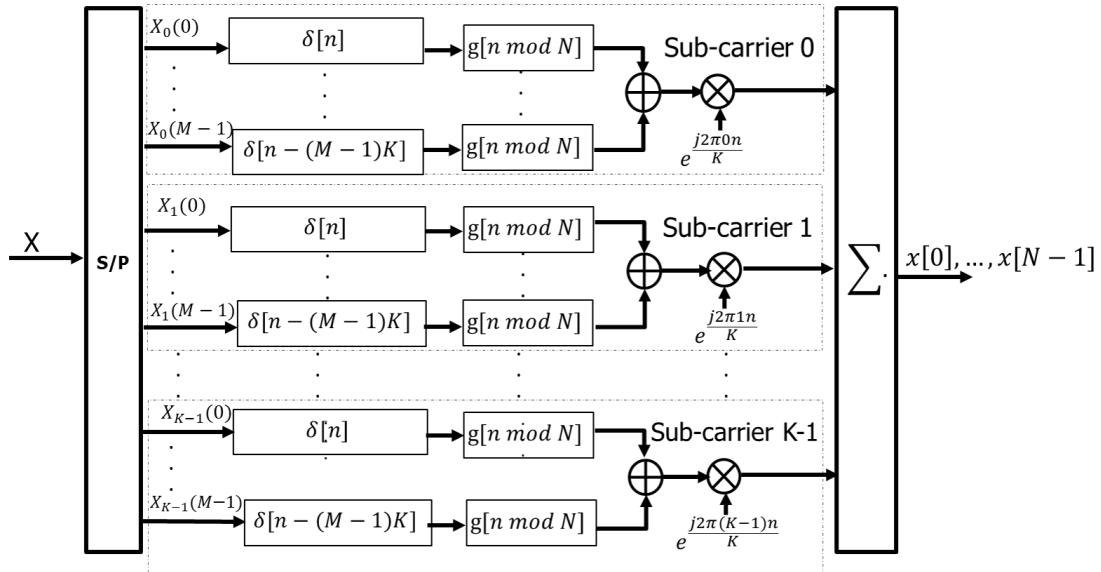
Figure 11.2: *Block diagram of the GFDM modulator with pulse shaping filter $g[n]$.*

11.2 GFDM System Model with Matched Filter

The block diagram of the GFDM system is shown in Fig. 11.1 where, for compactness, vector notation is adopted to denote variables. The vector of transmitted bits **b** is applied to the input of a mapper that gives at its output an $M \times K$ data matrix **X** whose

160
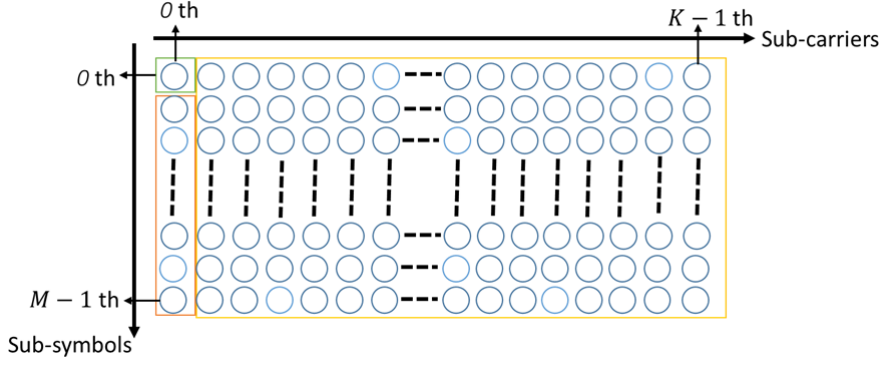
Figure 11.3: *Decomposition of the data matrix X with M sub-symbols (vertical direction) on the K sub-carriers (horizontal direction).*

$N = MK$ elements take values from a complex constellation, *e.g.*, PSK or QAM. The data matrix $\mathbf{X}$ is sent to the GFDM modulator, based on K sub-carriers, where each sub-carrier is used to transmit M sub-symbols. The scheme of the GFDM modulator is shown in Fig. 11.2. According to this model the data matrix $\mathbf{X}$ can be represented as the composition of K column vectors

$$\mathbf{X} = [\mathbf{X}_0, \mathbf{X}_1, \cdots, \mathbf{X}_{K-1}]$$

where

$$\mathbf{X}_k = [X_k(0), X_k(1), \cdots, X_k(M-1)]^T,$$

with $X_k(m)$ representing the mth sub-symbol from the set of M symbols transmitted on the kth sub-carrier and $(\cdot)^T$ denoting the transposition operation. The logical representation of $\mathbf{X}$ is shown in Fig. 11.3. The time-duration of each symbol vector $\mathbf{X}_k$ is MT_s with sub-carrier spacing equal to $1/(MT_s)$, T_s being the symbol interval. The kth group of M symbols is applied to the input of a pulse shaping filter with N coefficients. After pulse shape filtering, the nth transmitted sample in the time-domain is written as

$$x(n) = \sum_{k=0}^{K-1}\sum_{l=0}^{M-1} X_k(l)g_{k,l}[n] = \sum_{k=0}^{K-1}\sum_{l=0}^{M-1} X_k(l)g\left[\langle n - lK \rangle_N\right] e^{\frac{j2\pi kn}{K}}, \tag{11.1}$$

where $n = 0, 1, \cdots, KM - 1$ is the sampling index and $\langle \cdot \rangle_N$ denotes the modulo N operation that implements the circular shifting of the prototype discrete-time impulse response $g[n]$ obtained from the sampling of a continuous time impulse response $g(t)$ with sampling interval of T_s. Throughout this chapter, we assume that the first data symbol transmitted on the first sub-carrier is defined by $X_0(0)$. With this assumption ISI is introduced from sub-symbols 1 to $M-1$ transmitted on 0th sub-carrier and ICI, together with ISI, is introduced from all remaining sub-symbols transmitted on the other sub-carriers

After passing through the channel the received signal is written as

$$y(n) = e^{\frac{j2\pi\Delta\varepsilon n}{K}} \sum_{i=0}^{L-1} h_i \tilde{x}(n-i) + w(n), \tag{11.2}$$

161

where $w(n)$ represents the complex AWGN with zero mean and variance σ^2 per dimension and $\Delta\varepsilon = \Delta f M T_s$ is the residual CFO Δf normalized to the sub-carrier spacing.

Under the assumption $N_{CP} \geq L-1$, by removing the effect of the cyclic prefix and by replacing (11.1) in (11.2) we get

$$y(n) = e^{\frac{j2\pi\Delta\varepsilon n}{K}} \sum_{i=0}^{L-1} h_i \sum_{k=0}^{K-1} \sum_{l=0}^{M-1} X_k(l) g[\langle n-i-lK\rangle_N] e^{\frac{j2\pi k(n-i)}{K}} + w(n). \qquad (11.3)$$

In order to recover the transmitted symbols, the DGT defined in (**??**) is applied to the received signal, when we have $\gamma[n] = g[n]$, means that filtering implemented at the receiver with the analysis function $\gamma[n]$ can be therefore interpreted as matched filtering (MF). After passing through the MF receiver, the mth received sample on the qth sub-carrier is given by

$$\begin{aligned}
Y_q(m) &= \sum_{n=0}^{N-1} \gamma_{q,m}^*[n] y(n) = \sum_{n=0}^{N-1} \gamma^*[\langle n-mK\rangle_N] y(n) e^{-\frac{j2\pi qn}{K}} \\
&= \sum_{n=0}^{N-1} \left(\gamma^*[\langle n-mK\rangle_N] e^{\frac{j2\pi\Delta\varepsilon n}{K}} \sum_{k=0}^{K-1}\sum_{l=0}^{M-1} X_k(l) \sum_{i=0}^{L-1} h_i g[\langle n-i-lK\rangle_N] e^{\frac{j2\pi k(n-i)}{K}} + w(n) \right) e^{-\frac{j2\pi qn}{K}} \\
&= \sum_{k=0}^{K-1}\sum_{l=0}^{M-1} X_k(l) \sum_{n=0}^{N-1} \left(\gamma^*[\langle n-mK\rangle_N] \left\{ \sum_{i=0}^{L-1} h_i g[\langle n-i-lK\rangle_N] e^{\frac{-j2\pi ki}{K}} \right\} e^{\frac{j2\pi(q-k-\Delta\varepsilon)n}{K}} \right) + W_q(m) \\
&= \sum_{k=0}^{K-1}\sum_{l=0}^{M-1} X_k(l) \sum_{i=0}^{L-1} h_i \left\{ \sum_{n=0}^{N-1} \gamma^*[\langle n-mK\rangle_N] g[\langle n-i-lK\rangle_N] e^{-\frac{j2\pi(q-k-\Delta\varepsilon)n}{K}} \right\} e^{\frac{-j2\pi ki}{K}} + W_q(m) \\
&= \sum_{k=0}^{K-1}\sum_{l=0}^{M-1} X_k(l) \sum_{i=0}^{L-1} h_i \underbrace{\left\{ \sum_{n=0}^{N-1} \gamma^*[n] g[\langle n-i+(m-l)K\rangle_N] e^{-\frac{j2\pi(q-k-\Delta\varepsilon)n}{K}} \right\}}_{S_k(l,i,\Delta\epsilon)} e^{\frac{-j2\pi ki}{K}} + W_q(m),
\end{aligned}$$

$$(11.4)$$

where $W_q(m)$ is the DGT of the AWGN. The term $S_k(l, i, \Delta\epsilon)$ can be further written as

$$\begin{aligned}
S_k(l, i, \Delta\epsilon) &= \sum_{n=0}^{N-1} \gamma^*[n] g[\langle n-i+lK\rangle_N] e^{\frac{j2\pi M\Delta\epsilon n}{N}} e^{-\frac{j2\pi Mkn}{N}} \\
&= \sum_{n=0}^{N-1} \left(p[n,l,i] e^{\frac{j2\pi Mkn}{N}} \right) \cdot e^{\frac{j2\pi M\Delta\epsilon n}{N}} = P_{kM}^{\Delta\epsilon}[l, i], \ k=0,\dots,K-1, \ l=0,\dots,M-1,
\end{aligned}$$

$$(11.5)$$

where

$$P_k^{\Delta\epsilon}[l;i] = \sum_{n=0}^{N-1} p[n,l,i]e^{-\frac{j2\pi kn}{N}}e^{\frac{j2\pi M\Delta\epsilon n}{N}}$$

$$= P_k[l,i] \otimes_k \left\{ \frac{1}{N}\frac{\sin(\pi(k-M\Delta\epsilon))}{\sin\left(\frac{\pi(k-M\Delta\epsilon)}{N}\right)}e^{-\frac{j\pi(N-1)(k-M\Delta\epsilon)}{N}} \right\}, \quad (11.6)$$

being $\otimes_k$ the circular convolution computed over k and

$$P_{kM}[l,i] = \sum_{n=0}^{N-1} \gamma^*[n]g\left[\langle n-i+lK\rangle_N\right]e^{-\frac{j2\pi kn}{K}}$$

$$= \frac{1}{N}\sum_{q=0}^{N-1}\Gamma_q^* G_{\langle q+kM\rangle_N}e^{-\frac{j2\pi(kM+q)(i-lK)}{N}}$$

$$= \left(\frac{1}{N}\sum_{q=0}^{N-1}\Gamma_q^* G_{\langle q+kM\rangle_N}e^{\frac{j2\pi ql}{M}}e^{-\frac{j2\pi qi}{N}}\right)e^{-\frac{j2\pi ki}{K}}. \quad (11.7)$$

We consider in the following as function that satisfies the Wexler-Raz identity a Dirichlet pulse, also referred *discrete sinc*, which is characterized by a DFT that is a rectangular pulse

$$G_k^D = \begin{cases} 1, & (0 \le k \le \lceil\frac{M}{2}\rceil - 1) \cup (N - \lfloor\frac{M}{2}\rfloor \le k \le N-1), \\ 0 & otherwise, \end{cases} \quad (11.8)$$

where k is an integer, $\lceil\cdot\rceil$ denotes the nearest upper integer, and $\lfloor\cdot\rfloor$ nearest lower integer. With Dirichlet kernel function in frequency domain the orthogonality in frequency domain is always guaranteed. With the use of Dirichlet function we have $\gamma[n] = g[n]$, and the filtering implemented at the receiver with the analysis function $\gamma[n]$ can be therefore interpreted as matched filtering. By substituting the pulse shaping filter in (11.7), the equation (11.7) can be written as

$$P_{kM}[l,i] = \left(\frac{1}{N}\sum_{q=0}^{N-1}\Gamma_q^* G_{\langle q+kM\rangle_N}e^{\frac{j2\pi ql}{M}}e^{-\frac{j2\pi qi}{N}}\right)e^{-\frac{j2\pi ki}{K}}$$

$$= \begin{cases} \delta[k]\frac{1}{N}\sum_{q=-(M-1)/2}^{(M-1)/2}e^{-\frac{j2\pi q(i-lK)}{N}} = \delta[k]\frac{1}{N}\frac{\sin(\frac{\pi(i-lK)}{K})}{\sin\left(\frac{\pi(i-lK)}{N}\right)}, & M\text{odd} \\ \delta[k]\frac{1}{N}\sum_{q=-M/2}^{M/2-1}e^{-\frac{j2\pi q(i-lK)}{N}} = \delta[k]\frac{1}{N}\frac{\sin(\frac{\pi(i-lK)}{K})}{\sin\left(\frac{\pi(i-lK)}{N}\right)}e^{\frac{j\pi(i-lK)}{N}}, & M\text{even} \end{cases}$$

$$(11.9)$$

By substituting $P_kM[l,i]$ given in (11.9) into the (11.6), after some mathematical ma-

nipulation (11.6) can we rewritten as

$$
P_k^{\Delta\epsilon}[l;i] = \begin{cases} \delta[k]\frac{1}{N}\frac{\sin(\frac{\pi(i-lK)}{K})}{\sin\left(\frac{\pi(i-lK)}{N}\right)}, & M\,\text{odd} \\ \delta[k]\frac{1}{N}\frac{\sin(\frac{\pi(i-lK)}{K})}{\sin\left(\frac{\pi(i-lK)}{N}\right)}e^{\frac{j\pi(i-lK)}{N}}, & M\,\text{even} \end{cases} \otimes_k \underbrace{\left\{\frac{1}{N}\frac{\sin(\pi(k-M\Delta\epsilon))}{\sin\left(\frac{\pi(k-M\Delta\epsilon)}{N}\right)}e^{-\frac{j\pi(N-1)(k-M\Delta\epsilon)}{N}}\right\}}_{S_k(M\Delta\epsilon)}
$$

$$
= \begin{cases} S_k(M\Delta\epsilon)\frac{1}{N}\frac{\sin(\frac{\pi(i-lK)}{K})}{\sin\left(\frac{\pi(i-lK)}{N}\right)}, & M\,\text{odd} \\ S_k(M\Delta\epsilon)\frac{1}{N}\frac{\sin(\frac{\pi(i-lK)}{K})}{\sin\left(\frac{\pi(i-lK)}{N}\right)}e^{\frac{j\pi(i-lK)}{N}}, & M\,\text{even} \end{cases} \tag{11.10}
$$

By substituting $P_k^{\Delta\epsilon}[l;i]$ given in (11.10) into the (11.4), after some mathematical manipulation (11.4) can we rewritten as

$$
Y_q(m) = \sum_{k=0}^{K-1}\sum_{l=0}^{M-1}X_k(l)S_k(M\Delta\epsilon)\sum_{i=0}^{L-1}h_i\frac{\sin\left(\frac{\pi((m-l)K-i)}{K}\right)}{\sin\left(\frac{\pi((m-l)K-i)}{N}\right)}e^{\frac{-j2\pi qi}{K}} + W_q(m).
$$

$$
= \sum_{k=0}^{K-1}\sum_{l=0}^{M-1}X_k(l)S_k(M\Delta\epsilon)\bar{H}_q(m-l) + W_q(m). \tag{11.11}
$$

where the even property of the periodic Dirichlet sinc function has been used. The above equation shows that in case of Dirichlet function the interference is generated only by sub-symbols transmitted on the same sub-carrier and not from sub-symbols transmitted on other sub-carriers. The "windowed" channel is given by

$$
\bar{H}_q(m) = \sum_{i=0}^{N-1}h_i^{(ZP)}w_{\langle i-m\rangle_N}e^{\frac{-j2\pi qi}{N}}\Bigg|_{q=qK}, \tag{11.12}
$$

where $w_{\langle i-m\rangle_N}$ corresponds to a shifting of m samples of the periodic windowing function

$$
w_n = \frac{\sin\left(\frac{\pi n}{K}\right)}{\sin\left(\frac{\pi n}{N}\right)}, \qquad n = 0,\dots,N-1,
$$

and

$$
h_i^{(ZP)} = \begin{cases} h_i & i = 0,\dots,L-1, \\ 0 & i = L,\dots,N-1. \end{cases} \tag{11.13}
$$

Equation (11.12) can be rewritten

$$
\bar{H}_q(m) = H_q \otimes_N W_q e^{-j\frac{2\pi mq}{N}}, \tag{11.14}
$$

which is the circular convolution between the DFT of the channel and the DFT of the shifted windowing function, where $W_q = G_q^D$. According to the definition of G_k^D given in (11.8), eq. (11.14) realizes a weighted average of M frequency domain values of H_k around $k = q$, where the weights are obtained from the complex exponential for a given

m. The M samples H_k involved in the average are $k = \langle q - \lfloor \frac{M}{2} \rfloor, \ldots, q - 1 \rangle_N$ and $k = \langle q, \ldots, q + \lceil \frac{M}{2} \rceil - 1 \rangle_N$, which define the M points around q taking into account of the periodic nature of H_k. After some straightforward mathematical manipulations, (11.11) can be rewritten as

$$Y_q(m) = \underbrace{X_q(m)\,\bar{H}_{qM}(0)S_q(M\Delta\epsilon)}_{\substack{m\text{th sample received}\\ \text{on the }q\text{th sub-carrier}}} + \underbrace{\sum_{\substack{l=0,\\l\neq m}}^{M-1} X_q(l)\bar{H}_{qM}((m-l)K)S_q(M\Delta\epsilon)}_{\substack{\text{ISI induced by sub-symbols}\\ \text{other than }X_q(m)\text{ transmitted}\\ \text{on the }q\text{th sub-carrier}}}$$

$$+ \underbrace{\sum_{\substack{k=0,\\k\neq q}}^{K-1}\sum_{\substack{l=0,\\l\neq m}}^{M-1} X_k(l)\bar{H}_{kM}((m-l)K)S_k(M\Delta\epsilon)}_{\substack{\text{ICI and ISI due to}\\ \text{all sub-symbols transmitted}\\ \text{on sub-carriers other than }q}} + \underbrace{W_q(m)}_{\text{AWGN Noise}}, \qquad (11.15)$$

It is worth noting that the term $P_k^{\Delta\epsilon}[l;i]$ given in (11.10), which is responsible for the introduction of ICI and ISI terms defined in (11.15), includes both the effect of CFO and that of pulse shaping filter. Considering that GFDM is a generalization of OFDM, the inclusion of the pulse shaping filter effect represents one the main contributions of this work in comparison to the standard procedure to evaluate ICI introduced by CFO in OFDM - see, for example, [100, 101, 105].

11.3 SEP Analysis

In this section we present the derivation of the exact SEP expression for BPSK, QPSK and 16-QAM-based GFDM in AWGN and for BPSK modulation scheme in the frequency selective Rayleigh fading channel. Before proceeding with the derivation of an exact analytical expression of the SEP, worth recalling

$$\prod_{k=1}^{M} \cos(\varphi_k) = \frac{1}{2^{M-1}} \sum_{k=1}^{2^{M-1}} \cos(\phi^{\mathbf{T}}\mathbf{e_k}) = \frac{1}{2^M} \sum_{k=1}^{2^{M-1}} e^{j\phi^{\mathbf{T}}\mathbf{e_k}} + e^{-j\phi^{\mathbf{T}}\mathbf{e_k}}, \qquad (11.16)$$

where $\phi = [\varphi_1, \varphi_2, \ldots, \varphi_M]^{\mathbf{T}}$ and e_k is the kth column of the $M \times 2^{M-1}$ matrix $\boldsymbol{E}_M$ that defines the binary representation of the number $2^M - k$, where zeros are replaced by -1s.

11.3.1 AWGN

In this section, we derive an exact SEP expression for GFDM in the presence of CFO for BPSK, QPSK and 16-QAM modulations when transmission takes place over the AWGN channel. The ideal AWGN channel is obtained by setting $L = 1$ with $h_0 = 1$ in (10.5), so that $\bar{S}_k(l)$ turns out in $S_k(l, 0)$. Now, for AWGN channel, we replace $\bar{S}_k(l)$ with $S_k(l, 0)$ in (10.17) for deriving the analytical expressions of SEP.

BPSK

The symbols are drawn from the set $\{\pm 1\}$. Without loosing generality we assume that $X_0(0) = +1$. With this assumption the received signal on the zeroth sub-carrier is expressed as

$$Y_0(0) = S_0(0,0) + \sum_{l=1}^{M-1} X_0(l)S_0(l,0) + \sum_{k=1}^{K-1}\sum_{l=0}^{M-1} X_k(l)\, S_k(l,0) + W_0(0). \quad (11.17)$$

The expression of SEP $P_s(\zeta)$ can be obtained by resorting to the characteristic function (CHF) approach described in [138]. Since BPSK constellation is purely real, only the real part of (11.17) will be considered for computation of the CHF. After some mathematical manipulations, the CHF of the real part of $Y_0(0)$ is written as

$$\varphi_{\Re[Y_0(0)]}(\omega) = E\left[e^{j\omega\Re[S_0(0,0)]}\right] \times \prod_{l=1}^{M-1} E\left[e^{j\omega\Re[X_0(l)S_0(l,0)]}\right]$$

$$\times \prod_{k=1}^{K-1}\prod_{l=0}^{M-1} E\left[e^{j\omega\Re[X_k(l)S_k(l,0)]}\right] \times E\left[e^{j\omega\Re[W_0(0)]}\right], \quad (11.18)$$

where $E[\cdot]$ denotes the statistical expectation and $\Re[\cdot]$ denotes the real part. By applying straightforward algebra and by using the trigonometric identity given in (11.16), (11.18) can be rewritten as

$$\varphi_{\Re[Y_0(0)]}(\omega) = e^{j\omega\Re[S_0(0,0)] - \frac{\omega^2\sigma^2}{2}} \times \left\{ \frac{1}{2^{M-1}} \sum_{n=1}^{2^{M-2}} e^{j\omega \boldsymbol{S}^T \boldsymbol{\xi}_n} + e^{-j\omega \boldsymbol{S}^T \boldsymbol{\xi}_n} \right\}$$

$$\times \left\{ \prod_{l=0}^{M-1} \left(\frac{1}{2^{K-2}} \sum_{k=1}^{2^{K-2}} \cos\left(\omega \boldsymbol{S}(l)^T \boldsymbol{\epsilon}_k\right) \right) \right\}, \quad (11.19)$$

where $\boldsymbol{S} = \Re\left[S_{0,0}(1), S_{0,0}(2), \cdots, S_{0,0}(M-1)\right]^T$, $\boldsymbol{\xi}_n$ is the nth column of the $M - 1 \times 2^{M-2}$ matrix $\mathbf{E}_{M-1}$, $\boldsymbol{S}(l) = \Re[S_{1,0}(l), S_{2,0}(l), \cdots, S_{K-1,0}(l)]^T$, and $\boldsymbol{\epsilon}_k$ is the kth column of the $K - 1 \times 2^{K-2}$ matrix $\mathbf{E}_{K-1}$. Now, we need to exchange the order of the sum with that of the product in the last part of (11.19). To do this we must take into account all the possible dispositions with repetition of length M of the 2^{K-2} vectors defining columns of matrix $\mathbf{E}_{K-1}$, which are a total of $2^{(K-2)M}$. After some straightforward passages we get

$$\varphi_{\Re[Y_0(0)]}(\omega) = e^{j\omega\Re[S_0(0,0)] - \frac{\omega^2\sigma^2}{2}} \times \frac{1}{2^{M-1}} \sum_{n=1}^{2^{M-2}} e^{j\omega \boldsymbol{S}^T \boldsymbol{\xi}_n} + e^{-j\omega \boldsymbol{S}^T \boldsymbol{\xi}_n}$$

$$\times \left\{ \frac{1}{2^{K-2}} \sum_{p=1}^{2^{(K-2)M}} \prod_{l=0}^{M-1} \cos\left(\omega \boldsymbol{S}(l)^T \boldsymbol{d}_{l,p}\right) \right\}, \quad (11.20)$$

where $\boldsymbol{d}_{p,l}$ is the lth column of the pth disposition matrix with size $(K-1) \times M$ given by

$$\mathbf{D}_p = [\boldsymbol{d}_{p,1} \ \ \boldsymbol{d}_{p,2} \ \ \cdots \ \ \boldsymbol{d}_{p,M}], \tag{11.21}$$

being $\mathbf{d}_{i,p}$ the vector in position i in disposition p, with $p = 1, \cdots, 2^{(K-2)M}$. The $2^{(K-2)M}$ dispositions define the column indexes of E_M. Applying again trigonometric identity given in (11.16) to the last product in (11.20) we get

$$\varphi_{\Re[Y_0(0)]}(\omega) = \frac{1}{2^{K+2M-3}} \sum_{l=0}^{2^{M-1}-1} \sum_{p=1}^{2^{(K-2)M}} \sum_{n=1}^{2^{M-2}}$$
$$e^{j\omega\alpha_{l,p}^n - \frac{\omega^2\sigma^2}{2}} + e^{j\omega\beta_{l,p}^n - \frac{\omega^2\sigma^2}{2}} + e^{j\omega\delta_{l,p}^n - \frac{\omega^2\sigma^2}{2}} + e^{j\omega\gamma_{l,p}^n - \frac{\omega^2\sigma^2}{2}}, \tag{11.22}$$

where

$$\begin{aligned}
\alpha_{l,p}^n &= \Re\left[S_0(0,0) + \boldsymbol{S}^T\boldsymbol{\xi}_n + \boldsymbol{\Lambda}_{l,p}{}^T\boldsymbol{e}_l\right], \\
\beta_{l,p}^n &= \Re\left[S_0(0,0) - \boldsymbol{S}^T\boldsymbol{\xi}_n + \boldsymbol{\Lambda}_{l,p}{}^T\boldsymbol{e}_l\right], \\
\delta_{l,p}^n &= \Re\left[S_0(0,0) + \boldsymbol{S}^T\boldsymbol{\xi}_n - \boldsymbol{\Lambda}_{l,p}{}^T\boldsymbol{e}_l\right], \\
\gamma_{l,p}^n &= \Re\left[S_0(0,0) - \boldsymbol{S}^T\boldsymbol{\xi}_n - \boldsymbol{\Lambda}_{l,p}{}^T\boldsymbol{e}_l\right],
\end{aligned}$$

with $\boldsymbol{\Lambda}_{l,p} = \boldsymbol{S}(l)^T\boldsymbol{d}_{p,l}$. It can be observed that (11.22) represents the CHF of a mixture of Gaussian densities. Now, an error will occur only if $\Re[Y_0(0)] < 0$. The probability of this event can be computed as

$$P_s(\zeta) = \int_{-\infty}^{0} f_{\Re[Y_0(0)]}(x)\, dx, \tag{11.23}$$

where $f_{\Re[Y_0(0)]}(\cdot)$ is the PDF obtained from the inverse Fourier transform of the CHF given in (11.22). The solution of (11.23) gives the following expression for the SEP

$$P_s(\zeta) = \frac{1}{2^{K+2M-3}} \sum_{l=1}^{2^{M-1}-1} \sum_{p=1}^{2^{(K-2)M}} \sum_{n=1}^{2^{M-2}} Q\left(\sqrt{2\rho}\alpha_{l,p}^n\right) + Q\left(\sqrt{2\rho}\beta_{l,p}^n\right) + Q\left(\sqrt{2\rho}\delta_{l,p}^n\right) + Q\left(\sqrt{2\rho}\gamma_{l,p}^n\right), \tag{11.24}$$

where $\rho = E_s/N_0$ is the signal-to-noise ratio (SNR) and $Q(\cdot)$ is the Gaussian Q function. One should note that in our case $E_s = 1$ and $N_0 = 2\sigma^2$. By substituting $M = 1$ and $g[n] = \mathrm{rect}\left(\frac{t-NT_s/2}{NT_s}\right)\Big|_{t=nT_s}$, we get the conventional OFDM. In this case (11.24) reduces to (6) of [100].

QPSK

To analyze the SEP performance of QPSK transmission, we write the received signal as

$$Y_0(0) = \underbrace{X_0(0)S_0(0,0) + \sum_{l=1}^{M-1} X_0(l)S_0(l,0) + \sum_{k=1}^{K-1}\sum_{l=0}^{M-1} X_k(l)S_k(l,0)}_{R_0(0)} + W_0(0).$$

(11.25)

In this case the symbols are drawn from the set $\{\pm 1 \pm j\}$. Without loss of generality, we assume $X_0(0) = 1 + j$. With this assumption we do not have any error when $Y_0(0)$ lies in the first quadrant D_1 of the complex plan. The probability of making a correct decision conditioned to the transmission of symbol $1 + j$ on the zeroth sub-carrier of the zeroth transmitted symbol is given by [138]

$$P(Y_0(0) \in D_1 | X_0(0) = 1 + j, R_0(0)) = Q\left(-\frac{\Re[R_0(0)]}{\sigma}\right) Q\left(-\frac{\Im[R_0(0)]}{\sigma}\right),$$

(11.26)

where $\Im[c]$ denotes the imaginary part of complex number c. By doing considerations similar to those done in Sec. 11.3.1, the probability of correct decision is obtained by averaging (11.26) over the PDF of the useful part of received signal $R_0(0)$ given in (11.25). Since $R(0)$ is a two-dimensional (2-D) random variable, the resulting CHF is also 2-D and can be written as

$$\varphi_{\Re[R(0)]}(\omega_I, \omega_Q) = e^{j\left(\omega_I(\Re[S_0(0,0)] - \Im[S_0(0,0)]) + \omega_Q(\Im[S_0(0,0)] + \Re[S_0(0,0)])\right)}$$

$$\times \prod_{l=1}^{M-1} \cos(\omega_I \Re[S_0(l,0)] + \omega_Q \Im[S_0(l,0)]) \times \cos(\omega_I \Im[S_0(l,0)] - \omega_Q \Re[S_0(l,0)])$$

$$\times \prod_{K=1}^{K-1}\prod_{l=0}^{M-1} \cos(\omega_I \Re[S_k(l,0)] + \omega_Q \Im[S_k(l,0)]) \times \cos(\omega_I \Im[S_k(l,0)] - \omega_Q \Re[S_k(l,0)]).$$

(11.27)

Equation (11.27) can be simplified using a vector notation as

$$\varphi_{\Re[R(0)]}(\omega_I, \omega_Q) = e^{\left(j\boldsymbol{\Omega}^T\left(\mathbf{S}_0^A(0,0) - \mathbf{S}_0^B(0,0)\right)\right)} \times \prod_{n=1}^{M-1} \cos\left(\boldsymbol{\Omega}^T \mathbf{S}_0^A(n,0)\right) \times \cos\left(\boldsymbol{\Omega}\boldsymbol{S}_0^B(n,0)\right)$$

$$\times \prod_{K=1}^{K-1}\prod_{l=0}^{M-1} \cos\left(\boldsymbol{\Omega}^T \mathbf{S}_k^A(l,0)\right) \times \cos\left(\boldsymbol{\Omega}\boldsymbol{S}_k^B(l,0)\right),$$

(11.28)

168

where $\mathbf{S}_k^A(l,0)=\begin{bmatrix}\Re[S_k(l,0)]\\\Im[S_k(l,0)]\end{bmatrix}, \mathbf{S}_k^B(l,0)=\begin{bmatrix}\Im[S_k(l,0)]\\-\Re[S_k(l,0)]\end{bmatrix}$ and $\boldsymbol{\Omega}=\begin{bmatrix}\omega_I & \omega_Q\end{bmatrix}^T$. Now, (11.28) can be expressed using the trigonometric identity given in (11.16) as

$$\varphi_{\Re[R(0)]}\big(\omega_I,\omega_Q\big)=e^{j\boldsymbol{\Omega}^T\big(\mathbf{S}_0^A(0,0)-\mathbf{S}_0^B(0,0)\big)}\times\left\{\frac{1}{2^{2(M-2)}}\sum_{n=1}^{2^{M-2}}\sum_{q=1}^{2^{M-2}}\cos\big(\boldsymbol{\Omega}^T\mathbf{S}_0^A e_n\big)\cos\big(\boldsymbol{\Omega}^T\mathbf{S}_0^B e_q\big)\right\}$$

$$\times\prod_{l=0}^{M-1}\left\{\frac{1}{2^{2(K-2)}}\sum_{l=1}^{2^{K-2}}\sum_{m=1}^{2^{K-2}}\cos\big(\boldsymbol{\Omega}^{\mathrm{T}}\mathbf{S}^A(l)e_l\big)\cos\big(\boldsymbol{\Omega}^{\mathrm{T}}\mathbf{S}^B(l)e_m\big)\right\}, \quad (11.29)$$

where $\mathbf{S}_0^A=[\mathbf{S}_0^A(1,0),\mathbf{S}_0^A(2,0),\cdots,\mathbf{S}_0^A(M-1,0)], \mathbf{S}_0^B=[\mathbf{S}_0^B(1,0),\mathbf{S}_0^B(2,0),\cdots,\mathbf{S}_0^B(M-1,0)],$ $\mathbf{S}^A(l)=[\mathbf{S}_1^A(l,0),\mathbf{S}_2^A(l,0),\cdots,\mathbf{S}_{K-1}^A(l,0)]$ and $\mathbf{S}^B(l)=[\mathbf{S}_1^B(l,0),\mathbf{S}_2^B(l,0),\cdots,\mathbf{S}_{K-1}^B(l,0)]$.

As done for BPSK in Sec. 11.3.1, we need to consider all the combinations in the last part of (11.29) because the exchanging of sum and product operations. Again, using the identity given in (11.16), we can rewrite (11.29) as

$$\varphi_{\Re[R(0)]}\big(\omega_I,\omega_Q\big)=e^{j\boldsymbol{\Omega}^T\big(\mathbf{S}_0^A(0,0)-\mathbf{S}_0^B(0,0)\big)}\times\frac{1}{2^{2(M-2)}}\sum_{n=1}^{2^{M-2}}\sum_{q=1}^{2^{M-2}}\cos\big(\boldsymbol{\Omega}^T\mathbf{S}_0^A e_n\big)\cos\big(\boldsymbol{\Omega}^T\mathbf{S}_0^B e_q\big)$$

$$\times\frac{1}{2^{2(K-2)}}\frac{1}{2^{2M}}\sum_{p=1}^{2^{(K-2)M}}\sum_{r=1}^{2^{(K-2)M}}\sum_{l_1=0}^{2^{M-1}-1}\sum_{l_2=0}^{2^{M-1}-1}\cos\big(\boldsymbol{\Omega}^T\boldsymbol{\lambda}_{l_1,p}^A e_{l_1}\big)\cos\big(\boldsymbol{\Omega}^{\mathrm{T}}\boldsymbol{\lambda}_{l_2,r}^B e_{l_2}\big), \quad (11.30)$$

where $\boldsymbol{\lambda}_{l_1,p}^A=\mathbf{S}^A(l_1)e_{l_1,p}$, $\boldsymbol{\lambda}_{l_2,p}^B=\mathbf{S}^B(l_2)e_{l_2,r}$, $\mathbf{e}_{p,l_1}$ and $\mathbf{e}_{p,l_2}$ is the lth column of pth $(K-1)\times M$ matrix given in (11.21), respectively. After the simplification we can rewrite the above equation as

$$\varphi_{\Re[R(0)]}\big(\omega_I,\omega_Q\big)=\frac{1}{2^{2(K+2M-2)}}\sum_{n=1}^{2^{M-2}}\sum_{q=1}^{2^{M-2}}\sum_{p=1}^{2^{(K-2)M}}\sum_{r=1}^{2^{(K-2)M}}\sum_{l_1=0}^{2^{M-1}-1}\sum_{l_2=0}^{2^{M-1}-1}\{C1+C2+\cdots+C16\},$$

$$(11.31)$$

where $\boldsymbol{C}_{n,q,p,r,l_1,l_2}(i)=e^{j\boldsymbol{\Omega}^T(\mathbf{S}_0^A(0,0)-\mathbf{S}_0^B(0,0))}+\boldsymbol{G}_{n,q,p,r,l_1,l_2}(i)$, for $i=1,2,\ldots,16$, and $\boldsymbol{G}_{n,q,p,r,l_1,l_2}=\boldsymbol{A}\times\boldsymbol{B}$, in which $\boldsymbol{A}$ and $\boldsymbol{B}$ are defined as

$$\boldsymbol{A}=e^{j\boldsymbol{\Omega}^T(\mathbf{S}_0^A e_n+\mathbf{S}_0^B e_q)}+e^{j\boldsymbol{\Omega}^T(-\mathbf{S}_0^A e_n+\mathbf{S}_0^B e_q)}+e^{j\boldsymbol{\Omega}^T(\mathbf{S}_0^A e_n-\mathbf{S}_0^B e_q)}+e^{j\boldsymbol{\Omega}^T(-\mathbf{S}_0^A e_n-\mathbf{S}_0^B e_q)}$$

and

$$\boldsymbol{B}=e^{j\boldsymbol{\Omega}^T(\boldsymbol{\lambda}_{l_1,p}^A e_{l_1}+\boldsymbol{\lambda}_{l_2,p}^B e_{l_2})}+e^{j\boldsymbol{\Omega}^T(-\boldsymbol{\lambda}_{l_1,p}^A e_{l_1}+\boldsymbol{\lambda}_{l_2,p}^B e_{l_2})}+e^{j\boldsymbol{\Omega}^T(\boldsymbol{\lambda}_{l_1,p}^A e_{l_1}-\boldsymbol{\lambda}_{l_2,p}^B e_{l_2})}+e^{j\boldsymbol{\Omega}^T(-\boldsymbol{\lambda}_{l_1,p}^A e_{l_1}-\boldsymbol{\lambda}_{l_2,p}^B e_{l_2})},$$

respectively. By taking the inverse Fourier transform of the CHF given in (11.31) we get the 2D PDF of the real and imaginary parts of the received signal used to average (11.26), as done in [138]. Finally, the SEP expression is obtained by subtracting the probability of correct decision to 1 as

$$P_s\left(\zeta\right)=1-\frac{1}{2^{2(K+2M-4)}}\sum_{n=1}^{2^{M-2}}\sum_{q=1}^{2^{M-2}}\sum_{p=1}^{2^{(K-2)M}}\sum_{r=1}^{2^{(K-2)M}}\sum_{l_1=0}^{2^{M-1}-1}\sum_{l_2=0}^{2^{M-1}-1}\sum_{f=1}^{16}$$

$$Q\left(-\sqrt{2\rho}\,\kappa_{n,q,p,r,l_1,l_2}\left[1,m\right]\right)\times Q\left(-\sqrt{2\rho}\,\kappa_{n,q,p,r,l_1,l_2}\left[2,m\right]\right). \qquad (11.32)$$

where $\kappa_{n,q,p,r,l1,l2}\left[p,q\right]$ is the p,q entry of the 2×16 matrix $\mathbf{G}\triangleq[\mathbf{C}1,\mathbf{C}2,\mathbf{C}3,\cdots,\mathbf{C}16]$. By substituting $M=1$ and $g[n]=\left.\mathrm{rect}\left(\frac{t-NT_s/2}{NT_s}\right)\right|_{t=nT_s}$, (11.32) reduces to (18) of [100], this confirms again the correctness of the derived SEP expression.

16-QAM

By following Sec. 11.3.1, in what follows we assume that symbol transmitted on the zeroth sub-carrier is $X_0\left(0\right)\in\{1+j,1+3j,3+j,3+3j\}$. Here, we consider that the first transmitted symbol $X_0(0)=1+j$ lies in the area $D_{s1}=\{a+bj|0\leq a\leq2,0\leq b\leq2\}$ of the complex plane. Thus, the probability of making a correct decision corresponds to the probability that

$$P_{c,1}(Y_0(0)\in D_{s1}|X_0(0)=1+j,R_0(0))=\int_0^2\frac{1}{\sqrt{2\pi}\sigma}e^{-\frac{(x-\Re[R_0(0)])^2}{2\sigma^2}}dx\times\int_0^2\frac{1}{\sqrt{2\pi}\sigma}e^{-\frac{(y-\Im[R_0(0)])^2}{2\sigma^2}}dy$$

$$=\left[Q\left(\frac{-\Re[R_0(0)]}{\sigma}\right)-Q\left(\frac{2-\Re[R_0(0)]}{\sigma}\right)\right]\times\left[Q\left(\frac{-\Im[R_0(0)]}{\sigma}\right)-Q\left(\frac{2-\Im[R_0(0)]}{\sigma}\right)\right]$$

$$=\kappa(0,0)-\kappa(0,2)-\kappa(2,0)+\kappa(2,2), \qquad (11.33)$$

where $\kappa(a,b)$ is defined as

$$\kappa(a,b)=\mathrm{Q}\left(\frac{a-\Re\left[R_0\left(0\right)\right]}{\sigma}\right)\times\mathrm{Q}\left(\frac{b-\Im\left[R_0\left(0\right)\right]}{\sigma}\right). \qquad (11.34)$$

So, for the computation of the SEP, we first need to compute the individual probability of correct decision, then compute the average and, finally, subtract the result from 1. The computation of the probability of correct decision of the individual terms is obtained by averaging (11.35) over the 2D-PDF defined by the real and imaginary parts of $R_0\left(0\right)$ as

$$P_{c,1\,avg}(Y_0(0)\in D_{s1}|X_0(0)=1+j)=\int_{-\infty}^{\infty}\int_{-\infty}^{\infty}P_{c,1}(Y_0(0)\in D_{s1}|X_0(0)=1+j,\Re[R_0(0)]\Im[R_0(0)])$$

$$p(\Re[R_0(0)],\Im[R_0(0)]|X_0(0)=1+j)\,d\Re[R_0(0)]d\Im[R_0(0)]. \qquad (11.35)$$

To evaluate (11.35) we need to derive a expression of $p(\Re[R_0(0)],\Im[R_0(0)]|X_0(0)=1+j)$. The simplest way to do this is to compute its 2D CHF in the frequency domain. Following the analysis done in Sec. 11.3.1, the computation of the 2D-CHF is written

as

$$\varphi_{\Re[R_0(0)]}\left(\omega_I,\omega_Q\right)=E\left[e^{\left[j\{\Omega^T \boldsymbol{S}_0^A(0,0)\Re[X_0(0)]-\Omega^T \boldsymbol{S}_0^B(0,0)\Im[X_0(0)]\}\right]}\right]\times\prod_{n=1}^{M-1}$$

$$E\left[e^{\left[j\left(\Omega^T \boldsymbol{S}_0^A(n,0)\Re[X_0(n)]-\Omega^T \boldsymbol{S}_0^A(n,0)\Im[X_0(n)]\right)\right]}\right]\times\prod_{k=1}^{K-1}\prod_{l=0}^{M-1}E\left[e^{\left[j\left(\Omega^T \boldsymbol{S}_k^A(l,0)\Re[X_k(l)]-\Omega^T \boldsymbol{S}_k^A(l,0)\Im[X_k(l)]\right)\right]}\right].$$

(11.36)

Let us assume that the transmitted symbol is $X_0(0) = 1 + j$. After substituting the value of $X_0(0)$ the above equation is written as

$$\varphi_{\Re[R_0(0)]}\left(\omega_I,\omega_Q\right)=E\left[e^{\left[j\{\Omega^T \boldsymbol{S}_0^A(0,0)-\Omega^T \boldsymbol{S}_0^B(0,0)\}\right]}\right]\times\prod_{n=1}^{N-1}\cos\left(\Omega^T \boldsymbol{S}_0^A(n,0)\right)\cos\left(2\Omega^T \boldsymbol{S}_0^A(n,0)\right)$$

$$\times\cos\left(\Omega^T \boldsymbol{S}_0^B(n,0)\right)\cos\left(2\Omega^T \boldsymbol{S}_0^B(n,0)\right)\times\prod_{k=1}^{N-1}\prod_{l=0}^{N-1}\cos\left(\Omega^T \boldsymbol{S}_k^A(l,0)\right)\cos\left(2\Omega^T \boldsymbol{S}_k^A(l,0)\right)$$

$$\times\cos\left(\Omega^T \boldsymbol{S}_k^B(l,0)\right)\cos\left(2\Omega^T \boldsymbol{S}_k^B(l,0)\right).$$

(11.37)

Now, (11.37) can be expressed using the trigonometric identity given in (11.16) as

$$\varphi_{\Re[R(0)]}\left(\omega_I,\omega_Q\right)= e^{\left(j\Omega^T\left(\mathbf{S}_0^A(0,0)-\mathbf{S}_0^B(0,0)\right)\right)}\times$$

$$\left\{\frac{1}{2^{4(M-2)}}\sum_{n_1=1}^{2^{M-2}}\sum_{n_2=1}^{2^{M-2}}\sum_{q_1=1}^{2^{M-2}}\sum_{q_2=1}^{2^{M-2}}\cos(\Omega^T\mathbf{S}_0^A e_{n_1})\cos(2\Omega^T\mathbf{S}_0^A e_{n_2})\cos(\Omega^T\mathbf{S}_0^B e_{q_1})\cos(2\Omega^T\mathbf{S}_0^B e_{q_2})\right\}$$

$$\times\prod_{l=0}^{M-1}\left\{\frac{1}{2^{4(K-2)}}\sum_{l_1=1}^{2^{K-2}}\sum_{l_2=1}^{2^{K-2}}\sum_{m_1=1}^{2^{K-2}}\sum_{m_2=1}^{2^{K-2}}\cos(\Omega^T\mathbf{S}^A(l)e_{l_1})\cos(2\Omega^T\mathbf{S}^A(l)e_{l_2})\cos(\Omega^T\mathbf{S}^B(l)e_{m_1})\cos(2\Omega^T\mathbf{S}^B(l)e_{m_2})\right\}.$$

(11.38)

As done in Sec. 11.3.1, we need to consider all the combinations in the last part of (11.38) because the exchanging of sum and product operations. Again, using the identity given in (11.16), we can rewrite (11.38) as

$$\varphi_{\Re[R(0)]}\left(\omega_I,\omega_Q\right)= e^{\left(j\Omega^T\left(\mathbf{S}_0^A(0,0)-\mathbf{S}_0^B(0,0)\right)\right)}$$

$$\times\frac{1}{2^{4(M-2)}}\sum_{n_1=1}^{2^{M-2}}\sum_{n_2=1}^{2^{M-2}}\sum_{q_1=1}^{2^{M-2}}\sum_{q_2=1}^{2^{M-2}}\cos(\Omega^T\mathbf{S}_0^A e_{n_1})\cos(2\Omega^T\mathbf{S}_0^A e_{n_2})\cos(\Omega^T\mathbf{S}_0^B e_{q_1})\cos(2\Omega^T\mathbf{S}_0^B e_{q_2})$$

$$\times\frac{1}{2^{4(K-2)}}\frac{1}{2^{4M}}\sum_{p=1}^{2^{(K-2)M}}\sum_{q=1}^{2^{(K-2)M}}\sum_{r=1}^{2^{(K-2)M}}\sum_{s=1}^{2^{(K-2)M}}\sum_{l1=0}^{2^{M-1}-1}\sum_{l2=0}^{2^{M-1}-1}\sum_{l3=0}^{2^{M-1}-1}\sum_{l4=0}^{2^{M-1}-1}$$

$$\times\cos\left(\Omega^T\boldsymbol{\lambda}_{l_1,p}^A e_{l1}\right)\cos\left(2\Omega^T\boldsymbol{\lambda}_{l_2,q}^A e_{l2}\right)\cos\left(\Omega^T\boldsymbol{\lambda}_{l_3,r}^B e_{l3}\right)\cos\left(2\Omega^T\boldsymbol{\lambda}_{l_4,s}^B e_{l4}\right).$$

(11.39)

After the simplification, we can rewrite the above equation as

$$\varphi_{\Re[R(0)]}(\omega_I,\omega_Q)=\frac{1}{2^{4(K+2M-2)}}\sum_{n_1=1}^{2^{M-2}}\sum_{n_2=1}^{2^{M-2}}\sum_{q_1=1}^{2^{M-2}}\sum_{q_2=1}^{2^{M-2}}\sum_{p=1}^{2^{(K-2)M}}\sum_{q=1}^{2^{(K-2)M}}\sum_{r=1}^{2^{(K-2)M}}\sum_{s=1}^{2^{(K-2)M}}$$

$$\sum_{l1=0}^{2^{M-1}-1}\sum_{l2=0}^{2^{M-1}-1}\sum_{l3=0}^{2^{M-1}-1}\sum_{l4=0}^{2^{M-1}-1}\big\{\ \boldsymbol{C}(1)+\boldsymbol{C}(2)+\cdots+\boldsymbol{C}(256)\ \big\}.$$

(11.40)

where $\boldsymbol{C}_{n_1,n_2,q_1,q_2,p,q,r,s,l_1,l_2,l_3,l_4}(i)=e^{j\boldsymbol{\Omega}^T(\mathbf{S}_0^A(0,0)-\mathbf{S}_0^B(0,0))}+\boldsymbol{G}_{n_1,n_2,q_1,q_2,p,q,r,s,l_1,l_2,l_3,l_4}(i)$ for $1,2,\cdots256$ and $G_{n_1,n_2,q_1,q_2,p,q,r,s,l_1,l_2,l_3,l_4}=\boldsymbol{A}\times\boldsymbol{B}$. In this case $\boldsymbol{A}$ and $\boldsymbol{B}$ are defined as

$$A=e^{j\boldsymbol{\Omega}^T(\mathbf{S}_0^A e_{n_1}+2\mathbf{S}_0^A e_{n_2}+\mathbf{S}_0^B e_{q_1}+2\mathbf{S}_0^B e_{q_2})}+e^{j\boldsymbol{\Omega}^T(-\mathbf{S}_0^A e_{n_1}+2\mathbf{S}_0^A e_{n_2}+\mathbf{S}_0^B e_{q_1}+2\mathbf{S}_0^B e_{q_2})}$$

$$+e^{j\boldsymbol{\Omega}^T(\mathbf{S}_0^A e_{n_1}-2\mathbf{S}_0^A e_{n_2}+\mathbf{S}_0^B e_{q_1}+2\mathbf{S}_0^B e_{q_2})}+e^{j\boldsymbol{\Omega}^T(-\mathbf{S}_0^A e_{n_1}-2\mathbf{S}_0^A e_{n_2}+\mathbf{S}_0^B e_{q_1}+2\mathbf{S}_0^B e_{q_2})}$$

$$+e^{j\boldsymbol{\Omega}^T(\mathbf{S}_0^A e_{n_1}+2\mathbf{S}_0^A e_{n_2}-\mathbf{S}_0^B e_{q_1}+2\mathbf{S}_0^B e_{q_2})}+e^{j\boldsymbol{\Omega}^T(-\mathbf{S}_0^A e_{n_1}+2\mathbf{S}_0^A e_{n_2}-\mathbf{S}_0^B e_{q_1}+2\mathbf{S}_0^B e_{q_2})}$$

$$+e^{j\boldsymbol{\Omega}^T(\mathbf{S}_0^A e_{n_1}-2\mathbf{S}_0^A e_{n_2}-\mathbf{S}_0^B e_{q_1}+\mathbf{S}_0^B e_{q_2})}+e^{j\boldsymbol{\Omega}^T(-\mathbf{S}_0^A e_{n_1}-2\mathbf{S}_0^A e_{n_2}-\mathbf{S}_0^B e_{q_1}+\mathbf{S}_0^B e_{q_2})}$$

$$+e^{j\boldsymbol{\Omega}^T(\mathbf{S}_0^A e_{n_1}+2\mathbf{S}_0^A e_{n_2}+\mathbf{S}_0^B e_{q_1}-2\mathbf{S}_0^B e_{q_2})}+e^{j\boldsymbol{\Omega}^T(-\mathbf{S}_0^A e_{n_1}+2\mathbf{S}_0^A e_{n_2}+\mathbf{S}_0^B e_{q_1}-2\mathbf{S}_0^B e_{q_2})}$$

$$+e^{j\boldsymbol{\Omega}^T(\mathbf{S}_0^A e_{n_1}-2\mathbf{S}_0^A e_{n_2}+\mathbf{S}_0^B e_{q_1}-2\mathbf{S}_0^B e_{q_2})}+e^{j\boldsymbol{\Omega}^T(-\mathbf{S}_0^A e_{n_1}-2\mathbf{S}_0^A e_{n_2}+\mathbf{S}_0^B e_{q_1}-2\mathbf{S}_0^B e_{q_2})}$$

$$+e^{j\boldsymbol{\Omega}^T(\mathbf{S}_0^A e_{n_1}+2\mathbf{S}_0^A e_{n_2}-\mathbf{S}_0^B e_{q_1}-2\mathbf{S}_0^B e_{q_2})}+e^{j\boldsymbol{\Omega}^T(-\mathbf{S}_0^A e_{n_1}+2\mathbf{S}_0^A e_{n_2}-\mathbf{S}_0^B e_{q_1}-2\mathbf{S}_0^B e_{q_2})}$$

$$+e^{j\boldsymbol{\Omega}^T(\mathbf{S}_0^A e_{n_1}-2\mathbf{S}_0^A e_{n_2}-\mathbf{S}_0^B e_{q_1}-2\mathbf{S}_0^B e_{q_2})}+e^{j\boldsymbol{\Omega}^T(-\mathbf{S}_0^A e_{n_1}-2\mathbf{S}_0^A e_{n_2}-\mathbf{S}_0^B e_{q_1}-2\mathbf{S}_0^B e_{q_2})}$$

and

$$B=e^{j\boldsymbol{\Omega}^T(\boldsymbol{\lambda}_{l_1,p}^A e_{l_1}+2\boldsymbol{\lambda}_{l_2,q}^A e_{l_2}+\boldsymbol{\lambda}_{l_3,r}^B e_{l_3}+2\boldsymbol{\lambda}_{l_4,s}^B e_{l_4})}+e^{j\boldsymbol{\Omega}^T(-\boldsymbol{\lambda}_{l_1,p}^A e_{l_1}+2\boldsymbol{\lambda}_{l_2,q}^A e_{l_2}+\boldsymbol{\lambda}_{l_3,r}^B e_{l_3}+2\boldsymbol{\lambda}_{l_4,s}^B e_{l_4})}$$

$$+e^{j\boldsymbol{\Omega}^T(\boldsymbol{\lambda}_{l_1,p}^A e_{l_1}-2\boldsymbol{\lambda}_{l_2,q}^A e_{l_2}+\boldsymbol{\lambda}_{l_3,r}^B e_{l_3}+2\boldsymbol{\lambda}_{l_4,s}^B e_{l_4})}+e^{j\boldsymbol{\Omega}^T(-\boldsymbol{\lambda}_{l_1,p}^A e_{l_1}-2\boldsymbol{\lambda}_{l_2,q}^A e_{l_2}+\boldsymbol{\lambda}_{l_3,r}^B e_{l_3}+2\boldsymbol{\lambda}_{l_4,s}^B e_{l_4})}$$

$$+e^{j\boldsymbol{\Omega}^T(\boldsymbol{\lambda}_{l_1,p}^A e_{l_1}+2\boldsymbol{\lambda}_{l_2,q}^A e_{l_2}-\boldsymbol{\lambda}_{l_3,r}^B e_{l_3}+2\boldsymbol{\lambda}_{l_4,s}^B e_{l_4})}+e^{j\boldsymbol{\Omega}^T(-\boldsymbol{\lambda}_{l_1,p}^A e_{l_1}+2\boldsymbol{\lambda}_{l_2,q}^A e_{l_2}-\boldsymbol{\lambda}_{l_3,r}^B e_{l_3}+2\boldsymbol{\lambda}_{l_4,s}^B e_{l_4})}$$

$$+e^{j\boldsymbol{\Omega}^T(\boldsymbol{\lambda}_{l_1,p}^A e_{l_1}-2\boldsymbol{\lambda}_{l_2,q}^A e_{l_2}-\boldsymbol{\lambda}_{l_3,r}^B e_{l_3}+\boldsymbol{\lambda}_{l_4,s}^B e_{l_4})}+e^{j\boldsymbol{\Omega}^T(-\boldsymbol{\lambda}_{l_1,p}^A e_{l_1}-2\boldsymbol{\lambda}_{l_2,q}^A e_{l_2}-\boldsymbol{\lambda}_{l_3,r}^B e_{l_3}+\boldsymbol{\lambda}_{l_4,s}^B e_{l_4})}$$

$$+e^{j\boldsymbol{\Omega}^T(\boldsymbol{\lambda}_{l_1,p}^A e_{l_1}+2\boldsymbol{\lambda}_{l_2,q}^A e_{l_2}+\boldsymbol{\lambda}_{l_3,r}^B e_{l_3}-2\boldsymbol{\lambda}_{l_4,s}^B e_{l_4})}+e^{j\boldsymbol{\Omega}^T(-\boldsymbol{\lambda}_{l_1,p}^A e_{l_1}+2\boldsymbol{\lambda}_{l_2,q}^A e_{l_2}+\boldsymbol{\lambda}_{l_3,r}^B e_{l_3}-2\boldsymbol{\lambda}_{l_4,s}^B e_{l_4})}$$

$$+e^{j\boldsymbol{\Omega}^T(\boldsymbol{\lambda}_{l_1,p}^A e_{l_1}-2\boldsymbol{\lambda}_{l_2,q}^A e_{l_2}+\boldsymbol{\lambda}_{l_3,r}^B e_{l_3}-2\boldsymbol{\lambda}_{l_4,s}^B e_{l_4})}+e^{j\boldsymbol{\Omega}^T(-\boldsymbol{\lambda}_{l_1,p}^A e_{l_1}-2\boldsymbol{\lambda}_{l_2,q}^A e_{l_2}+\boldsymbol{\lambda}_{l_3,r}^B e_{l_3}-2\boldsymbol{\lambda}_{l_4,s}^B e_{l_4})}$$

$$+e^{j\boldsymbol{\Omega}^T(\boldsymbol{\lambda}_{l_1,p}^A e_{l_1}+2\boldsymbol{\lambda}_{l_2,q}^A e_{l_2}-\boldsymbol{\lambda}_{l_3,r}^B e_{l_3}-2\boldsymbol{\lambda}_{l_4,s}^B e_{l_4})}+e^{j\boldsymbol{\Omega}^T(-\boldsymbol{\lambda}_{l_1,p}^A e_{l_1}+2\boldsymbol{\lambda}_{l_2,q}^A e_{l_2}-\boldsymbol{\lambda}_{l_3,r}^B e_{l_3}-2\boldsymbol{\lambda}_{l_4,s}^B e_{l_4})}$$

$$+e^{j\boldsymbol{\Omega}^T(\boldsymbol{\lambda}_{l_1,p}^A e_{l_1}-2\boldsymbol{\lambda}_{l_2,q}^A e_{l_2}-\boldsymbol{\lambda}_{l_3,r}^B e_{l_3}-2\mathbf{S}_0^B e_{q_2})}+e^{j\boldsymbol{\Omega}^T(-\boldsymbol{\lambda}_{l_1,p}^A e_{l_1}-2\boldsymbol{\lambda}_{l_2,q}^A e_{l_2}-\boldsymbol{\lambda}_{l_3,r}^B e_{l_3}-2\boldsymbol{\lambda}_{l_4,s}^B e_{l_4})},$$

respectively.

Following the mathematical derivation given in Sec. 11.3.1, the probability of correct decision is obtained by (11.35) by calculating the 2D PDF based on the inverse Fourier transform of the CHF given in (11.40). Thus, the probability of correct deci-

sion is

$$P_{c,1avg}(\zeta) = \frac{1}{2^{4(K+2M-2)}} \sum_{n_1=1}^{2^{M-2}} \sum_{n_2=1}^{2^{M-2}} \sum_{q_1=1}^{2^{M-2}} \sum_{q_2=1}^{2^{M-2}} \sum_{p=1}^{2^{(K-2)M}} \sum_{q=1}^{2^{(K-2)M}} \sum_{r=1}^{2^{(K-2)M}} \sum_{s=1}^{2^{(K-2)M}} \sum_{l1=0}^{2^{M-1}-1} \sum_{l2=0}^{2^{M-1}-1}$$

$$\sum_{l3=0}^{2^{M-1}-1} \sum_{l4=0}^{2^{M-1}-1} \sum_{f=1}^{256} Q\!\left(-\sqrt{2\rho}\,\kappa_1^1(0)\right) Q\!\left(-\sqrt{2\rho}\,\kappa_2^1(0)\right) Q\!\left(-\sqrt{2\rho}\kappa_1^1(0)\right) Q\!\left(-\sqrt{2\rho}\kappa_2^1(2)\right)$$

$$Q\!\left(-\sqrt{2\rho}\,\kappa_1^1(2)\right) Q\!\left(-\sqrt{2\rho}\kappa_2^1(0)\right) Q\!\left(-\sqrt{2\rho}\,\kappa_1^1(2)\right) Q\!\left(-\sqrt{2\rho}\kappa_2^1(2)\right), \quad (11.41)$$

where $\kappa_1^i(g)$ and $\kappa_2^i(g)$ equal $\kappa_{n_1,n_2,q_1,q_2,p,q,r,s,l_1,l_2,l_3,l_4}^i [1,m] - g$ and $\kappa_{n_1,n_2,q_1,q_2,p,q,r,s,l_1,l_2,l_3,l_4}^i$ $[2,m] - g$, respectively, and $\kappa_{n_1,n_2,q_1,q_2,p,q,r,s,l_1,l_2,l_3,l_4} [p,q]$ is the p,q entry of the 2×256 matrix $\mathbf{G} \triangleq [\mathbf{C}(1), \mathbf{C}(2), \cdots, \mathbf{C}(256)]$, being $i = 1,2,3,4$.

Similarly, for transmitted symbol $X_0(0) = 1 + 3j$, the correct decision lies in the region $D_{s2}=\{a+bj|0 \leq a \leq 2, b=2\}$

$$P_{c,2}(Y_0(0) \in D_{s1}|X_0(0)) = \frac{1}{2^{4(K+2M-2)}} \sum_{n_1=1}^{2^{M-2}} \sum_{n_2=1}^{2^{M-2}} \sum_{q_1=1}^{2^{M-2}} \sum_{q_2=1}^{2^{M-2}} \sum_{p=1}^{2^{(K-2)M}} \sum_{q=1}^{2^{(K-2)M}} \sum_{r=1}^{2^{(K-2)M}} \sum_{s=1}^{2^{(K-2)M}} \sum_{l1=0}^{2^{M-1}-1}$$

$$\sum_{l2=0}^{2^{M-1}-1} \sum_{l3=0}^{2^{M-1}-1} \sum_{l4=0}^{2^{M-1}-1} \sum_{f=1}^{256} Q\!\left(-\sqrt{2\rho}\,\kappa_1^2(0)\right) Q\!\left(-\sqrt{2\rho}\kappa_2^2(2)\right) Q\!\left(-\sqrt{2\rho}\kappa_1^2(2)\right) Q\!\left(-\sqrt{2\rho}\kappa_2^2(2)\right).$$

$$(11.42)$$

For transmitted symbol $X_0(0) = 3 + j$, the correct decision lies in the region $D_{s3}=\{a+bj|a=2, 0 \leq b \leq 2\}$

$$P_{c,3}(Y_0(0) \in D_{s1}|X_0(0)) = \frac{1}{2^{4(K+2M-2)}} \sum_{n_1=1}^{2^{M-2}} \sum_{n_2=1}^{2^{M-2}} \sum_{q_1=1}^{2^{M-2}} \sum_{q_2=1}^{2^{M-2}} \sum_{p=1}^{2^{(K-2)M}} \sum_{q=1}^{2^{(K-2)M}} \sum_{r=1}^{2^{(K-2)M}} \sum_{s=1}^{2^{(K-2)M}} \sum_{l1=0}^{2^{M-1}-1}$$

$$\sum_{l2=0}^{2^{M-1}-1} \sum_{l3=0}^{2^{M-1}-1} \sum_{l4=0}^{2^{M-1}-1} \sum_{f=1}^{256} Q\!\left(-\sqrt{2\rho}\,\kappa_1^3(2)\right) Q\!\left(-\sqrt{2\rho}\,\kappa_2^3(0)\right) Q\!\left(-\sqrt{2\rho}\kappa_1^3(2)\right) Q\!\left(-\sqrt{2\rho}\kappa_2^3(2)\right).$$

$$(11.43)$$

Finally, for transmitted symbol $X(k) = 3 + 3j$, the correct decision lies in the region $D_{s4}=\{a+bj|a=2, b=2\}$

$$P_{c,4}(Y_0(0) \in D_{s1}|X_0(0)) \frac{1}{2^{4(K+2M-2)}} \sum_{n_1=1}^{2^{M-2}} \sum_{n_2=1}^{2^{M-2}} \sum_{q_1=1}^{2^{M-2}} \sum_{q_2=1}^{2^{M-2}} \sum_{p=1}^{2^{(K-2)M}} \sum_{q=1}^{2^{(K-2)M}} \sum_{r=1}^{2^{(K-2)M}}$$

$$\sum_{s=1}^{2^{(K-2)M}} \sum_{l1=0}^{2^{M-1}-1} \sum_{l2=0}^{2^{M-1}-1} \sum_{l3=0}^{2^{M-1}-1} \sum_{l4=0}^{2^{M-1}-1} \sum_{f=1}^{256} Q\!\left(-\sqrt{2\rho}\,\kappa_1^4(2)\right) Q\!\left(-\sqrt{2\rho}\,\kappa_2^4(2)\right).$$

$$(11.44)$$

By taking into account the symmetry of the 16-QAM modulation, the average probability of correct decision is obtained by dividing the individual probabilities of correct decision given in (11.41), (11.42), (11.43), and (11.44) by 4 and then subtract from 1. The resulting SEP expression is given by

$$
P_s\left(\zeta\right)= 1 -\frac{1}{4\times 2^{4(K+2M-2)}}\sum_{n_1=1}^{2^{M-2}}\sum_{n_2=1}^{2^{M-2}}\sum_{q_1=1}^{2^{M-2}}\sum_{q_2=1}^{2^{M-2}}\sum_{p=1}^{2^{(K-2)M}}\sum_{q=1}^{2^{(K-2)M}}\sum_{r=1}^{2^{(K-2)M}}\sum_{s=1}^{2^{(K-2)M}}\sum_{l1=0}^{2^{M-1}-1}
$$

$$
\sum_{l2=0}^{2^{M-1}-1}\sum_{l3=0}^{2^{M-1}-1}\sum_{l4=0}^{2^{M-1}-1}\sum_{f=1}^{256} Q\!\left(-\sqrt{2\rho}\,\kappa_1^1(0)\right)Q\!\left(-\sqrt{2\rho}\,\kappa_2^1(0)\right) Q\!\left(-\sqrt{2\rho}\kappa_1^1(0)\right)
$$

$$
Q\!\left(-\sqrt{2\rho}\kappa_2^1(2)\right) Q\!\left(-\sqrt{2\rho}\,\kappa_1^1(2)\right)Q\!\left(-\sqrt{2\rho}\kappa_2^1(0)\right)Q\!\left(-\sqrt{2\rho}\,\kappa_1^2(2)\right)Q\!\left(-\sqrt{2\rho}\kappa_2^1(2)\right)
$$

$$
Q\!\left(-\sqrt{2\rho}\,\kappa_1^2(2)\right)Q\!\left(-\sqrt{2\rho}\,\kappa_2^2(0)\right) Q\!\left(-\sqrt{2\rho}\kappa_1^2(2)\right)Q\!\left(-\sqrt{2\rho}\kappa_2^2(2)\right) Q\!\left(-\sqrt{2\rho}\,\kappa_1^3(2)\right)
$$

$$
Q\!\left(-\sqrt{2\rho}\,\kappa_2^3(0)\right) Q\!\left(-\sqrt{2\rho}\kappa_1^3(2)\right)Q\!\left(-\sqrt{2\rho}\kappa_2^3(2)\right) Q\!\left(-\sqrt{2\rho}\,\kappa_1^4(2)\right)Q\!\left(-\sqrt{2\rho}\,\kappa_2^4(2)\right).
$$
(11.45)

In the case of 16-QAM, we also verify performance by substituting $M=1$ and $g[n] = \mathrm{rect}\left(\frac{t-NT_s/2}{NT_s}\right)\Big|_{t=nT_s}$, (11.45) reduces to (13) of [152].

11.3.2 Frequency selective Rayleigh fading

For the frequency selective Rayleigh fading channel case we limit performance analysis to BPSK modulation only. In the case of BPSK modulation, symbols are drawn from the set $\{\pm 1\}$. Without loosing generality we assume that data symbol $X_0(0) = +1$ is transmitted on the zeroth sub-carrier under the frequency selective fading channel. With this assumption, the received signal on the zeroth sub-carrier is

$$
Y_0\left(0\right)= \bar{S}_0(0) + \sum_{\substack{l=0,\\ l\neq m}}^{M-1} X_0\left(l\right)\bar{S}_0(l) + \sum_{\substack{k=0,\\ k\neq q}}^{K-1}\sum_{\substack{l=0,\\ l\neq m}}^{M-1} X_k\left(l\right)\bar{S}_k(l) + W_0(0).
$$
(11.46)

Since the receiver signal is affected by multipath fading channel, in this chapter we consider equalization of the received signal on the zeroth sub-carrier.This is obtained by multiplying (11.46) by the complex conjugate of $\bar{S}_0(0)$, denoted as $\bar{S}_0^*(0)$, is given by

$$
Y_0(0)\,\bar{S}_0^*(0)=|\bar{S}_0(0)|^2+\sum_{\substack{l=0,\\ l\neq m}}^{M-1} X_0\left(l\right)\bar{S}_0^*(0)\bar{S}_0(l)+\sum_{\substack{k=0,\\ k\neq q}}^{K-1}\sum_{\substack{l=0,\\ l\neq m}}^{M-1} X_k\left(l\right)\bar{S}_0^*(0)\bar{S}_k(l)+\bar{S}_0^*(0)W_0(0).
$$
(11.47)

The term $\bar{S}_0^*(0)$ include the effect of the channel and CFO ($\Delta\epsilon$). The SEP can be calculated as

$$
P_s\left(\zeta_k\right) = \int_{\boldsymbol{\beta}}P_s(\zeta|\boldsymbol{\beta})p_{\boldsymbol{B}}(\boldsymbol{\beta})\,d\boldsymbol{\beta},
$$
(11.48)

where $\boldsymbol{\beta} = \boldsymbol{F}_{1:L}\boldsymbol{h}$, with $\boldsymbol{h} = [h(0), \cdots, h(L-1)]^T$ being the time-domain vector of channel coefficients and $\boldsymbol{F}_{1:L}$ corresponding to the first L columns of the $N \times N$ DFT matrix, $P_s(\zeta|\boldsymbol{\beta})$ is the SEP conditioned to a given $\boldsymbol{\beta}$, this latter being described by the N-dimensional vector with joint PDF $p_{\boldsymbol{B}}(\boldsymbol{\beta})$. Since the evaluation of the above multidimensional integral is difficult, its solution can be simplified by using the following factorization

$$p_{\boldsymbol{B}}(\boldsymbol{\beta}) = p_{\boldsymbol{\beta}_S|\bar{S}_0(0)}\big(\boldsymbol{\beta}_s|\bar{S}_0(0)\big)\, p_{\bar{S}_0(0)}\bar{S}_0(0), \tag{11.49}$$

where $\boldsymbol{\beta}_S = [\beta(1), \cdots, \beta(N-1)]^T$, $p_{\bar{S}_0(0)}\big(\bar{S}_0(0)\big)$ is the one-dimensional PDF of $\bar{S}_0(0)$, and $p_{\boldsymbol{\beta}_S|\bar{S}_0(0)}\big(\boldsymbol{\beta}_S|\bar{S}_0(0)\big)$ is the conditional PDF of $\boldsymbol{\beta}_S$ given $\bar{S}_0(0)$. By replacing (11.49) in (11.48) we obtain

$$P_s(\zeta) = \int_0^\infty P_s\big(\zeta|\bar{S}_0(0)\big)\, p_{\bar{S}_0(0)}\big(\bar{S}_0(0)\big)\, d\bar{S}_0(0), \tag{11.50}$$

where

$$P_s\big(\zeta|\bar{S}_0(0)\big) = \int_{\boldsymbol{\beta}_S} P_s\big(\zeta|\bar{S}_0(0),\boldsymbol{\beta}_S\big) p_{\boldsymbol{\beta}_S|\bar{S}_0(0)}\big(\boldsymbol{\beta}_S|\bar{S}_0(0)\big) d\boldsymbol{\beta}_S. \tag{11.51}$$

The expression of $P_s\big(\zeta|\bar{S}_0(0),\boldsymbol{\beta}_S\big)$ can be obtained by resorting to the CHF approach. We consider the conditional CHF of the real part of the equalized received signal $\Re\big[Y_0(0)\,\bar{S}_0^*(0)|\bar{S}_0(0),\boldsymbol{\beta}_S\big]$ in (11.47) given by

$$\varphi_{\Re[Y_0(0)\bar{S}_0^*(0)|\bar{S}_0(0),\boldsymbol{\beta}_S]}(\omega) = E\Big[e^{jw\Re[Y_0(0)\bar{S}_0^*(0)]}|\bar{S}_0(0),\boldsymbol{\beta}_S\Big]. \tag{11.52}$$

By substituting the value $Y_0(0)\,\bar{S}_0^*(0)$ from (11.47) in (11.52) and by computing the average over all the possible combination of symbols and by using the trigonometric identity given by (11.16), we get

$$\varphi_{\Re[Y_0(0)\bar{S}_0^*(0)|\bar{S}_0(0),\boldsymbol{\beta}_S]}(\omega) = e^{jw\Re[|\bar{S}_0(0)|^2]} \times e^{-\frac{\omega^2\sigma_{\bar{s}}^2}{2}} \times \left\{\frac{1}{2^{M-1}}\sum_{n=1}^{2^{M-2}} e^{jw\Re[\bar{S}_0^*(0)\boldsymbol{e}_n^T\boldsymbol{\Upsilon}]} + e^{-jw\Re[\bar{S}_0^*(0)\boldsymbol{e}_n^T\boldsymbol{\Upsilon}]}\right\}$$

$$\times \left\{\prod_{l=0}^{M-1}\left(\frac{1}{2^{K-1}}\sum_{k=1}^{2^{K-2}}\cos\big(\omega\Re[\bar{S}_0^*(0)\boldsymbol{\epsilon}_k^T\boldsymbol{S}_k(l)]\big)\right)\right\}, \tag{11.53}$$

where $\sigma_{\bar{s}}^2 = \big|\bar{S}_0^*(0)\big|^2\sigma^2$ and $\boldsymbol{\Upsilon} = \mathrm{diag}\,(S_0(1), S_0(2), \cdots, S_0(M-1))$, $\boldsymbol{S}_k(l) = \mathrm{diag}(S_1(l), S_2(l), \cdots, S_{K-1}(l))$ and $\boldsymbol{e}_q$ and $\boldsymbol{\epsilon}_k$ is an $N \times 1$ vector corresponding to the binary codeword of the number $2^{N-1} - q$, in which zeros have been substituted with -1s. By following considerations similar to those in 11.3.1 and after straightforward passages we get

$$\varphi_{\Re[Y_0(0)\bar{S}_0^*(0)|\bar{S}_0(0),\boldsymbol{\beta}_S]}(\omega) = e^{jw\Re[|\bar{S}_0(0)|^2] - \frac{\omega^2\sigma_{\bar{s}}^2}{2}} \times \left\{\frac{1}{2^{M-1}}\sum_{n=1}^{2^{M-2}} e^{jw\Re[\bar{S}_0^*(0)\boldsymbol{e}_n^T\boldsymbol{\Upsilon}]} + e^{-jw\Re[\bar{S}_0^*(0)\boldsymbol{e}_n^T\boldsymbol{\Upsilon}]}\right\}$$

$$\times \left\{\sum_{p=1}^{2^{K-2}M}\left(\frac{1}{2^{K-1}}\prod_{l=0}^{M-1}\cos\big(\omega\Re[\bar{S}_0^*(0)\boldsymbol{d}_{p,l}^T\boldsymbol{\Lambda}_{l,p}]\big)\right)\right\}, \tag{11.54}$$

where $\boldsymbol{\Lambda}_{p,l} = \mathrm{diag}(\boldsymbol{S}_1(l), \boldsymbol{S}_2(l), \cdots, \boldsymbol{S}_{K-1}(l))$. Applying again trigonometric identity given in (11.16) to the last product in (11.54), we get

$$\varphi_{\Re[Y_0(0)\bar{S}_0^*(0)|\bar{S}_0(0),\boldsymbol{\beta}_S]}(\omega) = e^{jw\Re[|\bar{S}_0(0)|^2] - \frac{\omega^2 \sigma_{\bar{s}}^2}{2}} \times \left\{ \frac{1}{2^{M-1}} \sum_{n=1}^{2^{M-2}} e^{j\omega\Re[\bar{S}_0^*(0)\boldsymbol{e}_n^T\boldsymbol{\Upsilon}]} + e^{-j\omega\Re[\bar{S}_0^*(0)\boldsymbol{e}_n^T\boldsymbol{\Upsilon}]} \right\}$$

$$\times \left\{ \frac{1}{2^{K-1}} \frac{1}{2^M} \sum_{p=1}^{2^{(K-2)M}} \sum_{l=0}^{2^{M-1}} e^{j\omega\Re[\bar{S}_0^*(0)(\boldsymbol{d}_{p,l}^T\boldsymbol{\Lambda}_{l,p})^T\boldsymbol{e}_l]} + e^{-j\omega\Re[\bar{S}_0^*(0)(\boldsymbol{d}_{p,l}^T\boldsymbol{\Lambda}_{l,p})^T\boldsymbol{e}_l]} \right\}. \tag{11.55}$$

It is obvious that (11.55) represents the CHF of a mixture of Gaussian densities. Now, an error will occur only if $\Re\left[Y_0(0)\bar{S}_0^*(0)|\bar{S}_0(0),\boldsymbol{\beta}_S\right] < 0$. After some mathematical transforms and substituting the random variables $V_n = \Re[\bar{S}_0^*(0)\boldsymbol{e}_n^T\boldsymbol{\Upsilon}]$ and $Z_{l,p} = \Re[\bar{S}_0^*(0)(\boldsymbol{d}_{p,l}^T\boldsymbol{\Lambda}_{l,p})^T\boldsymbol{e}_l]$, the conditional SEP is given by

$$P_s\left(\zeta|\bar{S}_0(0),\boldsymbol{\beta}_S\right) = \frac{1}{2^{K+2M-2}} \sum_{l=1}^{2^{M-1}} \sum_{p=1}^{2^{(K-2)M}} \sum_{n=1}^{2^{M-2}} Q\left(\frac{\Re\left[|\bar{S}_0(0)|^2\right] + V_n + Z_{l,p}}{\sigma_{\bar{s}}}\right)$$

$$+Q\left(\frac{\Re\left[|\bar{S}_0(0)|^2\right] - V_n + Z_{l,p}}{\sigma_{\bar{s}}}\right) + Q\left(\frac{\Re\left[|\bar{S}_0(0)|^2\right] + V_n - Z_{l,p}}{\sigma_{\bar{s}}}\right) + Q\left(\frac{\Re\left[|\bar{S}_0(0)|^2\right] - V_n - Z_{l,p}}{\sigma_{\bar{s}}}\right). \tag{11.56}$$

The expression of $P_s\left(\zeta|\bar{S}_0(0)\right)$ can now be obtained by substituting (11.57) in (11.51) and averaging over Gaussian PDF $p_{\boldsymbol{\beta}_S|\bar{S}_0(0)}\left(\boldsymbol{\beta}_S|\bar{S}_0(0)\right)$, with mean $E[\boldsymbol{\beta}_S|\bar{S}_0(0)]$ and covariance $C_{\boldsymbol{\beta}_S|\bar{S}_0(0)}$. The resulting expression is

$$P_s\left(\zeta|\bar{S}_0(0)\right) = \frac{1}{2^{K+2M-2}} \sum_{l=1}^{2^{M-1}} \sum_{p=1}^{2^{(K-2)M}} \sum_{n=1}^{2^{M-2}} Q\left(\frac{\bar{S}_0(0)\left(\Re\left[\bar{S}_0(0)\right] + \mu_n^+ + \mu_{l,p}^-\right)^2}{\sigma\sqrt{\left(1 + \frac{\nu_n^+}{2\sigma^2} + \frac{\nu_{l,p}^-}{2\sigma^2}\right)}}\right)$$

$$+Q\left(\frac{\bar{S}_0(0)\left(\Re[\bar{S}_0(0)] + \mu_n^+ + \mu_{l,p}^-\right)^2}{\sigma\sqrt{\left(1 + \frac{\nu_n^+}{2\sigma^2} + \frac{\nu_{l,p}^-}{2\sigma^2}\right)}}\right) + Q\left(\frac{\bar{S}_0(0)\left(\Re[\bar{S}_0(0)] + \mu_n^+ + \mu_{l,p}^-\right)^2}{\sigma\sqrt{\left(1 + \frac{\nu_n^+}{2\sigma^2} + \frac{\nu_{l,p}^-}{2\sigma^2}\right)}}\right) + Q\left(\frac{\bar{S}_0(0)\left(\Re[\bar{S}_0(0)] + \mu_n^+ + \mu_{l,p}^-\right)^2}{\sigma\sqrt{\left(1 + \frac{\nu_n^+}{2\sigma^2} + \frac{\nu_{l,p}^-}{2\sigma^2}\right)}}\right), \tag{11.57}$$

where μ_n^+, $\mu_{l,p}^-$ and ν_n^+, $\nu_{l,p}^-$ are related to the means and variances of the conditional random variables $V_n|\bar{S}_0(0)$ and $Z_{l,p}|\bar{S}_0(0)$, respectively. These are defined as

$$\mu_n^+ = \frac{E\left(V_n|\bar{S}_0(0)\right)}{|\bar{S}_0(0)|^2} = C_{\bar{S}_0(0)\bar{S}_0(0)}^{-1} \Re[\boldsymbol{e}_n^T\boldsymbol{\Upsilon} C_{\boldsymbol{\beta}_S\bar{S}_0(0)}],$$

$$\mu_{l,p}^- = \frac{E\left(Z_{l,p}|\bar{S}_0(0)\right)}{|\bar{S}_0(0)|^2} = C_{\bar{S}_0(0)\bar{S}_0(0)}^{-1} \Re[(\boldsymbol{d}_{p,l}^T\boldsymbol{\Lambda}_{l,p})^T\boldsymbol{e}_l C_{\boldsymbol{\beta}_S\bar{S}_0(0)}], \tag{11.58}$$

and

$$\nu_n^+ = 2\frac{\mathrm{Var}\left(V_n|\bar{S}_0(0)\right)}{\left|\bar{S}_0(0)\right|^2} = \boldsymbol{e}_n^T \boldsymbol{\Upsilon} C_{\boldsymbol{\beta}_S \bar{S}_0(0)} \bar{\boldsymbol{\Upsilon}} \boldsymbol{e}_n,$$

$$\nu_{l,p}^- = 2\frac{\mathrm{Var}\left(Z_{l,p}|\bar{S}_0(0)\right)}{\left|\bar{S}_0(0)\right|^2} = (\boldsymbol{d}_{p,l}^T \boldsymbol{\Lambda}_{l,p})^T \boldsymbol{e}_l C_{\boldsymbol{\beta}_S \bar{S}_0(0)} (\boldsymbol{d}_{p,l}^T \bar{\boldsymbol{\Lambda}}_{l,p})_{l,p} \boldsymbol{e}_l. \tag{11.59}$$

where $\bar{\boldsymbol{\Upsilon}}$ and $\bar{\boldsymbol{\Lambda}}_{l,p}$ denotes the conjugate of the $\boldsymbol{\Upsilon}$ and $\boldsymbol{\Lambda}_{l,p}$, respectively, $C_{\boldsymbol{\beta}_S|\bar{S}_0(0)} = E\left[\boldsymbol{\beta}_S \bar{S}_0(0)\right]$, $C_{\left(\boldsymbol{\beta}_S|\bar{S}_0(0)\right)} = C_{\boldsymbol{\beta}_S \boldsymbol{\beta}_S} - C_{\bar{S}_0(0)\bar{S}_0(0)}^{-1} \times C_{\boldsymbol{\beta}_S \bar{S}_0(0)} C_{\boldsymbol{\beta}_S \bar{S}_0(0)}^H$, $\mathrm{var}(\cdot)$ and $(\cdot)^H$ denotes the variance and Hermitian matrix, respectively.

In order to calculate the overall SEP performance, first introduce the change of variable $\gamma = \left|\bar{S}_0(0)\right|^2/N_0$, which allows us to express (11.50) as a function of the instantaneous SNR γ. Then, the unconditional symbol error probability is determined as

$$P_s(\zeta) = \int_0^\infty P_s(\zeta|\gamma) p_\gamma(\gamma) d\gamma \tag{11.60}$$

where

$$p_\gamma(\gamma) = \frac{1}{\bar{\gamma}} e^{\frac{\gamma}{\bar{\gamma}}} \tag{11.61}$$

is the PDF of Rayleigh fading with average SNR $\bar{\gamma} = E\left[|\bar{S}_0(0)|^2\right]/N_0$. In what follows we adopt the polar form definition given in [114] for the Q-function in (11.57). The overall SEP is computed by using the moment generating function (MGF) approach in (11.60) as

$$P_s(\zeta) = \frac{1}{2^{K+2M-2}} \sum_{l=1}^{2^{M-1}} \sum_{p=1}^{2^{(K-2)M}} \sum_{n=1}^{2^{M-2}} \int_0^{\frac{\pi}{2}} \left\{ \underbrace{\int_0^\infty \exp\left(-\frac{\gamma\left(\Re\left[\bar{S}_0(0)\right] + \mu_n^+ + \mu_{l,p}^-\right)^2}{\left(1 + \frac{\nu_n^+}{2\sigma^2} + \frac{\nu_{l,p}^-}{2\sigma^2}\right)\sin^2\theta}\right) p_\gamma(\gamma) d\gamma}_{M_\gamma(s_1)} \right.$$

$$+ \underbrace{\int_0^\infty \exp\left(-\frac{\gamma\left(\Re\left[\bar{S}_0(0)\right] - \mu_n^+ + \mu_{l,p}^-\right)^2}{\left(1 + \frac{\nu_n^+}{2\sigma^2} + \frac{\nu_{l,p}^-}{2\sigma^2}\right)\sin^2\theta}\right) p_\gamma(\gamma) d\gamma}_{M_\gamma(s_2)} + \underbrace{\int_0^\infty \exp\left(-\frac{\gamma\left(\Re\left[\bar{S}_0(0)\right] + \mu_n^+ - \mu_{l,p}^-\right)^2}{\left(1 + \frac{\nu_n^+}{2\sigma^2} + \frac{\nu_{l,p}^-}{2\sigma^2}\right)\sin^2\theta}\right) p_\gamma(\gamma) d\gamma}_{M_\gamma(s_3)}$$

$$\left. + \underbrace{\int_0^\infty \exp\left(-\frac{\gamma\left(\Re\left[\bar{S}_0(0)\right] - \mu_n^+ - \mu_{l,p}^-\right)^2}{\left(1 + \frac{\nu_n^+}{2\sigma^2} + \frac{\nu_{l,p}^-}{2\sigma^2}\right)\sin^2\theta}\right) p_\gamma(\gamma) d\gamma}_{M_\gamma(s_4)} \right\}, \tag{11.62}$$

where $M_\gamma(s)$ is used to denote the scaled Laplace transform of $p_\gamma(\gamma)$ know as MGF. By following the MGF approach given in (1.8) of [114], the expression of MGF the for the Rayleigh distribution is defined as

$$M_\gamma(s) = (1 - s\bar{\gamma})^{-1}. \tag{11.63}$$

The computation of the SEP $P_s(\zeta)$ is done using (1.8) and (5.6) of [114]. Finally, $P_s(\zeta)$ can be obtained as

$$P_s(\zeta) = \frac{1}{2^{K+2M-2}} \sum_{l=1}^{2^{M-1}} \sum_{p=1}^{2^{(K-2)M}} \sum_{n=1}^{2^{M-2}}$$

$$\left\{ A_1 \sqrt{\frac{\bar{\gamma} C_{\bar{S}_0(0)\bar{S}_0(0)} \left(\Re\left[\bar{S}_0(0)\right] + \mu_n^+ + \mu_{l,p}^-\right)^2}{1 + \bar{\gamma}(C_{\bar{S}_0(0)\bar{S}_0(0)} \left(\Re\left[\bar{S}_0(0)\right] + \mu_n^+ + \mu_{l,p}^-\right)^2 + \nu_n^+ + \nu_{l,p}^-)}} \right.$$

$$+ A_2 \sqrt{\frac{\bar{\gamma} C_{\bar{S}_0(0)\bar{S}_0(0)} \left(\Re\left[\bar{S}_0(0)\right] - \mu_n^+ + \mu_{l,p}^-\right)^2}{1 + \bar{\gamma}(C_{\bar{S}_0(0)\bar{S}_0(0)} \left(\Re\left[\bar{S}_0(0)\right] - \mu_n^+ + \mu_{l,p}^-\right)^2 + \nu_n^+ + \nu_{l,p}^-)}}$$

$$+ A_3 \sqrt{\frac{\bar{\gamma} C_{\bar{S}_0(0)\bar{S}_0(0)} \left(\Re\left[\bar{S}_0(0)\right] + \mu_n^+ - \mu_{l,p}^-\right)^2}{1 + \bar{\gamma}(C_{\bar{S}_0(0)\bar{S}_0(0)} \left(\Re\left[\bar{S}_0(0)\right] + \mu_n^+ - \mu_{l,p}^-\right)^2 + \nu_n^+ + \nu_{l,p}^-)}}$$

$$\left. + A_4 \sqrt{\frac{\bar{\gamma} C_{\bar{S}_0(0)\bar{S}_0(0)} \left(\Re\left[\bar{S}_0(0)\right] - \mu_n^+ - \mu_{l,p}^-\right)^2}{1 + \bar{\gamma}(C_{\bar{S}_0(0)\bar{S}_0(0)} \left(\Re\left[\bar{S}_0(0)\right] - \mu_n^+ - \mu_{l,p}^-\right)^2 + \nu_n^+ + \nu_{l,p}^-)}} \right\} \tag{11.64}$$

where $A_1 = \text{sgn}\left(\Re\left[\bar{S}_0(0)\right] + \mu_n^+ + \mu_{l,p}^-\right)$, $A_2 = \text{sgn}\left(\Re\left[\bar{S}_0(0)\right] - \mu_n^+ + \mu_{l,p}^-\right)$, $A_3 = \text{sgn}\left(\Re\left[\bar{S}_0(0)\right] + \mu_n^+ - \mu_{l,p}^-\right)$, and $A_4 = \text{sgn}\left(\Re\left[\bar{S}_0(0)\right] - \mu_n^+ - \mu_{l,p}^-\right)$. Substituting $C_{\bar{S}_0(0)\bar{S}_0(0)} = 2|S(0)^2|\sigma^2$ and $g[n] = \text{rect}\left(\frac{t-NT_s/2}{NT_s}\right)\Big|_{t=nT_s}$, we get the conventional OFDM where there is only one sub-symbol for each sub-carrier, i.e., $M = 1$, and we get $P_k(0) = \delta_k$, with δ_k denoting the Kronecher delta. In this case (11.64) reduces to (9) of [101].

11.4 Simulation Results

In order to verify the correctness of the analysis done in Sec. 11.3, SEP results obtained from Monte Carlo simulations, marked as $\times$, are compared to those given in equations (11.24), (11.32) and (11.45) in AWGN channel and for frequency selective Rayleigh fading channel in (11.64).

Figure 11.4 shows the SEP versus E_s/N_0 for BPSK, QPSK and 16-QAM modulations transmission over the AWGN channel with $K = 64$ and $M = 1$ obtained using Dirichlet pulse shaping filter with and without CFO, which makes GFDM system equivalent to OFDM in terms of SEP performance. In order to verify the derived SEP expressions given in (11.24), (11.32) and (11.45), we also plotted the SEP OFDM system for $\Delta\epsilon = 0.1$ and without CFO ($\Delta\epsilon = 0$) in the case of transmission over AWGN
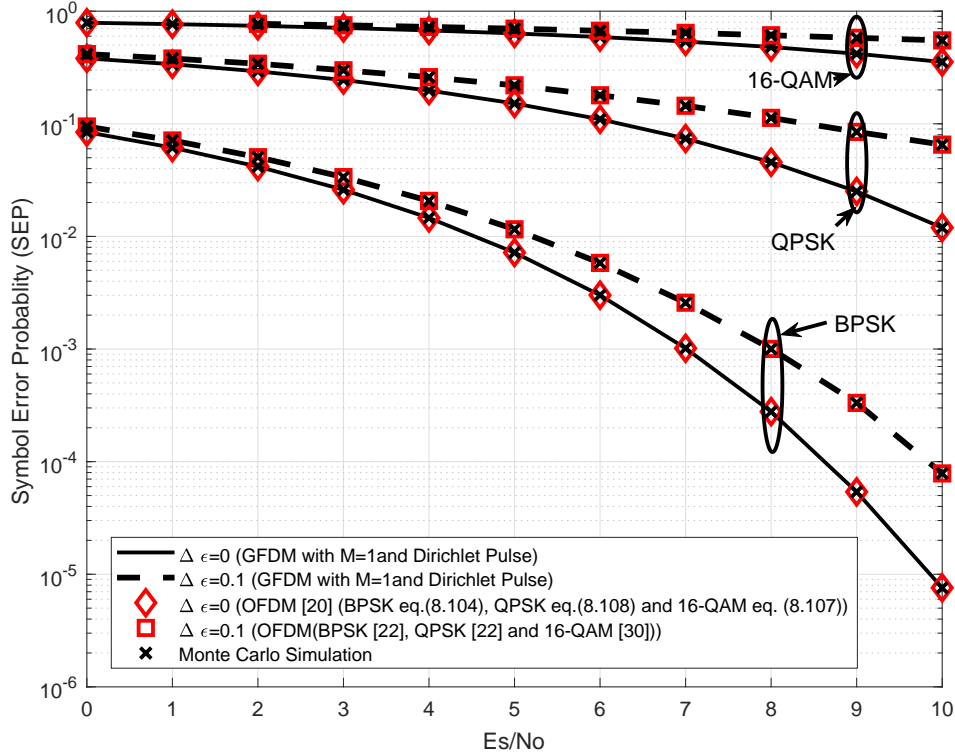
Figure 11.4: *SEP comparison of GFDM and OFDM system in AWGN channel with (at $\Delta\epsilon = 0.1$) and without CFO with Dirichlet pulse shaping filter for BPSK, QPSK and 16-QAM modulation schemes with $M = 1$ and $K = 64$.*

channel. Form the results shown in Fig. 11.4, it is clearly visible that our proposed SEP results coincide with corresponding results of OFDM system given in [101], [100] and [152]. The correctness of derived SEP expressions was check also with MC simulations, marked as ×. This result confirms that GFDM is a generalized MCM scheme from which, as a particular case, we can also obtain OFDM. Similar considerations hold also for the frequency selective Rayleigh fading channel. Figure 11.5 shows the SEP versus $\bar{\gamma}$ for BPSK modulations transmission over the frequency selective Rayleigh fading channel with $K = 64$ and $M = 1$ obtained using Dirichlet pulse shaping filter with and without CFO. To verify our analysis, in Fig. 11.5 SEP versus $\bar{\gamma}$ is plotted with and without CFO. The SEP expression given in (11.64) is also reported to evaluate the OFDM performance for ($\Delta\epsilon = 0.1$) and without CFO transmission over frequency selective Rayleigh fading channel. Form the results shown in Fig. 11.5 we can observe that proposed SEP results match with corresponding results given in [101] for OFDM.

To check the SEP performance of GFDM at different values of CFO ($\Delta\epsilon$), we considered the fixed value of $E_s/N_0 = 10$ dB with $K = 64$ sub-carriers where, on each sub-carrier, $M = 9$ sub-symbols are transmitted. Figure 11.6 reports SEP versus $\Delta\epsilon$ for the BPSK, QPSK and 16-QAM GFDM system with the Dirichlet pulse shaping filter
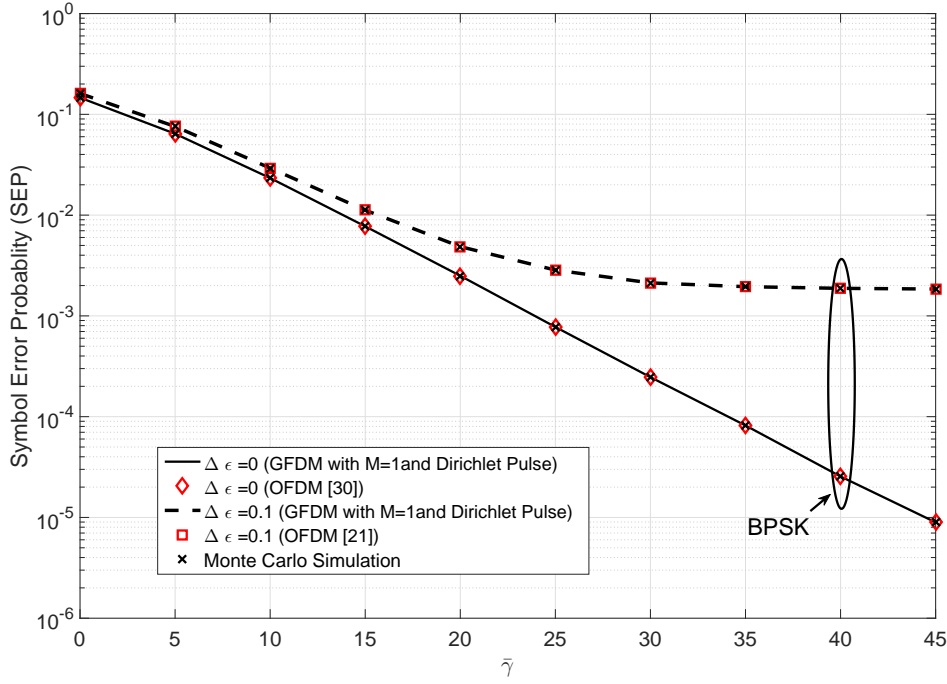
Figure 11.5: *SEP comparison of GFDM and OFDM system in frequency selective Rayleigh fading channel with (at $\Delta\epsilon = 0.1$) and without CFO with Dirichlet pulse shaping filter for BPSK modulation schemes with $M = 1$ and $K = 64$.*

at $\alpha = 0.1$. As CFO increases the performance of the GFDM system going worse and worse, thus conferring that our derived expressions are also valid for high values of the CFO. Again, a perfect match can be observed between analytical and simulation results for different values of CFO.

The impact of the pulse shaping on OOB is the key factor that makes GFDM more suitable for MTC physical layer. Hence, in our simulation, we have considered the Gaussian pulse shaping filter, which is well-localized in the time-frequency and reduces to large extent the OOB emission. Its impact on the SEP performance is evaluated. As explained in Sec. 11.3, since Gaussian pulse does not satisfy the orthogonality condition, the IOTA method is used to obtain a filter which preserves the optimum concentration property of Gaussian filter and, at the same time, makes it orthogonal to prevent interference with neighboring sub-symbols. Similarly, Fig. 11.7 shows the SEP versus CFO ($\Delta\epsilon$) for the BPSK, QPSK and 16-QAM GFDM system at $E_s/N_0 = 10$dB with Gaussian pulse shaping filter orthogonalized by using the IOTA algorithm with roll-off $\alpha = 0.1$.

Finally, in Fig. 11.8 it is reported the SEP versus $\Delta\epsilon$ at $\bar{\gamma} = 45$ dB for BPSK GFDM system with Dirichlet pulse shaping filter and Gaussian pulse shaping filter orthogonalized by using the IOTA algorithm with roll-off $\alpha = 0.1$ in the case of transmission over the frequency selective Rayleigh fading channel. From the figure we observe that for

low CFO values the performance achieved with this filter is worse in comparison to that achieved by Dirichlet pulse shaping filter.

Our derived SEP expressions allows to quantify the sensitivity to CFO of GFDM for different orthogonal prototype pulse shaping filters. Since our derived analytical expressions take into account the shape of the impulse response it is possible to evaluate the impact of a given CFO for different values of M. In order to evaluate the sensitivity of GFDM system as compared to OFDM, we need to consider both at same spectral efficiency. Moreover, in the presence of a CP of length $N_{CP;GFDM}$, transmission rate of GFDM as a function of the symbol rate Rs is given by

$$R_{s_{GFDM}} = \frac{MK + N_{CP;GFDM}}{MK} \, R_s. \tag{11.65}$$

Similarly, the transmission rate of the OFDM system CP of length $N_{CP;OFDM}$ is

$$R_{s_{OFDM}} = \frac{N + N_{CP;OFDM}}{N} \, R_s, \tag{11.66}$$

where N is the number of sub-carriers. The ratio between the transmission rates given in (11.65) and (11.66) is

$$\frac{R_{s_{GFDM}}}{R_{s_{OFDM}}} = \frac{MK + N_{CP;GFDM}}{M \, (N + N_{CP;OFDM})} \tag{11.67}$$

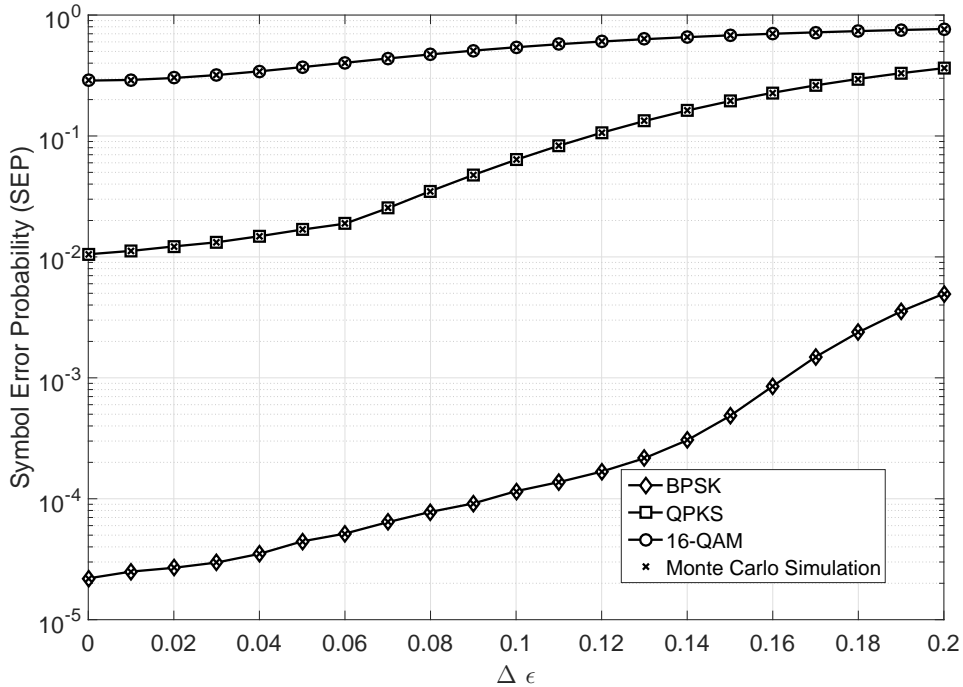**Figure 11.6:** *SEP verses CFO ($\Delta\epsilon$) of BPSK, QPSK and 16-QAM GFDM in AWGN channel with Dirichlet pulse shaping filter with $M = 9$ and $K = 64$ at $E_s/N_0 = 10dB$.*
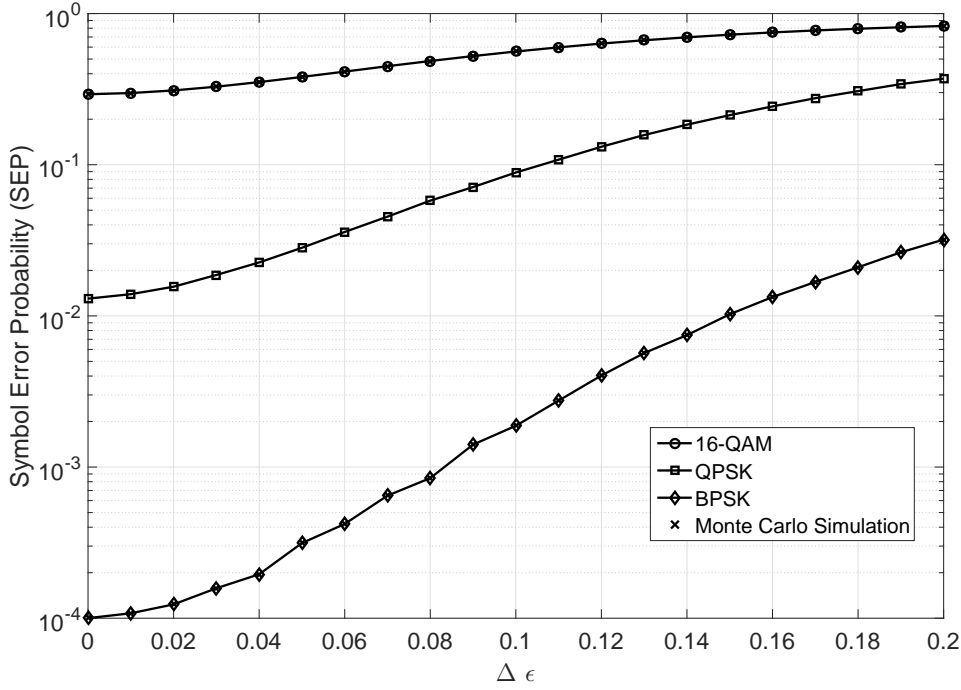
Figure 11.7: *SEP verses CFO ($\Delta\epsilon$) of BPSK, QPSK and 16-QAM GFDM in AWGN channel with IOTA Gaussian pulse shaping filter with roll-off (α) = 0.1 with $M = 9$ and $K = 64$ at $E_s/N_0 = 10dB$.*

In the following we assume that $N_{CP;OFDM} = N_{CP;GFDM} = N_{CP}$

$$R_{s_{OFDM}} = \frac{M \ (N + N_{CP})}{K + N_{CP}} R_{s_{GFDM}} = \xi R_{s_{GFDM}} \qquad (11.68)$$

As observed in [153], a fair comparison between GFDM and OFDM must be done for the same spectral efficiency. For a given bandwidth, the same spectral efficiency can be obtained by reducing the sub-carrier spacing by a factor of M in OFDM compared to GFDM. This means that $N = MK$, if we set $N = K$, the same spectral efficiency is achieved by increasing transmission rate of OFDM by a factor of ξ compared to GFDM as defined in (11.68). This leads to a bandwidth expansion of ξ that, for a given power spectral density, implies an increase of the noise power as conventionally measured in a bandwidth equal to the symbol rate. For a given average power of the useful signal, the SNR associated with OFDM is scaled by the factor ξ with respect to that associated with GFDM. Since, in general, $\xi \geq 1$, the resulting SNR is lower and depends on the parameters *K* and M. Note that, when $M = 1$ OFDM and GFDM has same rate and, therefore, same SNR. In order to evaluate SEP versus $\Delta\epsilon$ performance in the case of 2-tap equal power delay profile frequency selective Rayleigh fading channel for the different values of M by considering the same bandwidth and $K = 64$ and $N_{CP} = 2$.

We computed the ξ for different values of *M*, due to change in the ξ, the value of SNR change ($SNR_{News} = 1/\xi \times SNR_{M=1}$).
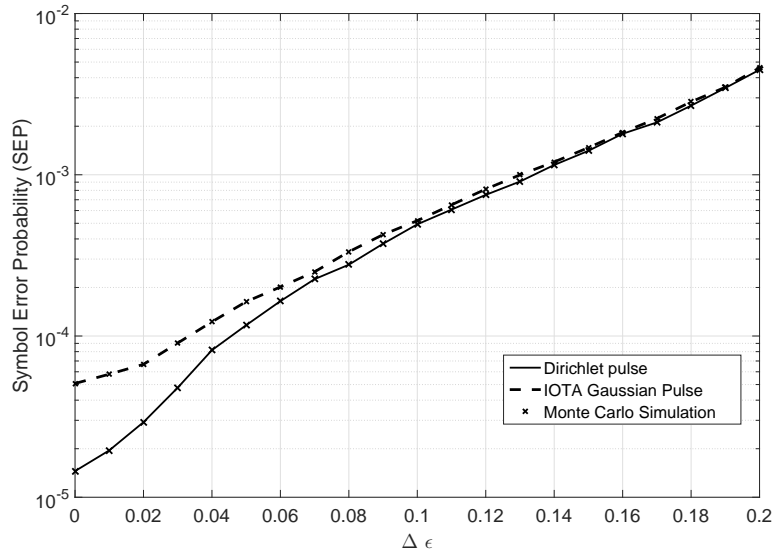
Figure 11.8: *SEP verses CFO ($\Delta\epsilon$) of BPSK GFDM in frequency selective Rayleigh fading channel with Dirichlet pulse shaping filter and orthogonal Gaussian pulse shaping filter of rolloff (α) = 0.1 with $M = 9$ and $K = 64$ at $\bar{\gamma} = 45dB$.*
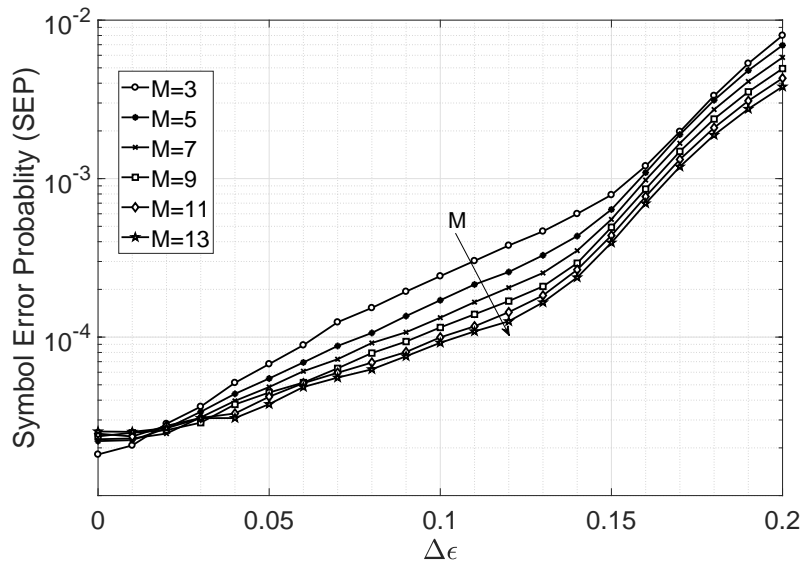
Figure 11.9: *SEP verses CFO ($\Delta\epsilon$) of BPSK GFDM in frequency selective Rayleigh fading channel with Dirichlet pulse shaping filter with different values of M for same value of the bandwidth for $K = 64$ at $\bar{\gamma} = 45dB$.*

Fig. 11.9 reported the SEP versus CFO ($\Delta\epsilon$) at $\bar{\gamma} = 45$ dB for BPSK GFDM system with Dirichlet pulse shaping filter in the case of transmission over the frequency selective Rayleigh fading channel for different values of M at $K = 64$ for same band-

183

width. Form the figure we observe that by increasing the values of M at a fixed K SEP performance is going better and better because of the change in the SNR. Moreover, by following [153] and [140], it is clearly viable by increasing value of M for the fixed K also spectral efficacy is improving.

11.5 Summary

The main novel contributions of this chapter are:

1. Definition of a GFDM system model with MF receiver for a generalized multipath channel that include CFO effects.

2. Derivation of exact SEP expressions for:

    - BPSK, QPSK, and 16-QAM modulation formats in case of transmission over AWGN channel;
    - BPSK in case of transmission over a frequency selective Rayleigh fading channel.

The correctness of our derived analytical expressions have been verified by comparison with OFDM system as a special case of GFDM system for which we get the conventional OFDM. Also perfect match has been observed between analytical SEP performance and Monte Carlo simulations. Two pulse shapes were considered: Dirichlet pulse shaping and orthogonalized Gaussian pulse shaping. We also compared the sensitivity of SEP versus CFO for GFDM and OFDM with the same spectral efficiency and bandwidth.

Conclusions and Further Scope

THIS chapter is organised as starting from the conclusions of Thesis and then after further scope of this work is decided through the problem formulation after making a literature survey thoroughly based on synchronization problem in the physical layer design and also its impact on the performance of the system. After that summary of further scope of this work are also given.

12.1 Conclusion

As it is well known, 4G cellular system based on LTE and LTE-A employ OFDM in PHY design. OFDM is a special case of wideband multi-carrier modulation in which multiple symbols are transmitted in parallel using different sub-carriers with overlapping frequency bands that are mutually orthogonal. An equivalent wideband frequency bandwidth is separated into a number of narrowband signals. The time dispersion caused by multipath delay is reduced because the symbol duration of a narrowband signal will be larger than that of a wideband transmission scheme.

Although OFDM has several advantages, it also presents some disadvantages that are mainly introduced by synchronization issues like high sensitivity to STO and CFO. CFO is due to either mismatching of transmitter and receiver oscillator's frequencies or Doppler spread while STO is caused by the discrepancy between the current sampling phase and the optimal one. The presence of CFO destroys the orthogonality among sub-carriers, generating ICI. The presence of STO introduces phase rotations in frequency domain, within the same symbol, and ISI, between successive symbols.

CFO and STO estimations methods are broadly categorized into two groups: data-aided approaches and non-data-aided approaches. However, data-aided approaches, *i.e.*, using null sub-carriers or special training symbols, can allow for faster timing and frequency synchronization, requiring a smaller number of received symbols at the cost of a reduced data rate. In this Thesis, we considered data aided approach, where chirp signal is considered as training sequences for the estimation of the CFO and STO. A comparison the MSE performance with the different methods available in the literature together with DFrFT-based chirp based signal has been done. From the results demonstrated in this Thesis it is shown that DFrFT-based chip method gives superior performance compared to other methods available in the literature. We also plotted the timing metric of different methods available in the literature, and found that the peak of timing metric gives us the information about the starting point of DFrFT window in a OFDM system of received frame.

After CFO and STO estimation, in the presence of oscillator drifts and time-varying Doppler shifts, residual CFO and STO are still present in the received signal after the application of synchronization algorithms. In order to improve the robustness of residual CFO and STO, an OFDM system based on DFrFT is considered in this Thesis. Moreover, to analyse the impact of residual CFO and STO in the OFDM system, an analytical performance analysis of the DFrFT-based OFDM system in the presence of the residual synchronization error is evaluated. Analytical results were verified with Monte Carlo simulation. The results presented in this Thesis demonstrate that at optimal value of the angle parameter α_{opt} of the DFrFT-based OFDM system outperforms DFT-based OFDM one because of lower sensitivity to STO and CFO. For $\alpha = \pi/2$ DFrFT-based OFDM system converts to DFT-OFDM system.

Finally, we also considered more practical aspect of the DFrFT-based OFDM system, related to the realization of SDR system that is used to implement hardware co-simulation of multi-carrier transmission techniques. A Simulink model was developed for OFDM system by following the model based design workflow. For the development of Simulink model, we follow the workflow design for rapid prototyping of DFrFT-based OFDM system in a FPGA and verification of SER performance of transmission over frequency selective Rayleigh fading channel with CFO was considered for rapid prototyping. Simulation results presented in this Thesis, clearly demonstrate that the FPGA implementation of a DFrFT-based OFDM system in presence of CFO has the same performance as that of Monte Carlo simulation. Also, the performance is validated with the fixed-point model of DFrFT-based OFDM. The approach described in this Thesis constitutes an efficient way to convert the floating-point model into a fixed-point one to be run in an FPGA and then verified its correctness through FIL co-simulation.

However, as it is well known for future cellular system, ITU has categorized the usage scenarios for IMT in the 2020 time frame and beyond into three main groups: eMBB, mMTC, and URLLC. The different variety of services are emerging as new applications based on the future need. In order to target all these scenarios, flexible waveforms is one of the major requirements. Where as OFDM based on DFT, uses a fixed set of waveform parameters, including sub-carrier spacing and length of the

CP, uniformly applied across the entire system bandwidth. A main issue of such a fixed design is the lack of flexibility to support mixed services with different waveform parameters within one carrier, which is a key requirement in physical layer of future cellular networks.

For this reason, we look for new waveforms that are able to support variable and customizable pulse shaping filters in order to achieve a better trade-off between time-domain and frequency-domain localization. This is one of the research priorities. With this aim, GFDM is one of the proposed modulation schemes, which is based on the use of circular filtering at sub-carrier level. Compared to OFDM, the main advantages of GFDM are in a reduction of OOBE, achieved by means of filtering at sub-carrier level, and an increase of the spectral efficiency, obtained through the introduction of tail biting, which makes the length of CP independent from that of pulse shaping filter. Moreover, the flexible frame structure of GFDM allows, the changing of number of time slots and sub-carriers in a frame, covering both conventional OFDM and DFT-s-OFDM, which result in complete backward compatibility with LTE.

Motivated by the fact of GFDM system, we started the studies of GFDM system in which, first we integrate GFDM signal in current LTE system that uses the same clock rate and is configured to fit the same time-frequency grid. After integration of GFDM into LTE system, we have analysed the impact of "Better than Nyquist" on OOB emission. Although the GFDM having low OOBE guarantees low interference in LTE signals but LTE OOBE will affect the GFDM signal. Another, motivation of this work is to investigate the sensitivity of SER performance of different pulse shaping filters.

Despite above mentioned advantages of GFDM compared to OFDM, a main issue is the need of equalization, implemented by block-based processing in time or frequency domain, that is required even in case of transmission over an ideal channel. For an efficient implementation of GFDM receiver in time-domain, a relationship between GFDM signal and DGT. We also extended the DGT-based GFDM system for SER performance by taking into the account of interference introduced by the sub-symbols on each sub-carrier. For SER performance evaluation at receiver side, we implemented the maximum likelihood detection.

Another issue of GFDM, is synchronization errors, *i.e.*, CFO and STO. In order to analyses the impact of synchronization errors in GFDM system, In this Thesis, we derived exact SEP expressions for GFDM system for the first time. Where, we considered the case where MF is used at the receiver in the presence of CFO for transmission over AWGN and frequency selective Rayleigh fading channels.

12.2 Future Scope

To strengthen the use of GFDM as a future wireless waveform, the natural continuation of the research effort is necessary. There are several future scopes listed below:

1. By developing the chirp-based DFrFT estimation algorithms for the estimation of CFO and STO in the GFDM system

2. As a future research, we intend apply to the concept of FrFT-based GFDM in order to reduce OOB emission and to improve tolerance to ICI and ISI and to consider the adaptation to GFDM.

3. To pave the way to practical implementation, not only synchronization, but also a method for channel estimation needs to be developed.

4. Massive MIMO is an another relevant technique that uses beam forming and diversity techniques to improve the system in terms of reliability, data rates, and multiple access capabilities. The presented analysis can be easily extended to the case of massive multiple-input and multiple-output (MIMO) channel. To this aim, the channel model given in (10.5) must be modified to include also the spatial characteristic. In particular, by focusing on the case of uniform planar array with M antennas at the transmitter and a single antenna at the receiver, in [154] a 3D space-time channel model is proposed by associating a steering vector, defined by azimuthal and the elevation angle of departures (AoDs), to each multi-path component. The resulting multipath channel model is

$$\mathbf{h}\left(t\right) = \sum_{l=0}^{L-1} h_l\left(t\right) \delta\left(t - \tau_l T\right) \mathbf{a}\left(\phi_l(t), \theta_l(t)\right), \tag{12.1}$$

where $\mathbf{a}\left(\phi_l(t), \theta_l(t)\right)$ is the time-varying steering vector associated with the lth path defined as

$$\mathbf{a}\left(\phi_l(t), \theta_l(t)\right) = \left[1, e^{j2\pi\frac{d}{\lambda}\sin(\theta_l(t))}, \cdots, e^{j2\pi\frac{d}{\lambda}(M_2-1)\sin(\theta_l(t))}\right]$$
$$\otimes \frac{1}{\sqrt{M}}\left[1, e^{j2\pi\frac{d}{\lambda}\cos(\theta_l(t))\sin(\phi_l(t))}, \cdots, e^{j2\pi\frac{d}{\lambda}(M_1-1)\cos(\theta_l(t))\sin(\phi_l(t))}\right]^T, \tag{12.2}$$

being $\otimes$ the Kronecker product, $\phi_{u,l}$ and $\theta_{u,l}$ the azimuthal and elevation AoD, respectively, and M_1 and M_2 are the number of horizontal and vertical antennas, respectively, and $M = M_1 \times M_2$. In general, as observed in [155], angle coherence time is higher compared to classical channel coherence time, which leads to slow variations in time of AoDs compared to those of complex amplitudes $h_l(t)$. Therefore, when the same block fading assumption done in Sec. II.C is made, the channel model given in (12.1) can be written as

$$\mathbf{h}\left(t\right) = \sum_{l=0}^{L-1} h_l \delta\left(t - \tau_l T\right) \mathbf{a}\left(\phi_l, \theta_l\right). \tag{12.3}$$

By adopting the classical narrowband channel assumption, the above equation reduces to the same spatial channel vector defined by [154, eq. (1)] giving rise to

$$\mathbf{h} = \sum_{l=0}^{L-1} h_l \mathbf{a}\left(\phi_l, \theta_l\right). \tag{12.4}$$

In massive MIMO, the spatial channel model defined in (12.4) is used by the transmitter to perform beam forming where the resulting channel is modeled as a scalar coefficient.

5. Due to the short frames of GFDM has a positive impact on mobility support and operational frequencies, it is possible either to support higher mobility or to operate in a higher frequency range. By keeping this motivation of GFDM, another possible solution is the development of PHY for High-speed trains. High speed is responsible for Doppler spreading that introduces a mismatch between carrier and oscillator frequencies.

6. Another possible extension is for cooperative multi-point, a challenge faced in cooperative multi-point is timing and frequency synchronization of different base stations. The problem arises both in downlink as well as in uplink. Investigated solutions to address this issue consists in adopting better timing and frequency synchronization methods, maybe by taking advantage from very good frequency localization properties of FrFT.

7. By applying the channel encoder in the future to confirm the improve the further SEP results.

8. By applying the source encoder in the future to confirm the improve the further SEP results.

Appendices

APPENDIX $\mathcal{A}$

Appendix of Derivate of BPSK SEP expression

The computation of $\partial P_s(\xi)/\partial\alpha$ is given in (A.1), where $P=\frac{Af_+(\alpha)}{1+Af_+(\alpha)+\bar{\gamma}_k a_q^k}$, $Q=\frac{Af_-(\alpha)}{1+Af_-(\alpha)+\bar{\gamma}_k a_q^k}$, with $f_+(\alpha) = (\Re[S(0,k)]+z_q^k)^2$ and $f_-(\alpha) = (\Re[S(0,k)]-z_q^k)^2$; $A = \bar{\gamma}_k C_{\beta(k)\beta(k)}$; $\frac{\partial f_+(\alpha)}{\partial\alpha} = 2(\Re[S(0,k)]+z_q^k)\left(\frac{\partial\Re[S(0,k)]}{\partial\alpha}+\frac{\partial z_q^k}{\partial\alpha}\right)$, and $\frac{\partial f_-(\alpha)}{\partial\alpha}=2(\Re[S(0,k)]-z_q^k)\left(\frac{\partial\Re[S(0,k)]}{\partial\alpha}-\frac{\partial z_q^k}{\partial\alpha}\right)$.

The individual terms appearing in the above equations are defined in (A.2), (A.4)-(A.6), (A.8), and (A.9). To compute $\partial P_s(\xi)/\partial\alpha$, we first need to compute the derivative of the several individual terms such as $S(0,k)$, z_q^k and the a_q^k with respect to α, where z_q^k and a_q^k are the mean and variance of conditional random variables $b_q^k|\beta(k)$, respectively given in (11.57). To this aim, we split the expression of $S(l,k)$, with $l=q-k, q\neq k$, given in (4.23) into two separate terms as

$$S(0,k)=\frac{b(k)}{N}\underbrace{e^{-j\frac{k^2 u^2 \cot(\alpha)}{2}}}_{f_1(\alpha)}\underbrace{\sum_{n=0}^{N-1}e^{j\frac{2\pi\Delta\epsilon n}{N}}e^{j\frac{n^2 T^2 \cot(\alpha)}{2}}}_{f_2(\alpha,\Delta\epsilon)}\underbrace{\sum_{m=0}^{N-1}e^{-j\frac{m^2 T^2 \cot(\alpha)}{2}}e^{j\frac{2\pi mk}{N}}}_{f_3(\alpha)}, \quad (A.2)$$

and

$$S(l,k)=\frac{b(l+k)}{N}\underbrace{e^{j\frac{(l^2-k^2)u^2 \cot(\alpha)}{2}}}_{f_4(l,\alpha)}\underbrace{\sum_{n=0}^{N-1}e^{j\frac{2\pi(\Delta\epsilon-l)n}{N}}e^{j\frac{n^2 T^2 \cot(\alpha)}{2}}}_{f_5(l,\alpha,\Delta\epsilon)}\underbrace{\sum_{m=0}^{N-1}e^{-j\frac{m^2 T^2 \cot(\alpha)}{2}}e^{j\frac{2\pi mk}{N}}}_{f_3(\alpha)},$$

$$(A.3)$$

Appendix A. Appendix of Derivate of BPSK SEP expression

$$\frac{\partial P_s\left(\xi\right)}{\partial\alpha}=\frac{1}{N2^N}\sum_{q=1}^{2^{N-2}-1}\sum_{k=0}^{N-1}\frac{\partial}{\partial\alpha}\left\{f_1\sqrt{P}+f_2\sqrt{Q}\right\}$$

$$=\frac{1}{N2^N}\sum_{q=1}^{2^{N-2}-1}\sum_{k=0}^{N-1}\left\{f_1\frac{\partial\sqrt{P}}{\partial\alpha}+\sqrt{P}\frac{\partial f_1}{\partial\alpha}+f_2\frac{\partial\sqrt{Q}}{\partial\alpha}+\sqrt{Q}\frac{\partial f_2}{\partial\alpha}\right\}$$

$$=\frac{-1}{N2^N}\sum_{q=1}^{2^{N-2}-1}\sum_{k=0}^{N-1}\left\{\frac{f_1}{2\sqrt{p}}\frac{A\frac{\partial f_+(\alpha)}{\partial\alpha}\left(1+Af_+(\alpha)+\bar{\gamma}_k a_q^k\right)-Af_+(\alpha)\frac{\partial}{\partial\alpha}\left(1+Af_+(\alpha)+\bar{\gamma}_k a_q^k\right)}{\left(1+Af_+(\alpha)+\bar{\gamma}_k a_q^k\right)^2}+\frac{\sqrt{P}\partial}{\partial\alpha}\left(sign\left(\sqrt{f_+(\alpha)}\right)\right)\right.$$

$$\left.+f_2\frac{1}{2\sqrt{Q}}\frac{A\frac{\partial f_-(\alpha)}{\partial\alpha}\left(1+Af_-(\alpha)+\bar{\gamma}_k a_q^k\right)-Af_-(\alpha)\frac{\partial}{\partial\alpha}\left(1+Af_-(\alpha)+\bar{\gamma}_k a_q^k\right)}{\left(1+Af_-(\alpha)+\bar{\gamma}_k a_q^k\right)^2}+\sqrt{Q}\frac{\partial}{\partial\alpha}\left(sign\left(\sqrt{f_-(\alpha)}\right)\right)\right\}$$

$$=\frac{1}{N2^N}\sum_{q=1}^{2^{N-2}-1}\sum_{k=0}^{N-1}\left\{\frac{f_1}{2\sqrt{p}}\frac{A\bar{\gamma}_k\left(a_q^k\frac{\partial f_+(\alpha)}{\partial\alpha}-f_+(\alpha)\frac{\partial a_q^k}{\partial\alpha}\right)+A\frac{\partial f_+(\alpha)}{\partial\alpha}}{\left(1+Af_+(\alpha)+\bar{\gamma}_k a_q^k\right)^2}+\sqrt{P}\frac{\partial}{\partial\alpha}\left(sign\left(\sqrt{f_+(\alpha)}\right)\right)\right.$$

$$\left.+f_2\frac{1}{2\sqrt{Q}}\frac{A\bar{\gamma}_k\left(a_q^k\frac{\partial f_-(\alpha)}{\partial\alpha}-f_-(\alpha)\frac{\partial a_q^k}{\partial\alpha}\right)+A\frac{\partial f_-(\alpha)}{\partial\alpha}}{\left(1+Af_-(\alpha)+\bar{\gamma}_k a_q^k\right)^2}+\sqrt{Q}\frac{\partial}{\partial\alpha}\left(sign\left(\sqrt{f_-(\alpha)}\right)\right)\right\}$$

$$\text{(A.1)}$$

After separating into two terms, by using $S(l,k)$ term given in (A.3), we can rewrite the expressions of z_q^k and a_q^k as

$$z_q^k=C_{\beta(k)\beta(k)}^{-1}\Re[\left(\boldsymbol{e}_q^T\operatorname{diag}(S(1,k),\cdots,S(N-1,k))\right)C_{\boldsymbol{\beta}_k\beta(k)}] \tag{A.4}$$

and

$$a_q^k=\left(\boldsymbol{e}_q^T\operatorname{diag}(S(1,k),\cdot,S(N-1,k))\right)C_{\boldsymbol{\beta}_k|\beta(k)}\left(\boldsymbol{e}_q^T\operatorname{diag}(S(1,k),\cdot,S(N-1,k))\right)^H \tag{A.5}$$

The derivative of the individual terms $S(0,k)$, z_q^k and a_q^k with respect to α are given in eqs. (A.6), (A.8) and (A.9) respectively, as

$$\frac{\partial z_q^k}{\partial\alpha}=C_{\beta(k)\beta(k)}^{-1}\Re\left[\boldsymbol{e}_q^T\begin{bmatrix}\frac{\partial S(1,k)}{\partial\alpha}&&\\&\ddots&\\&&\frac{\partial S(N-1,k)}{\partial\alpha}\end{bmatrix}C_{\boldsymbol{\beta}_k\beta(k)}\right], \tag{A.8}$$

and

$$\frac{\partial a_q^k}{\partial\alpha}=\left[\boldsymbol{e}_q^T\begin{bmatrix}\frac{\partial S(1,k)}{\partial\alpha}&&\\&\ddots&\\&&\frac{\partial S(N-1,k)}{\partial\alpha}\end{bmatrix}C_{\boldsymbol{\beta}_k|\beta(k)}\left(\boldsymbol{e}_q^T\operatorname{diag}(S(1,k),\cdot,S(N-1,k))\right)^H\right.$$

$$\left.+\left(\boldsymbol{e}_q^T\operatorname{diag}(S(1,k),\cdot,S(N-1,k))\right)C_{\boldsymbol{\beta}_k|\beta(k)}\left(\boldsymbol{e}_q^T\begin{bmatrix}\frac{\partial S(1,k)}{\partial\alpha}&&\\&\ddots&\\&&\frac{\partial S(N-1,k)}{\partial\alpha}\end{bmatrix}\right)^H\right]. \tag{A.9}$$

The result of $\partial S(l,k)/\partial\alpha$ is given in (A.7), for $l=1,\ldots N-1$.

$$\frac{\partial S(0,k)}{\partial \alpha} = \frac{b(k)}{N}\frac{\partial}{\partial \alpha}\Big(f_1(\alpha)\cdot f_2(\alpha,\Delta\epsilon)\cdot f_3(\alpha)\Big)$$

$$= \frac{b(k)}{N}\bigg(f_1(\alpha)\cdot f_2(\alpha,\Delta\epsilon)\cdot \frac{\partial f_3(\alpha)}{\partial \alpha} + f_1(\alpha)\cdot f_3(\alpha)\cdot \frac{\partial f_2(\alpha,\Delta\epsilon)}{\partial \alpha} + f_3(\alpha)\cdot f_2(\alpha,\Delta\epsilon)\cdot \frac{\partial f_1(\alpha)}{\partial \alpha}\bigg)$$

$$= \frac{b(k)}{N}\bigg(e^{-j\frac{k^2u^2\cot(\alpha)}{2}}\cdot \sum_{n=0}^{N-1}e^{j\frac{2\pi\Delta\epsilon n}{N}}e^{j\frac{n^2T^2\cot(\alpha)}{2}}\cdot \sum_{m=0}^{N-1}e^{j\frac{2\pi mk}{N}}\left(\frac{jm^2}{2}\left(\cot(\alpha)^2+1\right)e^{-\frac{jm^2T^2\cot(\alpha)}{2}}\right)$$

$$+ e^{-j\frac{k^2u^2\cot(\alpha)}{2}}\cdot \sum_{m=0}^{N-1}e^{-j\frac{m^2T^2\cot(\alpha)}{2}}e^{j\frac{2\pi mk}{N}}\cdot \sum_{n=0}^{N-1}e^{j\frac{2\pi\Delta\epsilon n}{N}}\left(\frac{-jn^2}{2}\left(\cot(\alpha)^2+1\right)e^{\frac{jn^2T^2\cot(\alpha)}{2}}\right)$$

$$+ \sum_{m=0}^{N-1}e^{-j\frac{m^2T^2\cot(\alpha)}{2}}e^{j\frac{2\pi mk}{N}}\sum_{n=0}^{N-1}e^{j\frac{2\pi\Delta\epsilon n}{N}}e^{j\frac{n^2T^2\cot(\alpha)}{2}}e^{-\frac{2jk^2\pi^2|\sin\alpha|^2\cot\alpha}{N^2}}$$

$$\left(\frac{2jk^2\pi^2|\sin\alpha|^2(\cot(\alpha)^2+1)}{N^2} - \frac{4jk^2\pi^2|\sin\alpha|sign\left(\sin(\alpha)\right)\cos\alpha\cot\alpha}{N^2}\right) \qquad \text{(A.6)}$$

$$\frac{\partial S(l,k)}{\partial \alpha} = \frac{b(k)}{N}\frac{\partial}{\partial \alpha}\Big(f_4(l,\alpha)\cdot f_5(l,\alpha,\Delta\epsilon)\cdot f_3(\alpha)\Big)$$

$$= \frac{b(k)}{N}\bigg(f_4(l,\alpha)\cdot f_5(l,\alpha,\Delta\epsilon)\cdot \frac{\partial f_3(\alpha)}{\partial \alpha} + f_4(l,\alpha)\cdot f_3(\alpha)\cdot \frac{\partial f_5(l,\alpha,\Delta\epsilon)}{\partial \alpha} + f_3(\alpha)\cdot f_5(l,\alpha,\Delta\epsilon)\cdot \frac{\partial f_4(l,\alpha)}{\partial \alpha}\bigg)$$

$$= \frac{b(k)}{N}\bigg(e^{j\frac{(l^2-k^2)u^2\cot(\alpha)}{2}}\cdot \sum_{n=0}^{N-1}e^{j\frac{2\pi(\Delta\epsilon-l)n}{N}}e^{j\frac{n^2T^2\cot(\alpha)}{2}}\cdot \sum_{m=0}^{N-1}e^{j\frac{2\pi mk}{N}}\left(\frac{jm^2}{2}\left(\cot(\alpha)^2+1\right)e^{-\frac{jm^2T^2\cot(\alpha)}{2}}\right)$$

$$+ e^{j\frac{(l^2-k^2)u^2\cot(\alpha)}{2}}\cdot \sum_{m=0}^{N-1}e^{-j\frac{m^2T^2\cot(\alpha)}{2}}e^{j\frac{2\pi mk}{N}}\cdot \sum_{n=0}^{N-1}e^{j\frac{2\pi(\Delta\epsilon-l)n}{N}}\left(\frac{-jn^2}{2}(\cot(\alpha)^2+1)e^{\frac{jn^2T^2\cot(\alpha)}{2}}\right)$$

$$+ \sum_{m=0}^{N-1}e^{-j\frac{m^2T^2\cot(\alpha)}{2}}e^{j\frac{2\pi mk}{N}}\cdot \sum_{n=0}^{N-1}e^{j\frac{2\pi(\Delta\epsilon-l)n}{N}}e^{j\frac{n^2T^2\cot(\alpha)}{2}\cdot}e^{\frac{4\pi^2|\sin\alpha|^2\cot\alpha\left(\frac{j}{2}\left(k^2-l^2\right)\right)}{N^2}}$$

$$\left(\frac{4\pi^2|\sin\alpha|^2(\cot(\alpha)^2+1)\left(\frac{j}{2}\left(k^2-l^2\right)\right)}{N^2} - \frac{8\pi^2|\sin\alpha|sign\left(\sin(\alpha)\right)\cos\alpha\cot\alpha\left(\frac{j}{2}\left(k^2-l^2\right)\right)}{N^2}\right)$$

$$\text{(A.7)}$$

Bibliography

[1] P. Wei, X. G. Xia, Y. Xiao, and S. Li, "Fast dgt-based receivers for gfdm in broadband channels," *IEEE Transactions on Communications*, vol. 64, pp. 4331–4345, Oct 2016.

[2] F. Luo and C. Zhang, *Signal Processing for 5G: Algorithms and Implementations*. Wiley - IEEE, Wiley, 2016.

[3] Y. Cai, Z. Qin, F. Cui, G. Y. Li, and J. A. McCann, "Modulation and multiple access for 5g networks," *IEEE Communications Surveys Tutorials*, vol. 20, pp. 629–646, Marchr 2018.

[4] X. Zhang, L. Chen, J. Qiu, and J. Abdoli, "On the waveform for 5g," *IEEE Communications Magazine*, vol. 54, pp. 74–80, November 2016.

[5] J. G. Andrews, S. Buzzi, W. Choi, S. V. Hanly, A. Lozano, A. C. K. Soong, and J. C. Zhang, "What will 5g be?," *IEEE Journal on Selected Areas in Communications*, vol. 32, pp. 1065–1082, June 2014.

[6] B. Furht and S. Ahson, *Long Term Evolution: 3GPP LTE Radio and Cellular Technology*. Internet and Communications, CRC Press, 2016.

[7] T. Taleb and A. Kunz, "Machine type communications in 3gpp networks: potential, challenges, and solutions," *IEEE Communications Magazine*, vol. 50, pp. 178–184, March 2012.

[8] G. P. Fettweis, "The tactile internet: Applications and challenges," *IEEE Vehicular Technology Magazine*, vol. 9, pp. 64–70, March 2014.

[9] C. J. Zhang, J. Ma, G. Y. Li, W. Yu, N. Jindal, Y. Kishiyama, and S. Parkvall, "New waveforms for 5g networks," *IEEE Communications Magazine*, vol. 54, pp. 64–65, November 2016.

[10] M. Shafi, P. J. Smith, P. Zhu, T. Haustein, and A. F. Molisch, "Guest editorial deployment issues and performance challenges for 5g, part 1," *IEEE Journal on Selected Areas in Communications*, vol. 35, pp. 1197–1200, June 2017.

[11] M. Shafi, P. J. Smith, P. Zhu, T. Haustein, and A. F. Molisch, "Guest editorial part 2: Deployment issues and performance challenges for 5g," *IEEE Journal on Selected Areas in Communications*, vol. 35, pp. 1697–1700, Aug 2017.

[12] A. A. Zaidi, R. Baldemair, H. Tullberg, H. Bjorkegren, L. Sundstrom, J. Medbo, C. Kilinc, and I. D. Silva, "Waveform and numerology to support 5g services and requirements," *IEEE Communications Magazine*, vol. 54, pp. 90–98, November 2016.

[13] P. Schulz, M. Matthe, H. Klessig, M. Simsek, G. Fettweis, J. Ansari, S. A. Ashraf, B. Almeroth, J. Voigt, I. Riedel, A. Puschmann, A. Mitschele-Thiel, M. Muller, T. Elste, and M. Windisch, "Latency critical iot applications in 5g: Perspective on the design of radio interface and network architecture," *IEEE Communications Magazine*, vol. 55, pp. 70–78, February 2017.

[14] G. Durisi, T. Koch, and P. Popovski, "Toward massive, ultrareliable, and low-latency wireless communication with short packets," *Proceedings of the IEEE*, vol. 104, pp. 1711–1726, Sept 2016.

[15] P. Popovski, K. F. Trillingsgaard, O. Simeone, and G. Durisi, "5g wireless network slicing for embb, urllc, and mmtc: A communication-theoretic view," *CoRR*, vol. abs/1804.05057, 2018.

[16] G. Wunder, P. Jung, M. Kasparick, T. Wild, F. Schaich, Y. Chen, S. T. Brink, I. Gaspar, N. Michailow, A. Festag, L. Mendes, N. Cassiau, D. Ktenas, M. Dryjanski, S. Pietrzyk, B. Eged, P. Vago, and F. Wiedmann, "5gnow: non-orthogonal, asynchronous waveforms for future mobile applications," *IEEE Communications Magazine*, vol. 52, pp. 97–105, February 2014.

[17] K. Pedersen, F. Frederiksen, G. Berardinelli, and P. Mogensen, "A flexible frame structure for 5g wide area," in *2015 IEEE 82nd Vehicular Technology Conference (VTC2015-Fall)*, pp. 1–5, Sept 2015.

[18] H. Li, L. Han, R. Duan, and G. M. Garner, "Analysis of the synchronization requirements of 5g and corresponding solutions," *IEEE Communications Standards Magazine*, vol. 1, pp. 52–58, March 2017.

[19] B. Farhang-Boroujeny and H. Moradi, "Ofdm inspired waveforms for 5g," *IEEE Communications Surveys Tutorials*, vol. 18, pp. 2474–2492, Fourthquarter 2016.

[20] A.-L. S. B. Nokia, "New radio waveforms for the multi-service air interface below 6 ghz," *3GPP, R1-165012, Nanjing, China*, pp. 23–27, May 2016.

[21] C. Kim, K. Kim, Y. H. Yun, Z. Ho, B. Lee, and J. Y. Seol, "Qam-fbmc: A new multi-carrier system for post-ofdm wireless communications," in *2015 IEEE Global Communications Conference (GLOBECOM)*, pp. 1–6, Dec 2015.

[22] Q. Inc., "Waveform candidates," *3GPP, R1-162199, Busan, Korea*, pp. 11–15, Apr 2016.

[23] X. Zhang, M. Jia, L. Chen, J. Ma, and J. Qiu, "Filtered-ofdm - enabler for flexible waveform in the 5th generation cellular networks," in *2015 IEEE Global Communications Conference (GLOBECOM)*, pp. 1–6, Dec 2015.

[24] I. N. Laboratory, "Waveform for the next generation radio interface," *3GPP, R1-162248, Busan, Korea*, pp. 11–15, Apr. 2016.

[25] F. Hlawatsch and F. Auger, *Time-frequency analysis*. John Wiley & Sons, 2013.

[26] R. W. Heath, G. Laus, T. Q. S. Quek, S. Talwar, and P. Zhou, "Signal processing for the 5g revolution [from the guest editors]," *IEEE Signal Processing Magazine*, vol. 31, pp. 12–13, Nov 2014.

[27] G. Wunder, H. Boche, T. Strohmer, and P. Jung, "Sparse signal processing concepts for efficient 5g system design," *IEEE Access*, vol. 3, pp. 195–208, 2015.

[28] M. Martone, "A multicarrier system based on the fractional fourier transform for time-frequency-selective channels," *IEEE Transactions on Communications*, vol. 49, pp. 1011–1020, Jun 2001.

[29] Z. Wang, L. Mei, X. Wang, and N. Zhang, "Bit error rate analysis of generalised frequency division multiplexing with weighted-type fractional fourier transform precoding," *IET Communications*, vol. 11, no. 6, pp. 916–924, 2017.

[30] D. Wei, Y. M. Li, and R. Wang, "Time 8211;frequency analysis method based on affine fourier transform and gabor transform," *IET Signal Processing*, vol. 11, no. 2, pp. 213–220, 2017.

[31] M. MatthÃ©, L. L. Mendes, and G. Fettweis, "Generalized frequency division multiplexing in a gabor transform setting," *IEEE Communications Letters*, vol. 18, pp. 1379–1382, Aug 2014.

[32] S. Sriram, N. Vijayakumar, P. A. Kumar, A. S. Shetty, V. Prasshanth, and K. Narayanankutty, "Spectrally efficient multi-carrier modulation using gabor transform," *Wireless Engineering and Technology*, vol. 4, no. 02, p. 112, 2013.

[33] A. Papoulis, *The Fourier Integral and Its Applications. Papoulis*. McGraw-Hill, 1962.

[34] S.-C. Pei and J.-J. Ding, "Closed-form discrete fractional and affine fourier transforms," *IEEE Transactions on Signal Processing*, vol. 48, pp. 1338–1353, May 2000.

[35] A. I. Zayed, "On the relationship between the fourier and fractional fourier transforms," *IEEE Signal Processing Letters*, vol. 3, pp. 310–311, Dec 1996.

[36] H. Bolcskei and F. Hlawatsch, "Discrete zak transforms, polyphase transforms, and applications," *IEEE Transactions on Signal Processing*, vol. 45, pp. 851–866, Apr 1997.

[37] R. N. Bracewell, "The fast hartley transform," *Proceedings of the IEEE*, vol. 72, pp. 1010–1018, Aug 1984.

[38] B. Bellalta, L. Bononi, R. Bruno, and A. Kassler, "Next generation ieee 802.11 wireless local area networks: Current status, future directions and open challenges," *Computer Communications*, vol. 75, pp. 1–25, 2016.

[39] C. Shahriar, M. L. Pan, M. Lichtman, T. C. Clancy, R. McGwier, R. Tandon, S. Sodagari, and J. H. Reed, "Phy-layer resiliency in ofdm communications: A tutorial," *IEEE Communications Surveys Tutorials*, vol. 17, pp. 292–314, Firstquarter 2015.

[40] F. Schaich and T. Wild, "Waveform contenders for 5g x2014; ofdm vs. fbmc vs. ufmc," in *2014 6th International Symposium on Communications, Control and Signal Processing (ISCCSP)*, pp. 457–460, May 2014.

[41] G. Wunder, P. Jung, M. Kasparick, T. Wild, F. Schaich, Y. Chen, S. T. Brink, I. Gaspar, N. Michailow, A. Festag, L. Mendes, N. Cassiau, D. Ktenas, M. Dryjanski, S. Pietrzyk, B. Eged, P. Vago, and F. Wiedmann, "5gnow: non-orthogonal, asynchronous waveforms for future mobile applications," *IEEE Communications Magazine*, vol. 52, pp. 97–105, February 2014.

[42] J. Abdoli, M. Jia, and J. Ma, "Filtered ofdm: A new waveform for future wireless systems," in *2015 IEEE 16th International Workshop on Signal Processing Advances in Wireless Communications (SPAWC)*, pp. 66–70, June 2015.

[43] L. Zhang, A. Ijaz, P. Xiao, M. M. Molu, and R. Tafazolli, "Filtered ofdm systems, algorithms, and performance analysis for 5g and beyond," *IEEE Transactions on Communications*, vol. 66, pp. 1205–1218, March 2018.

[44] B. Farhang-Boroujeny, "Ofdm versus filter bank multicarrier," *IEEE Signal Processing Magazine*, vol. 28, pp. 92–112, May 2011.

[45] M. Matthä©, L. L. Mendes, and G. Fettweis, "Generalized frequency division multiplexing in a gabor transform setting," *IEEE Communications Letters*, vol. 18, pp. 1379–1382, Aug 2014.

[46] P. Siohan, C. Siclet, and N. Lacaille, "Analysis and design of ofdm/oqam systems based on filterbank theory," *IEEE Trans. Signal Process*, vol. 50, pp. 1170–1183, May 2002.

[47] T. Erseghe, N. Laurenti, and V. Cellini, "A multicarrier architecture based upon the affine fourier transform," *IEEE Transactions on Communications*, vol. 53, no. 5, pp. 853–862, 2005.

[48] S. Weinstein and P. Ebert, "Data transmission by frequency-division multiplexing using the discrete fourier transform," *IEEE Transactions on Communication Technology*, vol. 19, pp. 628–634, October 1971.

[49] Y. Wang and X. Dong, "Comparison of frequency offset and timing offset effects on the performance of sc-fde and ofdm over uwb channels," *IEEE Transactions on Vehicular Technology*, vol. 58, pp. 242–250, Jan 2009.

[50] A. M. Hamza and J. W. Mark, "Closed form ser expressions for qpsk ofdm systems with frequency offset in rayleigh fading channels," *IEEE Communications Letters*, vol. 18, pp. 1687–1690, Oct 2014.

[51] G. Yi, L. Gang, and G. Jianhua, "A novel time and frequency synchronization scheme for ofdm systems," *IEEE Transactions on Consumer Electronics*, vol. 54, pp. 321–325, May 2008.

[52] H. Lin and P. Siohan, "Orthogonality improved gfdm with low complexity implementation," *2015 IEEE Wireless Communications and Networking Conference (WCNC)*, pp. 597–602, 2015.

[53] A. Farhang, N. Marchetti, and L. E. Doyle, "Low-complexity modem design for gfdm," *IEEE Transactions on Signal Processing*, vol. 64, pp. 1507–1518, March 2016.

[54] R. Chang and R. Gibby, "A theoretical study of performance of an orthogonal multiplexing data transmission scheme," *IEEE Transactions on Communication Technology*, vol. 16, pp. 529–540, August 1968.

[55] B. Saltzberg, "Performance of an efficient parallel data transmission system," *IEEE Transactions on Communication Technology*, vol. 15, pp. 805–811, December 1967.

[56] A. Peled and A. Ruiz, "Frequency domain data transmission using reduced computational complexity algorithms," in *ICASSP '80. IEEE International Conference on Acoustics, Speech, and Signal Processing*, vol. 5, pp. 964–967, Apr 1980.

[57] B. Hirosaki, "An analysis of automatic equalizers for orthogonally multiplexed qam systems," *IEEE Transactions on Communications*, vol. 28, pp. 73–83, January 1980.

[58] W. H. Tranter, D. P. Taylor, R. E. Ziemer, N. F. Maxemchuk, and J. W. Mark, *Analysis and Simulation of a Digital Mobile Channel Using Orthogonal Frequency Division Multiplexing*, pp. 692–. Wiley-IEEE Press, 2007.

[59] T. Keller and L. Hanzo, "Adaptive multicarrier modulation: a convenient framework for time-frequency processing in wireless communications," *Proceedings of the IEEE*, vol. 88, pp. 611–640, May 2000.

[60] R. Zayani, Y. Medjahdi, H. Shaiek, and D. Roviras, "Wola-ofdm: A potential candidate for asynchronous 5g," in *2016 IEEE Globecom Workshops (GC Wkshps)*, pp. 1–5, Dec 2016.

[61] N. C. Beaulieu and P. Tan, "On the effects of receiver windowing on ofdm performance in the presence of carrier frequency offset," *IEEE Transactions on Wireless Communications*, vol. 6, pp. 202–209, Jan 2007.

[62] I. Daubechies, *Ten Lectures on Wavelets*. CBMS-NSF Regional Conference Series in Applied Mathematics, Society for Industrial and Applied Mathematics, 1992.

[63] Y. Meyer and R. Coifman, "Ondelettes et opérateurs. ii, actualités mathématiques.[current mathematical topics], hermann, paris, 1990," *Opérateurs de Calderón-Zygmund.[Calderón-Zygmund operators]*.

[64] R. U. Mahesh and A. K. Chaturvedi, "Closed form ber expressions for bpsk ofdm systems with fractional timing offset and carrier frequency offset," in *2012 National Conference on Communications (NCC)*, pp. 1–4, Feb 2012.

[65] V. Vakilian, T. Wild, F. Schaich, S. ten Brink, and J. Frigon, "Universal-filtered multi-carrier technique for wireless systems beyond lte," in *2013 IEEE Globecom Workshops (GC Wkshps)*, pp. 223–228, Dec 2013.

[66] X. Wang, T. Wild, F. Schaich, and A. F. Dos Santos, "Universal filtered multi-carrier with leakage-based filter optimization," in *European Wireless Conference*, pp. 1–5, 2014.

[67] X. Zhang, M. Jia, L. Chen, J. Ma, and J. Qiu, "Filtered-ofdm - enabler for flexible waveform in the 5th generation cellular networks.," *CoRR*, vol. abs/1508.07387, 2015.

[68] M. Morelli, C. . J. Kuo, and M. Pun, "Synchronization techniques for orthogonal frequency division multiple access (ofdma): A tutorial review," *Proceedings of the IEEE*, vol. 95, pp. 1394–1427, July 2007.

[69] M. Speth, S. A. Fechtel, G. Fock, and H. Meyr, "Optimum receiver design for wireless broad-band systems using ofdm. i," *IEEE Transactions on Communications*, vol. 47, pp. 1668–1677, Nov 1999.

[70] T. Pollet, M. V. Bladel, and M. Moeneclaey, "Ber sensitivity of ofdm systems to carrier frequency offset and wiener phase noise," *IEEE Transactions on Communications*, vol. 43, pp. 191–193, Feb 1995.

[71] P. H. Moose, "A technique for orthogonal frequency division multiplexing frequency offset correction," *IEEE Transactions on Communications*, vol. 42, pp. 2908–2914, Oct 1994.

[72] X. Ma, C. Tepedelenlioglu, G. B. Giannakis, and S. Barbarossa, "Non-data-aided carrier offset estimators for ofdm with null subcarriers: identifiability, algorithms, and performance," *IEEE Journal on Selected Areas in Communications*, vol. 19, pp. 2504–2515, Dec 2001.

[73] J. J. van de Beek, M. Sandell, and P. O. Borjesson, "Ml estimation of time and frequency offset in ofdm systems," *IEEE Transactions on Signal Processing*, vol. 45, pp. 1800–1805, July 1997.

[74] N. Lashkarian and S. Kiaei, "Class of cyclic-based estimators for frequency-offset estimation of ofdm systems," *IEEE Transactions on Communications*, vol. 48, pp. 2139–2149, Dec 2000.

[75] T. M. Schmidl and D. C. Cox, "Robust frequency and timing synchronization for ofdm," *IEEE Transactions on Communications*, vol. 45, pp. 1613–1621, Dec 1997.

[76] M. Morelli, C. C. J. Kuo, and M. O. Pun, "Synchronization techniques for orthogonal frequency division multiple access (ofdma): A tutorial review," *Proceedings of the IEEE*, vol. 95, pp. 1394–1427, July 2007.

[77] J. J. van de Beek, M. Sandell, and P. O. Borjesson, "Ml estimation of time and frequency offset in ofdm systems," *IEEE Transactions on Signal Processing*, vol. 45, pp. 1800–1805, July 1997.

[78] G. Ren, Y. Chang, H. Zhang, and H. Zhang, "Synchronization method based on a new constant envelop preamble for ofdm systems," *IEEE Transactions on Broadcasting*, vol. 51, pp. 139–143, 2005.

[79] H. Minn, M. Zeng, and V. K. Bhargava, "On timing offset estimation for ofdm systems," *IEEE Communications Letters*, vol. 4, pp. 242–244, July 2000.

[80] H. Minn, V. K. Bhargava, and K. B. Letaief, "A robust timing and frequency synchronization for ofdm systems," *IEEE Transactions on Wireless Communications*, vol. 2, pp. 822–839, July 2003.

[81] A. B. Awoseyila, C. Kasparis, and B. G. Evans, "Robust time-domain timing and frequency synchronization for ofdm systems," *IEEE Transactions on Consumer Electronics*, vol. 55, pp. 391–399, May 2009.

[82] B. Park, H. Cheon, C. Kang, and D. Hong, "A novel timing estimation method for ofdm systems," *IEEE Communications Letters*, vol. 7, pp. 239–241, May 2003.

[83] A. J. Coulson, "Maximum likelihood synchronization for ofdm using a pilot symbol: algorithms," *IEEE Journal on Selected Areas in Communications*, vol. 19, pp. 2486–2494, Dec 2001.

[84] A. B. Awoseyila, C. Kasparis, and B. G. Evans, "Improved preamble-aided timing estimation for ofdm systems," *IEEE Communications Letters*, vol. 12, pp. 825–827, November 2008.

[85] R. Saxena and H. Joshi, "Frft based timing estimation method for an ofdm system," 2014.

[86] A. Stelter, "Random access and channel allocation scheme for hiperlan/2 system," in *2005 IEEE 16th International Symposium on Personal, Indoor and Mobile Radio Communications*, vol. 3, pp. 1484–1488 Vol. 3, Sept 2005.

[87] L. Wei, Y. Y. Xu, Y. M. Cai, and X. Xu, "Robust frequency offset estimator for ofdm over fast varying multipath channel," *Electronics Letters*, vol. 43, pp. 53–54, March 2007.

[88] P. A. Bello, "Selective fading limitations of the kathryn modem and some system design considerations,," *IEEE Trans. Commun. Technol.*, vol. 13, p. 1965, Sept. 1968.

[89] M. S. Zimmerman and A. L. Kirsch, "The an/gsc-10 (kathryn) variable rate data modem for hf radio,," *IEEE Trans. Commun.*, p. 1965, Sept.

[90] "Orthogonal frequency division multiplexing,," *U. S. Patent No. 3,488,445 and Filed Nov*, vol. 1970, 14, 1966, Issued Jan. 6.

[91] J. S. Chow, J. C. Tu, and J. M. Cioffi, "Discrete multitone transceiver system for hdsl applications,," *IEEE J. Select. Areas Commun.*, vol. 9, p. 908, August 1991.

[92] B. Hirosaki, "An analysis of automatic equalizers for orthogonally multiplexed qam systems," *Commun.*, vol. 28, January 1980.

[93] A. Peled and A. Ruiz, "Frequency doma in data transmission using reduced computationnal complexity algorithms," in *80, vol. 5, pp.964 -967*, (Speech, and Signal Processing, IEEE International Conference on ICASSP), Acoustics, April 1980.

[94] E. F. Casas and C. Lung, "Ofdm for data communication over mobile radio fm channels- part i analysis and experimental results,," *IEEE Trans. Commun.*, vol. 3, pp. 783–793, May 1991.

[95] M. Okada, S. Hara, and N. Morinaga, "A study on bit error rate performance for multicarrier modulation radio transmission systems,," tech. rep., Technical Report, RCS91-44, pp. 19-24, 1991.

[96] S. Hara, M. Mouri, M. Okada, and N. Morinaga, "Transmission performance analysis of multicarrier modulation in frequency selective fast rayleigh fading channel,," *Wireless Personal Commun.,*, vol. 2, no. 4, pp. 335–996.

[97] T. Pollet, M. V. Bladel, and M. Moeneclaey, "Ber sensitivity of ofdm to carrier frequency offset and wiener phase noise,," *IEEE Trans. Commun.,*, vol. 43, February 1995.

[98] K. Sathananthan and C. Tellambura, "Probability of error calculation of ofdm systems with frequency offset,," *IEEE Trans. on Commun*, vol. 49, no. 11, pp. 1884–1888, 2001.

[99] L. Rugini and P. Banelli, "Ber of ofdm systems impaired by carrier frequency offset in multipath fading channels," *IEEE Trans. on Wireless Commun.*, vol. 4, no. 5, pp. 2279–2288, 2005.

[100] P. Dharmawansa, N. Rajatheva, and H. Minn, "An exact error probability analysis of ofdm systems with frequency offset," *IEEE Trans. Commun*, vol. 57, pp. 26–31, January 2009.

[101] R. U. Mahesh and A. K. Chaturvedi, "Closed form ber expressions for bpsk ofdm systems with frequency offset," *in IEEE Comm. Lett*, vol. 14, pp. 731–733, August 2010.

[102] R. Uma Mahesh and A. Chaturvedi, "Closed form ber expressions for bpsk ofdm systems with fractional timing offset and carrier frequency offset," 02 2012.

[103] J. Zheng and Z. Wang, "Ici analysis for frft-ofdm systems to frequency offset in time-frequency selective fading channels," *IEEE Communications Letters*, vol. 14, pp. 888–890, October 2010.

[104] Y. Wang, Z. Zhang, and Y. Chen, "Ber analysis of bpsk ofdm systems with residual frequency and timing offsets over frequency selective rayleigh fading channels," vol. 8, pp. 10349–10357, 12 2012.

[105] e. a. S. Kumari Electron. Lett*, number = 20, pages = 1299-1301, title = "Exact BER analysis of FRFT-OFDM system over frequency selective Rayleigh fading channel with CFO,", volume = 49, year = 2013,*.

[106] Z. Wang, L. Mei, and X. Wang, ""ber analysis of hybrid carrier system based on wfrft with carrier frequency offset,"," Electron. Lett , vol. 51, no. 21, pp. 1708–1909, 2015.

[107] M. Mousavi and A. Shahzadi, "Hyperbolic frft-ofdm system ber analysis over high doppler rician fading channels," *Electron. Lett*, vol. 51, no. 24, pp. 2003–2005, 2015.

[108] A. M. Hamza and J. W. Mark, "Closed-form expressions for the ber/ser of ofdm systems with an integer time offset," *IEEE Transactions on Communications*, vol. 63, pp. 4461–4473, Nov 2015.

[109] A. Kumar, S. Bregni, and M. Magarini, "An exact ser expression for qpsk ofdm system in presence of residual cfo and sto," in *2016 8th IEEE Latin-American Conference on Communications (LATINCOM)*, pp. 1–6, Nov 2016.

[110] A. Kumar, M. Magarini, H. D. Joshi, and R. Saxena, "Exact ser analysis of dfrft-based qpsk ofdm system over frequency selective rayleigh fading channel with cfo," J. Computer Netw. Commun.,, vol. vol. 2016, p. 7, 2016.

[111] V. Trivedi, S. Kumari, and P. kumar, ""generalized error analysis of frft-ofdm over nakagami-m fading channel with arbitrary m," in," *IET Communications*, vol. 11, p. 9, 2017.

[112] P. Tan and N. C. Beaulieu, "Reduced ici in ofdm systems using the 'better than' raised-cosine pulse,," *IEEE Commun. Lett.,*, vol. 8, pp. 135–137, March 2004.

[113] N. C. Beaulieu and P. Tan, "On the effects of receiver windowing on ofdm performance in the presence of carrier frequency offset,," *IEEE Trans Wireless Commun*, vol. 6, no. 1, pp. 202–209, 2007.

[114] M. K. Simon and M. S. Alouini, *Digital Communication over fading channels*. -Interscience: Wiley, 2nd ed., 2005.

[115] A. Annamalai, C. Tellambura, and V. K. Bhargava, "A general method for calculating error probabilities over fading channels," *IEEE Trans. Commun*, vol. 53, pp. 841–852, May 2005.

[116] A. K. Singh and R. Saxena, "Dfrft: a classified review of recent methods with its application," *Journal of Engineering*, vol. 2013, 2013.

[117] S.-C. Pei, C.-C. Tseng, and M.-H. Yeh, "A new discrete fractional fourier transform based on constrained eigendecomposition of dft matrix by lagrange multiplier method," *IEEE Transactions on Circuits and Systems II: Analog and Digital Signal Processing*, vol. 46, pp. 1240–1245, Sep 1999.

[118] C. Candan, M. A. Kutay, and H. M. Ozaktas, "The discrete fractional fourier transform," *IEEE Transactions on Signal Processing*, vol. 48, pp. 1329–1337, May 2000.

[119] B. Santhanam and J. H. McClellan, "The discrete rotational fourier transform," *IEEE Transactions on Signal Processing*, vol. 44, pp. 994–998, Apr 1996.

[120] T. Erseghe, P. Kraniauskas, and G. Carioraro, "Unified fractional fourier transform and sampling theorem," *IEEE Transactions on Signal Processing*, vol. 47, pp. 3419–3423, Dec 1999.

[121] S. Liu, T. Shan, R. Tao, Y. D. Zhang, G. Zhang, F. Zhang, and Y. Wang, "Sparse discrete fractional fourier transform and its applications," *IEEE Transactions on Signal Processing*, vol. 62, pp. 6582–6595, Dec 2014.

[122] S.-C. Pei and J.-J. Ding, "Closed-form discrete fractional and affine fourier transforms," *IEEE Transactions on Signal Processing*, vol. 48, pp. 1338–1353, May 2000.

[123] A. C. Gilbert, P. Indyk, M. Iwen, and L. Schmidt, "Recent developments in the sparse fourier transform: A compressed fourier transform for big data," *IEEE Signal Processing Magazine*, vol. 31, pp. 91–100, Sept 2014.

[124] A. Kumar, M. Magarini, and S. Olivieri, "Rapid prototyping and fpga-in-the-loop verification of a dfrft-based ofdm system," in *2017 25th European Signal Processing Conference (EUSIPCO)*, pp. 2526–2530, Aug 2017.

[125] Y. H. Hu and S. Naganathan, "A novel implementation of chirp z transformation using a cordic processor,," *IEEE Transactions on ASSP,*, vol. 38, pp. 352–354.

[126] e. a. A. A. Zaidi, ""waveform and numerology to support 5g services and requirements,"," IEEE Commun. Mag.,, vol. 54, pp. 90–98, November 2016.

[127] S. Lien, S. Shieh, Y. Huang, B. Su, Y. Hsu, and H. Wei, "5g new radio: Waveform, frame structure, multiple access, and initial access," *IEEE Communications Magazine*, vol. 55, no. 6, pp. 64–71, 2017.

[128] G. Durgin, *Space-time Wireless Channels*. Prentice Hall communications engineering and emerging technologies series, Prentice Hall PTR, 2003.

[129] R. Chang, "High-speed multichannel data transmission with bandlimited orthogonal signals," *Bell Sys. Tech. J*, vol. 45, no. 10, pp. 1775–1796, 1966.

[130] B. Saltzberg, "Performance of an efficient parallel data transmission system," *IEEE Transactions on Communication Technology*, vol. 15, no. 6, pp. 805–811, 1967.

[131] M. Bellanger and J. Daguet, "Tdm-fdm transmultiplexer: Digital polyphase and fft," *IEEE Transactions on Communications*, vol. 22, no. 9, pp. 1199–1205, 1974.

[132] B. L. Floch, M. Alard, and C. Berrou, "Coded orthogonal frequency division multiplex [tv broadcasting]," *Proceedings of the IEEE*, vol. 83, pp. 982–996, June 1995.

[133] G. Cherubini, E. Eleftheriou, and S. Olcer, "Filtered multitone modulation for very high-speed digital subscriber lines," *IEEE Journal on Selected Areas in Communications*, vol. 20, pp. 1016–1028, June 2002.

[134] A. Viholainen, T. Ihalainen, T. H. Stitz, M. Renfors, and M. Bellanger, "Prototype filter design for filter bank based multicarrier transmission," in *European Signal Proc. Conf*, (Glasgow, Aug), pp. 1359–1363, Proc. of, 2009.

Bibliography

[135] N. Michailow, M. Matthé, I. S. Gaspar, A. N. Caldevilla, L. L. Mendes, A. Festag, and G. Fettweis, "Generalized frequency division multiplexing for 5th generation cellular networks," *IEEE Transactions on Communications*, vol. 62, pp. 3045–3061, Sept 2014.

[136] M. Nekovee, "Quantifying performance requirements of vehicle-to-vehicle communication protocols for rear-end collision avoidance," in *VTC Spring 2009 - IEEE 69th Vehicular Technology Conference*, pp. 1–5, April 2009.

[137] I. S. Gaspar, L. L. Mendes, N. Michailow, and G. Fettweis, "A synchronization technique for frequency division multiplexing," *EURASIP Journal on Advances in Signal Processing*, vol. 1, 2014.

[138] A. Kumar, M. Magarini, H. D. Joshi, and R. Saxena, "Exact sep analysis of dfrft-based qpsk ofdm system over frequency selective rayleigh fading channel with cfo," *Journal of Computer Networks and Communications,*, vol. 2016, 2016.

[139] C. H. Choi, B. J. Lim, Y. J. Kim, and Y. C. Ko, ""effect of timing and frequency synchronization errors on gfdm systems,"," *Information and Communication Technology Convergence (ICTC)*, pp. 1322–1325, 2015.

[140] B. Lim and Y. C. Ko, "Sir analysis of ofdm and gfdm waveforms with timing offset, cfo, and phase noise," *IEEE Trans. on Wire. Comm*, vol. 16, pp. 6979–6990, October 2017.

[141] D. Gaspar, L. Mendes, and T. Pimenta, ""gfdm ber under synchronization errors,"," *IEEE Comm. Lett*, vol. 21, pp. 1743–1746, April 2017.

[142] M. Matthé, N. Michailow, I. Gaspar, and G. Fettweis, "Influence of pulse shaping on bit error rate performance and out of band radiation of generalized frequency division multiplexing," in *2014 IEEE International Conference on Communications Workshops (ICC)*, pp. 43–48, June 2014.

[143] P. Siohan, C. Siclet, and N. Lacaille, "Analysis and design of ofdm/oqam systems based on filterbank theory," *IEEE Transactions on Signal Processing*, vol. 50, pp. 1170–1183, May 2002.

[144] D. Guimaraes, *Digital Transmission: A Simulation-Aided Introduction with Vis-Sim/Comm*. Signals and Communication Technology, Springer Berlin Heidelberg, 2010.

[145] I. Daubechies, *Ten Lectures on Wavelets*. CBMS-NSF Regional Conference Series in Applied Mathematics, Society for Industrial and Applied Mathematics, 1992.

[146] M. Misiti, Y. Misiti, G. Oppenheim, and J. Poggi, *Wavelets and their Applications*. ISTE, Wiley, 2013.

[147] W. W. Jones and J. C. Dill, "The square root raised cosine wavelet and its relation to the meyer functions," *IEEE Transactions on Signal Processing*, vol. 49, pp. 248–251, Jan 2001.

[148] A. Assalini and A. M. Tonello, "Improved nyquist pulses," *IEEE Communications Letters*, vol. 8, pp. 87–89, Feb 2004.

[149] A. Kumar and M. Magarini, "Improved nyquist pulse shaping filters for generalized frequency division multiplexing," in *LATINCOM*, (Nov), pp. 1–7, Proc. of, 2016.

[150] M. K. Simon and M. s. Alouini, *Digital Communication over Fading Channels, 2nd ed.* New York: Wiley, 2005.

[151] H. Artes, D. Seethaler, and F. Hlawatsch, "Efficient detection algorithms for mimo channels: a geometrical approach to approximate ml detection," *IEEE Trans. Sig. Proc*, vol. 51, no. 11, pp. 2808–2820, 2003.

[152] C. Wang and O. J. Kim in *Proc*, *CCECE*, title = the symbol error probability of 16-QAM based OFDM systems impaired by CFO, year = 2012,, April.

[153] A. B. Ü. and, "and a. ö yılmaz, "extended oobe comparisons for ofdm, gfdm and wcp-coqam at equal spectral efficiency," arxiv." preprint, 2016.

[154] R. W. Heath, l.-P. N. Gonz, S. Rangan, W. Roh, and A. M. Sayeed, "An overview of signal processing techniques for millimeter wave mimo systems," in *IEEE Journal of Selected Topics in Signal Processing*, (vol. 10, no. 3, , April, 2016), pp. 436–453, Proc, April 2012.

[155] W. Shen, L. Dai, B. Shim, Z. Wang, and R. W. Heath, "Channel feedback based on aod-adaptive subspace codebook in fdd massive mimo systems,"